Elasticity, Lattice Dynamics and Parameterisation Techniques for the Tersoff Potential Applied to Elemental and Type III-V Semiconductors

David Powell

The University Of Sheffield

Thesis submitted to the University of Sheffield
for the degree of Doctor of Philosophy

Semiconductor Materials and Devices Group
Department of Electronic and Electrical Engineering

October, 2006

Abstract

The focus of this thesis is the techniques used in constructing a library of improved parameters for the Tersoff bond-order potential energy model which is used in atomistic modelling applications. The parameters presented here are for the elemental type-IV diamond structure semiconductors and the binary III-As, III-P, III-Sb and the cubic III-N compound semiconductors. The parameters are fitted to a number of experimental and DFT predicted properties of the materials including the lattice parameter, the cohesive energy, the elastic constants and the lattice dynamical properties, including phonon frequency and mode-Grüneisen parameters, for three pertinent locations in the Brillouin zone.

The conclusions of this work demonstrate that the elastic and dynamical properties of a material cannot be simultaneously predicted with the Tersoff potential due to a lack of flexibility in the current functional form. The balance between the radial and angular force contributions available in the bond-order term cannot replicate the delicate nature of the equilibrium in a real system and so two modifications to the Tersoff potential energy model have been proposed. The modifications include the addition of a second parameter and a linear contribution to the crystal anti-symmetry modelling term and the addition of a fourth parameter to the angular bonding term, which has been re-designed to be a more flexible summation of cosine terms.

Also included in this work is: 1) a re-modelling of Keyes' relation which relates the dimensionless elastic properties of the cubic III-V semiconductors to the lattice parameter of the material to include a second-order term for the modelling of the III-N materials, 2) a simple method for the prediction of the effective ionic charge q^* of the cubic III-V semiconductor materials based upon the X-point phonon energies and 3) the first Tersoff parameterisation of the materials GaP, InP, GaSb and InSb available in the literature.

Author's Publications

Publications based upon this work:

"The Tersoff potential for phonons in GaAs"
D. Powell, M. A. Migliorato and A. G. Cullis
Physica E Vol. 32, pp 270-272 (2006)

"Anisotropy of the electron energy levels in $In_XGa_{1-X}As$/GaAs quantum dots with non-uniform composition"
M. A. Migliorato, D. Powell, E. A. Zibik, L. R. Wilson, M. Fearn, J. H. Jefferson, M. J. Steer, M. Hopkinson and A. G. Cullis
Physica E Vol. 26, pp 436 (2005)

"Influence of composition on the piezoelectric fields and on the conduction band energy levels of $In_XGa_{1-X}As$/GaAs Quantum Dots"
M. A. Migliorato, D. Powell, S. L. Liew, A. G. Cullis, M. Fearn, J. H. Jefferson, P. Navaretti, M. J. Steer and M. Hopkinson
J. Appl. Phys. Vol. 96, pp 5169, (2004)

Contents

Acknowledgements

Immeasurable gratitude is required to be given to many people. They have provided me with inspiration, motivation and patronage throughout the past three years and kept me going through difficult and interesting times.

On a professional note, I owe a great deal of thanks and I could not have possibly completed this tome without the supervision, support, encouragement and proficient guidance of PROF. TONY CULLIS and DR. MAX MIGLIORATO.

Personally there are a great number of people who have looked out for me during my time studying in Sheffield, whether it be the endless cups of tea from KJ, the always friendly ears of ALISON, KIERON and ELENOR, the excuse to blow off some steam after work with band members KATE, BONGO and PAOLO and the computing knowledge passed on from OWAIN and DOUG. Special notes of thanks are due to JAMIE for well over a decade of personal support and friendship and to ALLEY for continually challenging me and my views of the world and for always making me smile. Thank you all.

Finally, my family have always been there to encourage me and assist me throughout my studies. I could not have made it this far through life without the undying support and revitalising faith of MUM, DAD and PHIL.

For MUM & DAD.

An ancient Greek named Democritus first came up with the idea that the world was made of indivisible particles called atoms. (He didn't base this on any physical evidence - it's just that there were so many Greeks coming up with random ideas that one of them was bound to be right.)

- J. F. BLINN

COMPUTER GRAPHICS SUPREMO

Chapter 1

Introduction

The role of compound semiconductors

Silicon is the cardinal example of a versatile multipurpose elemental semiconductor. Many applications exist for silicon; over the last 50 years it has been extremely well characterised and has provided an unparallelled technological advancement in fields including computing and telecommunications. However, silicon has a number of severe shortcomings in the sphere of semiconductor properties. Most notably silicon has an indirect bandgap, meaning that the carriers will not directly recombine to produce luminescence. To date there has been a failure to produce any high efficiency silicon optoelectronics, even with some of the more exotic strained silicon in oxide devices. Silicon will operate very efficiently at mid-range speeds but the current commercial Si technologies are hitting a processing size and associated speed limit. This has become obvious recently from the plateau of commercial CPU clock frequencies (at $\sim$ 3GHz) which is a good benchmark of the state of the art of silicon devices. The miniaturisation of on-die track widths and the associated Ohmic resistance, the power consumption and the linked thermal issues seem to have pushed progress towards parallel processing rather than research into a further increase in clock speeds. The thermal issues associated with silicon are further highlighted as commercial silicon devices are usually considered to be effective in a room temperature friendly band from -20°C to 60°C, which has been found to be a major disappointment for military and space applications. For optical purposes, high speed devices, temperature tolerant utilisation or specialist applications it is common to look towards the compound semiconductors.

The choices are many and the material properties are widely varied when considering which elements can be combined to make compound semiconductors. The section of the periodic table normally used to choose materials to make

II	III	IV	V	VI
	B	C	N	O
	Al	Si	P	S
Zn	Ga	Ge	As	Se
Cd	In	Sn	Sb	Te
Hd	Tl	Pb	Bi	Po

Table 1.1: The section of the periodic table commonly used for semiconductors

semiconductor devices from is shown in Figure 1.1. Manufacturers frequently select III-V or II-VI binary compounds such as Gallium Arsenide (GaAs), Zinc Sulphide (ZnS) or Gallium Nitride (GaN) or may combine additional materials to make ternary compounds (which are actually alloys of two binary compounds with a common element) such as $In_xGa_{1-x}As$ or quarternary compounds such as $Ga_xAl_{1-x}As_yP_{1-y}$.

Most III-V binary materials have a direct bandgap transition and are useful for optical devices such as LEDs and lasers[1]. A common characteristic of compound semiconductors is the increased carrier mobility resulting in very high speed switching (speeds ~40GHz are achievable) and due to the material hardness of the Nitride devices an opportunity is presented for high temperature operation when compared to Silicon. Nitride based devices can be useful for process control and measurement applications in extreme conditions. Compound semiconductors may be used to make devices which operate in the mid and far infra-red bands ($\lambda > 1.1\mu m$) for military applications and for telecommunications at the important $1.3\mu m$ and $1.55\mu m$ wavelengths.

Figure 1.1 shows a plot of the bandgap energy of many common cubic phase III-V semiconductors against the lattice constant of the material. Using the relation $\lambda = hc/E_g$ [2] there is a broad spectrum of photonic emissions available from the binary compounds ranging from the near infrared wavelength ($5\mu m$) of InSb through the red (CdSe at 729nm), green (ZnTe at 549nm) and blue (ZnSe at 458nm) to the near ultraviolet of ZnS at 337nm.

As an example, a semiconductor may have its bandstructure modified for a large direct energy gap transition which could be useful in ultra-violet detection ($\lambda < 0.5\mu m$) for counterfeit currency detection and skin health monitoring purposes[2]. An even more impressive feat is the ability to tune an individual semiconductor to achieve an exact emission frequency by incorporating other compound species during growth. As a simple example GaAs can have InGaAs grown upon it in a series of small strained layers to create a heterostructure *superlattice* to produce a $1.3\mu m$ emission, which is very important for modern fibre optic telecommunications. The deposition of a thin film of one material upon another that maintains the bulk substrate lattice parameter is called *pseudomorphic*

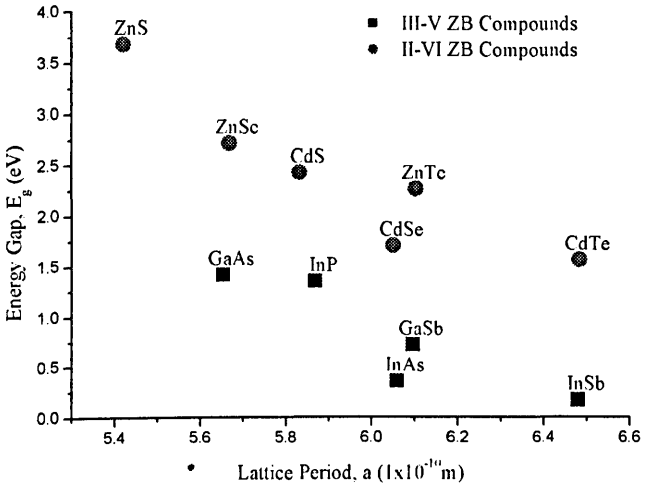

Figure 1.1: A chart of the direct bandgap binary compounds available with the Zinc Blende structure

growth and is of great importance to our ability to create semiconductor nanostructures.

Nanostructures

The strained superlattice briefly mentioned above is an example of a *nanostructure* [3]. Nanostructures have nanometre (1×10^{-9}m) sized features of interest. A nanometre is roughly 4 semiconductor atom widths, or $1/50000^{th}$ the width of a human hair. For nanostructures to operate correctly and to be useful to us they are usually embedded in a bulk semiconductor material to protect them against the atmosphere and allow for connectivity to the outside world. Semiconductor surfaces have non-radiative combination centres which stop the nanostructure from operating correctly and hence should be as far as possible from the active parts of the device.

The first nanostructure we shall briefly consider is the quantum well [4]. A quantum well is constructed when a few layers of material B are grown onto a bulk substrate material A. This is typically then capped with material A to produce a region in the bulk semiconductor which has a different set of material properties to the main part of the crystal. This is illustrated in figure 1.2. The material properties of the quantum well can be altered or tuned as described above by growing e.g. InGaAs on GaAs providing a region of quantum confinement in the semiconductor. This region can be considered to be a planar system or 2D nanostructure and the sheet of different material can act as a carrier trap until the

system obtains a certain applied bias. This is very useful to make devices such as lasers which naturally require confinement to obtain population inversion by electrical pumping. The density of states in the planar system is altered, due to the material strain, to produce a series of step edges (compared to the smooth function of a 3D density of states) where the finite size of the lowest step provides an energy gain in systems such as quantum well lasers.

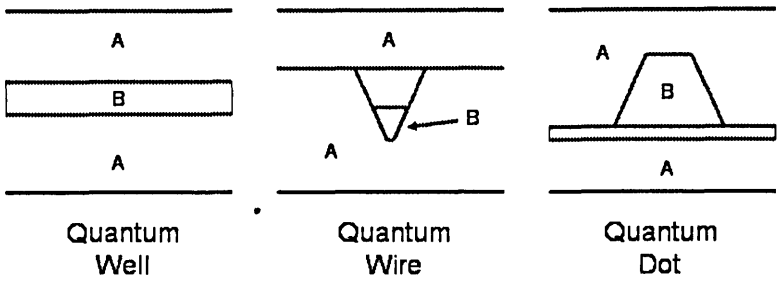

Figure 1.2: Simple illustration of a quantum well, a quantum wire and a quantum dot

A second type of nanostructure of note is the quantum wire [4]. This is formed when a V-shaped trench of material is etched away from a bulk matrix of material A and the bottom of the V is filled with material B. This feature is then capped with material A to produce a 1D line of quantum confinement in the bulk material that allows free carrier movement only along the length of the wire. Figure 1.2 has a simple illustration of this process. If we assume that material B is a semiconductor (instead of a traditional metal as the name wire would imply) then we can demonstrate that the system would have a series of singularities in the density of states, providing an opening of bandgaps and the ability to tune the semiconductor system for a desired energy output.

The third type of nanostructure we consider here briefly is the quantum dot [4, 5, 6]. An ideal quantum dot (a cube of material B embedded into the bulk of material A) would exhibit a three-dimensional confinement of the carriers and the associated 0D density of states takes the form of a series of delta functions. A cubic dot produces a ground state involving a two-fold degeneracy (including spin) and a first excited state containing six-fold degeneracy - which is similar to an atom with a two-fold degenerate s state and a six-fold degenerate p state. Quantum dots are often referred to as artificial atoms due to these properties. The ideal cubic quantum dot is however very unlikely to be produced due to the currently available growth and manufacturing processes but what we are able to achieve is a pyramid or dome shaped growth on the planar surface of material A by growing a few monolayers of material B, which is highly lattice mis-

matched with material A, until the *critical thickness*[1] [7, 8] is obtained and leads to a Stranski-Krastanow transition [9, 10] from a 2D planar growth to a 3D surface feature growth. A 3D nanostructure pyramid is shown simply grown onto a lattice mismatched wetting layer in figure 1.2.

A common feature of all of these semiconductor nanostructures is the fact that they all take advantage of pseudomorphic growth in III-V semiconductors. Pseudomorphic growth occurs when a material of a different lattice constant is grown onto a bulk substrate. If we are to take the growth of an InAs layer onto a GaAs bulk lattice as an example, from Figure 1.1 we can see that the lattice constants of GaAs (5.65325Å) and InAs (6.05833Å) do not match and we can find the level of mismatch in the system to be 7.165% from the simple equation

$$\%_{mismatch} = 100 \times \frac{a_{layer} - a_{bulk}}{a_{bulk}}$$

This 7% lattice parameter mismatch must be accounted for by the pseudomorphic growth mode, where the growth material must be able to elastically deform to take account of the lattice mismatch and strain in the growth direction. If this process does not take place or if there is more than the critical thickness of growth material in the upper layer then the system will contain misfit dislocations (where the planes in the growth direction do not correctly align). This will degrade the device electrical and optical properties due to the reduction of free carrier mobility. Epitaxial growth is illustrated diagramatically in Figure 1.3.

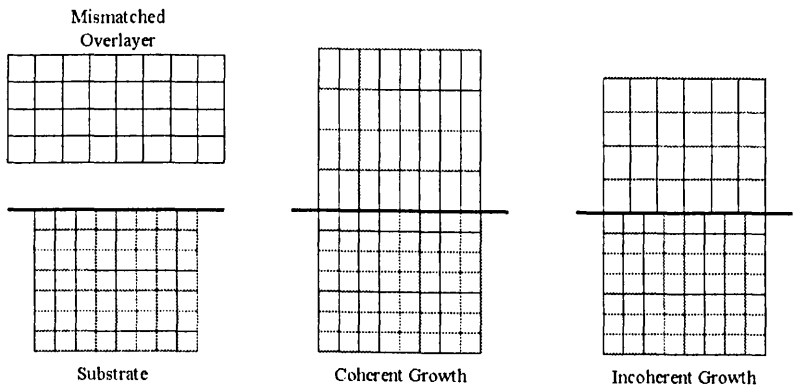

Figure 1.3: Strained layer epitaxy showing coherent (pseudomorphic) growth and incoherent growth due to misfit dislocations

When grown without defects or dislocations the material upon the substrate

[1]The critical thickness occurs when the strained material being grown upon the bulk substrate can no longer accommodate the strain energy required and growth dislocations become probable. This is usually measured in monolayers of growth material.

can have large levels of localised strain in the atomic lattice and this strain provides us with the ability to tailor the electrical properties and optical characteristics of the nanostructure devices under consideration. Although we can typically grow only a few monolayers of highly strained material before we risk dislocations appearing in the device, we can incorporate strain relief layers and begin to sandwich layers of quantum wells to create so called superlattices of material that exhibit very interesting and useful properties exploited in semiconductor laser technology. If we briefly consider using a high percentage of Indium (50% - 80%) in an InGaAs grown on GaAs device, the Stranski-Krastanow transition from 2D planes to 3D surface features takes place due to the segregation of the unincorporated Indium onto the upper surfaces of the growth material layers and growing the material to obtain a critical surface concentration of In (calculated as 80% - 85% [10]) will cause the growth surface to bulge, creating small islands. These islands can be overgrown with material for a few monolayers and then capped to form quantum dots. This well controlled self assembly mechanism provides us with an excellent opportunity to exploit the properties of the artificial atoms in optical technology for detectors, lasers or even *qubits* (quantum bits) for quantum computing.

These advances in thin film epitaxy methods, our understanding of pseudomorphic growth, electron microscopy and characterisation techniques have provided a means to experimentally explore the properties of sub-micron scale devices. However, such devices are very expensive to manufacture, especially in a research laboratory where a 10% useful device yield is not unusual. More financially acceptable is the computer modelling and prediction of the material properties of the semiconductors under consideration and the characteristics of the intended devices.

Atomistic modelling

Atomistic simulation is based upon the requirement to calculate the interatomic forces that underlie atomic bonding to investigate the properties of a piece of material. The term *atomistic modelling* encompasses a variety of computerised techniques for the simulation of condensed matter at atomic-level resolution which are widely used in materials research, engineering and physical science disciplines. The materials that we are specifically interested in here are the cubic lattice forms of the elemental type IV and the binary type III-V semiconductors. A couple of methods currently exist to provide us with the atomic force information we require about the materials of interest. Quantum mechanical simulations are con-

sidered to be highly accurate but due to the massive computational complexity inherent in the calculations they are limited to a few atoms per simulation. Classical methods are based upon Newtons Laws and can provide detailed information relating to large scale systems in a timely manner, however the simulations are considered less accurate due to the number of approximations involved in the calculations. Hence, we are faced with a classic engineering trade-off.

Classical simulation is in the unique position to bridge the gap between theoretical predictions and experimental findings. Sometimes the modelling of physical phenomena is the only choice to simulate a system as a purely theoretical *ab initio* approach can be too computationally intensive. On the other hand it is also possible that we don't have enough computational power to model huge systems - even with the reduced computational complexity of the Molecular Dynamics (MD) approach.

An atomistic simulation begins with a model of a system of roughly spherical objects that could represent atoms, molecules or defects in the system and a set of equations governing the energetics of the system with respect to the potential and kinetic energies. An important property of the energy equations is that they should be differentiable to provide calculation of the forces on the atoms (for studying atomic movements) and higher order derivatives for the investigation of elastic properties, vibrational modes and thermodynamic properties.

A number of different atomic resolution modelling techniques exist and the ones considered in this work are Molecular Statics (MS) for the relaxation of molecular systems into a lowest energy configuration and MD to study lattice properties under changing pressure and temperature. MS works by considering the system energy at an individual atomic level and manipulating the positions of the atomic species to locate a global energy minimum. This is done using a conjugated gradient or similar total energy minimisation routine. Molecular dynamics is concerned with the forces on the individual atomic locations due to the local geometry. MD reduces the amount of energy in the structure in a systematic time-step process by solving Newton's second law ($F = ma$) per atom.

Currently it is common to use quantum mechanical methods to consider detailed atomic information for models of up to 10^2 atoms in small clusters to solve specific small scale problems. Reduced scale simulations of this type can provide accurate and detailed structural information which can then be employed to improve the quality of the large scale (10^8 atoms) classical atomistic simulations. As reasonably priced computing power increases with time, it will be possible to perform larger scale atomic simulations using quantum mechanical methods, but for now we are happy to combine the two methods for reasonable results in

a reasonable amount of time. When atomistic modelling is combined with theoretical predictions and the results are compared to experimental data we have a valuable tool that allows us to predict atomic phenomena and physical processes in a timely, cost effective and reliable manner. Interestingly, with the advent of cheap multiprocessor computing and inexpensive computer memory devices we are now in a position where we can study whole nanostructure systems in a single computer simulation and models comprising 10^8 atoms are not unusual for high performance computing (HPC) clusters. This work comprises research into providing a detailed transferable energy model for classical simulation methods and the problems surrounding the parameterisation of the energy function to increase the accuracy of the classical simulation techniques.

The modelling chain

The classical atomistic simulation technique encompasses a group of operations that we label *the modelling chain*. To perform an investigation into the effects of the atomic composition in quantum dots on the piezoelectric field and the conduction band energy levels the modelling chain of Migliorato *et al* [5, 6] was as follows:

1. *Experimental data*: Initially a number of cross-sectional transmission electron microscope (TEM) samples were studied in detail to obtain the shape, size and composition of quantum dots in $In_XGa_{1-X}As$ grown on a GaAs sample.

2. *Construct model*: A 800,000 atom computer model that would reproduce a quantum dot in bulk material complete with wetting layer and a good amount of capping material was produced that would correctly model the system to the correct scale.

3. *Structural relaxation*: Although the computer model was subject to a coarse "plane bending" algorithm to allow for the ternary material present in the quantum dot, the positions of the atoms in the computer model needed to be refined to more accurately resemble the real device. A structural relaxation was performed via MD simulation that allowed the atoms to move around into local energy minima to provide a highly accurate model of a realistic quantum dot.

4. *Gridding*: Once the quantum dot and the surrounding bulk material had been relaxed into a lowest energy state, the individual point energies of the atoms were passed through a "gridding" algorithm that provided a regular three-dimensional lattice of energy values so that the grid could be subject to calculus operations for investigations of the dot properties.

5. *Piezoelectric field calculation*: Here the regular energy grid calculated in step 4 was transformed into a piezoelectric field providing information about the local strain energy in the system based upon the concentration of the ternary atoms in the quantum dot system.

6. *Wavefunction calculation*: From the energy grid provided in step 4, the quantum wave functions of the system were calculated for the ground state and the first excited energy level using $\mathbf{k} \cdot \mathbf{p}$ theory. This is expained in some detail in Appendix B which deals with the quantum dot model and the computational techniques used to calculated the wavefunctions. Derivation of the analytic integrals used in the work and the system Hamiltonian (including the effective mass approximation for the varying local strain in the model) are presented alongside the core of the computer code.

This work is mainly concerned with the operations involved in step 3 of the modelling chain, and specifically improving the quality of the potential energy function required to perform the structural relaxation of the atomic models. The structural relaxation step can be considered analogous to a molecular dynamics simulation. In a MD simulation Newton's 2^{nd} Law is iteratively solved in a time-step fashion for each atom in the system, moving each atom and re-calculating the atomic energies, until the whole structure has been reduced to its lowest energy level. We may calculate the acceleration experienced by each atomic site via the calculation of the force on each atom and dividing by the mass of that atom. The force on each atom is simply calculated as a first derivative of the energy on each atomic site and so we need a potential energy function (PEF) to relate the atoms in the system to their neighbours. The Tersoff semi-empirical potential energy model had already been chosen as the PEF of choice in the previous work of Migliorato *et al*[5, 6]. It allows for accurate and rapid simulation of multi-component systems and demands only an average computational burden in comparison to similar semi-empirical potentials.

Goals

Here we define the goals of this work as the following:

- To investigate the nature of the Tersoff potential energy function that is used to provide highly detailed and accurate structural relaxation in the modelling of large scale quantum nanostructure systems.

- To investigate methods of parameterisation of the Tersoff potential for elastic and vibrational properties. In particular, to investigate whether an in-

dividual parameterisation of the Tersoff potential (e.g. for the structural character of the material) can be transferred to provide accurate results for other material properties such as the phonon frequencies.

- To provide detailed parameterisations of the Tersoff potential for a number of different semiconductor systems and to construct a library of parameters enabling simulation of a number of different compound semiconductors.
- To attempt to reduce the computational time required to find a parameter fit of the Tersoff potential to an individual semiconductor system.

To achieve the above goals a number of things are required and are listed below:

1. *A computer*: The type of computer we choose for our atomic simulation is entirely based upon the amount of time we wish to wait for the simulation results and the amount of money we have available. The amount of time involved in an atomistic simulation is roughly proportional to the complexity of the functions we are attempting to solve and the scale of the atomic model. This time can be reduced by exchanging simple desktop computers for expensive workstations, multi-processing cluster computers or even buying processing time from high-performance computing (HPC) facilities - if we can meet the associated increasing costs.

2. *An atomic model*: In molecular dynamics simulations the atomic model typically comprises a vector of data per atom. This vector can consist of a triplet of real-valued data describing the position of the atom in three dimensional space on Cartesian axes and the atomic element at that location. It is common, however, to include more detailed information in the vector detailing the mass of the atom, the velocity of the atom (in a time stepped MD simulation), a list of neighbouring atoms and the energy at the atomic location.

3. *A potential energy function*: The PEF is an essential part of a classical simulation as it allows us to calculate the atomic site and system energies. If the PEF is continuous and differentiable it can provide information about the force on the atomic site due to the local bonding neighbourhood. If the second derivatives of the PEF are available we may calculate detailed material properties.

4. *Calculation of the material properties*: In order to parameterise the potential we need to form accurate and robust methods of calculation of the material properties of the semiconductor systems of interest. We also need

a set of values to compare our calculated values against. A comparison database of material values can be formed from experimental observations, first-principles mathematics or highly accurate quantum mechanical simulations.

Detailed consideration of each of the above points is provided in chapter 2 and is followed by a section about the theory of the material properties of the semiconductor, the elastic properties of the material, the vibrational frequencies and the phase stability of the simulated material.

The computing platform

Although it is not unusual to perform atomistic simulations on large-scale multiprocessor computing clusters, the parameterisation of the potential energy function can be performed on a much smaller system. The parameterisations listed in this work were all performed on a standard desktop machine running Fedora Core 4 Linux. The desktop machine contains a 3GHz Pentium 4 processor with 2Gb 400MHz RAM and an nVidia GeForce 5800 graphics card. Code development work was done on a laptop computer containing a 3GHz Pentium 4 processor with 512Mb 400MHz RAM and an ATI Radeon 7000 GPU. All computer code was written in ANSI standard C/C++ and the code was developed in Eclipse 3.1.1 and compiled with gcc 4.0.2 under Linux. Matrix diagonalisation for the solutions to eigenvalue equations was provided via the BLAS 3.0.36 and LAPACK 3.0.36 libraries.

Scope of this work

After this brief introduction to compound semiconductors, nanostructures and atomistic modelling there follows a chapter of background information. Details are given regarding the types of atomic lattices and the properties of the materials that are to be modelled. The material properties are defined and examined from a physical perspective and information about the elasticity theory of crystals and lattice dynamics is provided.

Chapter 3 is an introduction to the Tersoff potential energy function and includes an exhaustive literature review of the work of other authors and groups around the world and their applications of the Tersoff potential energy model. Chapter 4 comprises the results of the energy and elasticity modelling for 13 different semiconductor systems. Here results are provided for elemental type IV semiconductors, type III-arsenides, type III-phosphides, type III-antimonides

and cubic III-nitride crystals. A couple of different computation methods are discussed and all results are compared to other work wherever possible.

Chapter 5 contains the details of the lattice dynamics modelling and includes predictions given by the Tersoff potential energy function for the phonon vibrational frequencies and the associated mode-Grüneisen parameters. These results are discussed in some detail and a conclusion leading to a modification of the functional form of the Tersoff potential is provided. Chapter 6 is a general review of the work and includes a global discussion and conclusion. Future work is identified and a short plan of action is set out.

Appendix A contains the first and second derivatives of the Tersoff potential which were analytically derived and are used extensively in the calculations of the results provided in chapter 5. Appendix B contains a derivation of the Hamiltonian used to solve Schrödinger's equation for a realistic quantum dot model and the analytic integrals used in the computer program to increase the accuracy and the speed of the results.

Bibliography

[1] F. A. Ponce and D. P. Bour, "Nitride-based semiconductors for blue and green light-emitting devices," *Nature*, vol. 386, no. 6623, p. 351, 1997.

[2] J. Singh, *The physics of semiconductors and their heterostructures.* McGraw-Hill Inc., 1993.

[3] F. J. Himpsel, A. Kirakosian, J. N. Crain, J. L. Lin, and D. Y. Petrovykh, "Self-assembly of one-dimensional nanostructures at silicon surfaces," *Sol. State Comm.*, vol. 117, no. 01, pp. 149–157, 2001.

[4] C. Delerue and M. Lannoo, *Nanostructures: theory and modelling.* Springer-Verlag Berlin, 2004.

[5] M. A. Migliorato, D. Powell, S. L. Liew, A. G. Cullis, M. Fearn, J. H. Jefferson, P. Navaretti, M. J. Steer, and M. Hopkinson, "Influence of composition on the piezoelectric fields and on the conduction band energy levels of $In_XGa_{1-X}As/GaAs$ quantum dots," *J. Appl. Phys.*, vol. 96, p. 5169, 2004.

[6] M. A. Migliorato, D. Powell, E. A. Zibik, L. R. Wilson, M. Fearn, J. H. Jefferson, M. J. Steer, M. Hopkinson, and A. G. Cullis, "Anisotropy of the electron energy levels in $In_XGa_{1-X}As/GaAs$ quantum dots with non-uniform composition," *Physica E*, vol. 26, p. 436, 2005.

[7] J. W. Matthews and A. E. Blakeslee, "Defects in epitaxial multilayers: I. misfit dislocations," *J. Crys. Grow.*, vol. 27, no. 01, pp. 118–125, 1974.

[8] K. R. Elder, M. Katakowski, M. Haataja, and M. Grant, "Modelling elasticity in crystal growth," *Phys. Rev. Lett.*, vol. 88, no. 24, p. 245701, 2002.

[9] T. Walther, A. G. Cullis, D. J. Norris, and M. Hopkinson, "Nature of the Stranski-Krastanow transition during epitaxy of InGaAs on GaAs," *Phys. Rev. Lett.*, vol. 86, no. 11, pp. 2381–2384, 2001.

[10] A. G. Cullis, D. J. Norris, T. Walther, M. A. Migliorato, and M. Hopkinson, "Stranski-Krastanow transition and epitaxial island growth," *Phys. Rev. B*, vol. 66, no. 08, p. 081305, 2002.

Chapter 2

Background Theory

2.1 The lattice model

Before we can begin to model a semiconductor system with a computer we need an accurate method of representing the atomic positions and elements in computer memory. To do this we will use a lattice model. A lattice is a regular arrangement of points in three dimensional space and has the property that the units are arranged in a periodic array[1]. The internal structure of a crystal can be represented by a *Bravais lattice* which summarises the unit periodicity inside the structure and the points may be single atoms, groups of atoms or molecules.

A three dimensional Bravais lattice consists of all points with position vectors R of the form

$$\mathbf{R} = n_1\mathbf{a}_1 + n_2\mathbf{a}_2 + n_3\mathbf{a}_3 \tag{2.1}$$

where $\mathbf{a}_1$, $\mathbf{a}_2$ and $\mathbf{a}_3$ represent the three shortest (or *primitive*) vectors not lying in a plane and n_1, n_2 and n_3 cover all integer values. The Bravais lattice has the periodicity property that the array looks identical from any viewpoint.

A crystal structure is composed of a unit cell, the smallest set of atoms that allows periodic replication of the structure. The unit cell is described by the primitive vectors and the *basis set* which is periodically repeated in three dimensions to form the lattice. In this work we consider only cubic lattices that have a lattice parameter a that describes the length of all three unit cell dimensions on the normal orthogonal Cartesian axes[2]. An unstrained cubic lattice has the property

$$\hat{\mathbf{a}}_1 \cdot \hat{\mathbf{a}}_2 = \hat{\mathbf{a}}_2 \cdot \hat{\mathbf{a}}_3 = \hat{\mathbf{a}}_3 \cdot \hat{\mathbf{a}}_1 = 0$$

It is also useful sometimes to consider our lattice in reciprocal, Fourier, or k

space[3, 4]. Reciprocal space can be defined by the vector, G which is given by

$$\mathbf{G} = m_1\mathbf{b}_1 + m_2\mathbf{b}_2 + m_3\mathbf{b}_3 \tag{2.2}$$

As before, m is any integer value and the lattice is made up of b vectors which are related to the previous primitive a vectors by

$$\mathbf{b}_1 = \frac{2\pi}{\Omega}(\mathbf{a_2} \times \mathbf{a_3})$$
$$\mathbf{b}_2 = \frac{2\pi}{\Omega}(\mathbf{a_3} \times \mathbf{a_1})$$
$$\mathbf{b}_3 = \frac{2\pi}{\Omega}(\mathbf{a_1} \times \mathbf{a_2})$$

It can easily be shown that $\mathbf{G} \cdot \mathbf{R} = 2\pi N$, where N is an integer. The primitive unit cell of the k-space lattice is formed by taking the Wigner-Seitz cell, called the central *Brillouin Zone* (BZ). The Wigner-Seitz cell displays the full symmetry of the crystal lattice and can be simply located by drawing lines from a central reciprocal point to all nearest neighbours, bisecting these lines and taking the smallest enclosed region of this construction to be the central Brillouin Zone. The BZ has the same point group symmetry as the reciprocal lattice and the direct lattice it is associated with and hence if a function $f(\mathbf{k})$ exists for a vector k inside the BZ, then it will obey the crystallographic point symmetry of the direct lattice.

Boundary conditions

We should take note of *periodic boundary conditions* or the Born-von Karman[5] boundary conditions. A real crystal has finite size and will terminate with a surface. Surfaces are very complex to model and we may reduce the complexity of our simulation by considering the crystal to be infinite in all directions. This is practical for modelling a small section of bulk semiconductor. To consider the system to be infinite we must impose cyclic or periodic boundaries on the system that implies that each surface of the crystal lattice is wrapped around and connected back to the surface opposite to it. This is clearly unrealistic but it will aid computation and can be formalised

$$\phi_k(\mathbf{r} + N_i\mathbf{a_i}) = \phi_k(\mathbf{r}), \qquad i = (1, 2, 3) \tag{2.3}$$

where N_i are integer values and $\mathbf{a_i}$ are the primitive translation vectors. We must be careful not to use a system that is too small inside our periodic boundaries as it becomes problematic for the simulation to consider a system that is linked

back and bonded to itself. We have effectively connected the edge of the simulation box in each direction to an exact replica of the original box. Hence the bulk material simulation is considered to be repeated in all directions to infinity to avoid any edge effects such as surface energy modelling, which is typically more complex and can disturb bulk simulation results.

Crystal lattices

The simplest cubic crystal lattice is called "simple cubic" (sc) and is described by a single basis atom at $\mathbf{x}_1 = [0, 0, 0]$ and the simplest primitive vectors

$$\begin{aligned} \mathbf{a}_1 &= [a, 0, 0] \\ \mathbf{a}_2 &= [0, a, 0] \\ \mathbf{a}_3 &= [0, 0, a] \end{aligned}$$

This implies that in each cubic cell that comprises the lattice system there is only one atom placed in the same origin corner of each cell. This is an elemental lattice as there is only one atom type in each cell and is labelled the **Ah** crystal in *Strukturbericht notation*[6]. Strukturbericht symbols are a partly systematic method for specifying the structure of a crystal. The A structures are monatomic elemental lattices and the B structures are diatomic lattices with equal numbers of atoms of each type.

The **A1** lattice is called face centred cubic (fcc) and comprises a basis set of one atom at $\mathbf{x}_1 = [0, 0, 0]$ and three primitive vectors

$$\begin{aligned} \mathbf{a}_1 &= [0, a/2, a/2] \\ \mathbf{a}_2 &= [a/2, 0, a/2] \\ \mathbf{a}_3 &= [a/2, a/2, 0] \end{aligned}$$

Hence the fcc lattice has 4 atoms per periodic cubic unit cell. The **A2** lattice is also known as the the body centred cubic (bcc) lattice and has 2 atoms in the basis set at locations

$$\begin{aligned} \mathbf{x}_1 &= [0, 0, 0] \\ \mathbf{x}_2 &= [a/2, a/2, a/2] \end{aligned}$$

and the primitive vectors

$$\mathbf{a}_1 = [a, 0, 0]$$
$$\mathbf{a}_2 = [0, a, 0]$$
$$\mathbf{a}_3 = [0, 0, a]$$

The first B-type lattice we briefly consider is the sodium-chloride (NaCl) lattice. This is also known as the **B1** lattice and is made up of

$$\mathbf{x}_1 = [0, 0, 0] \qquad \text{Species I}$$
$$\mathbf{x}_2 = [a/2, a/2, a/2] \qquad \text{Species II}$$

and the primitive vectors

$$\mathbf{a}_1 = [0, a/2, a/2]$$
$$\mathbf{a}_2 = [a/2, 0, a/2]$$
$$\mathbf{a}_3 = [a/2, a/2, 0]$$

Hence the NaCl type lattice has 8 atoms in the cubic unit cell. The caesium chloride, CsCl, or **B2** lattice has 2 atoms in the unit cell and is the diatomic analogue of the bcc lattice. The basis set is described

$$\mathbf{x}_1 = [0, 0, 0] \qquad \text{Species I}$$
$$\mathbf{x}_2 = [a/2, a/2, a/2] \qquad \text{Species II}$$

and the primitive vectors

$$\mathbf{a}_1 = [a, 0, 0]$$
$$\mathbf{a}_2 = [0, a, 0]$$
$$\mathbf{a}_3 = [0, 0, a]$$

The diamond structure

The diamond structure, also known as the **A4** lattice, can be considered to be two interpenetrating face centred cubic (fcc) substructures which have been displaced by $(a/4, a/4, a/4)$. The cubic unit cell has 8 atoms, four of which are from each substructure. This system has a co-ordination number, z, of 4 - meaning that each atom has 4 covalent bonds to nearest neighbours. It can be natural to think of

an atomic crystal matrix in terms of cubic units but for the modelling of semiconductor systems it is usually more convenient to consider the individual atoms and their immediate environment. Each atom in the diamond crystal structure has an identical local environment over an infinite mathematical lattice - and this can sometimes simplify our modelling procedure greatly.

In a covalently bonded crystal, such as elemental silicon, the atoms share their electrons with the neighbouring atoms to complete the outer electron shells of the bonded atoms. Covalent bonds typically form between atoms of a similar outer electron shell structure such as the type IV atoms in a Si-Si bond or the type III-V atoms in a mildly ionic Ga-As bond. Because of the nature of the hybrid bonding, the atoms in a condensed solid have a preferred relaxed geometry (based upon an energy minimum in the structure) which can be stated in terms of a favoured separation distance and preferred angles. Silicon has 4 outer shell electrons which can form four sp^3 bonds with 4 neighbouring atoms and by consideration of the lowest energy configuration of 4 spheres packed around a central atom, it is intuitive that the atoms will assemble into a regular tetrahedral shape.

This diamond crystal is considered an *open lattice* as it is not in one of the closest packing configurations. The diamond lattice primitive vectors are

$$\mathbf{a}_1 = [0, a/2, a/2]$$
$$\mathbf{a}_2 = [a/2, 0, a/2]$$
$$\mathbf{a}_3 = [a/2, a/2, 0]$$

and the atomic basis set is made up of a pair of atoms described

$$\mathbf{x}_1 = [0, 0, 0]$$
$$\mathbf{x}_2 = [a/4, a/4, a/4]$$

The volume of the primitive unit cell is given by: $\Omega = |\hat{\mathbf{a}}_1 \cdot (\hat{\mathbf{a}}_2 \times \hat{\mathbf{a}}_3)|$ and the volume of the BZ is given by: $\Omega_{BZ} = \frac{(2\pi)^3}{\Omega}$.

A simple x, y, z format file can also be used to enter the information for the primitive unit cell. This is shown in Figure 2.1 where we initially give the number of the atoms in the file, a comment line (or blank line) and then describe each of the 8 atoms with an element name and the x, y, and z Cartesian spatial co-ordinates. In the file below we have described the atomic co-ordinates in cubic unit cells:

Both of the above representations produce the same result shown in Figure 2.2(a).

```
8
### Comment ### Here is the primitive unit cell of silicon
Si      0.0       0.0       0.0
Si      0.25      0.25      0.25
Si      0.0       0.5       0.5
Si      0.5       0.0       0.5
Si      0.5       0.5       0.0
Si      0.75      0.75      0.25
Si      0.75      0.25      0.75
Si      0.25      0.75      0.75
```

Figure 2.1: An example xyz input file for a cubic unit cell of diamond silicon

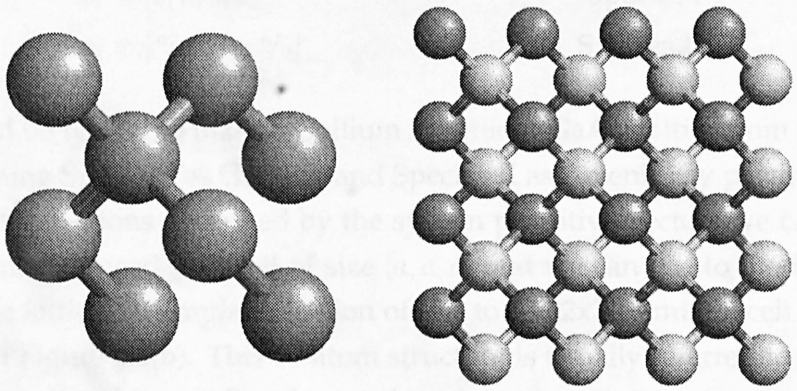

(a) Diamond Si primitive cell **(b)** Zinc Blende GaAs supercell

Figure 2.2: Examples of cubic crystal lattice structures both viewed along the [100] direction

The zinc blende structure

The Zinc Blende structure (a.k.a. the **B3** structure) is the two component analogue of the diamond structure. The stacking of the planes in the [111] direction is AB-CABC as seen in the diamond crystal. Where the silicon diamond structure can be considered as a combination of two fcc lattices, the Zinc Blende lattice can also be considered to be two interpenetrating fcc sublattices where one is made up of the Species I atoms and the other made up of the Species II element. Each Species I atom can be considered to lie at the centre of a regular tetrahedron formed by the four nearest neighbours (of Species II) and hence we can define the angle subtended by each of the neighbouring atoms as $\cos^{-1}(-1/3) = 109.47^{o}$. It is fully tetrahedrally bonded to 4 Species II atoms and these bonds are sp^3 hybrid covalent bonds[1]. Similarly, the Species II atoms are surrounded by 4 tetrahedrally

[1] sp^3 simply indicates that due to the *sp hybrid* created by the linear combination of the s orbital and the p orbital we have an asymmetric probability distribution of atomic charge in the direction of the axis of the p orbital and that we are 3 times more likely to find an electron in the p state (excited state) than the s state (ground state).

bonded Species I neighbours, in an inverted tetrahedral shape. In a III-V system such as gallium-arsenide (GaAs) the atoms will be predominantly covalently bonded but will also have a mild amount of ionic interaction energy. Furthermore, in a III-V system such as GaAs it is common to refer to the type III species as the metallic atom or the *cation* indicating a less positively charged ion and the type-V atom, the more positive ion, as the *anion* or semi-metal[7]. The system primitive vectors are described identically to the diamond lattice but the atomic basis set now contains two atomic types

$$\mathbf{x}_1 = [0, 0, 0] \qquad \text{Species I}$$
$$\mathbf{x}_2 = [{}^{a}/_{4}, {}^{a}/_{4}, {}^{a}/_{4}] \qquad \text{Species II}$$

It would be typical to make a Gallium Arsenide (GaAs) lattice from this basis set by defining Species I as Gallium and Species II as Arsenic. By placing the basis set in the positions described by the system primitive vectors we can obtain an eight atom reduced unit cell of size $[a, a, a]$ that we can use to model a bulk Zinc Blende lattice. A simple extension of this to a 2x2x2 primitive cell structure is shown in Figure 2.2(b). This 64-atom structure is usually referred to as a simulation *supercell* and is usually taken as the minimum number of atoms required to perform a simple simulation due to the periodic boundary conditions imposed upon the system and the potential cut-off function which limits the computation to the nearest neighbours of the atom under consideration.

2.2 The potential energy function

Potential energy modelling is of fundamental importance to atomistic simulation as it provides the ability to simulate the levels of energy provided in the semiconductor model under investigation on a per atom basis. A good potential energy model should be able to balance both the *radial forces* in the system which resist a change in the bond lengths from the equlibrium value and the *angular forces* in the system which resist change in the shape of the preferred tetrahedral angles at the unstrained equlibrium state. The potential should be able to replicate both of these important bonding forces found in covalent and partly ionic semiconductor systems and should be differentiable to provide atomic resolution values for force which are required to solve Newtons second law for MD simulations.

A classical potential can take the form

$$V = \sum_i V_1(r_i) + \sum_{i,j} V_2(r_i, r_j) + \sum_{i,j,k} V_3(r_i, r_j, r_k) + \cdots$$

Where: V is the total energy of the system under consideration. There are N atoms in the system and the atomic sum loop indices $i, j, k = [1...N]$. V_1 represents a single particle potential, V_2 is a pair-potential (or two-body potential) and only depends upon the distance between the atoms i and j. V_3 is the three-body interactions in the system and may contain angular dependence terms. Three-body and higher order potentials are grouped into a category called many-body potentials and are typically computationally difficult and impractical to solve numerically.

It is also typical that potential energy functions of this form will count the contribution of each atom pair twice in the nature of the summation. Hence we will calculate the contribution from atom pair $i-j$ and also $j-i$, so it is common to find the whole potential divided by a factor of 2.

There are a number of ways to calculate the force f_{ij} acting upon atom$_i$ due to atom$_j$. A common method is to take the first derivative of the energy function with respect to the atomic separation

$$\begin{aligned}
\mathbf{f}_{ij} &= -\nabla_{\mathbf{r}_i} V(r_{ij}) \\
&= -\nabla_{\mathbf{r}_{ij}} V(r_{ij}) \\
&= -\left[\frac{dV}{dr}\right]_{r=r_{ij}} \times \frac{\mathbf{r_{ij}}}{r_{ij}}
\end{aligned}$$

where $\mathbf{r}_{ij} = \mathbf{r}_i - \mathbf{r}_j$ and ∇ operates on position $\mathbf{r}_i$ of atom$_i$. This can be ignored for simple pair potentials.

It is also common to include a cut-off function (with a radius r_c) for a potential energy model to avoid massive computation of overly-complex long-range forces beyond the 1^{st} nearest neighbour (first nn) shell. Hence $V(r_{ij}) \rightarrow 0$ for values $r_{ij} > r_c$. However, this cut-off function will lead to a discontinuity in the second derivatives as the function jumps to zero at $r_{ij} = r_c$ and presents us with unphysical behaviour and a problem finding the derivatives of the potential. We can accommodate this by including a trigonometric smoothing function in the interval $r_c < r_{ij} < (r_c + \Delta r)$ which will make the potential and the force continuous.

We shall now examine a few potential energy models and the pros and cons associated with them.

Two-body potentials

The most simple example of a two-body potential (or pair-potential) is the *Morse potential*

$$De^{-2\alpha(r-r_0)} - 2De^{-\alpha(r-r_0)} \tag{2.4}$$

This is based upon the three fitting parameters r_0 which shifts the energy minimum in the potential form to account for the equlibrium bonding distance, α which scales the effect of the exponentials to model the change in energy as a function of the bonding distance and D which scales the whole potential form. The Morse potential has led to many other authors suggesting modifications based upon the physical properties of a number of close packed materials such as the *Lennard-Jones potential* (LJ), which is another classic example of a pair-potential[8]

$$V(r) = 4\epsilon\left[\left(\frac{\sigma}{r}\right)^{12} - \left(\frac{\sigma}{r}\right)^{6}\right]$$

where ϵ represents the cohesive energy and σ is the equilibrium atomic separation and are usually fitted from experimental data. The attractive $1/r^6$ term is also known as the Van Der Waals or fluctuating dipole potential[1] and is obtained from consideration of two atoms separated by a distance r. Although there will be no net charge distribution, instantaneously we can consider an electric field $\propto 1/r^3$ in one of the atoms, hence the two dipoles represented by the two-atom interaction can be multiplied together to form a lowering of the energy of the form $\propto 1/r^6$. The $1/r^{12}$ term is not necessarily physically motivated but comes from the idea that the repulsive term must be shorter-ranged than the attractive term and computationally $(1/r^6)^2$ is easily found.

The LJ potential has performed well in the past for simulation of Noble gasses, but is severely limited for semiconductor systems. It performs very badly with open lattices like the diamond or zinc blende cystals as no angular bonding information is taken into account. Furthermore, there is a lack of flexibility with the model parameters to consider the covalent though partially ionic bonds found in compound semiconductors.

Many other pair-potentials have been proposed based upon the pioneering work of Morse but they all have the same shortcomings in terms of modelling open structures and ionic systems. It has been proposed that these potentials may be modified to only consider short-range interactions with the potential cut-off functions and that the Coulombic interactions between ions may be modelled

via

$$V_{total}(r_{ij}) = V_{short-range\ pair}(r_{ij}) + V_{ionic}(r_{ij})$$
$$= V_{short-range\ pair}(r_{ij}) + \frac{z_1 z_2 e^2}{4\pi\epsilon_0 r_{ij}}$$

Many-body potentials

This group of potentials was called *cluster potentials* by Balamane[9] and contains an explicit angular bonding term. They generally take the form

$$V = \sum_{i,j} V_2(r_i, r_j) + \sum_{i,j,k} V_3(r_i, r_j, r_k)$$

An example of a many-body potential is the Stillinger-Weber (SW)[10] potential which takes the form shown above and includes an explicit angular bonding term. It was suggested that the potential worked well to model silicon and the parameters of the potential were fitted to lattice constant, cohesive energy and melting point, but the authors made light of the fact that to obtain the correct melting point, the cohesive energy is 7% adrift. Other authors have reported success in reproducing reasonable lattice constant data from the (SW) potential.

A bond order potential takes the form[11]

$$V(r_{ij}) = V_{repulsive}(r_{ij}) + b_{jik} V_{attractive}(r_{ij}) \tag{2.5}$$

and is so called because the b_{jik} term weakens the attractive component of the potential based upon the local chemical bonding geometry notably as number of neighbours or coordination number z increases. Physically this seemes reasonable: if an atom has N outer electrons as the system forms covalent bonds with other atoms it can share N electrons with one another single atomic neighbour or share $^N/_2$ electrons with two nearest neighbours, etc. Hence, as the number of neighbours increases the individual bond strength decreases. Hence the strength of the bond is a monotonically decreasing function of z[12]

$$b_{jik} \propto z^{-\delta}$$

and the scaling factor δ has been successfully hypothesised (for example in a carbon system[13]) to take a fixed value of $\delta = {}^1/_2$ providing us with

$$b_{jik} \propto \frac{1}{\sqrt{z}}$$

This type of potential hides the angular dependence in the b_{jik} term of equation 2.5 and these potentials were named by Balamane[9] as *cluster functionals*. The attractive and repulsive components of the potential provide a purely pair potential such as the Morse potential 2.4 and the many-body term, b_{jik} provides all scaling necessary to describe the bonding environment. It must also contain a hidden three body-loop of the form $\sum_{i,j,k}(r_{ij}, r_{ik})$ to provide the angular dependence information.

The Tersoff empirical potential is an example of a bond-order potential and is the potential energy function of choice for this work. The empirically derived b_{jik} term in the Tersoff potential approximates the second-order moment of electronic density[14] and makes the functional form of the potential a very powerful and accurate tool for modelling covalent solids such as the bulk semiconductors. Chapter 3 is devoted to a comprehensive review of the Tersoff potential, its functional form and the success of other workers using the Tersoff potential.

2.3 Simulated properties

By combining the lattice model and the potential energy model we hope to model bulk semiconductor systems. However, the potential energy function needs to be tuned to each semiconductor system of interest individually and to do this correctly we need to provide a number of measures, or metrics, that we can fit the potential to. A number of material properties that can be explicitly measured are required so that we can make the computer model replicate the behaviour of the bulk semiconductor. Two of the chosen material properties are the lattice parameter a and the cohesive energy E_{coh} which may be found by simple hydrostatic relaxation of the lattice model with the potential energy function. Material properties that are more difficult to calculate from the lattice model are derived from the elastic constants c_{11} and c_{12} and are called the bulk modulus B and the shear modulus C'. The elastic property c_{44} and the Kleinman internal displacement parameter ζ provide further material properties that we may attempt to fit our potential energy model to. We will also consider the material dynamical properties in the form of the phonon frequencies ω_n and the mode-Grüneisen parameters γ_n.

Elastic properties

General elasticity theory [5] begins with *Hooke's law* which tells us that, for a sufficiently small extension of a material sample, the force F is proportional to the extension Δl of the material and the initial length l. The force is also proportional

to the cross-sectional area of the material A. We can write and equation for the force

$$F = Y \cdot A \cdot \frac{\Delta l}{l}$$

where Y is a property of the material and is called *Young's modulus*.

We define *stress* as the force per unit area and *strain* as the stretch per unit length of the material, providing

$$Y = \frac{stress}{strain} \tag{2.6}$$

Another part of Hooke's law tells us that if we stretch a material sample in one direction, it will contract at right angles to the stretch[15]. If we define the sample width, w and a height, h we can write

$$\frac{\Delta w}{w} = \frac{\Delta h}{h} = -\sigma \frac{\Delta l}{l}$$

where σ is a property of the material called *Poisson's ratio*. With the properties Y and σ we can completely specify the elastic properties of a homogeneous isotropic (non-crystalline) material.

The deformation of crystalline materials under small strain is more complex and must be described in terms of the local strain at every point in the elastic body [16, 17]. We now consider *stress* from the following definition: A body in which one part exerts a force on neighbouring parts is said to be in a state of stress. We consider a small volume element inside a body of material. The forces exerted on the surface of the element by the material surrounding it exert a force proportional to the surface area of the material.

It is convenient to formalise this in terms of *tensor notation*. To calculate the force at a point, P, inside a material we can consider an area, δS that passes through P and a unit vector l perpendicular to δS. We can now label the force transmitted across the area as pδS and as $\delta S \rightarrow 0$ and the relation between the two vectors as

$$\begin{aligned} p_1 &= \sigma_{11} l_1 + \sigma_{12} l_2 + \sigma_{13} l_3 \\ p_2 &= \sigma_{21} l_1 + \sigma_{22} l_2 + \sigma_{23} l_3 \\ p_3 &= \sigma_{31} l_1 + \sigma_{32} l_2 + \sigma_{33} l_3 \end{aligned}$$

where $\sigma_{11}, \sigma_{12}, ..., \sigma_{33}$ forms a second rank tensor and is called the *tensor of stress*

given by

$$\sigma_{ij} = \begin{bmatrix} \sigma_{11} & \sigma_{12} & \sigma_{13} \\ \sigma_{21} & \sigma_{22} & \sigma_{23} \\ \sigma_{31} & \sigma_{32} & \sigma_{33} \end{bmatrix}$$

We may write the above equations more conveniently as

$$p1 = \sum_{j=1}^{3} \sigma_{1j} l_j$$

$$p2 = \sum_{j=1}^{3} \sigma_{2j} l_j$$

$$p3 = \sum_{j=1}^{3} \sigma_{3j} l_j$$

or as

$$p_i = \sum_{j=1}^{3} \sigma_{ij} l_j \qquad (i = 1, 2, 3)$$

and finally we may use the *Einstein summation convention* which states: "When a letter suffix occurs twice in the same term, summation with respect to that suffix is to be automatically understood"[17] and write the tensor relations as

$$p_i = \sigma_{ij} l_j$$

where j is the dummy suffix and i is the free suffix.

The components $\sigma_{ij}(i = j)$ are called the *normal components* of stress and the components $\sigma_{ij}(i \neq j)$ are called the *shear components* of stress. Positive values of $\sigma_{ij}(i = j)$ imply a *tensile stress* and negative values are termed a *compressive stress*.

Homogeneous stress occurs if the force acting upon the surface of an element of fixed shape and position is independent of the position of the element inside the body. And *inhomogeneous stress* occurs when the stress in the element varies from point to point internally.

A number of special cases of the stress tensor exist and are listed below for convenience

$$\text{Uniaxial stress,} \begin{bmatrix} \sigma & 0 & 0 \\ 0 & 0 & 0 \\ 0 & 0 & 0 \end{bmatrix}$$

$$\text{Biaxial stress,} \begin{bmatrix} \sigma_1 & 0 & 0 \\ 0 & \sigma_2 & 0 \\ 0 & 0 & 0 \end{bmatrix}$$

$$\text{Triaxial stress, normal stress, } \begin{bmatrix} \sigma_1 & 0 & 0 \\ 0 & \sigma_2 & 0 \\ 0 & 0 & \sigma_3 \end{bmatrix}$$

$$\text{Hydrostatic pressure, } p, \begin{bmatrix} -p & 0 & 0 \\ 0 & -p & 0 \\ 0 & 0 & -p \end{bmatrix}$$

$$\text{Pure shear stress, } \begin{bmatrix} -\sigma & 0 & 0 \\ 0 & \sigma & 0 \\ 0 & 0 & 0 \end{bmatrix} \equiv \begin{bmatrix} 0 & \sigma & 0 \\ \sigma & 0 & 0 \\ 0 & 0 & 0 \end{bmatrix}$$

It should be noted here that σ_{ij} is a symmetrical tensor in the absence of body torques - which will assist us in simplifying our notation later in the chapter.

Previously we described *strain* as the stretch per unit length of material. We shall now formalise this and introduce some more tensor notation

$$\text{strain} = \frac{\text{increase in length}}{\text{original length}} = \frac{\Delta u}{\Delta x}$$

and we can define a tensor e_{ij} as:

$$e_{ij} = \frac{\partial u_i}{\partial x_j}$$

Element e_{ij} has 2 components

$$e_{ij} = \epsilon_{ij} + \omega_{ij}$$

where ϵ_{ij} is a symmetrical tensor which we call the *tensor of strain*

$$\epsilon_{ij} = {}^1/_2(e_{ij} + e_{ji}) = \epsilon_{ji}$$

and ω_{ij} is an antisymmetric tensor which represents rotation

$$\omega_{ij} = {}^1/_2(e_{ij} - e_{ji}) = -\omega_{ji}$$

The strain tensor, ϵ_{ij} can be written

$$\epsilon_{ij} = \begin{bmatrix} e_{11} & {}^1/_2(e_{12} + e_{21}) & {}^1/_2(e_{13} + e_{31}) \\ {}^1/_2(e_{21} + e_{12}) & e_{22} & {}^1/_2(e_{23} + e_{32}) \\ {}^1/_2(e_{31} + e_{13}) & {}^1/_2(e_{32} + e_{23}) & e_{33} \end{bmatrix}$$

The diagonal components of ϵ_{ij} are the *tensile strains* (stretches) and the other components represent *shear strains. Homogeneous strain* occurs when the strains are referred to the principal axes and the shear components vanish leaving only the principal strains, $\epsilon_1, \epsilon_2, \epsilon_3$

$$\text{Principle strain, } \begin{bmatrix} \epsilon_{11} & \epsilon_{12} & \epsilon_{13} \\ \epsilon_{21} & \epsilon_{22} & \epsilon_{23} \\ \epsilon_{31} & \epsilon_{32} & \epsilon_{33} \end{bmatrix} \rightarrow \begin{bmatrix} \epsilon_1 & 0 & 0 \\ 0 & \epsilon_2 & 0 \\ 0 & 0 & \epsilon_3 \end{bmatrix}$$

We can define *dilation* as the change in volume of a unit cube. The tensor that provides dilation, or *hydrostatic strain*, is

$$\text{Dilation, } \begin{bmatrix} (1+\epsilon_1) & 0 & 0 \\ 0 & (1+\epsilon_2) & 0 \\ 0 & 0 & (1+\epsilon_3) \end{bmatrix}$$

It is common to find the strain tensor ϵ_{ij} written in terms of γ, the shear components of strain (also called the *engineering shear strains*)

$$\epsilon_{ij} = \begin{bmatrix} \epsilon_x & {}^1/_2\gamma_{xy} & {}^1/_2\gamma_{zx} \\ {}^1/_2\gamma_{xy} & \epsilon_y & {}^1/_2\gamma_{yz} \\ {}^1/_2\gamma_{zx} & {}^1/_2\gamma_{yz} & \epsilon_z \end{bmatrix} \qquad (\text{where: } \gamma_{xy} = 2\epsilon_{12})$$

It should also be noted that when talking of engineering strains

$$\begin{bmatrix} 0 & \gamma & 0 \\ 0 & 0 & 0 \\ 0 & 0 & 0 \end{bmatrix} = \begin{bmatrix} 0 & {}^1/_2\gamma & 0 \\ {}^1/_2\gamma & 0 & 0 \\ 0 & 0 & 0 \end{bmatrix}$$

Returning to Hooke's Law we have defined (Eq 2.6) the following relation

$$\sigma = c \cdot e$$

where c is the *elastic stiffness*, or Young's modulus of the material calculated from $c = {}^1/_s$. The s term is known as *compliance*. It is found that if a general stress σ_{ij} is applied to a crystal then the resulting strain ϵ_{ij} is such that each component is

linearly related thus

$$\begin{aligned}\sigma_{11} = c_{1111}\epsilon_{11} + c_{1112}\epsilon_{12} + c_{1113}\epsilon_{13} \\ + c_{1121}\epsilon_{21} + c_{1122}\epsilon_{22} + c_{1123}\epsilon_{23} \\ + c_{1131}\epsilon_{31} + c_{1132}\epsilon_{32} + c_{1133}\epsilon_{33}\end{aligned}$$

and eight other similar equations exist for the other components of σ_{ij}. We may write (using the Einstein notation)

$$\sigma_{ij} = c_{ijkl}\epsilon_{kl}$$

where c_{ijkl} represents the 81 stiffness constants (called *elastic constants*) of the material and forms a 4^{th} rank tensor. Due to symmetry properties of the crystal ($c_{ijkl} = c_{ijlk}$ and $c_{ijkl} = c_{jikl}$) only 36 of the 81 components of c_{ijkl} are independent. Taking the symmetry properties into account we may achieve a simpler notation using a single suffix notation

$$\sigma_{ij} = \begin{bmatrix}\sigma_{11} & \sigma_{12} & \sigma_{13} \\ \sigma_{21} & \sigma_{22} & \sigma_{23} \\ \sigma_{31} & \sigma_{32} & \sigma_{33}\end{bmatrix} \rightarrow \begin{bmatrix}\sigma_1 & \sigma_6 & \sigma_5 \\ \sigma_6 & \sigma_2 & \sigma_4 \\ \sigma_5 & \sigma_4 & \sigma_3\end{bmatrix}$$

$$\epsilon_{ij} = \begin{bmatrix}\epsilon_{11} & \epsilon_{12} & \epsilon_{13} \\ \epsilon_{21} & \epsilon_{22} & \epsilon_{23} \\ \epsilon_{31} & \epsilon_{32} & \epsilon_{33}\end{bmatrix} \rightarrow \begin{bmatrix}\epsilon_1 & 1/2\epsilon_6 & 1/2\epsilon_5 \\ 1/2\epsilon_6 & \epsilon_2 & 1/2\epsilon_4 \\ 1/2\epsilon_5 & 1/2\epsilon_4 & \epsilon_3\end{bmatrix}$$

Hence Now we may write

Tensor notation	11	22	33	23, 32	31, 13	12, 21
Matrix notation	1	2	3	4	5	6

$$c_{ijkl} = c_{mn}$$

where $i, j, k, l = [1, 2, 3]; m, n = [1, 2, 3, 4, 5, 6]$ and

$$c_{ij} = \begin{bmatrix}c_{11} & c_{12} & c_{13} & c_{14} & c_{15} & c_{16} \\ c_{21} & c_{22} & c_{23} & c_{24} & c_{25} & c_{26} \\ c_{31} & c_{32} & c_{33} & c_{34} & c_{35} & c_{36} \\ c_{41} & c_{42} & c_{43} & c_{44} & c_{45} & c_{46} \\ c_{51} & c_{52} & c_{53} & c_{54} & c_{55} & c_{56} \\ c_{61} & c_{62} & c_{63} & c_{64} & c_{65} & c_{66}\end{bmatrix}$$

Nye[17] demonstrates that for a cubic crystal system we may, through sym-

metry arguments, reduce the number of elastic constants c_{ij} required to fully describe the elasticity of the crystal, to just 3 values

$$c_{11} = c_{22} = c_{33} \equiv c_{11}$$
$$c_{12} = c_{13} = c_{23} \equiv c_{12}$$
$$c_{44} = c_{55} = c_{66} \equiv c_{44}$$

The strain energy of the crystal must be positive otherwise the crystal would be unstable, hence for a cubic crystal we have the following relations which must be obeyed

$$c_{44} > 0, \qquad c_{11} > |c_{12}|, \qquad c_{11} + 2c_{12} > 0$$

The bulk modulus B and the shear modulus C' are the material properties we wish to calculate from our lattice simulation. B and C' can be calculated directly from the lattice model using the potential energy function and the stress/strain relations described above. These are related to the elastic properties of the material via the following definitions[16]

$$B = (c_{11} + 2c_{12})/3$$
$$C' = (c_{11} - c_{12})/2$$

and the inverse transforms are

$$c_{11} = B + \frac{4}{3}C'$$
$$c_{12} = B - \frac{2}{3}C'$$

which can provide us with the elastic constants c_{11} and c_{12} from the calculated values of B and C'. We may also calculate the elastic property c_{44} from our lattice model, an induced shear strain and the Tersoff potential. However, this calculation requires an energy relaxation step of the Species II internal sublattice. This method is covered fully in section 4.1 and includes an explanation of the Kleinman internal displacement parameter which is a measure of the magnitude of the sublattice relaxation when calculating the c_{44} crystal property.

Lattice dynamics

We can consider the dynamics of a crystal by considering both the atom ion cores and the electrons in the outer shells separately[18]. At temperatures above absolute zero (0 Kelvin) the atoms will be excited by thermal energy that will cause

lattice vibrations as the atoms move about around their equilibrium positions. In a crystal a description of this motion may be made simpler by consideration that the system is periodically bounded and has translational periodicity, enabling us to split it into primitive unit cells as described in Equation 2.1. We may now consider only the unit cell with n ion cores and the electrons associated with them. Even this small system is very complicated to describe so we shall make a couple of approximations to aid us:

Adiabatic approximation We shall treat the motion of the ion cores of the atoms and the motion of the electrons separately. This is reasonable since the mass of the atom core is generally much larger than that of the electrons surrounding it and hence the electrons will have a small effect on the vibration of the atom core. The two caveats associated with this approximation are:

1. When we are considering the motion of the electrons we shall assume that the atom cores are in their equilibrium positions.

2. The motion of the atom cores will be considered due to a potential energy field generated by the average motion of the electrons.

And a couple of other things we need to bear in mind are noted:

1. It is important to note here that using a potential of the form shown below, we are also only considering the interaction of the nearest neighbours upon the atom of interest.

2. We shall also assume in all of this work that the Born - von Kármán periodic boundary conditions are met. This implies that a given function is periodic on a certain Bravais lattice. See eq 2.3.

The harmonic approximation If we consider the potential energy function inside the crystal due to the atomic bonding, we may use an expansion of the potential energy models presented earlier (e.g. eq 2.5) in a Taylor series for powers of a small value $h = r_{ij} - r_0$ to consider the dynamics of the problem. We will consider a general potential energy function, $V(r_{ij})$, and make the assumption that close to the equilibrium interatomic lattice spacing, r_0, the potential will be parabolic

$$V(r_{ij}) = V(r_0) + \left(\frac{\partial V}{\partial r_{ij}}\right)_0 \cdot h + \frac{1}{2}\left(\frac{\partial^2 V}{\partial r_{ij}^2}\right)_0 \cdot h^2 + \ldots \tag{2.7}$$

where the first term given above is a constant and considered to go to zero in dynamical problems. The second term relates to a force on the system, and as we have already stated we are considering the system to be in an equilibrium

position and so this term will go to zero. Consideration of only the third term, the quadratic term, is called the harmonic approximation. We are considering each atom in the crystal to be a harmonic oscillator and hence the quadratic term represents an interatomic force constant.

A monatomic linear chain

Hooke's Law for spring force states

$$F = -k \cdot x$$

where the force exerted by the spring, F, is related linearly to the extension of the spring, x, and a constant, k, known as the spring constant. If we now consider a series of n atoms placed in a line and equally spaced a distance a apart, as shown in Figure 2.3, and consider the small displacements u_n of the atom n and the displacements of the neighbouring atoms $n-1$ and $n+1$, using Newton's 2^{nd} we can write an equation to follow Hooke

$$m\frac{d^2u_n}{dt^2} = \Lambda\left[(u_{n+1} - u_n) + (u_{n-1} - u_n)\right] \tag{2.8}$$

where m is the mass of the atom and Λ is the nearest neighbour force constant.

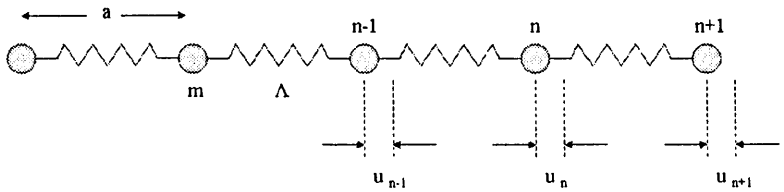

Figure 2.3: A monatomic linear chain showing the small displacement u_n of atom n

We are looking for the normal modes of the crystal and the energies (or frequencies) of the non-interacting vibrations as a function of their wave vectors(q). We can relate ω, the angular velocity of the wave, and q with $\omega = \omega(\mathbf{q})$ which portrays a dispersion relation. A dispersion relation describes how the energy is dispersed across the mass and spring chain of interest in terms of the waves. It is more convenient to express the displacement in terms of a wave so we try a solution

$$u_n = A\exp\left[i(qna - \omega t)\right] \tag{2.9}$$

where A indicates both the magnitude and the direction of the atomic motion of particle u_n. Only one mode of vibration is allowed here since neither u_n nor A is

a vector quantity. The vibration may be *longitudinal* where the atoms will vibrate along the chain or *transverse* where the atomic vibration will be perpendicular to the chain. If we incorporate 2.8 and 2.9 we obtain

$$\begin{aligned}\omega^2 A &= \frac{2\Lambda}{m}(1-\cos qa)A \\ &= DA\end{aligned}$$

which is a dynamical equation providing an eigenvalue solution. In this case the D-matrix is a (1×1) matrix and for a non-trivial solution ($A \neq 0$) we have

$$\omega = 2\sqrt{\frac{\Lambda}{m}}\left|\sin\frac{qa}{2}\right|$$

Due to the sinusoidal nature of the above expression, we can easily see that it will be periodic in q space with: $\omega(q + G_n) = \omega(q)$ where $G_n = \pm 2n\pi/a$ for integers n is the magnitude of a reciprocal lattice vector corresponding to the chain. In fact, the region $\frac{-\pi}{a} \leq q \leq \frac{\pi}{a}$ corresponds to the first Brillouin Zone in the lattice.

A diatomic linear chain

Further to the study of the method for solving the simple case of a monatomic linear chain we can study the more useful diatomic linear chain - which is beginning to approximate our two atom primitive cell (assuming one-dimension again). Now we shall consider $2N$ atoms forming N unit cells in the system. The two basis atoms each have different masses, m and M and we shall now consider the unit cell to have length $2a$ as shown in Figure 2.4.

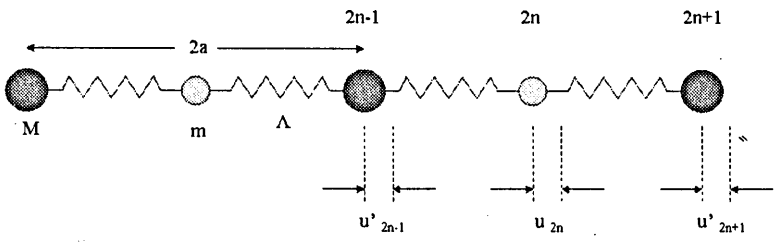

Figure 2.4: A diatomic linear chain showing the different masses in the system and the lattice spacing $2a$

As with the monatomic chain we may form the equations of motion for the

two atom types

$$m\frac{d^2u_{2n}}{dt^2} = \Lambda\left[u'_{2n+1} + u'_{2n-1} - 2u_{2n}\right]$$
$$M\frac{d^2u'_{2n+1}}{dt^2} = \Lambda\left[u_{2n+2} + u_{2n} - 2u'_{2n+1}\right]$$

and try the wave solutions

$$u_{2n} = A_1 \exp\left[i(2nqa - \omega t)\right]$$
$$u'_{2n+1} = A_2 \exp\left[i\left((2n+1)qa - \omega t\right)\right]$$

and combine the above to produce the coupled eigenvalue equations

$$-\omega^2 m A_1 = \Lambda\left[A_2 e^{iqa} + A_2 e^{-iqa} - 2A_1\right] \tag{2.10}$$
$$-\omega^2 M A_2 = \Lambda\left[A_1 e^{-iqa} + A_1 e^{iqa} - 2A_2\right] \tag{2.11}$$

The coupled eigenvalue equations (eq. 2.10) may be combined into a dynamical equation

$$\omega^2 A_i = \sum_{j=1}^{2} D_{ij} A_i \qquad i = [1, 2]$$

where D is the (2×2) dynamical matrix given by

$$D = \begin{pmatrix} 2\Lambda/m & -(2\Lambda/m)\cos qa \\ -(2\Lambda/m)\cos qa & 2\Lambda/m \end{pmatrix}$$

The non-trivial solutions of the above equation are given by solution of

$$\left|D_{ij} - \omega^2\delta_{ij}\right| = 0 \qquad \delta_{ij} = \begin{cases} 1 & i = j = 1 \\ 0 & \text{otherwise} \end{cases}$$

which can be specifically solved

$$\omega^2 = \Lambda\left(\frac{1}{m} + \frac{1}{M}\right) \pm \Lambda\left[\left(\frac{1}{m} + \frac{1}{M}\right)^2 - \frac{4}{mM}\sin^2 qa\right]^{0.5}$$

and from Equation 2.10 we can find that

$$\frac{A_1}{A_2} = \frac{2\Lambda\cos qa}{2\Lambda - \omega^2 m} = \frac{2\Lambda - M\omega^2}{2\Lambda\cos qa}$$

This important result will be examined more closely in terms of a three di-

mensional model of a 2-atom basis set in a primitive unit cell next. Mathematical operations can be performed on a crystal Brillouin Zone and are usually referred to as being in k-space (or q-space) where k is the momentum vector. As we are only considering tetrahedrally bonded crystals, we can resolve our system into simple basis vectors and need only consider the *primitive lattice wavenumbers* for a unit cell of Zinc Blende, which restrict the vibrational modes to the Brillouin Zone: $[111]2\pi/a$, $[1\bar{1}\bar{1}]2\pi/a$ and $[\bar{1}\bar{1}1]2\pi/a$

The non-linear diatomic chain

Phonon dispersion curves can be measured experimentally from crystal samples using methods such as inelastic neutron scattering or Raman spectroscopy and provide valuable information about how the crystal behaves under strained conditions. By fitting our potential energy model to the crystal phonon frequencies we hope to improve our computer model of the crystal lattice to make it more realistic so we can provide valuable predictions about how the crystal behaves under various conditions.

If we consider a primitive unit cell of crystal lattice with the harmonic approximation then we can visualise N atoms connected together by harmonic springs. These springs have normal modes of vibration described as travelling waves of the form $A\exp\left[i(\mathbf{q}\cdot\mathbf{r}-\omega t)\right]$ where $\mathbf{q}$ is the wave vector (direction of propagation), ω is the angular frequency of the travelling wave and A is the amplitude of the oscillation. The normal modes in a crystal are quantised in $\mathbf{q}$ (which is now a three dimensional wave vector to relate to the fact that the atoms in the primitive unit cell are not connected as a linear chain) into energies[19, 18]

$$E_{\mathbf{q}} = \left(n_{\mathbf{q}} + \frac{1}{2}\right)\hbar\omega(\mathbf{q}), \qquad n_{\mathbf{q}} = 0, 1, 2, ...$$

and the quantum of energy associated with each of these normal lattice vibrations is called a *phonon*. A phonon can be considered analogous to a photon, which is a quantised energy packet in an electromagnetic field. Phonons are important to understand how energy is absorbed into the crystal lattice. One of the consequences of using the harmonic approximation is that we have a picture of non-interacting phonons in our crystal lattice.

Each wave vector in the crystal has three possible modes of vibration, one *longitudinal* and two *transverse*. The longitudinal vibrations occur when the atoms are vibrating along the length of the atomic chain and the transverse vibrations occur in the two orthogonal planes normal to the longitudinal vibrations. Two

different frequency groups for any wave vector exist in the crystal due to the two different atomic elements now in the three-dimensional lattice. The *acoustic* or low-frequency phonon modes occurs when the two different species of atoms are vibrating in phase with each other. The *optical* mode of vibration occur at a higher frequency and are due to the two atomic species vibrating out of phase, causing a higher energy vibration. The phonon vibrational modes are illustrated simply in figure 2.5. Furthermore, for each atomic species we have in the unit cell basis set we can describe a separated branch of the so called *phonon dispersion.* The phonon dispersion describes how the atomic chain disperses energy with relation to the wave vector. The phonon dispersion is plotted in reciprocal space with the angular frequency plotted against the reduced wave vector.

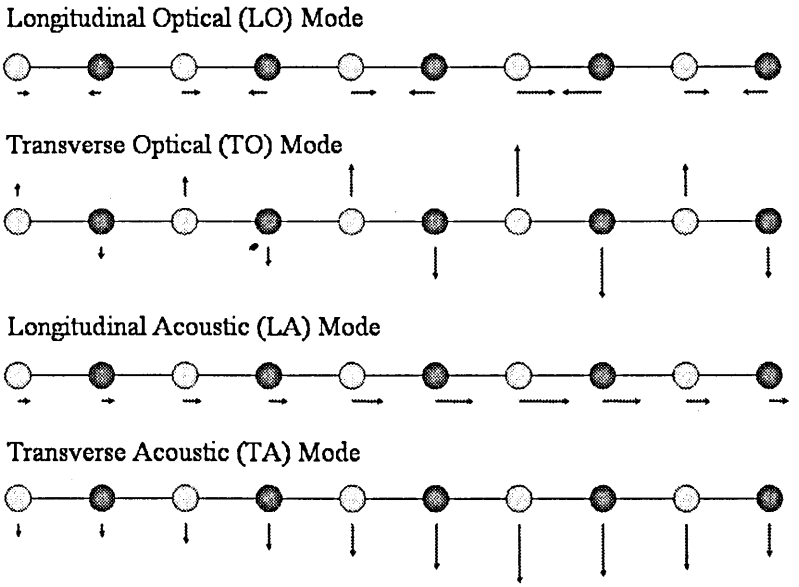

Figure 2.5: An illustration of the different phonon modes

We may now describe the equations of motion of the atoms in our primitive unit cell (with a method similar to the diatomic chain shown earlier) and then find a Hamiltonian for the crystal to calculate the phonon dispersion for a given crystal lattice. We shall start by considering a crystal with p atoms in a three dimensional unit cell. We shall let $\mathbf{u}(\mathbf{lb})$ represent the three dimensional displacement, $\mathbf{u}$ of the $\mathbf{b}^{th}$ atom in the $\mathbf{l}^{th}$ unit cell. We shall continue our potential energy assumptions from previous chapters that the potential energy of the crystal, V, is an instantaneous function of the position of the atoms and their neighbours and

we can expand upon equation 2.7 thus

$$V = V_0 + \sum_{\mathrm{lb}} \sum_{\alpha} \left. \frac{\partial V}{\partial u_\alpha(\mathrm{lb})} \right|_0 u_\alpha(\mathrm{lb}) + \frac{1}{2} \sum_{\mathrm{lbl'b'}} \sum_{\alpha,\beta} \Phi_{\alpha\beta}(\mathrm{lb;l'b'}) u_\alpha(\mathrm{lb}) u_\beta(\mathrm{l'b'}) + ...$$

$$V = V_0 + V_1 + V_2 + ...$$

where as previously stated terms V_0 and V_1 have no relevance in this particular problem so we shall concentrate on term V_2 for the harmonic approximation of crystal lattice dynamics. Note that $\alpha, \beta = [1, 2, 3]$ and the interatomic force constant matrix $\Phi_{\alpha\beta}(\mathrm{lb;l'b'})$ is

$$\Phi_{\alpha\beta}(\mathrm{lb;l'b'}) = \left. \frac{\partial^2 V}{\partial u_\alpha(\mathrm{lb}) \partial u_\beta(\mathrm{l'b'})} \right|_0$$

which represents the negative of the linear force on atom (lb) along the α direction due to a displacement of atom (l'b') along the β direction. Note the use of the abbreviation[20] $x(\mathrm{lb;l'b'}) = x(\mathrm{lb}) - x(\mathrm{l'b'})$.

Our harmonic approximation now becomes

$$V_{harm} = \frac{1}{2} \sum_{\mathrm{lb,l'b'}} \sum_{\alpha,\beta} \Phi_{\alpha\beta}(\mathrm{lb;l'b'}) u_\alpha(\mathrm{lb}) u_\beta(\mathrm{l'b'})$$

from which we may find the equations of motion extending Hooke ($F = -k \cdot x$) to three dimensions

$$m_b \ddot{u}_\alpha(\mathrm{lb}) = - \sum_{\mathrm{l'b'}\beta} \Phi_{\alpha\beta}(\mathrm{lb;l'b'}) u_\beta(\mathrm{l'b'})$$

where m_b is the mass of the b^{th} atom. Using lattice translational symmetry we can rewrite this as

$$m_b \ddot{u}_\alpha(\mathrm{lb}) = - \sum_{\mathrm{l'b'}\beta} \Phi_{\alpha\beta}(\mathrm{0b;l'b'}) u_\beta(\mathrm{l'b'}) \tag{2.12}$$

We can solve this equation by trying a solution of the form

$$U_\alpha(\mathrm{lb}) = \frac{1}{\sqrt{m_b}} \sum_{\mathrm{q}} U_\alpha(\mathrm{q;b}) \exp\left[i(\mathbf{q} \cdot \mathbf{x}(\mathrm{l}) - \omega t)\right] \tag{2.13}$$

where $\mathbf{x}(\mathrm{l})$ is the equilibrium position vector of the l^{th} unit cell and $U_\alpha(\mathrm{q;b})$ is independent of l. As with our diatomic chain described previously we can sub-

stitute this into equation 2.12 to obtain

$$\omega^2 U_\alpha(\mathbf{q};\mathrm{b}) = \sum_{\mathrm{b}'\beta} D_{\alpha\beta}(\mathrm{bb}'|\mathbf{q}) U_\beta(\mathbf{q};\mathrm{b}')$$

of which we may find a non-trivial solution by solving the *secular*[2] equation

$$\left| D_{\alpha\beta}(\mathrm{bb}'|\mathbf{q}) - \omega^2 \delta_{\alpha\beta}\delta_{\mathrm{bb}'} \right| = 0$$

where the δ_{mn} represent Kronecker Delta functions. The dynamical matrix expression is written

$$D_{\alpha\beta}(\mathrm{bb}'|\mathbf{q}) = \frac{1}{\sqrt{m_b m_{b'}}} \sum_{\mathrm{l}'} \Phi_{\alpha\beta}(0\mathrm{b};\mathrm{l}'\mathrm{b}') \exp\left[i\mathbf{q}\cdot\mathbf{x}(\mathrm{l}')\right] \tag{2.14}$$

and can be solved practically by introducing the various components of the vibrational energy calculations into a 6x6 Hamiltonian matrix and diagonalising to provide the eigenvalues - which directly provide the phonon vibrational energies. By calculating this a number of times for different wave vectors at and between the BZ high symmetry positions of X which occurs at $\mathbf{q} = [0,0,1] = [1,1,0]$ and L which occurs at $\mathbf{q} = [1/2, 1/2, 1/2]$ along with the Brillouin Zone centre Γ at $\mathbf{q} = [0,0,0]$ we are provided with phonon frequencies which we may directly compare to experimental measurements and DFT predictions. Section 5 contains the computational details associated with including the phonon frequency predictions into the crystal lattice model.

Mode Grüneisen parameters

Molecular dynamics approaches have found much success in handling the temperature and pressure dependence of semiconducting materials but a good MD simulation is only as good as the potential energy function used to simulate the energetics of the material under test. The ability of a potential energy function to predict the mode-Grüneisen parameters is a good indicator of its ability to correctly predict the anharmonic properties of the material[23] such as the temperature dependence of the phonon frequencies.

The mode-Grüneisen parameters per wave vector $\gamma(\mathbf{q})$ are expressed as

$$\gamma(\mathbf{q}) = -\frac{\partial \ln \omega(\mathbf{q})}{\partial \ln \Omega} \tag{2.15}$$

[2]A secular equation takes the form $|A - \lambda\delta| = 0$ and is sometimes called the *characteristic* equation of the matrix[21, 22]. For an $n \times n$ matrix, the solution is an n^{th} order algebraic equation with up to n eigenvalues in the result.

where $\omega(\mathbf{q})$ is the phonon frequency for a specified wave vector and Ω is the volume of the crystal unit cell. This can be decomposed for convenience as follows

$$\gamma(\mathbf{q}) = -\frac{\ln\omega(\mathbf{q})(x_0+\Delta x) - \ln\omega(\mathbf{q})(x_0-\Delta x)}{\ln\Omega(x_0+\Delta x) - \ln\Omega(x_0-\Delta x)}$$

$$\gamma(\mathbf{q}) = -\left[\ln\frac{\omega(\mathbf{q})(x_0+\Delta x)}{\omega(\mathbf{q})(x_0-\Delta x}\right] / \left[\ln\frac{\Omega(x_0+\Delta x)}{\Omega(x_0-\Delta x)}\right]$$

where $\Omega = \Omega_0(1 \pm 0.03)$ for a hydrostatic strain on a cubic system per axis of $\pm 0.01\%$.

Work has been carried out recently using a tight-binding approximation to increase the ability of MD simulations to predict the correct mode-Grüneisen parameters for the modelling of the dynamics of elemental crystal lattices under varied temperature conditions[24]. This work is cited in studies by Porter[25, 23], Eryigit[26] and Lazarenkova[27, 28] who have attempted to predict the mode-Grüneisen parameters using the Tersoff and VFF potential energy models. There is no evidence from the current literature that anyone has attempted to use the mode-Grüneisen parameters as a measure of the anharmonicity of the crystal lattice as a fitting parameter for the Tersoff potential energy model.

Phase stability

The check of the crystal phase stability is essential for a useful potential energy model for MD simulations. It is possible for the PEF to provide the correct material properties and yet the diamond or zinc blende configurations are not the lowest energy lattice model. This would cause massive problems in a MD simulation over time as if the crystal could break through the kinetic energy barrier required for a phase transformation in, for example, a high temperature simulation then the crystal would undergo a phase transformation and provide very different results.

It is intended to check the phase stability of the diamond crystal of the elemental semiconductors against the minimum energy states of the simple cubic, fcc and bcc lattice types to ensure that the energy per unit of atomic volume is in a minimum compared to the other structure polytypes. A similar calculation will be made for the zinc blende crystal against the other cubic structure polytypes types that III-V crystals form into including the NaCl and the CsCl structures.

This checking of the phase stability appears common in the literature but no other authors appear to use the information directly as a fitting parameter in the design of the potential parameters. This is because the lattice parameter and the

associated energy of the materials in uncommon phases is not often known.

Bibliography

[1] N. W. Ashcroft and N. D. Mermin, *Solid state physics.* CBS Publishing Asia Ltd., 1976.

[2] F. S. Galasso, *Structure and properties of inorganic solids.* Pergamon Press, Inc., 1970.

[3] G. P. Srivastava, *Theoretical modelling of semiconducting surfaces.* World Scientific Publishing, 1999.

[4] W. A. Harrison, *Electronic structure and the properties of solids.* Dover Publications, Inc., 1980.

[5] R. P. Feynman, R. B. Leighton, and M. Sands, *Lectures on physics II.* Addison-Wesley Publishing Company, 1964.

[6] C. Barrett and T. B. Massalski, *Structure of Metals 3rd revised edition: Crystallographic Methods, Principles, and Data.* International Series on Materials Science and Technology, Pergamon Press, Oxford, New York, 1987, vol. 35.

[7] E. Cartmell and G. W. A. Fowles, *Valency and molecular structure.* Butterworth & Co (Publishers), Ltd., 1977.

[8] P. Harrison, *Computational methods in physics, chemistry and biology.* J. Wiley & Sons Ltd., 2001.

[9] H. Balamane, T. Halicioglu, and W. A. Tiller, "Comparative study of silicon empirical interatomic potentials," *Phys. Rev. B*, vol. 46, no. 4, p. 2250, 1992.

[10] F. H. Stillinger and T. A. Weber, "Computer simulation of local order in condensed phases of silicon," *Phys. Rev. B*, vol. 31, no. 8, pp. 5262–5271, 1985.

[11] S. J. Stuart, Y. Li, O. Kum, J. W. Mintmire, and A. F. Voter, "Reactive bond-order simulations using both spatial and temporal approaches to parallelism," *Struct. Chem.*, vol. 15, no. 5, pp. 479–486, 2004.

[12] G. C. Abell, "Empirical chemical pseudopotential theory of molecular and metallic bonding," *Phys. Rev. B*, vol. 31, no. 10, pp. 6184–6196, 1985.

[13] K. Albe, K. Nordlund, and R. S. Averback, "Modeling the metal-semiconductor interaction: Analytical bond-order potential for platinum-carbon," *Phys. Rev. B*, vol. 65, no. 19, p. 195124, 2002.

[14] D. Conrad and K. Scheerschmidt, "Empirical bond-order potential for semiconductors," *Phys. Rev. B*, vol. 58, no. 8, pp. 4538–4542, 1998.

[15] E. N. Ramsden, *Materials science.* Stanley Thornes (Publishers) Ltd, 1995.

[16] J. Singh, *The physics of semiconductors and their heterostructures.* McGraw-Hill Inc., 1993.

[17] J. F. Nye, *Physical properties of crystals.* Oxford University Press, 1957.

[18] G. P. Srivastava, *The physics of phonons.* IOP Publishing Ltd, 1990.

[19] R. B. Barnes, R. R. Brattain, and F. Seitz, "On the structure and interpretation of the infrared absorption spectra of crystals," *Phys. Rev.*, vol. 48, no. 7, pp. 582–602, 1935.

[20] A. A. Maradudin, E. W. Montroll, G. H. Weiss, and I. P. Ipatova, *Theory of lattice dynamics in the harmonic approximation.* Academic Press, New York & London, 1971.

[21] H. S. John W. Harris, *Handbook of mathematics and computational science.* Springer-Verlag New York, Inc., 1998.

[22] K. A. Stroud, *Further engineering mathematics.*

[23] L. J. Porter, J. F. Justo, and S. Yip, "The importance of grüneisen parameters in developing interatomic potentials," *J. Appl. Phys.*, vol. 82, no. 11, pp. 5378–5381, 1997.

[24] C. Z. Wang, C. T. Chan, and K. M. Ho, "Tight-binding molecular-dynamics study of phonon anharmonic effects in silicon and diamond," *Phys. Rev. B*, vol. 42, pp. 11 276–11 283, 1990.

[25] L. J. Porter, S. Yip, M. Yamaguchi, H. Kaburaki, and M. Tang, "Empirical bond-order potential description of thermodynamic properties of crystalline silicon," *J. Appl. Phys.*, vol. 81, no. 1, pp. 96–106, 1997.

[26] I. P. H. R. Eryigit, "Lattice properties of strained GaAs, Si and Ge using a modified bond-charge model," *Phys. Rev. B*, vol. 53, no. 12, pp. 7775–7784, 1996.

[27] O. L. Lazarenkova, P. von Allmen, F. Oyafuso, S. Lee, and G. Klimeck, "An atomistic model for the simulation of acoustic phonons, strain distibution and Grüneisen coefficients in zinc-blende semiconductors," *Supperlattices and Microstructures*, vol. 34, pp. 553–556, 2003.

[28] ——, "Effect of anharmonicity of the strain energy on band offsets in semiconductor nanostructures," *Appl. Phys. Lett.*, vol. 85, no. 18, pp. 4193–4195, 2004.

Chapter 3

The Tersoff Potential

3.1 Background

An empirical interatomic potential energy function was originally suggested by J. Tersoff in 1986 and later refined to the form commonly used today for rapid and accurate semiconductor structure and molecular dynamics (MD) simulations [1, 2, 3]. The potential was originally proposed as a trade-off between accuracy and timing when performing a simulation to describe the material properties of solid Silicon. A comparison was made to the *ab initio* quantum mechanical local Density Functional Theory (DFT) approach which considers each electron in a quantum mechanical ensemble to describe the system [4]. Although the Local DFT Approach (LDA) provides highly accurate levels of structural and electronic information about the system under consideration it requires a massive computational effort and can only replicate results for systems of the order of 10^2 atoms in a reasonable amount of time. Thus, an empirical PEF form was proposed that would provide a more timely solution for complex multi-atom simulations. It would also provide more accurate and meaningful results than the potential proposed to simulate small distortions from the ground state in the diamond structure of Silicon by the Keating Valence Force Field (VFF) method [5, 6, 7].

Tersoff was originally more interested in the structural properties and energetics of non-tetrahedral elemental Silicon (e.g. surfaces and point defects) and attempted to form a potential that would reproduce cohesion in a large range of coordination and bonding topologies. At that time a two- and three-body empirical interaction potential had been proposed by Stillinger-Weber [8] which provided reasonable results for molten Silicon investigated with MD simulations although the system was designed to replicate a limited set of material properties. Also during that time the Keating method, which is analogous to a Taylor

series parabolic expansion of the energy around its minimum, was being used to simulate small strain elastic properties of the material and replicate phonon frequencies. The VFF method could not accurately describe energy states differing from the tetrahedral ground state. This is due to the parabolic nature of the original Keating potential and an associated inherent inability to replicate the anharmonic region of the atomic bonding behaviour accurately. Furthermore, a fit of the VFF potential is provided by only 3 material dependent parameters, suggesting that only three experimental values can be included in a parameterisation of the potential. The Tersoff potential takes a form known as a many-body potential and includes 12 material dependent parameters to account for the local structural chemistry (the bond environment) of the covalent system under consideration.

Tersoff has taken account of the fact that an atom with many neighbours forms weaker bonds than an atom with fewer neighbours and this is a large part of describing covalent systems in open lattice structures. The neighbour dependence in the Tersoff PEF stabilises structures with a smaller number of neighbours, described by z the *atomic coordination number*. Furthermore, the dependence on z allows the local system to relax into an energy minimum based upon the neighbouring atomic geometry. The energy per bond must decrease rapidly with increasing coordination to replicate this behaviour but contain enough repulsive energy to stop the system dropping into a close packed configuration by balancing the bond-order and the bond-count energies. His empirical potential is constructed to preserve the intuitive nature of the exponential Morse-like pair bonding (Equation 2.4) and to enhance this nature with the inclusion of a many-body term to account for local neighbours (both in terms of the distance from the atom under consideration and the subtended bonding angle).

Originally the potential was designed for use with elemental type IV semiconductors but has recently been proven to be very useful in characterising binary compounds of III-V [9, 10], II-VI [11, 12] and even I-VII [13, 14] semiconductor systems. In a system of elemental type IV atoms one set of material dependent parameters are required to describe the atomic interactions, for example: Si-Si. However, in a type III-V system 3 sets of material dependent parameters will be required to describe the 3 possible atomic interactions (e.g. Ga-As, Ga-Ga, As-As).

A final, very important rating of the PEF quality suggested by Tersoff is that it should have a high degree of *transferability*. He defines transferability as "applicability to systems very different from the ones used to determine the potential". The original paper designating the Tersoff parameters for Silicon demonstrated that the Tersoff potential has a great level of transferability and that the PEF seems

to capture some of the essential physics of covalent bonding in well-ordered type IV systems. Tersoff[3] fitted the potential parameters for Silicon to model the cohesive energy, the lattice constant and the bulk modulus. He also fitted to ensure that it correctly modelled the behaviour of the cohesive energy per bond against coordination number demonstrated by LDA calculations and the correct phase stability for a number of different structures to ensure correct behaviour in MD simulations. The results were found to estimate well the C_{11} and C_{12} elastic constants of the system, which directly contribute to the bulk modulus B but the parameters did not fit C_{44} and Kleinman's ζ very well. The model results were compared to LDA vacancy energies and found to be a reasonable match and a close match to interstitial defect energies. He also compared phonon frequencies at the Γ, X and L Brillouin Zone (BZ) symmetry points and found a reasonable match. In other tests he attempted to model surface energies and dimer bond lengths of various Silicon surface reconstructions and the parameters were found to be in reasonable agreement with some cases and rather adrift for others. But, the degree of transferability of the potential was well illustrated.

Other work using the Tersoff potential

Since the development of the potential and the initial work on the mixing of parameters to provide multi-component characterisations many studies have been performed using the Tersoff potential as a basis. The degree of transerability is evident by the wide range of work listed below. Motooka[15] is motivated by the prospect of low temperature solid phase epitaxy of amorphous silicon on crystalline silicon. He investigates ion bombardment of Si surfaces using the Tersoff potential with an interest in the amorphisation process in crystalline silicon and finds pleasing results via MD simulations. Yoon and Megusar[16] produced a molecular dynamics model of amorphous carbon and graphite from the Tersoff parameters of carbon and simulated crystal grain boundaries. De Brito Mota *et al*[17] parameterised silicon nitride for a wide range of nitrogen contents and demonstrated a good agreement with first principles calculations. He fitted to a database of values taken from *ab initio* calculations and experimental data including the lattice parameter and binding energy. He performed MD simulations on amorphous silicon nitride to study the structural properties under a range of temperatures. Erkoc and Ozkaymak[18] used the Tersoff potential to investigate the properties of a number of different carbon nanotubes. They used the Tersoff parameters for carbon to calculate the total interaction energies for the nanotubes and the variation of the binding energy due to the extension of the

tube. Marcos *et al*[19] use the Tersoff PEF to simulate C_{20} and C_{60} clusters as a precursor to investigation of nanotubes. They use MD to simulate phase changes with temperature and pressure and characterise thermal behaviour well. They draw conclusions that agree with the literature about the melting behaviour of small carbon clusters. Carbon clusters appear to be a popular research topic for the Tersoff potential with further investigations by authors Garrido *et al*[20], Ballone and Milani[21] and Lopez *et al*[22]. Hedstrom and Cheng[23] use the Tersoff potential and MD simulation techniques to characterise Si under low energy ion bombardment. Halac *et al*[24] model various SiC polytypes using the Tersoff PEF. They start with the original Tersoff parameters and modify them for a fit based upon the material properties, elastic properties and dynamical properties of the materials. Ishimaru *et al*[25] have modelled the structure and dynamic properties of various Si-Ge alloys using the Tersoff potential. Using MD simulation techniques they study amorphous Si and Ge under various conditions including a very clever simulation of the phonon density of states that allows direct comparison to Raman scattering spectroscopy. Montalenti *et al*[26] mix the Tersoff potential with *ab initio* calculations to demonstrate a theory about the pyramid to dome transition in SiGe quantum dots. A model was developed to demonstrate that the pyramid to dome transition occurs due to the increasing strain at the top of the pyramid dot and is irrespective of the size of the nanostructure. They do not, however, consider the full global thermodynamics of the system. Ivashchenko *et al*[27] have studied microcrystalline SiC and amorphous SiC using the Tersoff potential and MD simulation. They draw conclusions about the gaps in the conduction state due to the homopolar bonds formed by growth defects. Agrawal *et al*[28] offer a new parameterisation of silicon based upon melting behaviour. After a number of tests they concluded that the addition of a long range force term did not significantly improve the original Tersoff parameters to model melting behaviour. The new parameterisation was performed by modifying only 3 of the parameters and considering the liquid behaviour. Wang *et al*[29] have produced a study based upon modelling single-walled carbon nanotubes using the Tersoff potential. They have looked at the mechanical properties of nanotubes under various conditions via MD simulations and concluded that the Tersoff potential accurately modelled the elastic properties and stiffness of the nanotubes.

Smith[9] provided the first successful parameterisation of the Tersoff potential to III-V semiconductors. He modelled GaAs based upon the dimer energies, bond lengths, E_{coh} and a of the zinc blende formation and the bulk modulus. Smith used his parameterisation to predict the structure of a GaAs surface reconstruction and the energetics of GaAs clusters. Sayed and co-workers[10] employed the

Tersoff PEF successfully to demonstrate ion implantation and damage recovery in semiconductors. They parameterised GaAs and AlAs by modifying the Smith parameters to improve the level of angular dependence. Sayed demonstrated that ion implantation could be realistically modelled by the Tersoff model and MD simulation and found pleasing qualitative and quantitative results. Ashu *et al*[30] were motivated to use the Tersoff potential in MD simulations by the requirement to investigate the critical thickness in pseudomorphic growth. They performed atomistic simulations to consider the strain relief in thin film growth and he modelled some dislocations and growth defects in InGaAs on GaAs. They parameterised InAs based upon the dimer energies, bond lengths, cohesive energy and elastic constants. Nakamura *et al*[31] were also interested in simulating epitaxial growth and parameterised AlAs, InAs and GaAs based upon the addition of a long range ionic energy consideration to the Tersoff model. They find pleasing results with respect to the growth geometry when combining the long range potential with the Tersoff PEF. Nordlund and co-workers[32] use the Tersoff potential to simulate ion implantation damage and recovery at various semiconductor interfaces including Si/Ge, AlAs/GaAs and InAs/GaAs. They produce results based upon a new parameterisation of InAs and include the Kleinman internal displacement parameter ζ amongst the elastic properties in the fitting procedure. Migliorato *et al*[33] found that a new parameterisation for InAs was produced by inclusion of the shear modulus to provide a more realistic local relaxation process under static MD relaxation. This was used successfully by Migliorato and co-workers[34, 35] to simulate small scale atomic relaxation via MD in InGaAs/GaAs quantum dots and to model the strain induced piezoelectric fields and the associated s- and p- wavefunctions. Murdick *et al*[36] assess a number of interatomic potentials including the Tersoff PEF and conclude that Tersoff provides the best agreement with experimental behaviour when considering thin-film GaAs. They also looked at the performance of the potentials when representing the surface reconstructions in GaAs and concluded that further work was needed.

Many authors have started to investigate Tersoff parameters for the type III-nitride (III-N) materials, which are of great interest due to their high temperature, high power and high frequency operation. The hardness of the III-N materials makes them particularly attractive, as does the large band gap which makes many electroluminescent modes possible. Albe and Moller[37] use Tersoff to investigate cubic boron nitride (c-BN) growth via MD simulation and atomistic relaxation. They start with a conflict in the literature for 2 possible growth modes of c-BN ("the stress model"[38] and "the subplanar model"[39]) and continue to in-

vestigate after re-parameterising the Tersoff potential for c-BN. They demonstrate success with small scale growth simulations and surface atomic relaxations. The fitting procedure for the parameters is described elsewhere but the paper hints that the parameters were designed for the structure and energy of a number of BN polytypes. Benkabou *et al*[40] have re-parameterised the III-N set of GaN, AlN and InN starting from the original Tersoff carbon fit[3]. They fitted their parameters to the cohesive energy, the bulk modulus and the lattice parameter of the materials they was simulating. To check for transferability they simulated the change in lattice parameter with temperature via MD simulation and also checked the mean displacement of the atomic sites at 300K, demonstrating reasonable stability. Nord and co-workers[41] use the Tersoff PEF to simulate collision cascades in GaN. The potential was fitted to the zinc blende, wurtzite and simple dimer structures. They also considered the B1 and B2 lattice types. Moon and Hwang[42] use the Tersoff potential to re-parameterise cubic GaN starting from the Benkabou parameters and find a more accurate parameterisation to the elastic properties. Goumri-Said *et al*[43] modelled and parameterised cubic aluminium nitride (c-AlN). The c-AlN structure was optimised to the material parameters taken from *ab initio* calculations and they predicted the elastic constants and pressure of the phase transition from cubic to rocksalt structures with an MD simulation. They modelled the Debye temperature which they found in good agreement with experiment and found the thermal expansion coefficient, the specific heat and a melting temperature of the material (albeit with a large tolerance). Kang and Hwang[44] use the Tersoff potential to perform MD simulations on GaN nanotubes. They use the parameters designed by Benkabou and demonstrate (although nanotubes have sp^2 hybridisation and the parameters were designed for cubic III-N materials) a reasonable agreement with DFT simulations although they did draw attention to a problem with the c_{44} elastic constant. Zhou *et al*[45] studied wurtzite thin-film GaN growth using the Tersoff potential and MD simulation. They looked at the effects of temperature, film orientation and flux on growth conditions and various atomic assembly mechanisms.

Kirmse *et al*[11] produced multidisciplinary work studying CdSe/ZnSe quantum dots using myriad methods including molecular dynamics simulation via the Tersoff potential. They performed a structural MD relaxation of a quantum dot structure to compare and contrast to TEM methods to investigate the relaxation processes and structure of the dots. Genrich and co-workers[46] investigate Fe using MD simulations and the Tersoff potential. They modify the potential to take account of the structural nature of iron and locate the correct cohesive energy for a number of formations. They calculate the elastic properties for the BCC

phase in good agreement with the experimental results. Sekkal *et al*[13, 14] investigate the copper and silver halides successfully using the Tersoff potential. They find new Tersoff parameters for a selection of II-VI compounds and use Monte Carlo and MD methods to predict a number of elastic properties, thermodynamic properties and the mode-Grüneisen parameter. Lakshimi and Ramachandran[12] investigate the thermal expansion properties of CdS by MD simulation with the Tersoff PEF. They parameterise CdS based upon the thermal properties and the lattice parameter.

A number of authors have produced very stimulating discussions and results regarding the optimisation and speed-up of Tersoff potential calculations in different computing environments. Da Silva[47] included the Tersoff potential in a study to minimise computation time required to perform accurate MD simulations via the Metropolis Monte Carlo method. He demonstrated excellent results in terms of efficiency and accuracy when coupling the Tersoff potential with Verlet neighbour schemes and linked cell methods. Stuart *et al*[48] describes a method to speed up Tersoff potential MD calculation by the splitting of the bond-order properties of the potential across parallel machine boundaries both spatially and temporally. They demonstrate 90% parallel efficiency on 60+ machines for small and medium sized applications. Moloi and Ali[49] descibe a number of algorithms that are applied to the Tersoff potential to minimise the global energy of large scale atomic nanostructures. Their main motivation is the design and choice of algorithm but they provide numerical results to directly compare four different optimisation algorithms.

3.2 Functional form

The functional form of the Tersoff potential used in this work is similar to the one reworked by Smith [9] and modified by Sayed *et al*[10] and is shown below

$$
\begin{aligned}
E &= \sum_i E_i = \frac{1}{2}\sum_{j\neq i} V_{ij} \\
V_{ij} &= f_c\left(r_{ij}\right)\left[V_R\left(r_{ij}\right) - b_{ij}V_A\left(r_{ij}\right)\right] \\
f_c\left(r\right) &= \begin{cases} 1, & r < \left(R - R_{cut}\right) \\ \frac{1}{2}\left[1 - \sin\left[\frac{\pi(r-R)}{2R_{cut}}\right]\right], & R - R_{cut} < r < R + R_{cut} \\ 0, & r > \left(R + R_{cut}\right) \end{cases} \\
V_R\left(r_{ij}\right) &= \left[\frac{D_e}{S-1}\right]\exp\left(-\beta\sqrt{2S}\left(r_{ij} - r_e\right)\right) \\
V_A\left(r_{ij}\right) &= \left[\frac{SD_e}{S-1}\right]\exp\left(-\beta\sqrt{\frac{2}{S}}\left(r_{ij} - r_e\right)\right) \\
b_{ij} &= \left[1 + \left(\gamma\zeta_{ij}\right)^n\right]^{-\frac{1}{2n}} \\
\zeta_{ij} &= \sum_{k\neq i,j} f_c\left(r_{ik}\right) g\left(\theta_{jik}\right)\omega_{ik} \\
\omega_{ik} &= \exp\left[\lambda^3\left(r_{ij} - r_{ik}\right)^3\right] \\
g\left(\theta_{jik}\right) &= 1 + \left(\frac{c}{d}\right)^2 - \frac{c^2}{d^2 + \left(h - \cos\theta_{jik}\right)^2}
\end{aligned}
\tag{3.1}
$$

Here we note the following:

E is the total energy of the system of interest. E_i is the site energy of the atom labelled i. The indices i, j and k run over all of the atoms in the system.

V_{ij} is the interaction energy (also known as the bond energy) and is based upon a combination of an exponential Morse-like pair potentials. V_{ij} is a function of r_{ij}, the physical distance between atoms i and j. V_A and V_R respectively provide the attractive and repulsive pair-potential parts of the interaction energy for the exponential Morse-like pair relating atom i and atom j. A plot of the Morse-like pair potential provided by the Tersoff potential for silicon[3] is shown in figure 3.1 where the two exponential functions V_A and V_R are shown combined to make V_{ij}. The pair potential is tuned (scaled and shifted) with the four parameters: D_e representing the energy, r_e for the separation (the energy and separation were modelled on a dimer of the particular material in free space [9]) and the fitting constants S and β.

$f_c(r)$ provides a smooth spherical cut-off function around atom i based upon the distance to the first nearest-neighbour (1nn) shell. $f_c(r)$ has a continuous

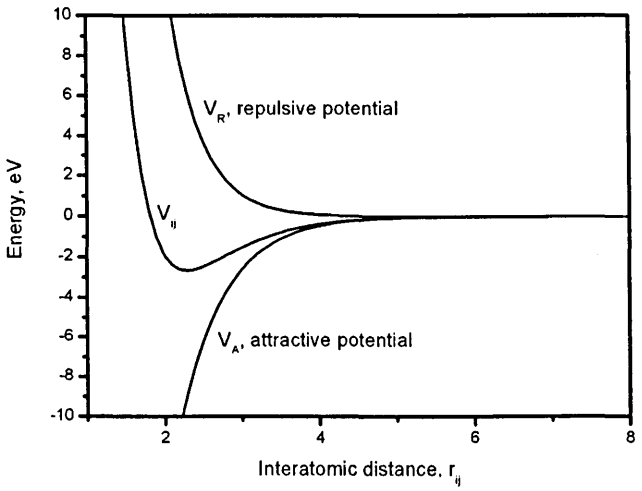

Figure 3.1: The Tersoff model of the Morse-like pair energy. r_{ij} is specified in Angstroms.

value and a derivative for all r and allows the computational complexity to be reduced to the 1nn, vastly reducing the effort required to solve large systems. The smooth cut-off function is centred around the distance parameter R (measured in Å) and is limited to 0 or 1 at a distance of R_{cut} on either side. The range of the cut-off function may provide awkward molecular dynamics results, especially when considering increased temperature models in which the bonds lengthen or phase change simulations, especially condensed matter to liquid transitions. This effect can be limited by the use of the cut-off function during parameterisation only and allowing the molecular dynamics code to select the relevant atomic interactions during a simulation. A plot of $f_c(r_{ij})$ using the Tersoff silicon parameters is shown in figure 3.2 and demonstrates the smooth continuous cut-off function that speeds up MD calculations and is differentiable.

b_{ij} is designed to represent the bond-order of the potential. Tersoff originally proposed that b_{ij} should provide, for the pair i-j, a monotonically[1] decreasing function of the number of competing bonds, the strength of the competing bonds and the cosines of the angles of the competing bonds. To explain the relatively weak dependence on coordination number z in Silicon, Tersoff chose $b_{ij} \propto z^{-1/2}$ for a large z. γ and n tune how rapidly the bond strength falls off with increasing effective coordination.

ζ_{ij} provides a weighted measure of the number of other bonds, labelled k, competing with the bond i-j. When only the first nn are present in the calcula-

[1]monotonic: each member of a monotone decreasing sequence is less than or equal to the preceding member

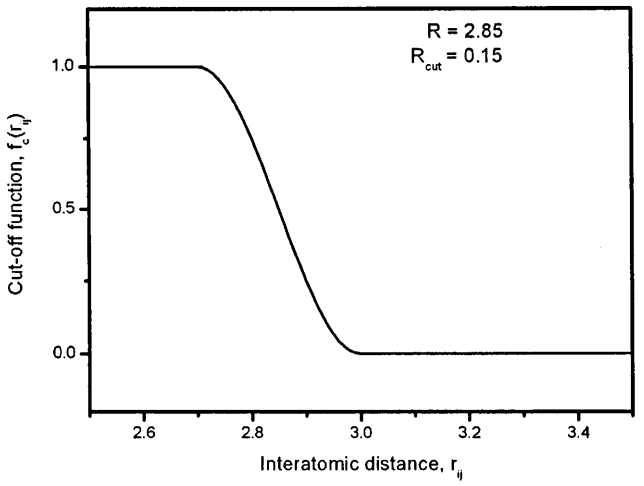

Figure 3.2: The smooth cut-off function included in the Tersoff potential. R, R_{cut} and r_{ij} are specified in Angstroms.

tions $\zeta_{ij} \rightarrow (z-1)$. Two additional features are involved in ζ_{ij} with the cut-off function on atom k labelled ω_{ik} and $g(\theta_{jik})$.

ω_{ik} provides a measure influenced by the relative distance of different neighbours when defining the effective coordination of the system. This is scaled with the parameter λ which is designed to only provide an effect when comparing the bond-lengths i-j and i-k. If this effect is prevalent then the difference is of the order of $1/\lambda$. This reduces the effect of distant neighbours on first nearest neighbour (nn) bonds which would otherwise be unrealistically large. This was done to help preserve the phonon frequency characteristics.

Finally $g(\theta_{jik})$ provides a measure of dependence on the bonding angle θ_{jik} subtended at atom i by atoms j and k. This is included to stabilise the atomic geometry under shear operations and provides an effective coordination contribution based upon the elastic energy of the current configuration. A sample plot (using the Tersoff[3] silicon parameters) of the angular bonding function $g(\theta_{jik})$ is shown in figure 3.3 and shows how the angular bonding coefficient is affected by the atomic bonding angle. The minimum at the covalent tetrahedral normal bond angle of 109^O is obvious from the plot. The function is made from three parameters to allow for a good level of tuning to a specific elasticity requirement: h which is formally the cosine of the energetically optimal bonding angle, d which determines how sharp the angular dependence is and c which provides tuning for the strength of the angular effect.

The third form of the Tersoff potential [3] is specified in terms of the parameters A_{ij}, B_{ij}, λ_{ij} and μ_{ij} which are reproduced by many authors and generally

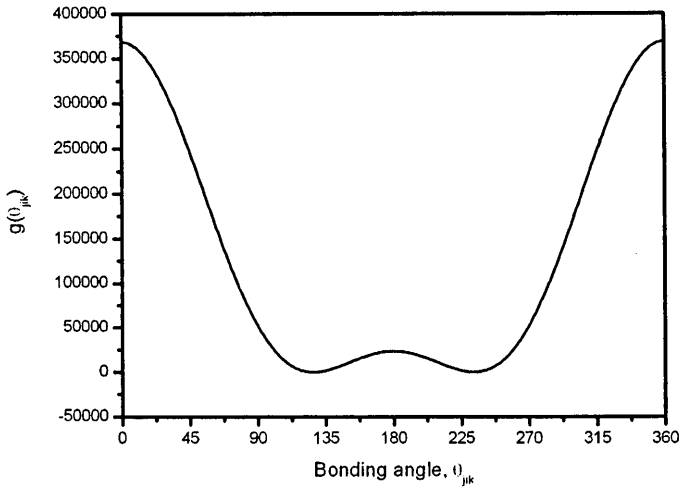

Figure 3.3: The Tersoff model of the angular bonding dependence parameter, $g(\theta_{ijk})$

labelled T3[50]. The conversion factors used to produce the parameters of the form used here from the original Tersoff notation are

$$
\begin{aligned}
S &= \frac{\lambda}{\mu} \\
\beta &= \frac{\lambda}{\sqrt{2S}} \\
r_e &= \frac{\ln \frac{SA}{B}}{\beta\left(\sqrt{2S} - \sqrt{2/S}\right)} \\
D_e &= A\left(S-1\right)\exp\left[-\beta \cdot r_e \cdot \sqrt{2S}\right] \\
R_{cut} &= \frac{S_{ij} - R_{ij}}{2} \\
R &= R_{ij} + R_{cut}
\end{aligned}
$$

and to invert the parameters from this form back to the original Tersoff form we

can use

$$
\begin{aligned}
A &= \frac{D_e}{S-1}\exp\left[\beta\cdot r_e\cdot\sqrt{2S}\right] \\
B &= \frac{SD_e}{S-1}\exp\left[\beta\cdot r_e\cdot\sqrt{2/S}\right] \\
\lambda &= \sqrt{2S} \\
\mu &= \sqrt{2/S} \\
S_{ij} &= R - R_{cut} \\
R_{ij} &= R + R_{cut}
\end{aligned}
$$

Multicomponent systems

The Tersoff potential was originally proposed for elemental silicon but it was quickly recognised that the potential would perform well if a different set of parameters were obtained to represent type IV compounds such as silicon-carbon or silicon-germanium[3]. The method that Tersoff suggested involved independently parameterising silicon, carbon and germanium and then blending the parameters to form a new parameterisation for the binary compounds using the following averaging scheme

$$
\begin{aligned}
\lambda_{ij} &= (\lambda_i + \lambda_j)/2 \\
\mu_{ij} &= (\mu_i + \mu_j)/2 \\
A_{ij} &= (A_i A_j)^{\frac{1}{2}} \\
B_{ij} &= (B_i B_j)^{\frac{1}{2}} \\
R_{ij} &= (R_i R_j)^{\frac{1}{2}} \\
S_{ij} &= (S_i S_j)^{\frac{1}{2}}
\end{aligned}
$$

Tersoff introduced a linear scaling factor to b_{ij} which he named χ_{ij} to assist in describing the *heat of formation* Δ_{hf} [3, 51, 52], which is important when calculating the energy of a surface or a surface reconstruction. It is yet to be tested whether this is entirely necessary when describing the Δ_{hf} of a system or whether the scaling factor was introduced to compensate for such a simple parameter blending scheme instead of a full re-parameterisation.

However, when dealing with partly ionic compounds such as the III-V semiconductors a more complex fitting method is required[9]. All twelve of the Tersoff parameters are usually allowed to vary in the fitting procedure as the dimer energy and dimer separation are not necessarily experimentally known for ma-

terials under investigation. This fitting procedure is known as *parameterisation*. Parameterisations have been provided by many authors and are usually based upon a table of material properties for a specific problem that the author is trying to solve.

3.3 Parameterisation

The so called *parameterisation* of the Tersoff potential is the process of fitting the twelve Tersoff parameters to provide a PEF that correctly reproduces a database of information related to the material under investigation. The usefulness of the potential critically depends upon the parameters selected for any particular application. The twelve parameters that may be varied for any material are: D_e, S, β, r_e, c, d, h, n, γ, λ, R and R_{cut}. Here it is noted that for any given material it is common to select R and R_{cut} before the fitting procedure begins and maintain the values selected throughout the parameter search. This is because R and R_{cut} are selected based upon the physical distance to the shell of the first nn in the crystal geometry under investigation. We are then left with a 10-dimensional parameter space to search to fit the potential energy function to correctly reproduce the table of values associated with the semiconductor.

The value for R can be found by taking the vector distance to the nearest neighbour shell and the vector distance to the second nearest neighbour shell and averaging the result, hence:

$$\begin{aligned} R &= \frac{r_{1nn} + r_{2nn}}{2} \\ &= \frac{\sqrt{\left(\frac{a}{4}\right)^2 + \left(\frac{a}{4}\right)^2 + \left(\frac{a}{4}\right)^2} + \sqrt{\left(\frac{a}{2}\right)^2 + \left(\frac{a}{2}\right)^2}}{2} \\ &= \frac{\sqrt{3\left(\frac{a}{4}\right)^2} + \sqrt{2\left(\frac{a}{2}\right)^2}}{2} \end{aligned}$$

In general the parameterisation coefficients have been found from other authors work to vary wildly. For example, when modelling boron nitride (BN) the author Albe[37] found values of c and d to be 1093 and 12.38 respectively whereas the author Sekkal[13, 14] found the values of c and d to be 38049 and 4.38. These numbers provide values of c/d of 88.28 and 8686.98 which have a two orders of magnitude difference between them, yet both results provide decent fits to the materials properties database. The plots of the two angular dependence functions resulting from the two parameter sets mentioned above are shown in figure 3.4. It can be clearly seen that although the Sekkal parameters needed scaling

by 2×10^{-5} so that the function could be plotted on the same axes as the Albe parameters, the shape of the functions and the local minima values are the same and hence the derivatives should provide similar values. It is assumed that this phenomenon arises because the 10 dimensional parameter space that we need to search has a number of local minima and possibly more than one global minimum.

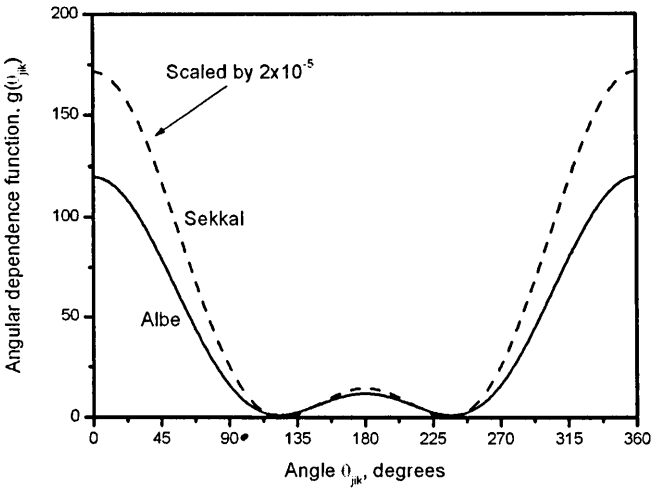

Figure 3.4: Two possible angular dependence functions for boron nitride

Material properties database

The uncertainty in the values in the database represents a source of possible compound error in selecting the correct parameters during the fitting procedure. Uncertainty can be introduced by the complexity of obtaining accurate experimental results from neutron scattering[53] or photoluminescence techniques[54]. Furthermore, it is common to use DFT values for parameter fits[3] but these are in themselves limited to structural information with the actual values for lattice constant and cohesive energy being reproduced with a limited tolerance - 2% error is common due to the local density approximation (LDA) [51, 55, 56]. First principles calculations are commonly relied upon to build a materials property database for a parameter fit, but these again introduce a source of possible error from various approximations made to simplify the problems involved in modelling semiconductor bonding[52, 57]. Physical intuition is required during the fitting process as it is not possible for the potential to reproduce all of the values in the database perfectly. It is practical and sometimes necessary to first have to decide how to weight the database fit based upon the application required.

The following values are commonly used by workers in the material properties database: *lattice parameter a, cohesive energy* E_{coh}*, bulk modulus B, shear modulus* C' [9, 10, 34]. However this still only provides a 6-dimensional solution space to a 10-dimensional problem search space and it is common to find many values of Tersoff parameters that will provide the correct database values for a given situation.

In this work we expand the bulk material properties database to provide more confidence in the Tersoff parameter fit by including the *Kleinman internal displacement parameter,* ζ, which in the one-dimensional case is required to fit c_{44}. We have also included the material Γ, X and L point phonons and the associated mode-Grüneisen parameters. A simple example material property database is shown below in table 3.1.

Property	Exp./Calc.	Units
E_{coh}	-4.63	eV
a	5.431	Å
B	0.9783	MBar
C'	0.509	MBar
c_{44}	0.796	MBar
ζ	0.524	

Table 3.1: The material properties of silicon

To locate the useful parameters some method of globally searching the parameter space to look for a minimum in the objective function, known here as the *parameterisation metric* is required.

Parameterisation metric

The objective function to optimise was chosen to be a weighted average of the sum-of-squares of the error between the values that particular set of Tersoff parameters returned for the material properties and the values of the material properties in the database. The weights of the errors were chosen depending upon how that particular Tersoff parameterisation was to be used. For example if the parameterisation was to be used for a molecular statics relaxation of a strained semiconductor heterostructure, then the elastic properties of the material, particularly c_{44} and shear properties, were weighted more importantly than the phonon frequency fit.

$$\begin{aligned} metric &= w_1(x_1 - d_1)^2 + w_2(x_2 - d_2)^2 + ... + w_n(x_n - d_n)^2 \\ &= \sum_n w_n(x_n - d_n)^2 \end{aligned}$$

Where: d_n is the nth element of the material property database, x_n is the associated material property returned from the search for a particular set of Tersoff parameters and w_n is the weighting for that particular property.

By choosing a weighted sum-of-squares objective function our results may be tuned to a specific set of materials properties that are deemed more important for a specific case we are trying to solve. It is usual to weight the cohesive energy and lattice constant fits equally and as the most important fit in the process as they have to be correct for the PEF to be useful. However the small strain elastic properties may be required to have a better fit than the phonon frequencies in some cases (e.g. small structure relaxation) and so they may be weighted more importantly than the phonon frequencies in a specific case. This choice of objective function allows us to investigate the properties of the Tersoff potential with respect to fitting to different material properties without having to change the underlying machine code, only a simple input instruction file.

The static testing of the potential to calculate the material properties can only be as successful as the parameter fit to the database. It is not possible to accurately predict the response of the potential under dynamic conditions using a finite set of static tests. However, by increasing the information in the database of material properties and the quality of the PEF fit to this data we may increase the level of confidence in the potential and thus increase the confidence that the function will perform as predicted under dynamic conditions.

Iterative searching

Iteratively searching a 10-dimensional parameter space is a daunting task. A naive and obvious way to perform this search would be to select, for each of the 10 parameters, a window of likely values. Then split each of these ranges into n parts to produce s steps in the parameter space to search. We now have $s = (n+1)^{10}$ discrete points in the parameter space to evaluate. As we are dealing with non-integer values for the Tersoff parameters we might assume an infinite precision but in practice we tend to find that most authors will reproduce 5 significant figures per parameter in press and during this work we have found that this is indeed required to reproduce the desired results. Therefore we may assume that $n \simeq 10,000$ which would produce an iterative parameter space search of $s \simeq 10^{40}$ steps.

Some of the assumptions made here are that the Tersoff equation only needs to be evaluated once per step (generally it needs to be evaluated of the order 10^2 times per search step to resolve the database values), that the "likely values"

chosen for the Tersoff parameter range can actually be predicted before run-time and that the resolution of the search will produce one obvious global minima.

This is clearly ridiculous in terms of the computational effort required and the data storage needed to save each of the steps for later comparison. A further practicality is that when all of the data is produced for each step then this needs to be sorted and classified for both global and local minima in the parameter space.

Some improved techniques for optimising this parameter search in terms of efficiency will be discussed in the relevant chapters later in this work.

3.4 Conclusion

It is evident from the large amount of previous work that has been done with the Tersoff PEF that is it highly suitable for myriad MD applications through studies of small scale structural bonding behaviour such as the carbon C_{60} clusters to the large scale simulations of entire quantum dots presented in the literature. The Tersoff potential shows a high degree of transferability to a number of applications such as surface reconstruction modelling and ion-impact investigations. However, many authors are relying upon parameterisations provided a number of years ago that were fitted to a very limited set of data. This can be improved by fitting the Tersoff potential to a larger number of material properties such as the c_{44} elastic constant and the ζ internal displacement parameter.

The cyclic sinusoidal nature of the bonding terms in the PEF provides a possible source of confusion with respect to parameterising the angular bonding terms correctly - which possibly accounts for a number of authors work showing promising results from vastly different parameterisations. Furthermore, the exponential and power terms involved in the PEF display a massive degree of sensitivity to the selected values of coefficient. It is thought that the number of minima in the 10-D parameter space can be reduced by inclusion of more materials properties in the fitting procedure.

To date the work presented in the literature using the Tersoff PEF has mainly been focused on the elemental type IV semiconductors, arsenide based compounds and the III-N semiconductor materials. No authors have presented work on the phosphide or antimonide semiconductor compounds. This will be rectified in the next chapter.

Bibliography

[1] J. Tersoff, "New empirical model for the structural properties of silicon," *Phys. Rev. Lett.*, vol. 56, no. 6, pp. 632–635, 1986.

[2] ——, "New empirical approach for the stucture and energy of covalent systems," *Phys. Rev. B*, vol. 37, no. 12, pp. 6991–7000, 1988.

[3] ——, "Modeling solid-state chemistry: Interatomic potentials for multicomponent systems," *Phys. Rev. B*, vol. 39, no. 8, pp. 5566–5568, 1989.

[4] J. Ihn, "Total energy calculations in solid state physics," *Rep. Prog. Phys.*, vol. 51, no. 1, pp. 105–142, 1988.

[5] P. N. Keating, "Effect of invariance requirements on the elastic strain energy of crystals with application to the diamond structure," *Phys. Rev.*, vol. 145, no. 2, pp. 637–645, 1966.

[6] ——, "Theory of the third-order elastic constants of diamond-like crystals," *Phys. Rev.*, vol. 149, no. 2, pp. 674–678, 1966.

[7] R. M. Martin, "Elastic properties of ZnS structure semiconductors," *Phys. Rev. B*, vol. 1, no. 10, pp. 4005–4011, 1970.

[8] F. H. Stillinger and T. A. Weber, "Computer simulation of local order in condensed phases of silicon," *Phys. Rev. B*, vol. 31, no. 8, pp. 5262–5271, 1985.

[9] R. Smith, "A semi-empirical many-body interatomic potential for modelling dynamical processes in gallium arsenide," *Nucl. Instr. Meth. Phys. Res. B*, vol. 67, pp. 335–339, 1992.

[10] M. Sayed, J. H. Jefferson, A. B. Walker, and A. G. Cullis, "Molecular dynamics simulations of implantation damage and recovery in semiconductors," *Nucl. Instr. Meth. Phys. Res. B*, vol. 102, pp. 218–222, 1995.

[11] H. Kirmse, R. Schneider, K. Scheerschmidt, D. Conrad, and W. Neumann, "TEM characterisation of self organised CdSe/ZnSe quantum dots," *J. Microsc.*, vol. 194, no. 1, pp. 183–191, 1999.

[12] P. V. B. Lakshmi and K. Ramachandran, "On the thermal expansion of CdS by experiment and simulation," *Cryst. Res. Technol.*, vol. 41, no. 5, pp. 498–504, 2006.

[13] W. Sekkal, A. Laref, H. Aourag, A. Zaoui, and M. Certier, "The miscibility of $Cu_XAg_{1-X}I$ using a Tersoff potential," *Superlatt. Microstruct.*, vol. 28, no. 1, pp. 55–66, 2000.

[14] ——, "The miscibility of copper halides using a three-body potential. Part II: $CuBr_XI_{1-X}$," *J. Mat. Sci.*, vol. 11, no. 1, pp. 123–129, 2000.

[15] T. Motooka, "Model for amorphization processes in ion-implanted Si," *Phys. Rev. B*, vol. 49, no. 23, p. 16367, 1994.

[16] C. S. Yoon and J. Megusar, "Molecular dynamics simulation of amorphous carbon and graphite interfaces," *Interface Science*, vol. 3, pp. 85–100, 1995.

[17] F. de Brito Mota, J. F. Justo, and A. Fazzio, "Structural properties of amorphous silicon nitride," *Phys. Rev. B*, vol. 58, no. 13, p. 8323, 1998.

[18] S. Erkoc and S. Ozkaymak, "Energetics of carbon nanotubes," *Eur. Pys. J. D*, vol. 4, pp. 331–333, 1998.

[19] P. A. Marcos, J. A. Alonso, A. Rubio, and M. J. Lopez, "Simulating the thermal stability andphase changes of small carbon clusters and fullerines," *Eur. Phys. J. D*, vol. 6, pp. 221–233, 1999.

[20] A. P. Garrido, J. D. Catala, and F. Alhama, "Fullerenes with symmetrically arranged defects: geometry and electronic structure," *Phys. Sol. State*, vol. 44, no. 3, pp. 569–570, 2002.

[21] P. Ballone and P. Milani, "Simulated annealing and collision properties of carbon clusters," *Z. Phys. D*, vol. 19, pp. 439–441, 1991.

[22] M. J. Lopez, P. A. Marcos, A. Rubio, and J. A. Alonso, "Thermal beaviour of carbon clusters and small fullerenes," *Z. Phys. D*, vol. 40, pp. 385–388, 1997.

[23] M. Hedstrom and H. P. Cheng, "Characteristics of sub-keV atom-Si (111) surface collisions," *Phys. Rev. B*, vol. 59, no. 16, p. 10701, 1999.

[24] E. Halac, E. Burgos, and H. Bonadeo, "Static and dynamical properties of SiC polytypes," *Phys. Rev. B*, vol. 65, p. 125202, 2002.

[25] M. Ishimaru, M. Yamaguchi, and Y. Hirotsu, "Molecular dynamics study of structural and dynamical properties of amorphous Si-Ge alloys," *Phys. Rev. B*, vol. 68, p. 235207, 2003.

[26] F. Montalenti, P. Raiteri, D. B. Migas, H. von Kanel, A. Rastelli, C. Manzano, G. Contantini, U. Denker, O. G. Schmidt, K. Kern, and L. Miglio, "Atomic scale pathway of the pyramid to dome transition during Ge growth on Si (001)," *Phys. Rev. Lett.*, vol. 93, no. 21, p. 216102, 2004.

[27] V. I. Ivashchenko, V. I. Shevchenko, L. A. Ivashchenko, G. V. Rusakov, and O. K. Porada, "The atomic patterns and electron structure of amorphous and microcrystalline SiC," *Powder Metallurgy and Metal Ceramics*, vol. 43, no. 9, pp. 520–524, 2004.

[28] P. M. Agrawal, L. M. Raft, and R. Komanduri, "Monte carlo simulations of void nucleated melting of silicon via modification in the tersoff potential parameters," *Phys. Rev. B*, vol. 72, p. 125206, 2005.

[29] J. B. Wang, X. Guo, H. W. Zhang, L. Wang, and J. B. Liao, "Energy and mechanical properties of single walled carbon nanotubes predicted using the higher order Cauchy-Born rule," *Phys. Rev. B*, vol. 73, p. 115428, 2006.

[30] P. A. Ashu, J. H. Jefferson, A. G. Cullis, W. E. Hagston, and C. R. Whitehouse, "Molecular dynamics simulation of (100) InGaAs/GaAs strained layer relaxation processes," *J. Crys. Grow.*, vol. 150, pp. 176–179, 1995.

[31] M. Nakamura, H. Fujioka, K. Ono, M. Takeuchi, T. Mitsui, and M. Oshima, "Molecular dynamics simulation of III-V compound semiconductor growth with MBE," *J. Crys. Grow.*, vol. 209, pp. 232–236, 2000.

[32] K. Nordlund, J. Nord, J. Frantz, and J. Keinonen, "Strain-induced Kirkendall mixing at semiconductor interfaces," *Comp. Mater. Sci.*, vol. 18, no. 3, pp. 283–294, 2000.

[33] M. A. Migliorato, A. G. Cullis, M. Fearn, and J. H. Jefferson, "Atomistic simulation of strain relaxation in $In_xGa_{1-x}As$/GaAs quantum dots with non uniform composition," *Phys. Rev. B*, vol. 65, p. 115316, 2002.

[34] M. A. Migliorato, D. Powell, S. L. Liew, A. G. Cullis, M. Fearn, J. H. Jefferson, P. Navaretti, M. J. Steer, and M. Hopkinson, "Influence of composition on the piezoelectric fields and on the conduction band energy levels of $In_XGa_{1-X}As$/GaAs quantum dots," *J. Appl. Phys.*, vol. 96, p. 5169, 2004.

[35] M. A. Migliorato, D. Powell, E. A. Zibik, L. R. Wilson, M. Fearn, J. H. Jefferson, M. J. Steer, M. Hopkinson, and A. G. Cullis, "Anisotropy of the electron energy levels in $In_XGa_{1-X}As$/GaAs quantum dots with non-uniform composition," *Physica E*, vol. 26, p. 436, 2005.

[36] D. A. Murdick, X. W. Zhou, and H. N. G. Wadley, "Assessment of interatomic potentials for molecular dyanmics simulations of GaAs deposition," *Phys. Rev. B*, vol. 72, p. 205340, 2005.

[37] K. Albe and W. Moller, "Modelling of boron nitride: Aomic scale simulations on thin film growth," *Comp. Mat. Sci.*, vol. 10, pp. 111–115, 1998.

[38] D. R. McKenzie, W. D. McFall, W. G. Sainty, C. A. Davis, and R. E. Collins, "Compressive stress induced formation of cubic boron nitride," *Diam. Rel. Mat.*, vol. 2, pp. 970–976, 1993.

[39] Y. Lifshitz, S. Kasi, J. Rabalais, and W. Eckstein, "Subplantation model for film growth from hyperthermal species," *Phys. Rev. B*, vol. 41, p. 10468, 1990.

[40] F. Benkabou, H. Aourag, P. J. Becker, and M. Certier, "Molecular dynamics study of zinc blende GaN, AlN and InN," *Molecular Simulation*, vol. 23, pp. 327–341, 2000.

[41] J. Nord, K. Nordlund, J. Keinonen, and K. Albe, "Molecular dynamics study of defect formation in gan cascades," *Nucl. Instr. Meth. Phys. Res. B*, vol. 202, pp. 93–99, 2003.

[42] W. H. Moon and H. J. Hwang, "Structural and thermodynamic properties of GaN: a molecular dynamics simulation," *Phys. Lett. A.*, vol. 315, pp. 319–324, 2003.

[43] S. Goumri-Said, M. B. Kanoun, A. E. Merad, G. Merad, and H. Aourag, "Prediction of structural and thermodynamic properties of zinc-blende AlN: molecular dynamics simulation," *Chem. Phys.*, vol. 302, pp. 135–141, 2004.

[44] J. W. Kang and H. J. Hwang, "Molecular dynamics simulation of single wall GaN nanotubes," *Mol. Sim.*, vol. 30, no. 1, pp. 29–35, 2004.

[45] X. W. Zhou, D. A. Murdick, B. Gillespie, and H. N. G. Wadley, "Atomic assembly during GaN film growth: molecular dyanmics simulations," *Phys. Rev. B*, vol. 73, p. 045337, 2006.

[46] L. K. Genrich, B. Rice, and S. Yip, "A bond order potential for atomistic simulations in iron," *J. Comp. Aided Mat. Design*, vol. 6, pp. 129–136, 1999.

[47] C. R. S. da Silva, "Optimizing metropolis monte carlo simulations of semiconductors," *Comp. Phys. Comm.*, vol. 152, pp. 392–396, 2003.

[48] S. J. Stuart, Y. Li, O. Kum, J. W. Mintmire, and A. F. Voter, "Reactive bond-order simulations using both spatial and temporal approaches to parallelism," *Struct. Chem.*, vol. 15, no. 5, pp. 479–486, 2004.

[49] N. P. Moloi and M. M. Ali, "An iterative global optimization algorithm for potential energy minimization," *Computational Optimization and Applications*, vol. 30, pp. 119–132, 2005.

[50] L. J. Porter, S. Yip, M. Yamaguchi, H. Kaburaki, and M. Tang, "Empirical bond-order potential description of thermodynamic properties of crystalline silicon," *J. Appl. Phys.*, vol. 81, no. 1, pp. 96–106, 1997.

[51] G. P. Srivastava, *Theoretical modelling of semiconducting surfaces.* World Scientific Publishing, 1999.

[52] W. A. Harrison, *Electronic structure and the properties of solids.* Dover Publications, Inc., 1980.

[53] J. L. T. Waugh and G. Dolling, "Crystal dynamics of gallium arsenide," *Phys. Rev.*, vol. 132, no. 6, pp. 2410–2412, 1963.

[54] K. Suto and J. Nishizawa, "Radiative recombination mechanisms in stoichiometry-controlled GaP crystals," *J. Appl. Phys.*, vol. 67, no. 1, p. 459, 1990.

[55] S. Q. Wang and H. Q. Ye, "First-principles study on elastic properties and phase stability of III-V compounds," *Phys. Stat. Sol. B*, vol. 240, no. 1, pp. 45–54, 2003.

[56] ——, "Ab initio investigation of the pressure dependences of phonon and dielectric properties for III-V semiconductors," *J. Phys.: Condens. Matter*, vol. 17, pp. 4475–4488, 2005.

[57] W. A. Harrison, *Elementary electronic structure.* World Scientific Publishing Co., Ltd., 1999.

Chapter 4

Elastic Property Modelling

The correct prediction of the material properties of semiconductor crystals with the Tersoff potential provides us with the ability to model large scale systems (10^6 atoms) in a reasonable amount of time. This is something that is not currently achieveable with first principles quantum mechanical calculations due to the computational complexity. But, before we can use the Tersoff potential to correctly model a semiconductor system, we must first parameterise the potential to correctly model the material of interest. A correct modelling of the system parameters will provide us with a potential that is useful in molecular dynamics applications and for molecular system relaxation (aka. Molecular Statics). A number of metrics exist to measure the quality of the potential energy function (PEF) that provides a level of confidence in the quality of the current parameterisation. The modelling of the elastic properties is fundamentally linked to modelling of more complex properties such as the crystal dynamics which include phonon frequencies and the mode-Grüneisen parameters. A correct parameterisation based upon the elastic properties of the material allows us to predict the behaviour of complicated strained systems such as superlattices and quantum dots - which is essential for providing useful models of real-world systems and applications.

4.1 The lattice model

Initially a simulation "supercell" of 64 atoms is created by assembling 2x2x2 eight atom reduced unit-cells of the diamond or zinc blende structure, illustrated in figure 4.1. This is the minimum number of reduced unit cells required to provide correct boundary conditions for the material and to meet the minimum image criteria for the lattice. The potential cut-off function provides a measure of the minimum image criteria and the lattice should be large enough so that no atoms

can be bonded back onto their neighbours.

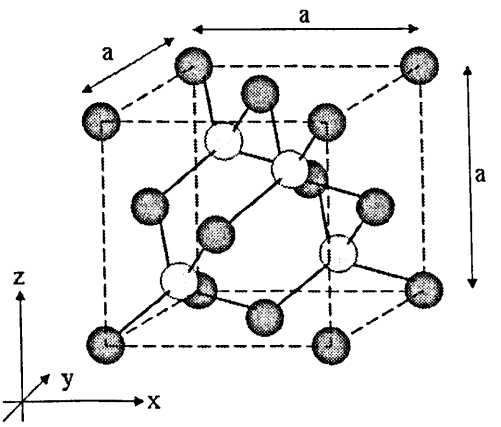

Figure 4.1: A single conventional cubic unit cell of the Zinc Blende structure

The lattice model is loaded into computer memory in reduced coordinates, so that each of the unit cells has unit length in each of the Cartesian axes. This is so that the computer program may automatically find the correct lattice constant for the system and scale the model accordingly. Each atom in the system has an associated position in 3D space which is measured in Angstroms and is given a type number based upon the periodic table element it is representing and the associated atomic mass in AMU.

The Tersoff parameters that are under test are loaded into the computer to tell the system how to relate each of the atoms in the neighbourhood of the others to each other and the testing begins.

Searching for the cohesive energy

A basic search for the *lattice constant*, a, that provides the energy minimum in the particular lattice system is performed. E_{coh}, the *cohesive energy* of the system is the energy required to break the crystal from a bulk lattice solid into isolated atomic species

$$E_{coh} = E(bulk) - \sum_{n} E(isolated)_n \qquad (4.1)$$

For each of the n isolated species. The computed values for cohesive energy are compared to the experimental ones which are obtained from measuring the latent heat of sublimation at various low temperatures and extrapolating this to zero Kelvin. The lattice constant in a cubic crystal, a, is the conventional unit cell length at equilibrium volume. This is obtained by computationally minimising the crystal energy as a function of cell volume.

Practically we need to incrementally scale the cubic lattice in computer memory and calculate the energy associated with that scaling. As we are dealing with a cubic lattice type we may scale the model equally in all three dimensions using an Affine transform[1, 2]. Affine transforms are generalisations of standard Euclidean geometric transforms but do not have the property that they must preserve lengths and angles of the object being transformed. Affine transforms can change the shape and size of an object by providing scaling and shear transforms.

The object lattice may be scaled up or down (stretch and shrink operations) using the scaling coefficients

$$\hat{S} = S_x, S_y, S_z$$

and the matrix equation:

$$\begin{bmatrix} x' \\ y' \\ z' \end{bmatrix} = \begin{bmatrix} S_x & 0 & 0 \\ 0 & S_y & 0 \\ 0 & 0 & S_z \end{bmatrix} \cdot \begin{bmatrix} x \\ y \\ z \end{bmatrix} \tag{4.2}$$

The inverse scaling can be performed using the scaling coefficients

$$\hat{S} = \frac{1}{S_x}, \frac{1}{S_y}, \frac{1}{S_z}$$

In general, to preserve accuracy in the system it is better to take a copy of the uniformly scaled atomic lattice in memory and scale it up to the desired lattice constant and then discard it, rather than scaling the original lattice model up and down repeatedly and introducing compound errors into the system.

A routine that simply takes a set of possible lattice constants (units of Å), say $a = [2...7]$ and a grain level of say $a_g = 1e^{-6}$ will have to perform 5 million iterations of the scaling operation, recording the energy result at each position and then performing a search over the numerical data to locate the minimum. The energy result at each position is found by calling the Tersoff energy evaluation routine with the current lattice model and a set of Tersoff parameters stored in memory. It returns a single double precision value that represents the lattice system energy. This is highly inefficient and has been improved by a granular search technique as follows:

1. Provide 2 search limits a_{min} and a_{max} and from these calculate the search width, $s_{wid} = a_{max} - a_{min}$ and the search pivot, $s_{piv} = \frac{s_{wid}}{2} + a_{min}$.

2. Split the search width region into n segments (typically $n = 10$) and calculate the energy at each location, x_n and label it e_n.

3. From the vector of n values, identify the minimum energy e_{min} at location x_{min}. This is the new search pivot $s'_{piv} = x_{min}$.

4. Redefine the search width as a tenth of the previous width, $s'_{wid} = \frac{s_{wid}}{10}$ and redefine the search limits to be: $a'_{min} = s'_{piv} - \frac{1}{2}s'_{wid}$, $a'_{max} = s'_{piv} + \frac{1}{2}s'_{wid}$.

5. Loop back to step 2 a number of times to iterate the process. The number of loops provides the search depth, s_{dep} (typically $s_{dep} = 6$).

Intuitively the above algorithm provides the same level of accuracy as the previous iterative search description, but completes a search at a granular accuracy of $a_g = 1e^{-6}$ in just 66 "moves" compared to a previous 5 million. This provides a massive level of computational speed up.

It should be noted that although this method provides a fast and simple granular search, it is only useful if the system has one global minimum to locate. In this case we are searching for the minimum energy with respect to lattice constant. This situation has only one global minimum provided the Tersoff parameters used are reliable and so the routine will always locate the energy minimum efficiently.

Bulk modulus B and shear modulus C'

Here we use rather standard means to predict the bulk and shear moduli of the materials under investigation.

Bulk modulus, B, relates how the volume of a piece of material changes when exposed to a uniform change in pressure and we can rewrite this in a more convenient form to relate an atomic distortion of the simulation box to a change in energy

$$B = -V\frac{dP}{dV} \tag{4.3}$$

$$= \frac{1}{\Omega}\frac{d^2E}{dv^2} \tag{4.4}$$

where Ω represents the atomic volume (simply the volume per atom) which is defined as $(a^3/8)$ in terms of the lattice constant a of the reduced unit cell used in the zinc blende or diamond simulation which contains 8 atoms. This is a measure of the curvature of the energy versus volume around the equilibrium volume. v is defined as the following uniform deformation on the system

$$R' = v^{1/3} \cdot R \tag{4.5}$$

As we are performing a uniform deformation x will vary at the same rate as y and z so we may rewrite this in terms of a, the lattice constant

$$x = v^{1/3} \cdot a \qquad \text{or: } \left(\frac{a}{x}\right)^2 = v^{-2/3} \tag{4.6}$$

Equation (4.4) requires the second derivative of v which would be simpler to deal with in terms of the box length x so we may use the following

$$dx = d\left(v^{1/3}a\right) \tag{4.7}$$
$$= \frac{a}{3}v^{-2/3}dv \tag{4.8}$$
$$= \frac{a}{3}\left(\frac{a}{x}\right)^2 dv \tag{4.9}$$
$$= \frac{a^3}{3x^2}dv \tag{4.10}$$

which we may simply square for

$$dv^2 = \frac{9x^4}{a^6}dx^2 \tag{4.11}$$

This allows us to rewrite (4.4) as

$$B = \frac{a^6}{9x^4\Omega}\frac{d^2E}{dx^2} \tag{4.12}$$
$$= \frac{a^6}{9a^4(a^3/8)}\frac{d^2E}{dx^2} \tag{4.13}$$
$$= \frac{8a^6}{9a^7}\frac{d^2E}{dx^2} \tag{4.14}$$
$$= \frac{8}{9a}\frac{d^2E}{dx^2} \tag{4.15}$$

Dimensional analysis of (4.15) gives a result in 10^{30} eV per m^{-3}. It is usual to represent the elastic properties in MBar which requires (4.15) to be multiplied by a conversion factor of 1.602. We note here that some authors publish figures for bulk modulus and shear modulus in dimensions of dyn/cm^2, and provide the following conversion factor

$$1MBar = 1 \cdot 10^{12} dyn/cm^2 \tag{4.16}$$

Practically, the atomic lattice in memory is copied three times with labels: m_0, m_- and m_+ then the lattices are scaled:

m_0 has the uniform Affine transform scaling vector $\hat{S} = [a, a, a]$ applied to it

and an associated energy e_0 is calculated from the Tersoff energy subroutine.

m_- has the uniform Affine transform scaling vector $\hat{S} = [a - dx, a - dx, a - dx]$ applied to it and an associated energy e_- is calculated from the Tersoff energy subroutine.

m_+ has the uniform Affine transform scaling vector $\hat{S} = [a + dx, a + dx, a + dx]$ applied to it and an associated energy e_+ is calculated from the Tersoff energy subroutine.

These operations are followed by a standard Euler numerical derivative and the coefficients named above are applied to calculate the bulk modulus

$$B = 1.602 \times \frac{8}{9a} \times \frac{e_+ + e_- - 2e_0}{dx^2} \tag{4.17}$$

Obviously the quality of the calculated bulk modulus has an error term as we are using a Euler approximation. The error is $O(dx^2)$ in "big O" notation and in general means we should assume that the answer is an approximation which is based upon the choice of dx. In the main calculation routines the values of dx are fixed at $1e^{-5}$ which is well within the machine precision and will provide a small enough error to be insignificant.

Many other authors use the Murnaghan equation of state [3] or the more sophisticated third-order Birch-Murnaghan equation of state [4] to calculate the bulk modulus of materials. The method described above, using an Euler approximation, may seem a little naive in comparison but the results were thoroughly tested in comparison to the analytic derivatives obtained later in the code development cycle as an artifact of the phonon calculations and proved reliable.

The *shear modulus*, C' can also be calculated from the second derivative of the Energy with a different simulation box transformation

$$C' = \frac{1}{4\Omega} \frac{d^2E}{d\epsilon^2} \tag{4.18}$$

where ϵ is provided by the system deformation

$$x = a \cdot (1 + \epsilon) \tag{4.19}$$

$$y = \frac{a}{(1 + \epsilon)} \tag{4.20}$$

$$z = a \tag{4.21}$$

We may now rework (4.18) using our deformation for x and the first derivative of x

$$dx = a \cdot d\epsilon \tag{4.22}$$

$$C' = \frac{1}{4\Omega}\frac{d^2E}{d\epsilon^2}\bigg|_{E=E_{coh}} \tag{4.23}$$

$$= \frac{a^2}{4\Omega}\frac{d^2E}{dx^2}\bigg|_{x=a} \tag{4.24}$$

$$= \frac{a^2}{4(a^3/8)}\frac{d^2E}{dx^2} \tag{4.25}$$

$$= \frac{2}{a}\frac{d^2E}{dx^2} \tag{4.26}$$

As with the bulk modulus, the shear modulus must be multiplied by the coefficient 1.602 to convert the figure into MBar.

To calculate the shear modulus practically, a similar method to the one above is used. The atomic lattice in memory is copied three times with labelling m_0, m_- and m_+. And then the lattices are scaled:

m_0 has the uniform Affine transform scaling vector $\hat{S} = [a, a, a]$ applied to it and an associated energy e_0 is calculated from the Tersoff energy subroutine.

m_- has the uniform Affine transform scaling vector $\hat{S} = [a(1-\epsilon), a/(1-\epsilon), a]$ applied to it and an associated energy e_- is calculated from the Tersoff energy subroutine.

m_+ has the uniform Affine transform scaling vector $\hat{S} = [a(1+\epsilon), a/(1+\epsilon), a]$ applied to it and an associated energy e_+ is calculated from the Tersoff energy subroutine.

These operations are followed by a standard Euler numerical derivative and the coefficients named above are applied to calculate the bulk modulus

$$dx = a\epsilon \tag{4.27}$$

$$C = 1.602 \times \frac{2}{a} \times \frac{e_+ + e_- - 2e_0}{dx^2} \tag{4.28}$$

The value calculated for the shear modulus C' will have the same numerical derivative issues as the bulk modulus due to the Euler approximation used in the calculation.

Simulation of c_{44} and ζ

Simulation of the c_{44}^0 elastic constant and from that number, the c_{44} elastic constant, requires a different type of Affine transformation - the shear transform. A shear transform has the effect of transforming the coordinates in one direction as a function of another whilst maintaining the coordinates in the third axis direction. When performing a c_{44}^0 simulation we talk about the engineering shear

factor, γ_{xy}, with which we transform the system. Consider the following matrix

$$\begin{bmatrix} x' \\ y' \\ z' \end{bmatrix} = \begin{bmatrix} 1 & \gamma_{xy} & 0 \\ 0 & 1 & 0 \\ 0 & 0 & 1 \end{bmatrix} \cdot \begin{bmatrix} x \\ y \\ z \end{bmatrix} \tag{4.29}$$

Here we are transforming the x-direction coordinates of the system as a function of the y-direction coordinates, whilst preserving the z-direction coordinates. The matrix produces the following distortion

$$\begin{aligned} x' &= x + (\gamma_{xy} \cdot y) \\ y' &= y \\ z' &= z \end{aligned}$$

After we have performed the shear transformation on the system we can then directly calculate a measure called c_{44}^0 from the following

$$c_{44}^0 = \frac{1}{\Omega} \frac{d^2E}{d\gamma_{xy}^2}\bigg|_{E=E_{coh}} \tag{4.30}$$

$$= \frac{8}{a^3} \frac{d^2E}{d\gamma_{xy}^2}\bigg|_{E=E_{coh}} \tag{4.31}$$

Again with the bulk and shear moduli, the c_{44}^0 elastic constant must be multiplied by the coefficient 1.602 to convert the figure into MBar.

Practically we perform the following operations:

The atomic lattice in memory is copied three times with labels m_0, m_- and m_+. And then the lattices are scaled:

m_0 has the uniform Affine transform scaling vector $\hat{S} = [a, a, a]$ applied to it and then an associated energy e_0 is calculated from the Tersoff energy subroutine.

m_- has the uniform Affine transform scaling vector $\hat{S} = [a, a, a]$ applied to it, then an engineering strain of $-\gamma_{xy}$ is applied to the system and an associated energy e_- is calculated from the Tersoff energy subroutine.

m_+ has the uniform Affine transform scaling vector $\hat{S} = [a, a, a]$ applied to it, then an engineering strain of $+\gamma_{xy}$ is applied to the system and an associated energy e_+ is calculated from the Tersoff energy subroutine.

These operations are followed by a standard Euler numerical derivative and the coefficients named above are applied to calculate the value of c_{44}^0

$$c_{44}^0 = 1.602 \times \frac{8}{a^3} \times \frac{e_+ + e_- - 2e_0}{d\gamma_{xy}^2} \tag{4.32}$$

The previously documented issues related to a numerical derivative approximation will still be present in the system, but with a well chosen value of γ_{xy} we can remain in the region between the computational limit and a value that is too large and will adversely affect our result.

To acquire the actual c_{44} elastic constant we need to perform an energy minimisation step between the shear strain transform and the numerical derivative calculation. Kleinman[5] had observed this effect and produced a paper suggesting an equation based upon the Affine shear transform and proposed an "internal displacement parameter" he labelled ζ. The energy minimisation step is due to a change in the 1 nn atomic bonding environment as an effect of the shear transformation. Due to this transform 2 of the atomic bonds have become lengthened and 2 of the atomic bonds have become shortened, at this point $\zeta = 0$. If the central atom was moved to a position where all of the atomic bonds have the same length then $\zeta = 1$. With a simple shear transformation, we find that the energy minimisation step produces a value of ζ somewhere between 0 and 1.

To obtain the correct value for the c_{44} elastic transform and the value of ζ we need to perform an energy minimisation. Using the shear transform above and γ_{xy}, the type V sublattice inside the III-V crystal needs to be moved in a positive z-direction. Again we are faced with a situation where we need to calculate the minimum energy of the atomic system in an iterative process. We could calculate this stepwise, as suggested before, but there are more efficient algorithms available.

We use the following simple algorithm to calculate the position of the energy minimisation:

1. Begin with the c_{44}^0 shear transformed lattice and calculate the initial energy, and make this the best energy value calculated thus far e_{best} with the Tersoff potential and the provided parameters.

2. Set two parameters $z_{dir} = 1.0$ and $depth = 3$.

3. Set $z_{scale} = 1e^{-depth}$. Move the atomic sublattice in the z-direction by an amount z_{move} where $z_{move} = z_{dir} \cdot z_{scale}$.

4. Calculate the energy at the new location e_{new}.

5. If $e_{new} < e_{best}$ then set $e_{best} = e_{new}$ and go to step 3.

6. If $e_{new} >= e_{best}$ then set $z_{dir} = -1 \cdot z_{dir}$ and $depth = depth + 1$.

7. If $depth > 7$ then end, else loop to step 3.

The values of depth can obviously be modified in the above system but under system testing the algorithm has been empirically observed to require an average of 23 "moves" to calculate the value of the sublattice displacement, δz to the nearest of $1e^{-7}$Å which is excellent efficiency compared to a similar iterative algorithm which may require up to 1 million system "moves".

Once the sublattice is in a relaxed state the c_{44} parameter can be calculated as described for the c_{44}^0 elastic property above. The value of the Kleinman internal displacement parameter ζ is directly calculated from the δz displacement as

$$\zeta = \frac{4 \cdot \delta z}{\gamma_{xy} \cdot a} \tag{4.33}$$

The cohesive energies of other phases

The cohesive energies and the lattice constants of the other cubic polytypes of the elemental type IV lattice and the zinc blende type III-V lattice were also checked to ensure that the Tersoff parameters were providing the lowest energy configuration for the desired lattice stoichiometry. This was done by building a lattice, as before, and using the lattice constant/cohesive energy search routine described above.

For the diamond structure semiconductors the simple cubic (sc) Ah structure, the face centred cubic (fcc) A1 structure and the body centred cubic A2 structure were checked against the diamond A3 structure type. For each of these structure types, a system containing the reduced uniform coordinates of the unit cell was entered into computer memory, along with the atomic type data. The lattices were then allowed to scale up according to the algorithm above and the cohesive energies and lattice parameters were recorded. The atomic volume, Ω was calculated per atomic system as the number of atoms per unit cell. In the case of the simple cubic lattice this is 1, for fcc it is 4, for bcc it is 2 and for diamond it is 8 atoms per unit cell.

A similar situation exists for the compound zinc blende structure semiconductors, the sodium-chloride (NaCl) B1 structure and the caesium-chloride (CsCl) B2 structure types were checked against the zinc blende B3 structure. For each of these structure types, a system containing the reduced uniform coordinates of the unit cell was entered into computer memory, along with the atomic type data. The lattices were then allowed to scale up according to the algorithm above and the cohesive energies and lattice parameters were recorded. The atomic volume, Ω was calculated per atomic system as the number of atoms per unit cell. In the case of the NaCl B1 structure this is 8, for CsCl B2 structure it is 2 and for B3 zinc

blende it is 8 atoms per unit cell.

Once the lattice constants of all of the above structure had been found to within the search depth tolerance, the program was then instructed to provide an output file with a 100 point energy curve for plotting purposes, as can be seen on the next few pages in the results section for each system. The data collection routine to evaluate the other cubic lattices takes 1.32 seconds to run on the laptop computing platform.

4.2 Parameterisation Method

A few of parameterisation methods have been developed with the aim of locating a set of Tersoff parameters that will satisfy the material properties and elastic constents database. In general this is quite a simple task - we have to choose between methods that involve locally searching the parameter space around a provided set of results (from e.g. another author) with the aim of improving them to a more refined set of properties. Or, we can globally search an entire parameter space hoping to locate a new set of Tersoff parameters.

Granular radial searching

Here we a start the search with a known search position and allow the system to do a steepest descent optimisation in a number of different directions, refining the search tolerance as we go. We call this a "radial" search as the system is limited to searching the radius defined by the granularity of the search immediately around the current position. The initial position in parameter space is generally provided by another author and it is our intention to improve upon their results.

The weighting method from the previous chapter was employed to provide a balanced search method and the weights were distributed uniformly $w_n = 1$ using the following parameterisation metric

$$m = \sum_n w_n (x_n - d_n)^2 \tag{4.34}$$

Where the vector of sought material properties is described as

$$x_n = [e_{coh}, a, B, C', c_{44}, \zeta] \tag{4.35}$$

And the d_n database values were taken from a mixture of DFT predictions and experimental results.

The algorithm for the granular radial search is as follows:

1. Start with the current parameter vector, v.
2. Calculate the current parameter metric, m_{curr}.
3. Start with an initial "grain size", g, e.g. 0.1.
4. Select one of the ten Tersoff parameters from the vector at random, v_n.
5. Create a "parameter tweak", t, from: Obtain a random number in the range $[0, 1)$, subtract 0.5 from this number to provide a random number in the range $[-0.5, 0.5)$ and multiply it by the grain size and the selected parameter to provide a tweak that is proportional to the original parameter, $t = [-0.5, 0.5) \cdot g \cdot v_n$.
6. Add the parameter tweak to the parameter value, $v'_n = v_n + t$.
7. And form a new parameter vector, v' from the nine previous values and the one new parameter.
8. Calculate the new parameter metric, m_{new}.
9. If $m_{new} < m_{curr}$ accept the move and make $v = v'$ and $m_{curr} = m_{new}$, else discard m_{new} and $v*$.
10. Maintain the statistical count of how many tweaks per 100 have been accepted as "good moves". If this number falls below 5% then shorten the grain size, e.g. make $g = g/10$.
11. Loop to Step 4 until the maximum number of iterations have been reached (typically 10,000) or until the grain size has become insignificant (typically 10^{-6}).

This algorithm is an improvement (in terms of program run timing) on the common Simplex Algorithm which, for a q dimensional search space, needs to construct a Simplex of $q + 1$ "moves" before a decision would be made regarding whether the current direction of "move" was correct. The Simplex Algorithm demands a theoretical maximum of 2^{q+1} possible "moves" to find a minimum energy movement in the search space, whereas the algorithm described above requires a maximum of only 2^1 moves before a movement direction has been identified as an improvement on the previous position. This is because it searches only one parameter dimension at once, which although it seems intuitively a possible

source of descent into a local minimum, the granular nature of the program provides an escape mechanism from this phenomenon. Furthermore, due to the high speed at which the program executes, there is no reason not to run it again if the results are not favourable. It has been empirically observed that the program will locate the same minimum from a given starting point 95% of the time - this is due to the granular nature of the stochastic search and a search space filled with local minima.

An average program run of this search (about 6500 iterations) will typically take 184.92 seconds (about 3 minutes) and will provide a Tersoff parameterisation with all parameters within 1-2% of the desired values. It has been found that an improvement in the quality of the set can be made if the program is then run again. It is generally observed in the second run that the program will immediately jump over the first one or two search depths and then begin further refinement at a smaller grain size. The random number generator is essential in a stochastic system such as this and the one chosen for this work is the "Mersenne Twister" which provides a random number generator that is 4 times faster then the machine supplied *rand*() function and has a periodicity of $2^{19937} - 1$ - which is more than adequate for this application[6].

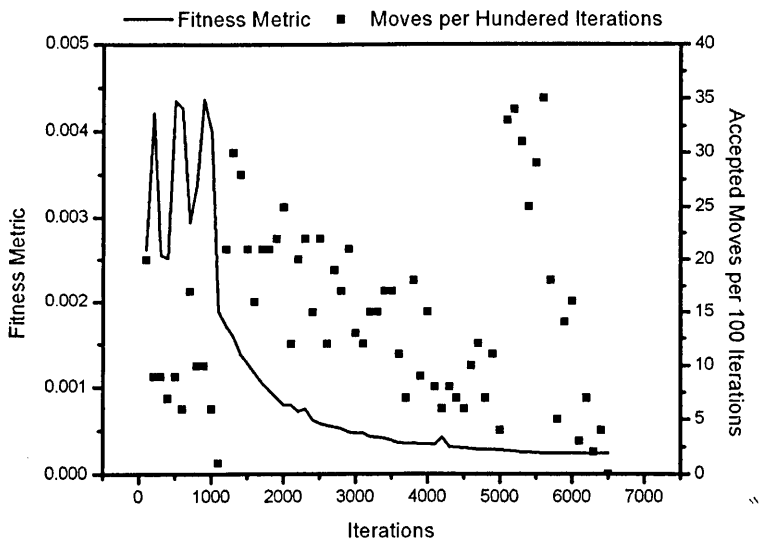

Figure 4.2: Granular radial search output showing the overall fitness metric of the silicon parameterisation and the "hit ratio" of the system

Figure 4.2 shows a sample data collection output of the program described above and it can be clearly seen when the grain size is reduced based on the triangular trend appearing in the "accepted moves" field. When the grain size is reduced the program is able to produce more "moves" in parameter space due to

the nature of the random search pattern to improve the metric. This correct move effect will fall-off until a prescribed limit (typically a 5% successful hit ratio) and then the grain size is reduced further. Stochastically speaking, the algorithm will initally avearage a 50% hit ratio as the grain size is first reduced and this will lower as the system becomes more refined towards the goals. This is due to the search space having already been searched via the 10 parameters and the 2 degrees of freedom per parameter. The solid line in the figure shows the fitness metric which can be seen to be asymptotic towards zero. The spikes in the fitness metric generally correlate with a reduction in the grain size. This is a very effective alogrithm and will generally produce an improved new set of Tersoff parameters in under 5 minutes on the laptop computing platform described previously.

Granular random searching

The granular radial search method described above is an example of a local parameter space search technique. It can be combined with a more complex algorithm to make it a global search technique over the whole unknown parameter space landscape. The algorithm begins with a random vector of Tersoff parameters and then proceeds to test each one, first to see if it will even evaluate (against the error trapping routine which looks for negative number under roots etc.) and then the surviving members of the vector are passed to the local granular search algorithm to be refined. The random vector of Tersoff parameters are generated be applying a random number in the range $[-0.5...0.5)$ to a set of predefined limits that will produce groups of Tersoff parameters that will probably evaluate. The values R and R_{cut} were predetermined before the program run to provide the first nn cut-off function correctly. The limits are highlighted in table 4.1 below

Parameter	Min.	Max.
D_e	1.0	5.0
S	0.5	2.5
β	0.5	2.5
r_e	1.0	5.0
c	1	1000
d	1	1000
h	-0.0001	-7
n	0.0001	15.0
γ	0.0001	10.0
λ	1.0	3.0

Table 4.1: The random Tersoff parameters ranges

1. Create a random vector of Tersoff parameters, T_n.

2. Loop from $1...n$
3. Will T_n evaluate? If not go back to step 2.
4. Pass T_n to the local granular search *twice* to improve the quality of the results.
5. Store and result and go to step 2.

An evaluation of the random search of the 10 dimensional space took 188336 seconds (over 52 hours) on the desktop computing platform. 5000 starting points were used, but ones which did not provide an evaluation or provided a $E_{coh} = 0$, (which is an artifact of the error trapping routine) were immediately discarded, leaving 513 possible points in the search space to explore with the local routine described above. Of the resulting 513 parameter sets that could be improved, only 61 of them had a small enough metric to be considered as "reasonable" results.

The data collection from the program is displayed below in a series of figures. Figure 4.3 shows the spread of the fitness metrics as final figures from the double evaluation with the local search routine for each of the surviving 513 Tersoff parameter sets. It can be clearly seen that most of these results became stuck in local minima that provided results which did not provide a fitness metric $m < 1$ (equation 4.34). A metric of $m < 1e^{-3}$ is considered a good result and as can be seen, only 61 of these results provided a metric in that range.

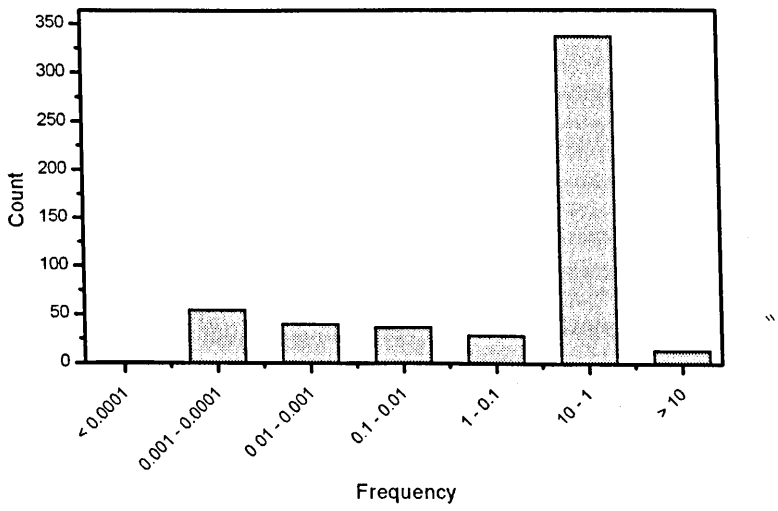

Figure 4.3: Granular random search output for silicon showing the spread of the fitness metrics of all 513 successful runs

Figures 4.4(a) to 4.4(f) show the spread of the material properties obtained for silicon. The experimental and DFT values that the program was searching for are: $E_{coh} = -4.63$ eV, $a = 5.431$ Angstroms, $B = 0.9783$ MBar, $C' = 0.509$ MBar, $c_{44} = 0.796$ MBar and $\zeta = 0.524$ (dimensionless) and as can be seen from the graphs the program had little difficulty in generally identifying a reasonable value for E_{coh}, a and B. However, the correct prediction of C', c_{44} and the coupled value of ζ were more problematic. This is evidently reflected in the large error in the majority of the search metrics.

On average the majority of large resultant metrics ($m = [1...10]$) from the program run reflected the likelihood of local search minima to produce good values of the lattice parameter, cohesive energy and bulk modulus and an inability to couple these good results with correct material properties that correctly predict the local strain effects with the shear modulus and other strain dependent elastic properties. The single best output from the above run was evaluated against the results provided in the next section and was found to be functionally equivalent.

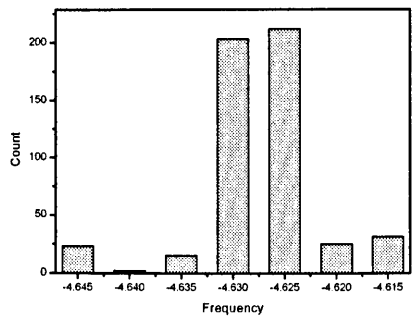

(a) E_{coh} distribution

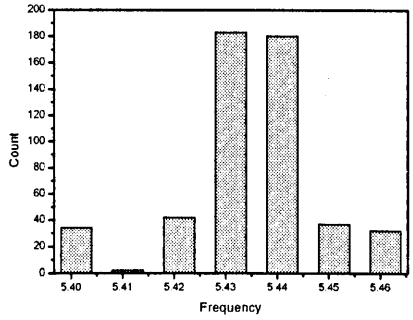

(b) a distribution

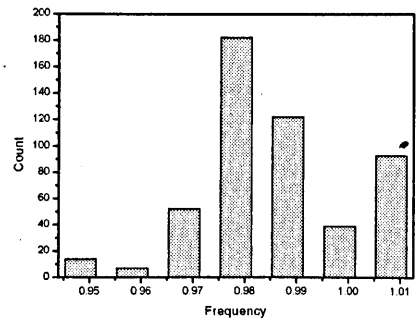

(c) B distribution

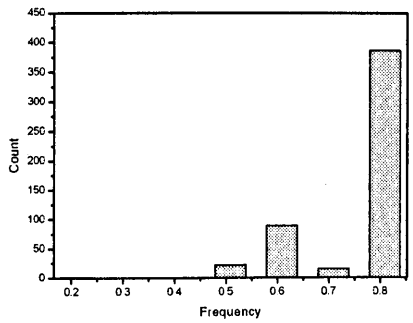

(d) C' distribution

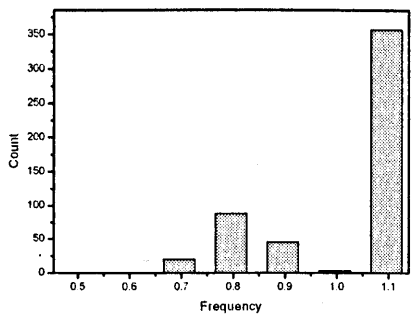

(e) C_{44} distribution

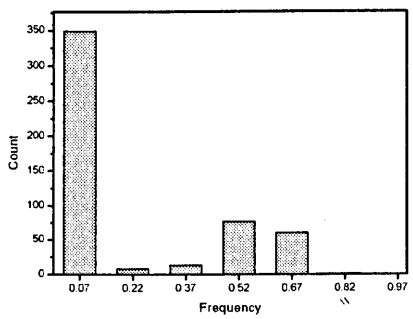

(f) ζ distribution

Figure 4.4: Granular random search output for silicon showing the spread of the material properties of all 513 successful runs

4.3 Results

The results of the above algorithms are described below for 13 different semiconductor systems. The local granular search program was used in each case due to the guarantee of finding reasonable results in a small amount of time, and all results are very pleasing. The global random searching routine has not been used to collect data on any other systems due to the massive amount of simulation time required and the inconsistent quality of the results.

All results have been fitted to the experimental values of lattice constant and cohesive energy and the DFT predictions of the elastic properties and ζ. This is because the DFT values of a and E_{coh} tend to be within a 2% tolerance and are not totally reliable. But the DFT predicitons for the elastic properties of the materials under deformation are not dependent upon the value of lattice parameter and are not subject to experimental measurement errors and hence are thought to be more accurate.

Experimentally, techniques such as Brillouin spectroscopy are used to measure the elastic properties of materials. Brillouin light scattering is generally referred to as inelastic scattering of an incident optical wave field by thermally excited elastic waves in a sample. In the case of a transparent solid, most of the scattered light emanates from the refracted beam in a region well away from the surface and the kinematic conditions relating wave vector and frequency shift of the light pertain to bulk acoustic wave scattering. The phonons present inside a solid move in thermal equilibrium with very small amplitudes creating fluctuations in the dielectric constant, which is viewed as a moving diffraction grating by an incident light wave. Therefore Brillouin scattering can be explained by the two concepts of Braggs reflection and Doppler shift. This technique is widely used for characterising the elastic properties of crystal samples and more details can be found in [7, 8, 9].

4.3.1 Silicon

Silicon is the principal component of most semiconductor devices. Silicon forms covalent bonds with neighbours in a tetrahedral pattern and in standard conditions it takes on the diamond phase. Silicon is widely used in semiconductor devices because it has a lower reverse leakage current than germanium (the material first used for semiconducting devices) and because its native oxide is easily grown in furnaces to form semiconductor/dielectric interfaces. In crystalline form pure silicon takes on a grey colour and is relatively inert in the at-

mosphere. Silicon has a negative temperature coefficient of resistance and can be easily doped to make the pn junctions required for active devices such as diodes and transistors.

Parameter	Tersoff (T3)	Powell (P1)
D_e	2.666029	2.36291
S	1.431648	1.48565
β	1.465552	1.46405
r_e	2.295161	2.34358
R	2.85	2.85
R_{cut}	0.15	0.15
c	100390	113031
d	16.217	14.248
h	-0.59825	-0.423876
n	0.78734	0.938777
γ	1.1e-06	1.2467e-06
λ	1.5[1]	1.4606

Table 4.2: The Tersoff parameters for diamond Silicon

Even though elemental silicon is being somewhat superseded in some fields of electronics, it still has a number of notable advantages over III-V materials such as GaAs. Firstly, silicon dioxide is an excellent insulator and can easily be formed in elemental silicon devices to provide dielectrics and patterned tracks in solid state devices. Furthermore, silicon is abundant and cheap to process with a good physical strength and so large scale wafers can be made more easily. Finally, silicon has a higher hole mobility than many III-V materials, providing an excellent basis for high speed p-channel FET devices for low-power, high-speed CMOS logic based electronics.

Property (units)	Exp./Calc.	Tersoff (T3)	Powell (P1)
$E_{coh}(eV)$	-4.63[2]	-4.629	-4.6305
a (Å)	5.431[4]	5.432	5.431
B (MBar)	0.9783[3]	0.977	0.976
C' (MBar)	0.509[3]	0.336	0.511
c_{11} (MBar)	1.657[3]	1.425	1.657
c_{12} (MBar)	0.639[3]	0.754	0.635
c_{44} (MBar)	0.796[3]	0.690	0.797
ζ	0.524[2]	0.674	0.519

Table 4.3: The material properties of Si

Silicon has been widely studied in the past 50 years and the experimental data regarding the lattice constant, energy states and elastic properties for silicon are very well known.

[1] Tersoff does not use the λ parameter in his fit so it is set to 1.5 here
[2] from Harrison[10]
[3] See [11]
[4] Ref. [12]

Phase	Tersoff (T3) E_{coh} (eV)	a (Å)	Powell (P1) E_{coh} eV	a (Å)
sc	-4.504	2.527	-4.622	2.513
fcc	-3.989	4.038	-3.094	4.167
bcc	-4.197	3.085	-3.590	3.149
diamond	-4.630	5.432	-4.630	5.431

Table 4.4: Crystal phase data for Silicon

We started with the Tersoff (T3) [12] parameterisation of Silicon and provide below another parameterisation of silicon for the Tersoff PEF (see table 4.2). The results obtained from the above parameters are shown in table 4.3 and as can be clearly seen, the error in the Tersoff values in the elastic properties were originally 34% and 13% respectively for the shear modulus and c_{44} value and these have been improved to less than 1% error in all metrics tested. The energy vs. lattice parameter plots shown in graph 4.5 and graph 4.7 both show that the material has a cohesive energy minimum of -4.63eV at a lattice parameter of 5.431Å.

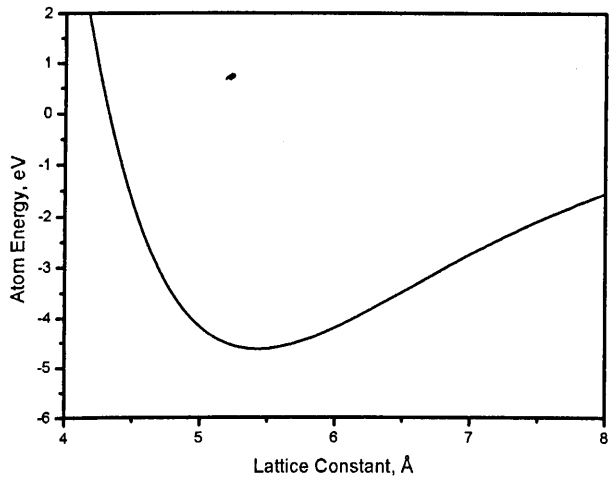

Figure 4.5: Cohesive energy of silicon from Tersoff (T3) parameters

The phase of the Tersoff parameterisations shown above was tested to demonstrate the transferability of the potential to high temperature or high pressure MD simulations and the results are shown in table 4.4. Here it can be noted that although the parameters have been changed to reflect a more accurate small scale strain model, the material phase plots (shown in graph 4.6 for the Tersoff (T3) parameters and graph 4.8 for the Powell (P1) parameters) are both stable with the diamond form of the material being the preferred state.

The fcc and bcc phases of the material have been translated further up the plot in the case of the Powell parameters which would provide a simulation that was

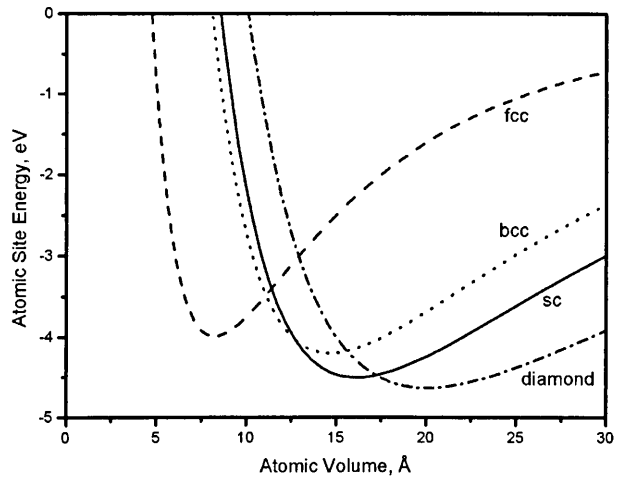

Figure 4.6: Energy vs. atomic volume for silicon with Tersoff (T3) parameters

more likely to prefer the natural diamond state of the material. The energetics of the simple cubic (sc) phase of the material have been moved closer to the diamond phase with the Powell parameters, but for the system to take on a simple cubic phase under MD conditions would require a significant change of atomic geometry and is unlikely.

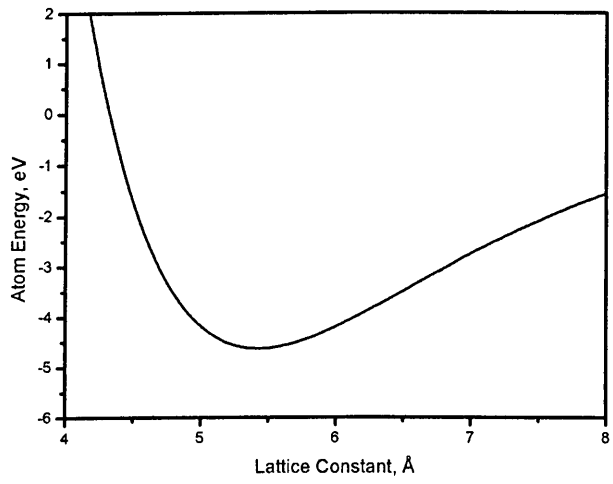

Figure 4.7: Cohesive energy of silicon from Powell (P1) parameters

Figure 4.8 may be directly compared to *ab initio* results obtained by Yin and Cohen [13]. In comparison it becomes clear that, although the Powell parameters provide an energy minimum for the diamond phase, the simple cubic (sc) energy is too low in the Powell parameterisation. This effect is due to the Tersoff model

being designed for an atomic coordination, z, of 4 and penalising any crystal systems that do not form 4 neighbour bonds. It is very difficult for the Tersoff model to replicate the simple cubic phase accurately due to the 6 neighbour bonds in the simple cubic structure. The work of Yin and Cohen also considers the β-tin phase (A5) of the type IV material and hexagonal systems including hexagonal close packed (hcp) and hexagonal diamond (aka. Lonsdaleite) which have not been considered in this work.

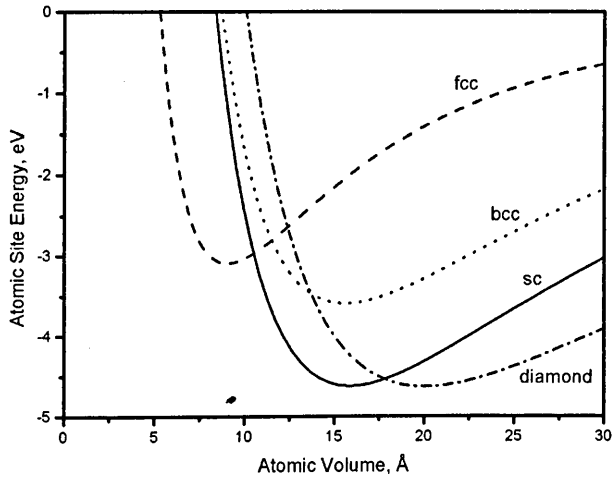

Figure 4.8: Energy vs. atomic volume for silicon with Powell (P1) parameters

4.3.2 Diamond Structure Carbon

Diamond carbon is an extremely hard material exhibiting extraordinary properties and potential for nanotechnology applications. Diamond has very short bond lengths, a high lattice thermal conductivity and a very wide band gap. Diamond carbon has already found myriad application in high pressure optical applications (as a hardened window) due to its natural high dispersion of light and in coating and hardening applications due to a very small lattice constant and high thermal conductivity. Diamond is considered to be the hardest naturally occurring material in the world (the hardest are mined from the New England area in Australia) and has many industrial applications for cutting, grinding and polishing. Diamond carbon is regularly synthesised for industrial applications but the quality of the material is not as good as the naturally occurring mined diamond. Some forms of diamond (blue diamond) have been found to be natural semiconductors whilst others are natural insulators. This makes diamond a very interesting proposition as a semiconductor material.

Parameter	Tersoff (T3)	Powell
D_e	5.164533	5.03634
S	1.576879	2.18415
β	1.964037	1.99468
r_e	1.447206	1.46388
R	1.95	1.95
R_{cut}	0.15	0.15
c	38049	40064
d	4.384	4.37865
h	-0.57058	-0.545985
n	0.72751	0.619052
γ	1.5724e-07	1.61144e-07
λ	1.5[1]	1.65768

Table 4.5: The Tersoff parameters for diamond Carbon

Although diamond carbon is not as stable as the rhomboidal graphite form as a material and diamond is considered metastable, it would take possibly the length of time that the universe has been in existence for the material to decay into graphite due to a extremely high kinetic barrier.

Property (units)	Exp./Calc.	Tersoff (T3)	Powell
$E_{coh}(eV)$	-7.37[4]	-7.422	-7.370
a (Å)	3.567[4]	3.561	3.564
B (MBar)	4.42[5]	4.294	4.408
C' (MBar)	4.755[5]	4.819	4.755
c_{11} (MBar)	10.76[5]	10.72	10.748
c_{12} (MBar)	1.25[5]	1.08	1.238
c_{44} (MBar)	5.77[5]	6.407	5.778
ζ	0.267[2]	0.229	0.309

Table 4.6: The material properties of diamond Carbon

Diamond carbon is currently being investigated thoroughly for nanotubes and related applications due to the proposition that diamond nanotubes may be even harder than mined diamond and furthermore as a substrate material for the growth of III-N electroluminescent devices due to the favourable lattice matching properties. A number of different carbon nanotubes can be formed by considering the bisection of a C_{60} molecule by a number of different planes[15].

Phase	Tersoff (T3) E_{coh} (eV)	a (Å)	Powell E_{coh} eV	a (Å)
sc	-4.919	1.776	-5.859	1.691
fcc	-3.246	2.961	-5.437	2.652
bcc	-3.839	2.228	-5.325	2.059
diamond	-7.422	3.561	-7.370	3.553

Table 4.7: Crystal phase data for Carbon

We started with the Tersoff (T3) [16, 12] parameterisation of carbon and proceeded to attempt to improve on the original parameter set provided by looking at the elastic properties and the small scale strain effects predicted by the internal displacement parameter ζ. The new parameters are provided in table 4.5.

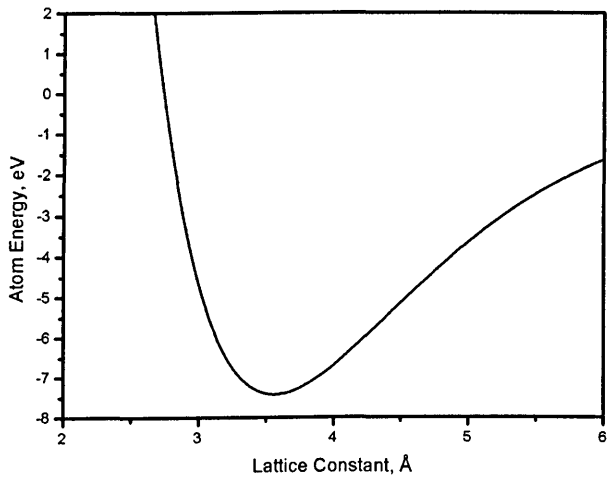

Figure 4.9: Cohesive energy of diamond carbon from Tersoff (T3) parameters

The results obtained from the above parameters are shown in table 4.6 and it can be seen that the Tersoff parameter set has been improved upon. Cohesive energy is now correctly identified as -7.37eV and the the lattice parameter is correct to less than 1%. The bulk modulus has been inproved from 3% error to less than 1% and although the shear modulus originally only had a 1% error - this has

[5]See [14]

been brought closer to the measured value. The c_{44} parameter value has been improved from 11% error to less than 1% error. The Kleinman internal displacement parameter still shows about a 15% error in the value.

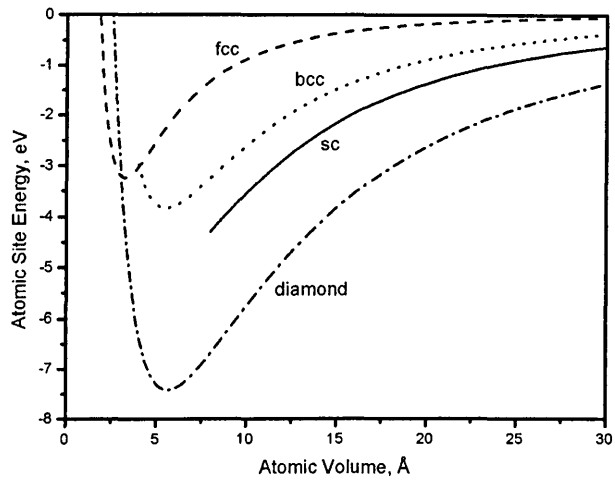

Figure 4.10: Energy vs. atomic volume for diamond carbon with Tersoff (T3) parameters

The energy vs. lattice parameter plots shown in figure 4.9 and figure 4.11 provide almost identical data, showing that minimum energy for the pair bonding between the atoms in the correct diamond crystal geometry occurs at -7.37eV and 3.567Å.

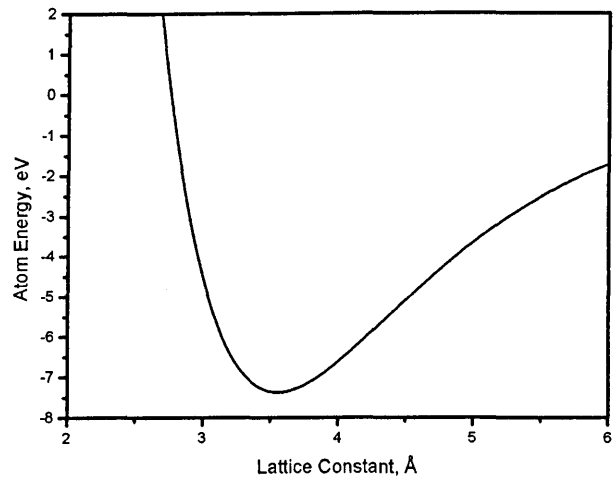

Figure 4.11: Cohesive energy of diamond carbon from Powell parameters

The material phase data given in table 4.7, figure 4.10 and figure 4.12 clearly

demonstrates that the parameters given above for both the Tersoff and the Powell fits will provide excellent phase stability for diamond under MD simulation conditions. The shortening of the simple cubic phase (sc) line is due to a cut-off of the simulation software at just under 2Å to stop the system testing unnecessary data under most conditions and to speed up the software run times. Although the Powell parameters bring the fcc and bcc plots closer to the diamond phase, the actual energy difference between the phases is still over 2eV.

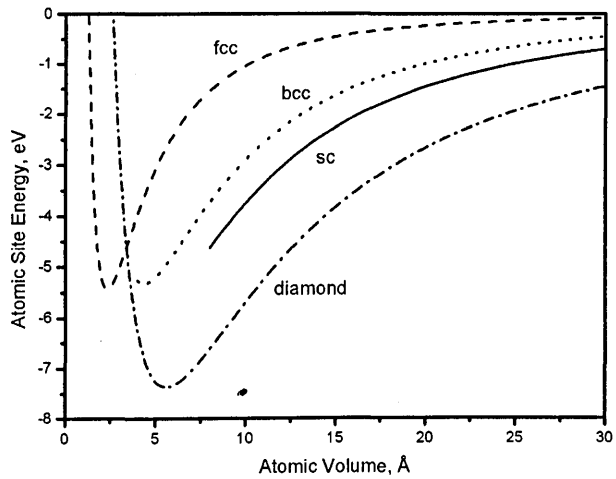

Figure 4.12: Energy vs. atomic volume for diamond carbon with Powell parameters

4.3.3 Germanium

Germanium is element number 32 in the periodic table and is a hard silver-white metalloid similar in chemical properties to tin. Under normal conditions germanium takes on the diamond lattice form and is a semiconductor material. The development of the germanium transistor in the 1950s provided a major solid state technological advancement and was the material of choice for electronic applications until the high quality refinement of silicon in the early 1970s. Demand for germanium devices is still high and a large number of applications still require germanium based semiconductors including fibre optic communications systems and night vision applications due to the small band gap and ability to efficiently respond to infrared light. Germanium devices are still favoured by some musicians who claim that the transistors provide a vintage "fuzz" tone in their amplifiers and effects equipment.

Parameter	Tersoff (T3)	Powell
D_e	2.010567	2.06459
S	1.434329	1.35835
β	1.443634	1.43283
r_e	2.431721	2.42024
R	2.95	2.95
R_{cut}	0.15	0.15
c	106430	113656
d	15.652	15.3874
h	-0.43884	-0.483616
n	0.75627	0.834411
γ	9.0166e-07	1.00689e-06
λ	1.5[1]	0.933196

Table 4.8: The Tersoff parameters for Germanium

The silicon-germanide alloy (usually just called silicon-germanium or SiGe) is being used increasingly in solid state devices due to the rapid switching characteristics and high speed operation of SiGe transistors.

Property (units)	Exp./Calc.	Tersoff (T3)	Powell
$E_{coh}(eV)$	-3.85[4]	-3.851	-3.850
a (Å)	5.658[4]	5.657	5.658
B (MBar)	0.7516[6]	0.758	0.746
C' (MBar)	0.403[6]	0.471	0.411
c_{11} (MBar)	1.2889[6]	1.385	1.293
c_{12} (MBar)	0.4829[6]	0.444	0.472
c_{44} (MBar)	0.671[6]	0.668	0.671
ζ	0.521[2]	0.504	0.519

Table 4.9: The material properties of Germanium

[6]Ref. [17]

The Tersoff (T3) parameters for Germanium were used as a starting point for the parameterisation and we attempted to improve upon the materials and elastic properties. The parameterisations are shown in table 4.8.

Phase	Tersoff (T3) E_{coh} (eV)	a (Å)	Powell E_{coh} eV	a (Å)
sc	-3.943	2.606	-3.539	2.657
fcc	-3.427	4.167	-2.416	4.402
bcc	-3.496	3.201	-2.845	3.316
diamond	-3.851	5.657	-3.850	5.658

Table 4.10: Crystal phase data for Germanium

The results obtained from the above parameters show a good agreement with the experimentally measured data for germanium (table 4.9). Both parameterisations correctly predict the cohesive energy, the lattice constant and the bulk modulus to about 0.1% accuracy. The shear modulus and c_{44} parameters are predicted by Tersoff to be in error by 17% and 1% respectively. These errors have been reduced to 2% and 0.1% respectively. The Tersoff parameters provide a 3% error in the prediction of the Kleinman internal displacement parameter, where the Powell parameterisation reduces this to below 1%.

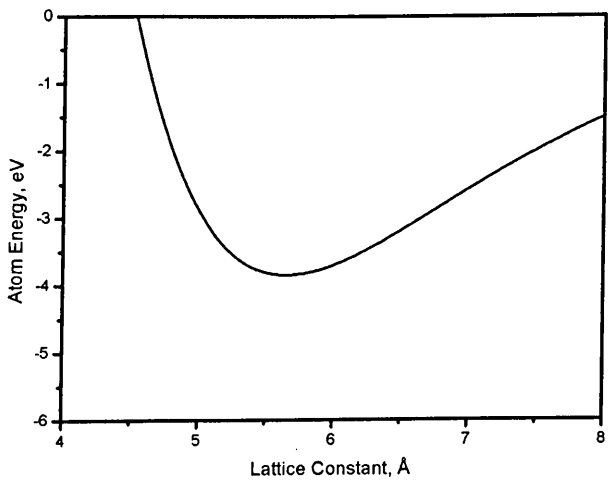

Figure 4.13: Cohesive energy of germanium from Tersoff (T3) parameters

The graphics shown in figures 4.13 and 4.15 show that both parameterisations correctly reproduce the cohesive energy of the material under minimum energy bonding conditions to be -3.85eV at 5.658Å.

Table 4.10 shows the data form the material phase tests. Here it can be seen that the Tersoff parameterisation shows a slightly lower energy state for the simple cubic (sc) phase of the material. This has been rectified in the Powell pa-

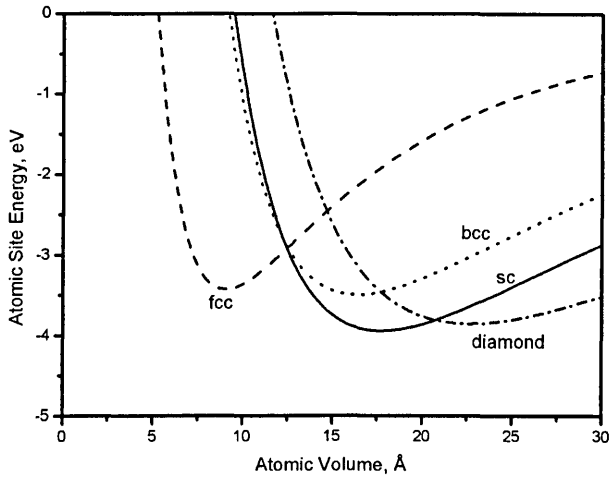

Figure 4.14: Energy vs. atomic volume for germanium with Tersoff (T3) parameters

rameterisation and the diamond phase of the material is now the lowest energy state by around 0.4eV. The phase plots of germanium for the Tersoff and Powell parameterisations are shown in figures 4.14 and 4.16 respectively.

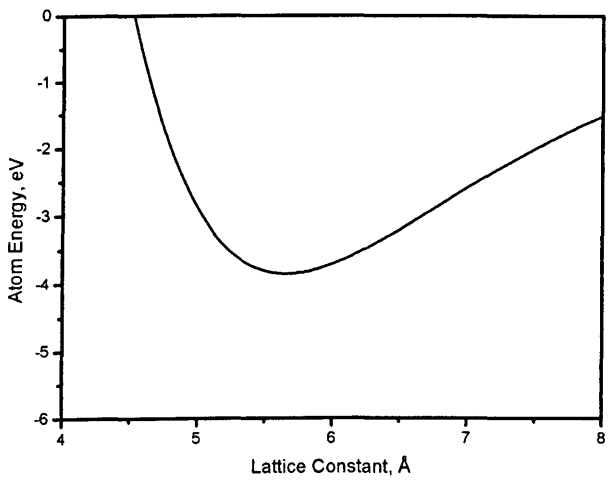

Figure 4.15: Cohesive energy of germanium from Powell parameters

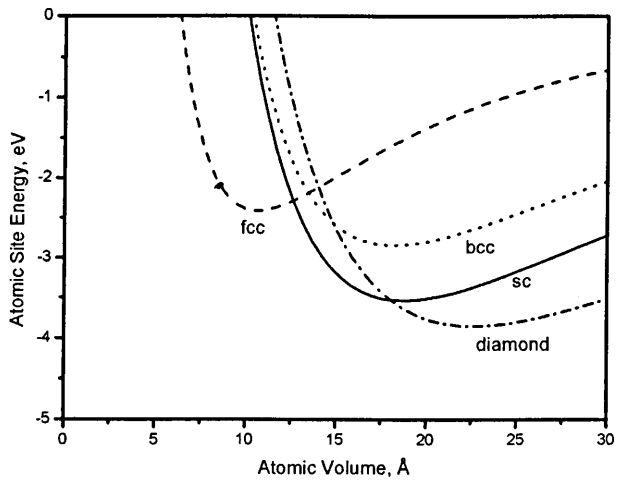

Figure 4.16: Energy vs. atomic volume for germanium with Powell parameters

4.3.4 Gallium Arsenide

Gallium arsenide (GaAs) is a type III-V compound semiconductor that naturally forms in the zinc blende structure configuration. The bonds that are formed in the material (as with all III-V semiconductors) are mainly covalent with a small amount of ionic bonding. GaAs has a direct band gap that allows the material to be used in optoelectronic devices and the material has a number of other advantages over silicon. GaAs has a higher electron mobility than silicon and it has been predicted that the material could provide high speed switching at up to 250GHz. GaAs devices produce less noise when operated at high speed than silicon devices and due to a higher breakdown voltage than silicon GaAs may be operated at higher power levels. It is common to find GaAs based devices in LED and optoelectronic applications and also as the RF modulator in mobile phones and satellite communications equipment.

Parameter	Smith	Sayed	Powell
D_e	2.180	2.180	2.12673
S	1.5351119	1.641366	1.60228
β	1.614	1.560903	1.56295
r_e	2.345	2.345	2.35218
R	3.5	3.5	3.5
R_{cut}	0.1	0.1	0.1
c	0.07837998	1.226302	1.20595
d	4.5049412	0.790396	0.800338
h	-3.4109679	-0.518489	-0.442817
n	5.5039372	6.317410	5.43647
γ	0.38090204	0.357192	0.363585
λ	1.5[7]	1.723	1.83057

Table 4.11: The Tersoff parameters for Gallium Arsenide

GaAs is a very important material for forming heterostructure devices. It is very well characterised and can be grown reliably with the Bridgeman technique to form substrate layers for the pseudomorphic growth of quantum nanostructures.

Property (units)	Exp./Calc.	DFT[8]	Smith	Sayed	Powell
$E_{coh}(eV)$	-3.25[2]	—	-3.251	-3.251	-3.250
a (Å)	5.65325[2]	—	5.655	5.655	5.654
B (MBar)	0.753[9]	0.757	0.800	0.748	0.750
C' (MBar)	0.3285[9]	0.364	-2.00656e-05	0.326	0.368
c_{11} (MBar)	1.191[9]	1.242	0.799	1.182	1.240
c_{12} (MBar)	0.534[9]	0.514	0.799	0.530	0.505
c_{44} (MBar)	0.596[9]	0.634	-3.16694e-05	0.687	0.639
ζ	0.581[2]	0.506	0.999	0.536	0.516

Table 4.12: The material properties of Gallium Arsenide

[7]The λ parameter is not included in the parameter fit of this author. It is arbitrarily set to 1.5 here.

The parameterisation was started with the Smith[21] and Sayed *et al*[22] parameterisations of Gallium Arsenide and the Sayed parameters were chosen to be refined due to their ability to better reproduce the elastic properties of the material. Here, the Powell parameters were chosen to fit to the DFT data provided by Wang[18] as this was thought to be a more reliable value of the elastic properties of the material than the data provided by older measurement techniques. The parameters used in the tests are shown in table 4.11.

Phase	Smith		Sayed		Powell	
	E_{coh} (eV)	a (Å)	E_{coh} eV	a (Å)	E_{coh} eV	a (Å)
NaCl	-2.776	5.187	-1.705	5.532	-1.704	5.538
CsCl	-2.133	3.283	-1.368	3.464	-1.319	3.485
zinc blende	-3.251	5.655	-3.251	5.655	-3.250	5.654

Table 4.13: Crystal phase data for Gallium Arsenide

The results obtained from the parameters are shown in table 4.12. Here it can be seen that all 3 parameterisations have been able to reliably replicate the material cohesive energy and lattice constant. The predicted bulk modulus value is 6% high for the Smith parameters and within good tolerance for the other parameterisations. The Smith parameters cannot replicate the shear modulus or c_{44} elasticity of the material, but the Sayed and Powell parameters are in reasonable agreement with the tolerances improved from 10% and 8% respectively to 1% and 0.1%. The internal displacement parameter predicted by the Powell parameters has been improved to only a 2% error providing more confidence in the parameters for use in small strain structural relaxations.

Graphs 4.17, 4.19 and 4.21 show the material lattice parameter plotted with the energy of the bonding. All graphs show that the parameters correctly predict the short-range bonding behaviour of the material and produce cohesive energies at -3.25eV at lattice constants of 5.65Å.

Table 4.13 shows the phase data calculated for the Smith, Sayed and Powell parameters. This data is plotted in figures 4.18, 4.20 and 4.22 and clearly demonstrates that all three parameterisations will provide a system that is most stable in the zinc blende formation. The Sayed and Powell parameterisations provide very similar results, both improve on the separation from the CsCl and NaCl structure types (by up to 1.55eV) when compared to the Smith parameters which predicts a separation of only 0.5eV.

Figure 4.22 can be compared to the *ab initio* modelling of the structural properties of III-V materials performed by Froyen and Cohen [23]. There is a good match between the phase separations and energies of the NaCl (Rocksalt) phase

[8] from first-principles study by Wang and Ye[18]
[9] Ref. [19, 20]

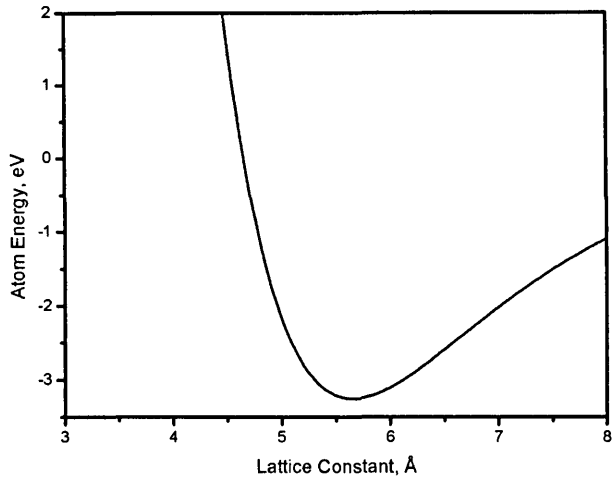

Figure 4.17: Cohesive energy of gallium arsenide from Smith parameters

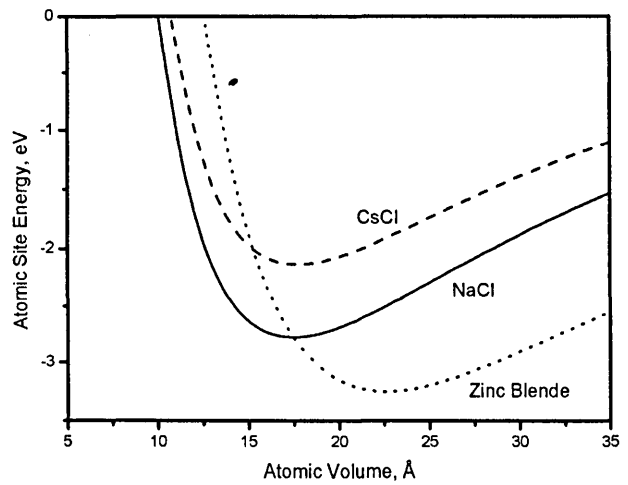

Figure 4.18: Energy vs. atomic volume for gallium arsenide with Smith parameters

and the CsCl phase when compared to the Powell parameters. The Sayed parameters also compare well to the Froyen and Cohen work, but the parameters of Smith provide predictions of the other phases that are very close to the zinc blende phase. This could provide a source of an incorrect phase transition under molecular dynamics simulations.

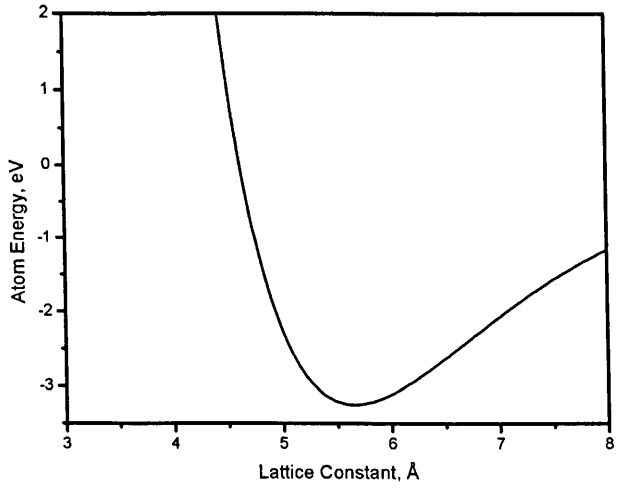

Figure 4.19: Cohesive energy of gallium arsenide from Sayed parameters

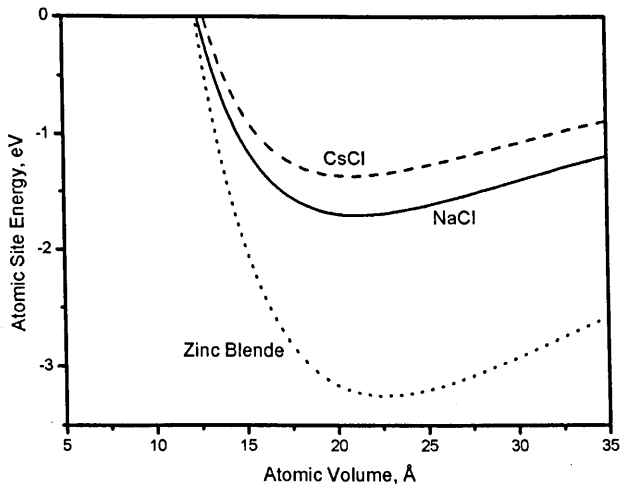

Figure 4.20: Energy vs. atomic volume for gallium arsenide with Sayed parameters

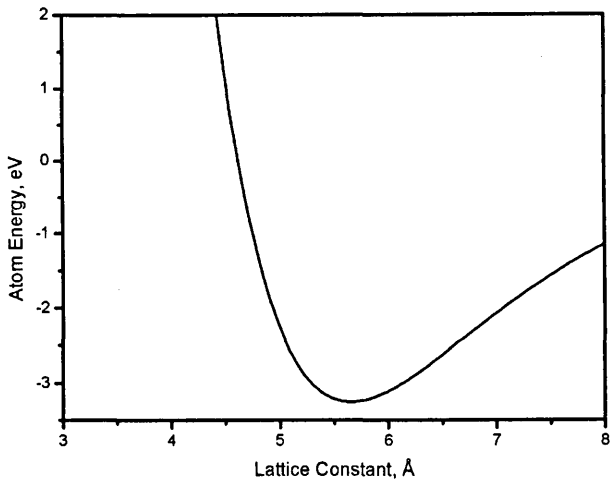

Figure 4.21: Cohesive energy of gallium arsenide from Powell parameters

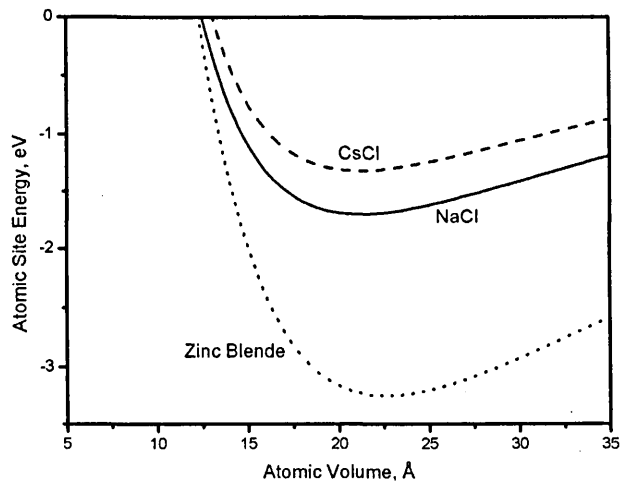

Figure 4.22: Energy vs. atomic volume for gallium arsenide with Powell parameters

4.3.5 Indium Arsenide

Indium arsenide (InAs) has a natural phase stability of zinc blende under standard temperature and pressure. It forms as a grey coloured type III-V crystalline semiconductor and has a melting point at 942°C. InAs crystals have a effective ionic charge $q* \approx 0.45e$ compared to $q* \approx 0.35e$ for GaAs but the material is still mainly composed of covalently bonded atoms[10]. It has similar properties and uses to GaAs and is regularly alloyed with GaAs to form InGaAs which is used in optoelectronic applications such as LEDs and solid state lasers. The bandgap of InGaAs devices is dependent on the In/Ga ratio and is easily tuned under MBE or MOCVD growth conditions when producing heterostructures such as quantum dots of quantum well laser devices. InAs is used in the construction of infrared detectors in the range 1-3.8μm which are usually photodiodes. Cryogenically cooled InAs detectors produce less noise and are used extensively in military applications but InAs is also commonly used at room temperature with commercial laser diode devices.

Parameter	Ashu	Nordlund	Migliorato	Powell
D_e	2.39804	5.17318	2.1643	2.13123
S	1.51406	1.826141	1.5	1.47058
β	1.45409	1.359198	1.45372	1.49807
r_e	2.44121	2.21379	2.4908	2.49936
R	3.7	3.7	3.7	3.7
R_{cut}	0.1	0.1	0.1	0.1
c	0.9989	5.162421	0.9989	1.00904
d	0.82608	1.665967	0.82608	0.82355
h	-0.5145	-0.5413316	-0.5145	-0.462045
n	7.141472	0.7561694	7.141472	7.03876
γ	0.3779	0.3186402	0.3779	0.379623
λ	1.5[7]	1.5[7]	1.5	1.4331

Table 4.14: The Tersoff parameters for Indium Arsenide

The parameterisation started by considering the Ashu *et al*[24], Nordlund *et al*[25] and Migliorato *et al*[26] parameterisations of Indium Arsenide. The parameters for all authors are shown in table 4.14 along with the new parameterisation. A further set of parameters were devised based upon the DFT results presented in table 4.15 as these elastic properties were thought to be more accurate than the experimental data. The other authors fit their results to the experimental data also included in the table.

The results obtained from the above parameters indicate that Ashu and Nordlund may have attempted to fit the parameters to an incorrect value of the cohesive energy. Migliorato and the new parametrisation provide the E_{coh} value

[10]See [27]

Property (units)	Exp./Calc.	DFT[8]	Ashu	Nordlund	Migliorato	Powell
$E_{coh}(eV)$	-3.10[2]	—	-3.456	-3.566	-3.101	-3.100
a (Å)	6.0583[10]	—	5.937	6.060	6.058	6.058
B (MBar)	0.580[10]	0.6173	0.657	0.581	0.577	0.613
C' (MBar)	0.190[10]	0.2285	0.219	0.191	0.189	0.232
c_{11} (MBar)	0.8333[10]	0.9219	0.950	0.835	0.823	0.922
c_{12} (MBar)	0.4533[10]	0.465	0.511	0.453	0.452	0.458
c_{44} (MBar)	0.395[10]	0.444	0.481	0.395	0.416	0.447
ζ	0.666[2]	0.598	0.632	0.651	0.641	0.605

Table 4.15: The material properties of Indium Arsenide

correctly. The Ashu parameters reproduce the lattice constant incorrectly but the other parameters appear to predict this correctly. The bulk modulus provided by Ashu is too high, even when compared to the DFT value which is predicting a value of B higher than the measured value. Authors Nordlund and Migliorato have fitted to the experimental values and provide a reasonable agreement. The new parameterisation provides an excellent value of B when compared to the DFT value.

Phase	Ashu E_{coh} (eV)	a (Å)	Nordlund E_{coh} eV	a (Å)
NaCl	-1.927	5.802	-2.678	5.662
CsCl	-1.389	3.701	-2.580	3.482
zinc blende	-3.456	5.937	-3.566	6.059
Phase	**Migliorato E_{coh} (eV)**	**a (Å)**	**Powell E_{coh} eV**	**a (Å)**
NaCl	-1.702	5.923	-1.616	5.949
CsCl	-1.210	3.779	-1.107	3.804
ZnS	-3.101	6.0583	-3.100	6.058

Table 4.16: Crystal phase data for Indium Arsenide

The value for the shear modulus C' provided by the DFT calculations is again higher than the experimental value and is well reproduced by Ashu and Powell. The experimental value of C' was fitted by Nordlund and Migliorato and is in agreement by 1%. Author Nordlund has accurately reproduced the experimental c_{44} elastic property of InAs with his parameterisation but the values for Ashu and Migliorato are wrong by 20% and 3% respectively. The new parameterisation is accurate to within 1% of the DFT value it was fitted to. Nordlund provides the most accurate fit to the experimental value of internal strain displacement and the Powell parameters correctly predict the DFT value of ζ to within 1%.

Figures 4.23, 4.25, 4.27 and 4.29 show the short-range energy properties of the material bonding as a function of lattice parameter. As can be seen, the graphs for Ashu and Nordlund reflect the fact that they had incorrectly predicted the cohesive energy of the material and in the case of Ashu - also the lattice constant. The graphs for Migliorato and Powell are identical, as would be expected for such

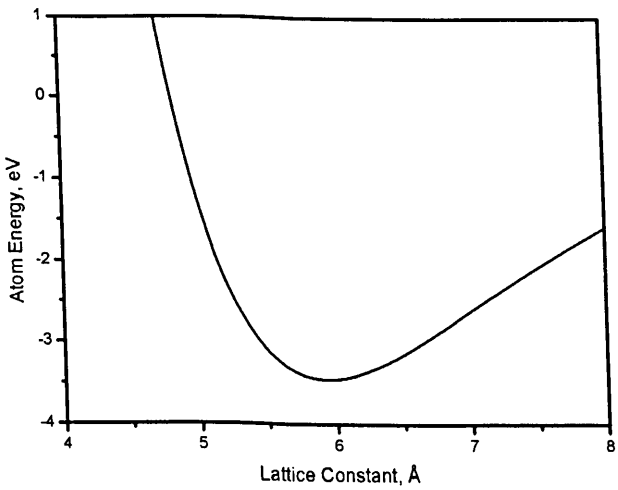

Figure 4.23: Cohesive energy of indium arsenide from Ashu parameters

similar values of E_{coh} at -3.1eV and a at 6.05833Å.

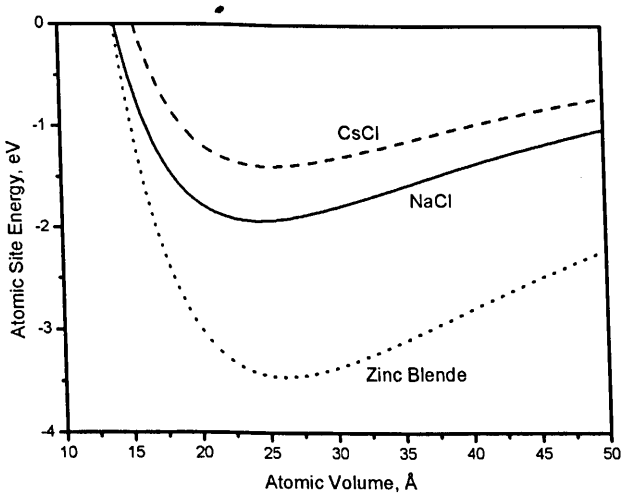

Figure 4.24: Energy vs. atomic volume for indium arsenide with Ashu parameters

Table 4.16 shows the crystal phase data for InAs as predicted by the 4 parameterisations available. These values are plotted in graphs 4.24, 4.26, 4.28 and 4.30 and demonstrate that the material is, in all cases, most stable in the zinc blende formation. In the Nordlund case the NaCl and CsCl crystal lattice types are closest to the zinc blende formation, but the energy difference is still about 1eV. The other parameters demonstrate a preferred energy state of zinc blende by about 1.5eV.

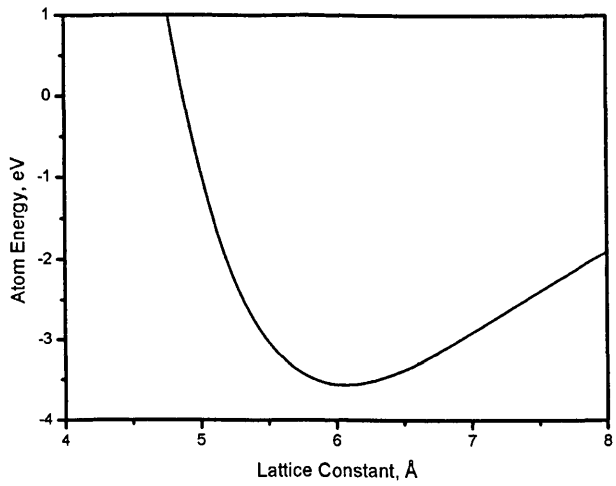

Figure 4.25: Cohesive energy of indium arsenide from Nordlund parameters

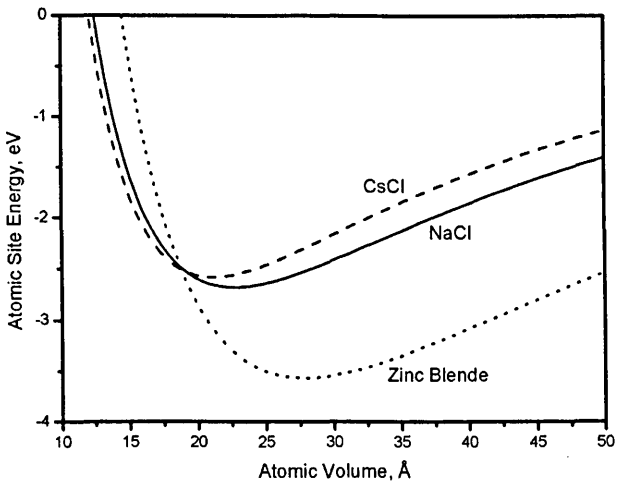

Figure 4.26: Energy vs. atomic volume for indium arsenide with Nordlund parameters

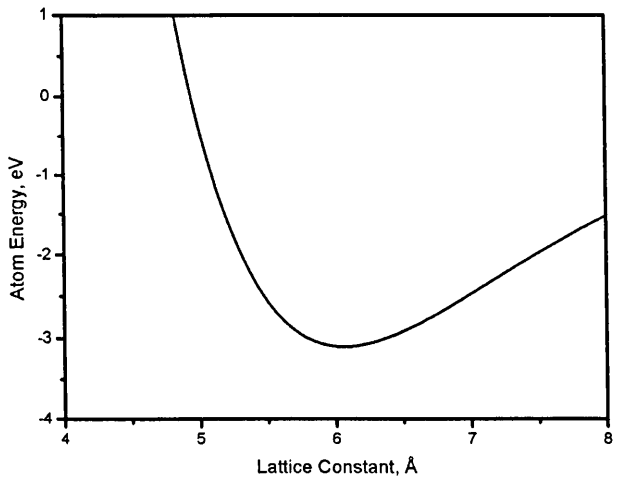

Figure 4.27: Cohesive energy of indium arsenide from Migliorato parameters

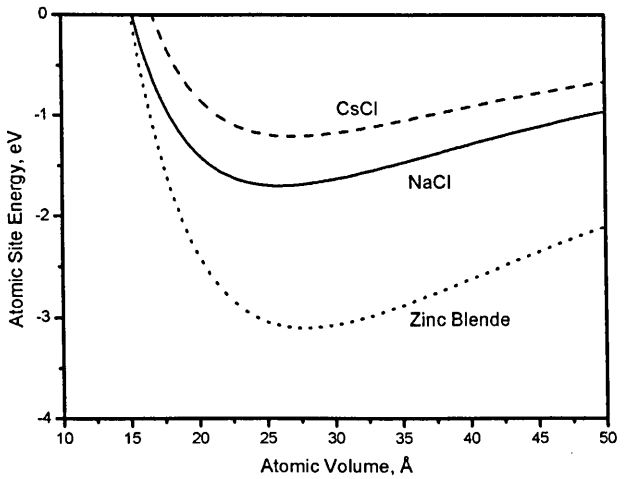

Figure 4.28: Energy vs. atomic volume for indium arsenide with Migliorato parameters

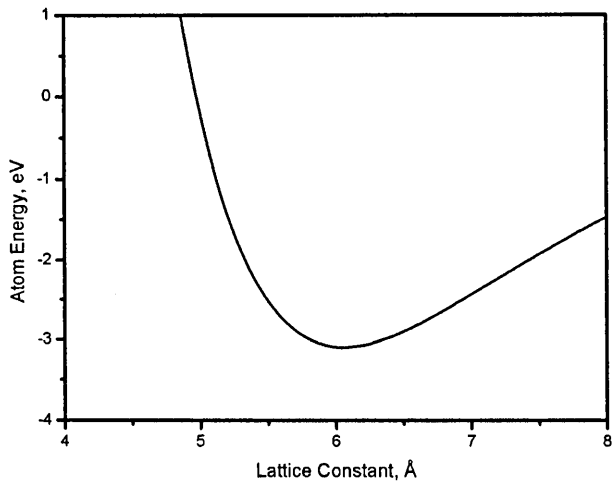

Figure 4.29: Cohesive energy of indium arsenide from Powell parameters

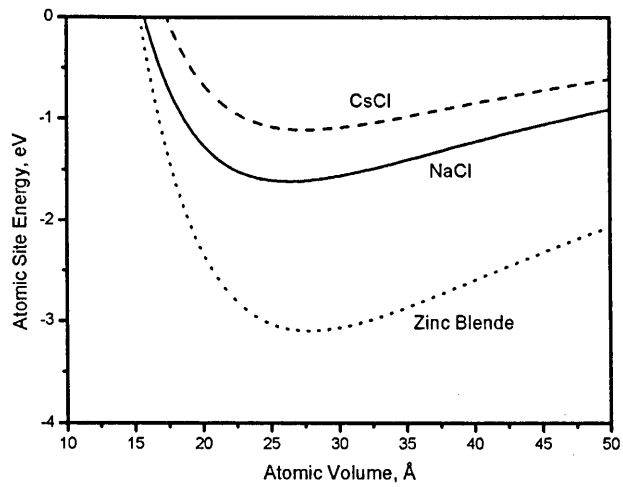

Figure 4.30: Energy vs. atomic volume for indium arsenide with Powell parameters

4.3.6 Gallium Phosphide

Gallium phosphide (GaP) is a compound III-V semiconductor material with an indirect bandgap of 2.26eV that forms in the zinc blende lattice configuration at normal conditions. GaP has the appearance of a pale orange crystal and is odourless and insoluble in water. Gallium phosphide has found great commercial success in the field of LED and optoelectronics manufacture since the 1960s. Low and standard brightness LEDs are now commonplace using GaP and alloys: pure GaP LEDs emit green light at 555nm whilst GaP doped with nitrogen emits yellow-green at 565nm and ZnO doped GaP emits red at 700nm. GaP is transparent to yellow and red light and therefore GaAsP/GaP LEDs are much more efficient than GaAsP/GaAs LEDs.

Parameter	Powell
D_e	2.20178
S	1.59411
β	1.62365
r_e	2.28675
R	3.1
R_{cut}	0.1
c	1.26417
d	0.799535
h	-0.433247
n	5.42195
γ	0.339811
λ	1.81771

Table 4.17: The Tersoff parameters for Gallium Phosphide

No previous Tersoff parameterisations for GaP have been found in the literature so a parameterisation was started from an arbitrary point in parameter space and is shown in table 4.17.

Property (units)	Exp./Calc.	DFT[8]	Powell
$E_{coh}(eV)$	-3.56[2]	—	-3.560
a (Å)	5.4505[11]	—	5.450
B (MBar)	0.882[11]	0.921	0.919
C' (MBar)	0.392[11]	0.439	0.443
c_{11} (MBar)	1.4046[11]	1.507	1.509
c_{12} (MBar)	0.6207[11]	0.628	0.624
c_{44} (MBar)	0.703[11]	0.763	0.763
ζ	0.574[2]	0.516	0.521

Table 4.18: The material properties of Gallium Phosphide

The results obtained from the GaP parameterisation as shown in table 4.18 and are in excellent agreement with the DFT properties for cubic gallium-phosphide. All properties are predicted to within 1% of the reported values. This is a great

[11] Ref. [28, 29]

result for a first parameterisation. Figure 4.31 shows the cohesive energy of the material to be -3.56eV at a lattice constant of 5.4505Å which is in excellent agreement with the experimental data.

Phase	Powell E_{coh} (eV)	a (Å)
NaCl	-1.83173	5.35209
CsCl	-1.40743	3.37088
zinc blende	-3.55997	5.45053

Table 4.19: Crystal phase data for Gallium Phosphide

The material phase properties were checked and are tabulated in table 4.19. From this data and figure 4.32 it is apparent that, when using the Powell parameters, the lowest energy configuration is the zinc blende crystal with a gap of 2eV to the NaCl and CsCl structure formations.

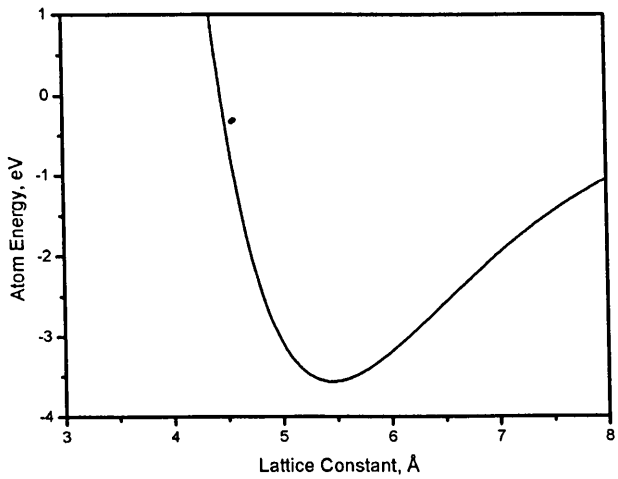

Figure 4.31: Cohesive energy of gallium phosphide from Powell parameters

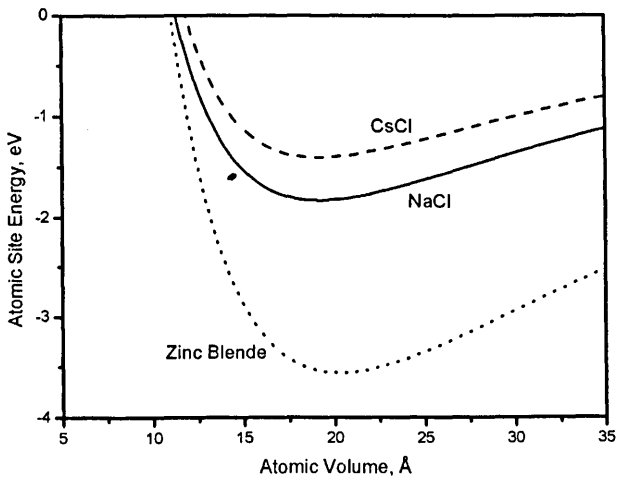

Figure 4.32: Energy vs. atomic volume for gallium phosphide with Powell parameters

4.3.7 Indium Phosphide

Indium phosphide (InP) is a binary III-V compound semiconductor with superior properties to silicon and GaAs due to a higher electron velocity. InP forms naturally as a black coloured cubic crystal in the zinc blende lattice stoichiometry and has a direct bandgap which makes it suitable for high power and high frequency optoelectronics devices like solid state lasers and LEDs. InP is used as a substrate for InGaAs devices and has one of the longest optical phonon lifetimes of all III-V zinc blende materials.

Parameter	Powell
D_e	2.17758
S	1.5811
β	1.52761
r_e	2.45854
R	3.3
R_{cut}	0.1
c	1.2179
d	0.831026
h	-0.461576
n	5.3449
γ	0.338811
λ	1.89106

Table 4.20: The Tersoff parameters for Indium Phosphide

No previous Tersoff PEF parameterisation for InP could be found in the literature so an arbitrary starting point was selected in parameter space and the local refinement search program was run on the parameters a number of times until a suitable set was found that predicted the properties of the DFT elastic data. The successful set of parameters are shown in table 4.20 and the results are shown in table 4.21.

Property (units)	Exp.	DFT[8]	Powell
$E_{coh}(eV)$	-3.48[2]	—	-3.479
a (Å)	5.8687[12]	—	5.869
B (MBar)	0.711[12]	0.736	0.739
C' (MBar)	0.225[12]	0.269	0.267
c_{11} (MBar)	1.011[12]	1.095	1.095
c_{12} (MBar)	0.561[12]	0.556	0.561
c_{44} (MBar)	0.456[12]	0.526	0.524
ζ	0.672[2]	0.615	0.610

Table 4.21: The material properties of Indium Phosphide

The results clearly demonstrate that the parameterisation is an excellent match to the material properties of InP. As shown in graph 4.33 the cohesive energy of -3.48 and the lattice parameter of 5.8687Å is correctly predicted and all elastic

[12]See [30]

properties are within 1% of the specified DFT values. The internal displacement parameter is also within 1% of the predicted DFT value.

Phase	Powell E_{coh} (eV)	a (Å)
NaCl	-1.93817	5.69815
CsCl	-1.47917	3.59244
zinc blende	-3.4794	5.86863

Table 4.22: Crystal phase data for Indium Phosphide

Table 4.22 shows the different cubic phases of the material and the computed minimum energies. It is shown (also using figure 4.34) that the material is stable in the zinc blende configuration with the NaCl lattice type being 1.5eV above. This demonstrates that the Powell parameters are very suitable for MD simulations using the Tersoff PEF and InP.

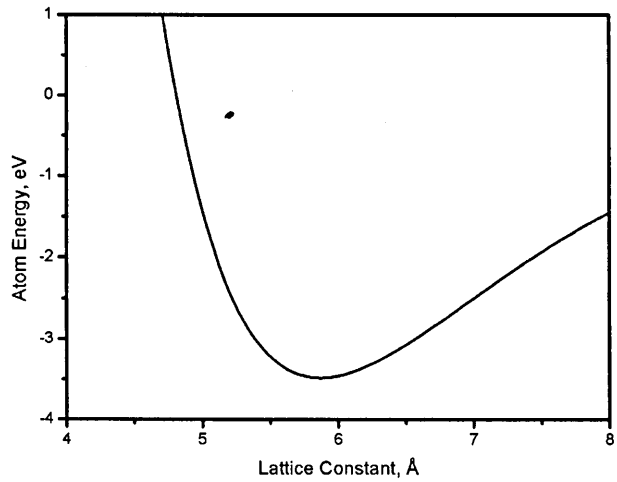

Figure 4.33: Cohesive energy of indium phosphide from Powell parameters

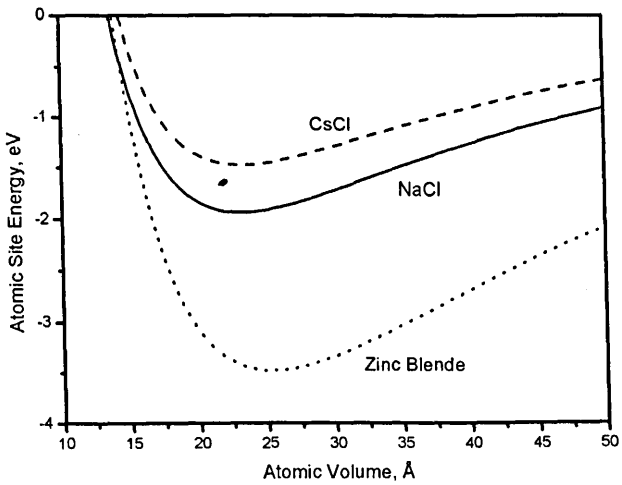

Figure 4.34: Energy vs. atomic volume for indium phosphide with Powell parameters

4.3.8 Gallium Antimonide

Gallium antimonide (GaSb) is a III-V semiconductor which exhibits excellent electron mobility and saturation velocity. GaSb has the zincblende cubic crystal structure and a bandgap energy of 0.73eV. GaSb is used in high power mid/far range infrared detectors, infrared LEDs and lasers and in HEMT field effect transistors. GaSb is grown with the Czochralski method and commercial samples of up to 3" are readily available. The electrical properties of GaSb and various latticed matched alloys could allow HEMT devices operating in the THz range to be achieved.

Parameter	Powell
D_e	2.17013
S	1.41256
β	1.47705
r_e	2.48549
R	3.5
R_{cut}	0.1
c	1.17945
d	0.842774
h	-0.429907
n	4.61625
γ	0.36953
λ	1.8244

Table 4.23: The Tersoff parameters for Gallium Antimonide

No parameterisation of GaSb was available in the literature, so an arbitrary point in the search space was chosen to begin the granular search program from. The parameterisation is shown in table 4.23 and the results appear in table 4.24 alongside experimental measurements and predicted DFT values.

Property (units)	Exp./Calc.	DFT[8]	Powell
$E_{coh}(eV)$	-2.96[2]	—	-2.96
a (Å)	6.09593[13]	—	6.096
B (MBar)	0.563[13]	0.567	0.566
C' (MBar)	0.240[13]	0.270	0.272
c_{11} (MBar)	0.883[13]	0.927	0.928
c_{12} (MBar)	0.403[13]	0.378	0.384
c_{44} (MBar)	0.432[13]	0.462	0.463
ζ	0.594[2]	0.530	0.532

Table 4.24: The material properties of Gallium Antimonide

The results show an excellent agreement with the experimental lattice constant and cohesive energy which is plotted in figure 4.35. The elastic properties of the material are correctly reproduced to within 1% of all DFT values and the internal displacement parameter is correct to within a 1% tolerance of the DFT

[13]See [31]

predicted value. This suggests that these parameters would be an excellent choice for structural MD relaxation of low strain systems.

Phase	Powell E_{coh} (eV)	a (Å)
NaCl	-1.382	6.095
CsCl	-0.874	3.938
zinc blende	-2.960	6.096

Table 4.25: Crystal phase data for Gallium Antimonide

The phase stability of the material using the above parameters is excellent. The zinc blende phase is the lowest energy configuration by 1.5eV and this is shown in the energy vs. atomic volume plot in figure 4.36 where it can be clearly seen that GaSb prefers the zinc blende lattice type when these parameters are used in MD simulations at room temperature and standard pressure.

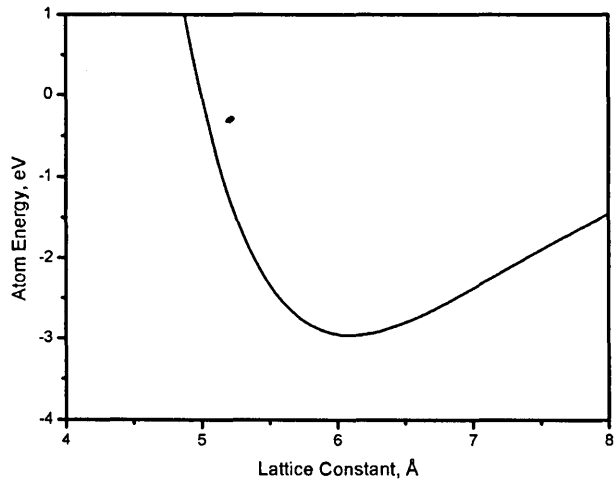

Figure 4.35: Cohesive energy of gallium antimonide from Powell parameters

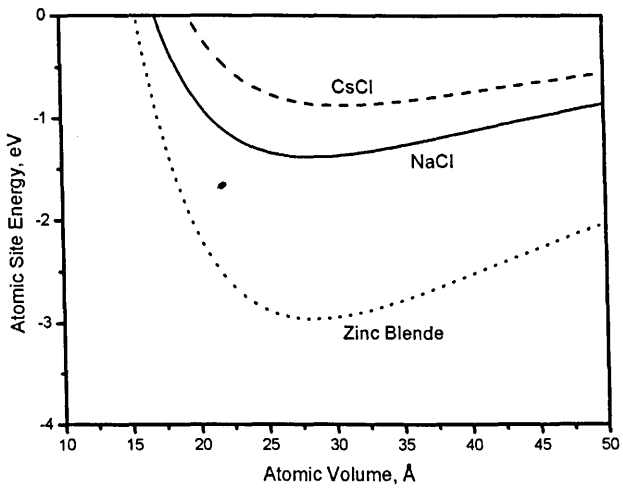

Figure 4.36: Energy vs. atomic volume for gallium antimonide with Powell parameters

4.3.9 Indium Antimonide

As with GaSb, indium-antimonide (InSb) is a high mobility direct bandgap III-V semiconductor. It has the appearance of a dark grey/silver metal and forms in the zinc blende cubic structure geometry. InSb based infrared detectors are common (sensitive to 1-5μm wavelengths) and commercial and military applications range from thermal imaging, missile guidance detectors and astronomical measurement systems. InSb has been used commonly in the past as an infrared detector in mechanical line-scanned array systems for the military, prompting much work in early characterisation and experimental studies. InSb detectors tend to be very complicated as they require cryogenically cooling to 80K to achieve good performance. Although they have excellent quantum efficiency (typ. 80-90%) they need frequent calibration and have fallen out of favour to more modern materials such as HgCdTe.

Parameter	Powell
D_e	2.1872
S	1.40689
β	1.43604
r_e	2.62026
R	3.7
R_{cut}	0.1
c	1.21528
d	0.90126
h	-0.443878
n	4.49087
γ	0.386354
λ	1.75633

Table 4.26: The Tersoff parameters for Indium Antimonide

Recent results in high speed switching applications by Intel and QinetiQ have demonstrated bipolar transistors based upon InSb at up to 85GHz and FET technology based upon indium-antimonide switching at 200GHz suggesting that InSb may be making a comeback as a compound semiconductor material.

Property (units)	Exp./Calc.	DFT[8]	Powell
$E_{coh}(eV)$	-2.80[2]	—	-2.780
a (Å)	6.479[14]	—	6.479
B (MBar)	0.470[14]	0.476	0.476
C' (MBar)	0.151[14]	0.183	0.185
c_{11} (MBar)	0.671[14]	0.720	0.722
c_{12} (MBar)	0.369[14]	0.354	0.353
c_{44} (MBar)	0.302[14]	0.341	0.340
ζ	0.664[2]	0.603	0.603

Table 4.27: The material properties of Indium Antimonide

[14]Ref. [32]

No parameterisations for InSb for the Tersoff potential exist in the literature so an arbitrary starting point was chosen in parameter space and the refinement program was run. The parameters chosen are shown in table 4.26 and the results are compared to DFT predictions and experimental measurements in table 4.27.

Phase	Powell	
	E_{coh} (eV)	a (Å)
NaCl	-1.375	6.410
CsCl	-0.858	4.139
zinc blende	-2.800	6.479

Table 4.28: Crystal phase data for Indium Antimonide

The results are excellent. The parameterisation predicts all elastic properties to within 1% of the DFT values. The cohesive energy of -2.80eV and the lattice parameter of 6.479Å is correctly predicted by the parameters and shown in figure 4.37. The internal displacement parameter is almost parfectly reproduced which suggest an excellent application of the parameters in small strain structural relaxation MD simulations.

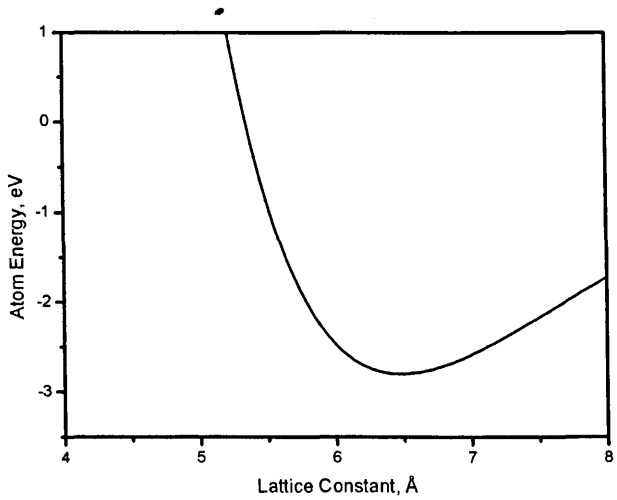

Figure 4.37: Cohesive energy of indium antimonide from Powell parameters

InSb phase properties were predicted using the Tersoff PEF and the above parameters and the results are shown in figure 4.38 and table 4.28. It is clear that the material is at a lowest energy configuration in the zinc blende structure and the NaCl and CsCl cubic structure types are at least 1.4eV above the zinc blende curve. This suggest excellent stability for the parameters in MD simulations.

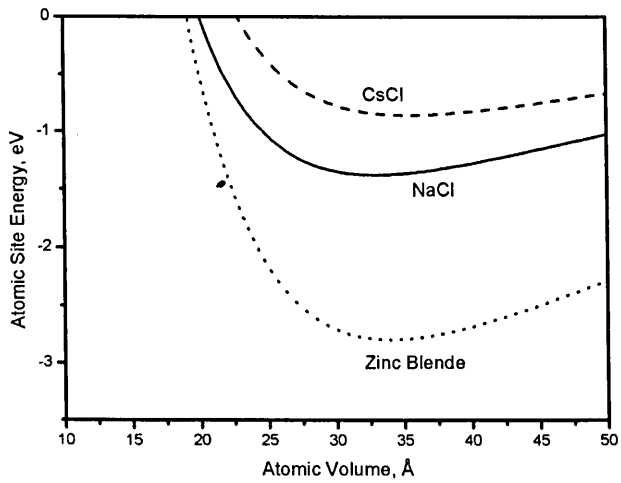

Figure 4.38: Energy vs. atomic volume for indium antimonide with Powell parameters

4.3.10 Boron Nitride

Boron Nitride (BN) in the cubic Zinc Blende phase is metastable under normal conditions. It appears as a white coloured solid hexagonal crystal at room temperature and standard pressure and was first synthesised in 1957 using a high pressure technique similar to synthesised diamond formation from graphite. It is currently commercially available in crystals of a few millimetres size and is of great interest as a material with similar properties to diamond. Cubic BN (c-BN) has outstanding physical properties, extreme hardness and chemical inertness. The wide band gap, high melting temperature and low dielectric constant of BN provides excellent potential for microelectronic devices, nanostructure applications and protective coating materials[33]. BN is commonly used as a boundary layer when growing GaN on SiC and it is of great interest as a material for growing nanotubes because it has recently been discovered that BN nanotubes have homogeneous electronic behaviour: the nanotube shape and size does not affect the bandgap.

Parameter	Albe	Sekkal	Powell
D_e	6.36	4.750	3.40327
S	1.0796	1.56216	2.45545
β	2.043057	1.96201	1.99278
r_e	1.33	1.47217	1.5658
R	2.0	1.95	1.95
R_{cut}	0.1	0.15	0.15
c	1092.9287	38049	6.55459
d	12.38	4.384	1.17872
h	-0.5413	-0.57085	-0.396692
n	0.364153367	0.72751	8.7359
γ	0.000011134	1.5724e-07	0.256813
λ	1.9925	1.5^7	1.06665

Table 4.29: The Tersoff parameters for Boron Nitride

The starting point for the BN parameterisation was provided by the Albe and Moller[33] and the Sekkal *et al*[34, 35] parameters for Boron Nitride. A further parameter set was achieved by improving upon the Sekkal parameters and the three sets are shown in table 4.29.

Property (units)	Exp./Calc.	DFT[8]	Albe	Sekkal	Powell
$E_{coh}(eV)$	-6.68[2]	—	-6.607	-6.785	-6.679
a (Å)	3.6157[15]	—	3.575	3.624	3.626
B (MBar)	4.00[15]	3.92	4.120	3.849	3.906
C' (MBar)	3.15[15]	3.191	4.084	4.246	3.201
c_{11} (MBar)	8.20[15]	8.174	9.560	9.510	8.174
c_{12} (MBar)	1.90[15]	1.792	1.400	1.018	1.771
c_{44} (MBar)	4.80[15]	4.699	5.724	5.713	4.704
ζ	—	0.117	0.316	0.238	0.233

Table 4.30: The material properties of Boron Nitride

The results obtained from the above parameters are displayed in table 4.30 alongside the experimental and DFT predicted results. The cohesive energies predicted by the Albe and Sekkal parameters are both 1% in error compared to the experimental value and the Powell value. The Albe lattice parameter is also in error by 1% but the Sekkal and Powell values are correct to 0.2%. The bulk and shear moduli predicted by Albe are 3% and 29% in error and the ones by Sekkal are 4% and 35% from the experimental values, whereas the values perdicted by the Powell parameters are within 1% of the DFT predictions that the potential was fit to.

Phase	Albe		Sekkal		Powell	
	E_{coh} (eV)	a (Å)	E_{coh} (eV)	a (Å)	E_{coh} eV	a (Å)
NaCl	-4.54869	3.51261	-3.92843	3.59849	-2.1442	3.76861
CsCl	-4.68565	2.18653	-3.4322	2.26961	-1.93225	2.31849
zinc blende	-6.60741	3.57545	-6.78527	3.62385	-6.67925	3.62583

Table 4.31: Crystal phase data for cubic Boron Nitride

The predictions made by Albe and Sekkal for the c_{44} value are both 19% adrift but the Powell parameter is successfully fit to the DFT value. The internal displacement value is double the value it should be using the Powell parameters. But this is the closest value of all three parameter sets.

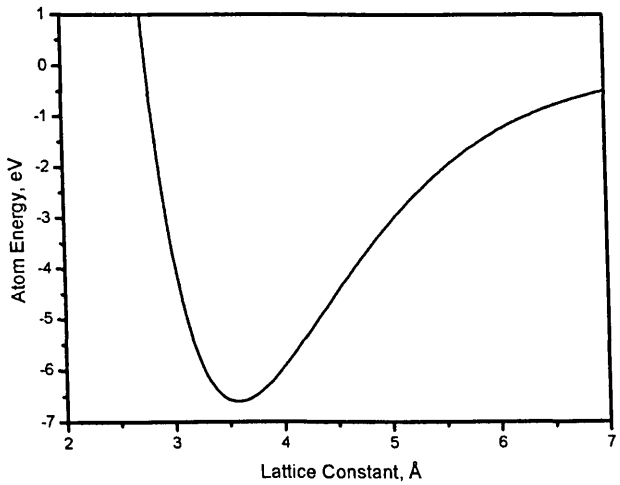

Figure 4.39: Cohesive energy of cubic boron nitride from Albe parameters

Figures 4.39, 4.41 and 4.43 show that all three authors can predict the material lattice constant and cohesive energy to within 1% percent tolerance of the experimental data.

[15]See [36, 37]

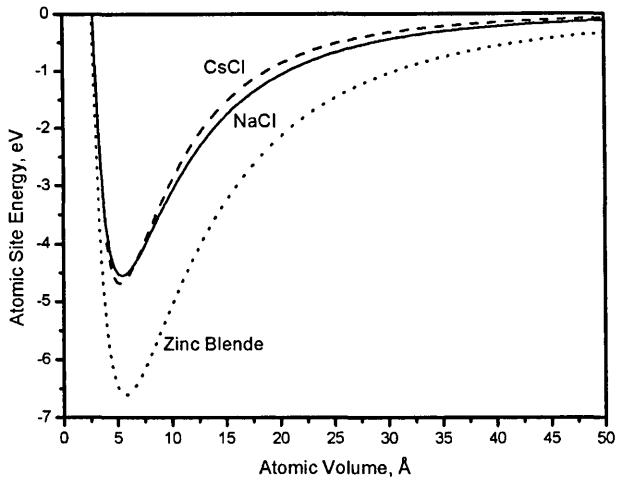

Figure 4.40: Energy vs. atomic volume for cubic boron nitride with Albe parameters

The crystal phase data is shown in table 4.31 and figures 4.40, 4.42, 4.44 and demonstrates that all three parameter sets can correctly reproduce the zinc blende phase as the preferred minimum energy phase. The Albe parameters have the closest phase relation with an energy of 1.9eV required to move from the zinc blende phase to the CsCl form. The Sekkal and Powell parameters require about 3eV to perform the same phase transformation indicating that they would be better choices for a hard material like BN in a MD simulation.

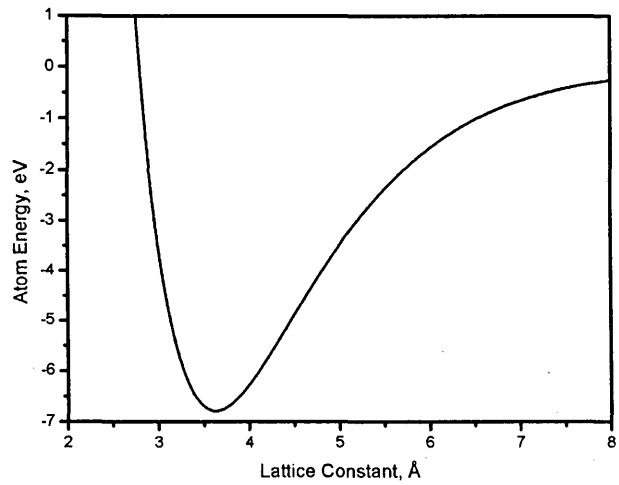

Figure 4.41: Cohesive energy of cubic boron nitride from Sekkal parameters

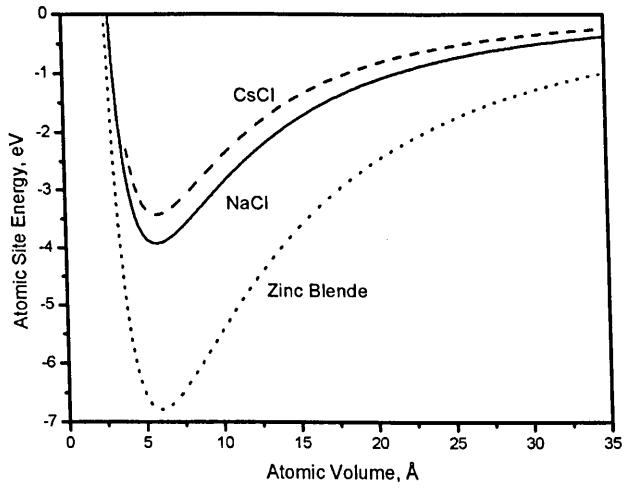

Figure 4.42: Energy vs. atomic volume for cubic boron nitride with Sekkal parameters

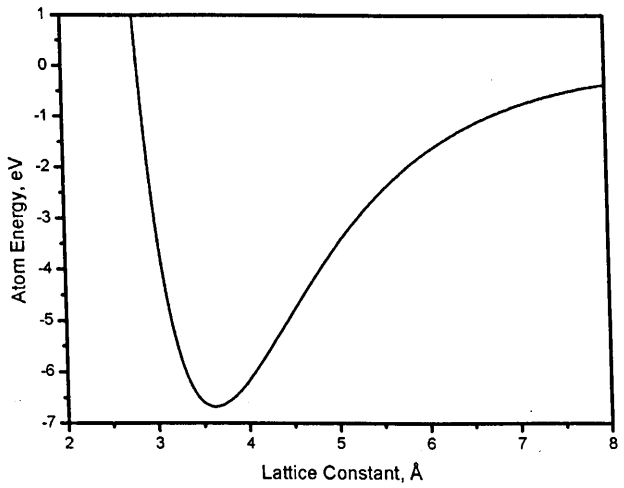

Figure 4.43: Cohesive energy of cubic boron nitride from Powell parameters

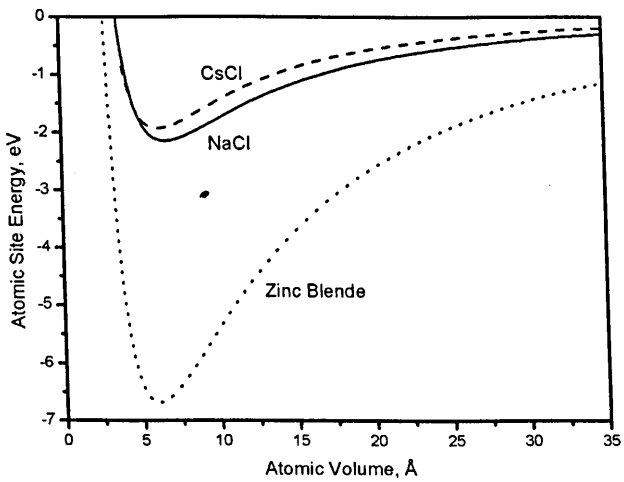

Figure 4.44: Energy vs. atomic volume for cubic boron nitride with Powell parameters

4.3.11 Gallium Nitride

Gallium nitride has outstanding physical and chemical properties[38]. It provides a short wavelength range, high temperature of operation and we can fabricate high power, high frequency devices from it - which make it a very attractive prospect for electroluminescent devices. GaN exhibits strong bonding properties (mixed covalent and ionic) and is the basic material for LEDs, blue lasers and UV optoelectronic devices, optical pumping structures and photodetectors[39, 40, 41]. GaN is stable in the wurtzite hexagonal lattice form under ambient conditions but the cubic zinc blende form has been successfully epitaxially grown on cubic substrates such as MgO and β-SiC. The cubic formation of GaN has technological advantages as it is able to produce cleaved laser cavities and can be doped easily. Cubic GaN can also be synthesised but there are problems with poor layer quality from planar defects and a tendency to transform to the wurtzite phase.

Parameter	Moon	Benkabou	Powell
D_e	2.77484	3.078133	2.38972
S	1.925	1.518829	1.85196
β	1.88503	1.93460	1.97764
r_e	1.92667	1.84401	1.93005
R	2.5	2.5	2.5
R_{cut}	0.1	0.1	0.1
c	7.2239	38049	1.09984
d	10.018	4.384	0.666512
h	-0.518	-0.57085	-0.488761
n	0.78734	0.72751	11.5642
γ	1.09e-06	1.572410e-06	0.295653
λ	1.5[7]	1.5[7]	1.60024

Table 4.32: The Tersoff parameters for cubic Gallium Nitride

Two other authors have attempted to parameterise cubic gallium nitride (c-GaN). We could not reproduce the results reported in Benkabou *et al*[42] or Moon and Hwang[43] from the parameters provided but the results we have obtained have been included here for completeness. It is not clear whether this was a problem with the software they were using, the elastic properties transform methods provided in the literature (they used the same model) or an error in the reproduction of the Tersoff parameters printed in the article.

The Benkabou parameters were fitted to E_{coh}, B and a. He has checked his parameters against the elastic constants c_{11}, c_{12} and c_{44} and reports a reasonable fit. Benkabou reports a good agreement with the change in the lattice parameter with increasing temperature via MD simulation and looks at the mean displacement of the atomic positions in the lattice at room temperature, 300K.

[16]See [44]
[17]See [45]

Property (units)	Exp.	DFT[8]	Moon	Benkabou	Powell
$E_{coh}(eV)$	-4.45[2]		-5.549	-1.483	-4.449
a (Å)	4.5[16]		4.450	5.233	4.501
B (MBar)	2.037[17]	2.06	2.366	0.566	2.064
C' (MBar)	0.67[17]	0.824	1.7e-04	1.019	0.824
c_{11} (MBar)	2.93[17]	3.1593	2.366	1.920	3.162
c_{12} (MBar)	1.59[17]	1.510	2.366	-0.110	1.514
c_{44} (MBar)	1.55[17]	1.976	3.4e-04	1.148	1.972
ζ	0.61[17]	0.477	0.999	0.041	0.464

Table 4.33: The material properties of cubic Gallium Nitride

Phase	Moon		Benkabou		Powell	
	E_{coh} (eV)	a (Å)	E_{coh} eV	a (Å)	E_{coh} eV	a (Å)
NaCl	-7.135	3.853	-0.278	5.673	-2.356	4.364
CsCl	-11.098	2.225	-0.157	3.623	-2.148	2.682
zinc blende	-5.549	4.449	-1.483	5.233	-4.449	4.501

Table 4.34: Crystal phase data for cubic Gallium Nitride

The Moon parameters were fit to the cohesive energy, the lattice parameter and the bulk modulus starting from the Benkabou parameters. The Ga-Ga and N-N interaction used in the paper was taken from Nakamura *et al*[46]. The Nakamura work checks the energy of the zinc blende material against the phase of the rocksalt lattice, but not other simple lattice types. Moon has investigated the thermodynamic properties of his parameters using MD simulation, although the tolerance given for the predicted melting temperature is $\pm 300K$.

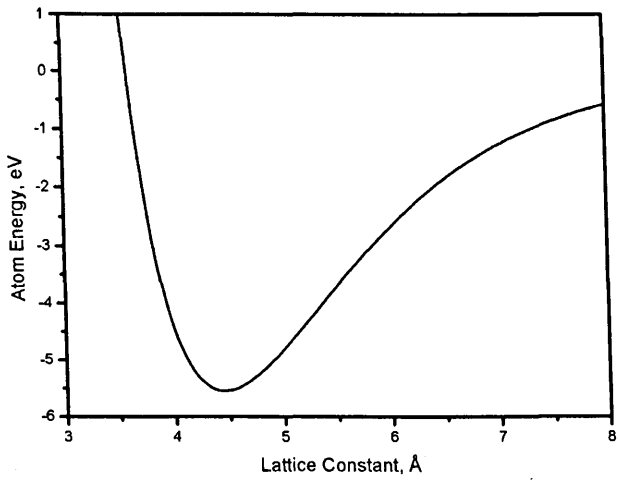

Figure 4.45: Cohesive energy of cubic gallium nitride from Moon parameters

The three parameterisations of cubic GaN are shown in table 4.32 and the associated results in table 4.33 alongside the DFT predictions and the measured experimental values. As can be seen from the predicted values in the table there

seems to be some serious discrepancies with the Benkabou parameters. Moon finds a reasonable fit for the lattice constant and a 1eV error in the cohesive energy but it was impossible to reproduce the cited Benkabou results. The Moon data for the elastic properties shows promise for the bulk modulus but completely fails to reproduce the shear and c_{44} behaviour. The Powell parameters are seen to be within 1% tolerance for all materials properties when compared to the DFT predicted values.

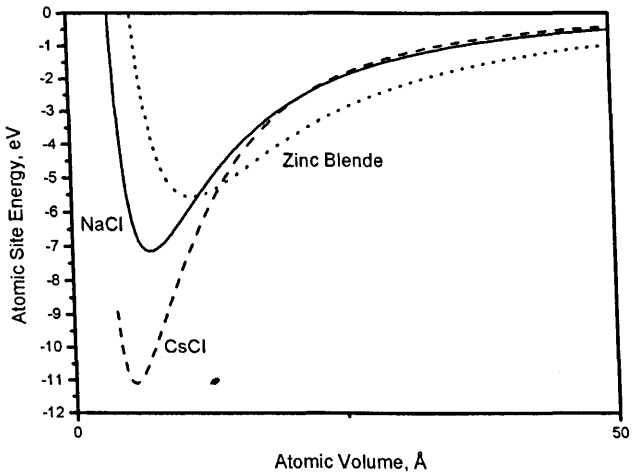

Figure 4.46: Energy vs. atomic volume for cubic gallium nitride with Moon parameters

The energy vs. lattice constant graphs in figures 4.45, 4.47 and 4.49 tell a similar story. There is a complete failure to reproduce any cited data for the cohesive energy and lattice parameter with the Benkabou parameters. The Moon parameters produce a better result but the cohesive energy is in error by 1eV. The Powell parameterisation reproduces the cohesive energy and lattice parameter of the system correctly.

Table 4.34 and figures 4.46, 4.48 and 4.50 shows the phase data for the cubic crystal polytypes possible with GaN. As can be seen there is a failure of the Benkabou parameters to give reasonable energies. The Moon parameters describe a system that prefers the CsCl polytype and then NaCl phase with lower energies per atom than the zinc blende formation, which would probably prompt a phase transformation, or at least unpredictable results, from an MD simulation. The Powell parameters look stable with a 2eV gap from the zinc blende phase to the nearest phase transformation.

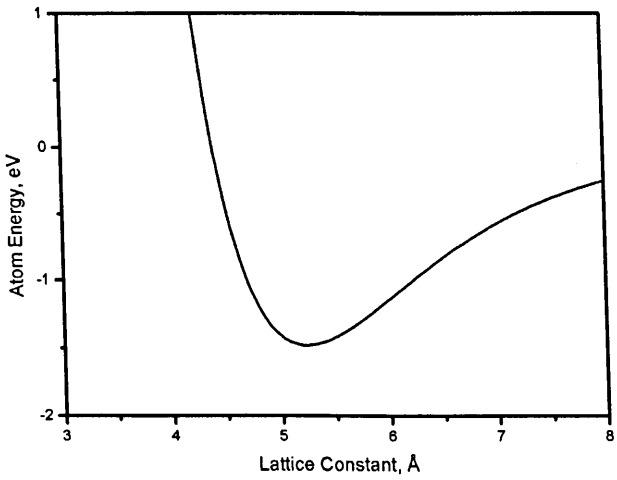

Figure 4.47: Cohesive energy of cubic gallium nitride from Benkabou parameters

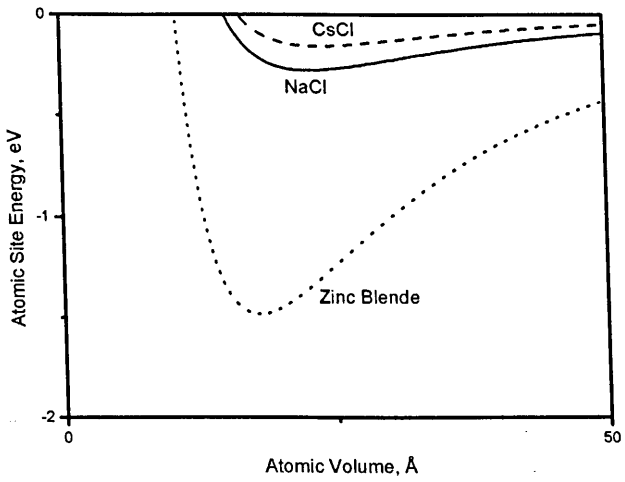

Figure 4.48: Energy vs. atomic volume for cubic gallium nitride with Benkabou parameters

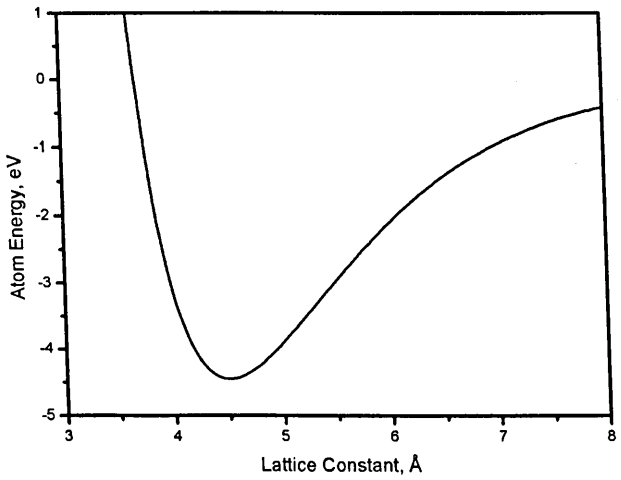

Figure 4.49: Cohesive energy of cubic gallium nitride from Powell parameters

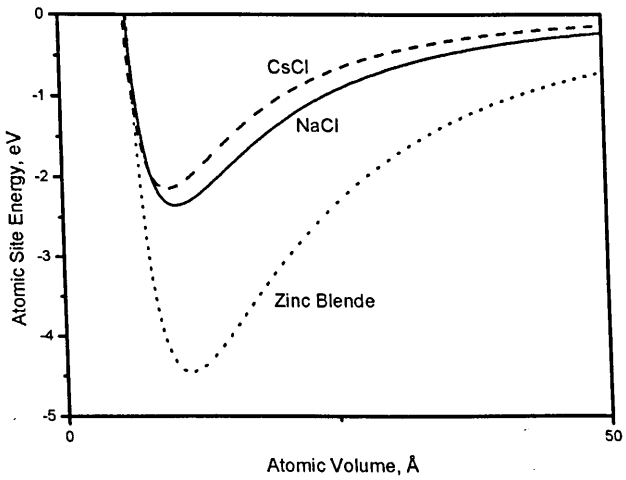

Figure 4.50: Energy vs. atomic volume for cubic gallium nitride with Powell parameters

4.3.12 Indium Nitride

Cubic Indium Nitride (c-InN) exhibits mixed bonding properties (partially covalent and ionic) and is predicted to have excellent material properties. As a member of the III-N family it exhibits great hardness, short bond lengths and a wide band gap making it an excellent choice for optoelectronic applications and high temperature, high frequency, high energy devices[38]. Although c-InN has been studied via first principles methods[47, 48, 49] there is little experimental data available due to the lack of good quality bulk crystals of a sufficient size. c-InN is stable under normal conditions in the wurtzite phase which has been used to some success to measure the elastic constants and transform them for a estimate of the zinc blende parameters[50]. InN is expected to be a successor to GaN for high temperature and high frequency electronics providing millimetre and μmeter wavelength applications devices. It is predicted to have a higher saturation velocity than GaN which will provide higher frequency power amplifier devices and due to the higher carrier mobility when compared to GaN it should provide less noise during high frequency high power operation.

Parameter	Benkabou	Powell
D_e	690.2616	2.20268
S	1.780896	1.69411
β	1.748556	1.89216
r_e	0.398836	2.11896
R	2.65	2.65
R_{cut}	0.1	0.1
c	10039	1.07074
d	16.217	0.725308
h	-0.598	-0.533599
n	0.72	9.74096
γ	1.11e-06	0.30813
λ	1.5^7	1.59607

Table 4.35: The Tersoff parameters for cubic Indium Nitride

Benkabou *et al*[42] has parameterised c-InN and the parameters were fitted to E_{coh}, B and a. Elastic constants c_{11}, c_{12} and c_{44} were checked and he reports a reasonable fit. A test was made via MD simulation to check the change in the lattice parameter with increasing temperature and Benkabou looks at the mean displacement of the atomic positions in the lattice at room temperature, 300K. We cannot reproduce the results given in the Benkabou paper using our software. It is unclear whether this is due to an incorrect calculation or poor reproduction of the Tersoff parameters used.

The two parameter sets for cubic InN are provided in table 4.35 and the associated results, tabulated alongside DFT predictions and experimental measurements, are shown in table 4.36.

Property (units)	Exp./Calc.	DFT[8]	Benkabou	Powell
$E_{coh}(eV)$	-3.86[2]		-1373.550	-3.858
a (Å)	4.98[18]		0.925	4.981
B (MBar)	1.457[17]	1.476	2424.620	1.481
C' (MBar)	0.31[17]	0.424	678.779	0.419
c_{11} (MBar)	1.87[17]	2.040	3341.659	
c_{12} (MBar)	1.25[17]	1.190	1966.101	
c_{44} (MBar)	0.86[17]	1.141	1297.470	1.136
ζ	0.8[17]	0.639	0.665	0.620

Table 4.36: The material properties of cubic Indium Nitride

From the material properties it is immediately obvious that the Benkabou parameters cannot even nearly replicate the experimental or DFT results. The cohesive energy is subject to a massive error and the lattice constant is tending towards the lower computational limit. The elastic properties are massively incorrect, but incredibly the Kleinman ζ parameter is close to the DFT value. The Powell parameters reproduce the elastic properties, cohesive energy and lattice parameter to within an excellent tolerance. The largest error is in the prediction of ζ which is in error by 3%.

Phase	Benkabou E_{coh} (eV)	a (Å)	Powell E_{coh} eV	a (Å)
NaCl	-1700.17	1.00032	-2.141	4.797
CsCl	-1853.37	1.00032	-1.796	2.974
zinc blende	-1369.28	1.00032	-3.858	4.981

Table 4.37: Crystal phase data for cubic Indium Nitride

Graphs 4.51 and 4.53 show the cohesive energy plots. It is obvious that the Benkabou data is massively in error. The Powell parameters correctly reproduce the cohesive energy of -3.86eV and the lattice parameter of 4.98Å.

The phase stability of the parameter sets is shown in table 4.37 and graphs 4.52 and 4.54. The Powell parameters show excellent promise for MD applications as the minimum energy formation is the zinc blende phase with a 2eV gap until the phase transformation into CsCl or NaCl.

[18] See [38]

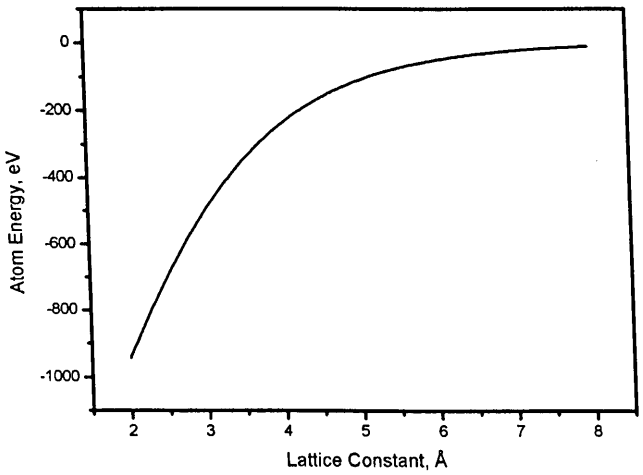

Figure 4.51: Cohesive energy of cubic indium nitride from Benkabou parameters

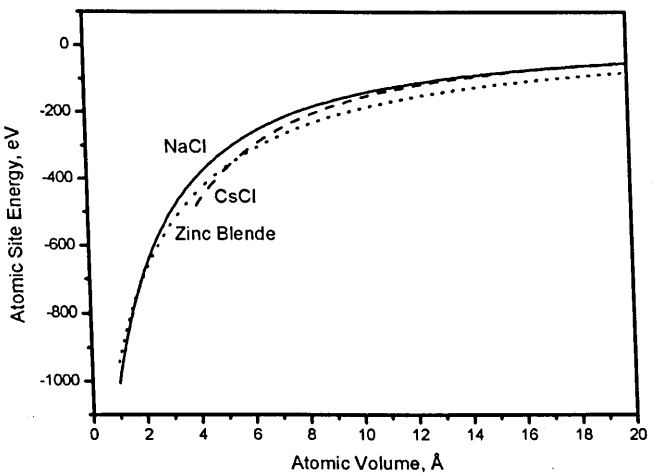

Figure 4.52: Energy vs. atomic volume for cubic indium nitride with Benkabou parameters

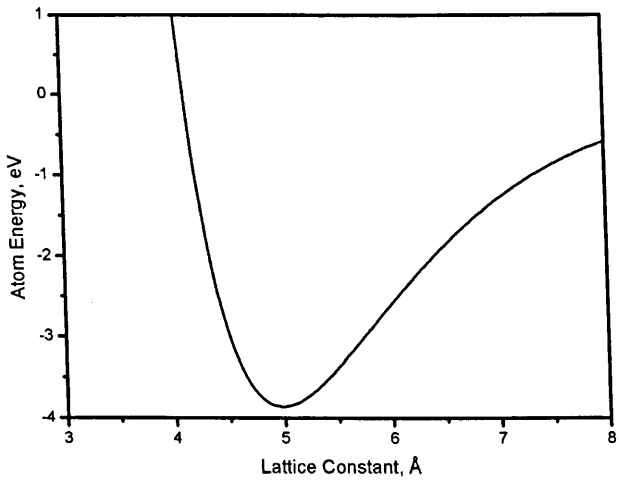

Figure 4.53: Cohesive energy of cubic indium nitride from Powell parameters

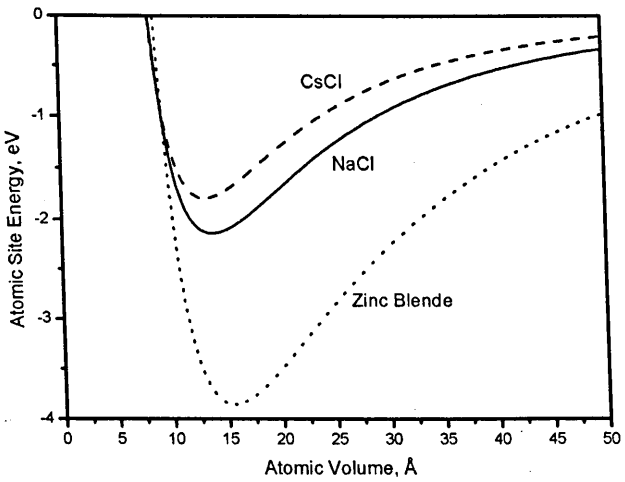

Figure 4.54: Energy vs. atomic volume for cubic indium nitride with Powell parameters

4.3.13 Aluminium Nitride

Aluminium nitride usually forms in the wurtzite phase at standard temperature and pressure but can be grown epitaxially on a cubic substrate (such as β-SiC) into a cubic zinc blende structure for a small number of layers[51, 38, 52]. Great interest has been shown in cubic aluminium nitride (c-AlN) due to the excellent optical and material properties available. Unfortunately c-AlN is very difficult to manufacture due to the extremely reactive nature of AlN[53]. Fabrication is difficult and requires high-purity source material and an oxygen free environment which has seen researchers using c-GaN as the III-N of choice. Due to complex epitaxial growth methods resulting in growth defects and spoiled samples c-AlN has been studied extensively with first principles calculations and there seems to be a good general agreement on the lattice properties and elastic constants[47, 54, 48, 49].

Parameter	Benkabou	Goumri-Said	Powell
D_e	3.340698	3.026364718	3.19655
S	1.726929	1.765299132	1.48636
β	1.721859	1.878941653	1.70916
r_e	1.853366	1.878365524	1.86255
R	2.35	2.335	2.335
R_{cut}	0.1	0.15	0.1
c	10039	20312	20673.3
d	16.217	16.5103	16.1559
h	-0.598	-0.58239	-0.659096
n	0.72	1.33041	1.55299
γ	1.11e-06	1.1566e-04	0.000122132
λ	1.5[7]	1.5[7]	1.45221

Table 4.38: The Tersoff parameters for cubic Aluminium Nitride

A parametrisation of c-AlN is available in Benkabou *et al*[42] and they demonstrate a fit to the elastic properties c_{11}, c_{12} and c_{44} from their parameters which were designed with the lattice parameter a, the cohesive energy E_{coh} and the bulk modulus B in mind. The material properties that Benkabou reports cannot be reproduced correctly here. It is unclear if this is due to a incorrect parameterisation or poorly reproduced data in the original report.

Property (units)	Exp./Calc.	DFT[8]	Benkabou	Goumri-Said	Powell
$E_{coh}(eV)$	-5.76[2]		-6.646	-5.757	-5.759
a (Å)	4.38[19]		4.284	4.371	4.383
B (MBar)	2.08[17]	2.03	2.457	2.483	2.049
C' (MBar)	0.72[17]	0.698	0.0342	0.544	0.750
c_{11} (MBar)	3.04[17]	2.96	2.500	3.207	3.049
c_{12} (MBar)	1.60[17]	1.564	2.430	2.119	1.549
c_{44} (MBar)	1.93[17]	2.004	0.0823	1.409	1.967
ζ	0.55[17]	0.55	0.984	0.704	0.511

Table 4.39: The material properties of cubic Aluminium Nitride

Goumri-Said *et al*[53] has also attempted a Tersoff parameterisation for c-AlN. He finds parameters that are correctly reproduced here with our software and has performed his fit using the lattice constant, bulk modulus and cohesive energy of c-AlN. He further demonstrates a reasonable fit for the phase change to the rocksalt lattice formation and demonstrates a reasonable fit with the elastic properties of both materials. The Tersoff parameters are used in an MD simulation to predict the thermodynamic properties of c-AlN including the lattice parameter change and the atom site energy variation with a change in temperature.

Phase	Benkabou		Goumri-Said		Powell	
	E_{coh} (eV)	a (Å)	E_{coh} (eV)	a (Å)	E_{coh} eV	a (Å)
NaCl	-8.42183	3.71916	-4.73208	4.03857	-3.65341	4.27549
CsCl	-12.9037	2.15279	-4.3513	2.50362	-2.4412	2.79953
zinc blende	-6.64624	4.28387	-5.75721	4.37056	-5.7591	4.38324

Table 4.40: Crystal phase data for cubic Aluminium Nitride

A parameterisation was attempted using the Goumri-Said set as a starting point. All three parameter sets are shown in table 4.38 and the results, experimental values and DFT predictions are in table 4.39. Here it can be seen that the Benkabou parameters once again fail to reproduce the properties of the material correctly. The Goumri-Said values provide reasonable results for the cohesive energy and the lattice parameter. The Powell parameters are also correct to a very small error.

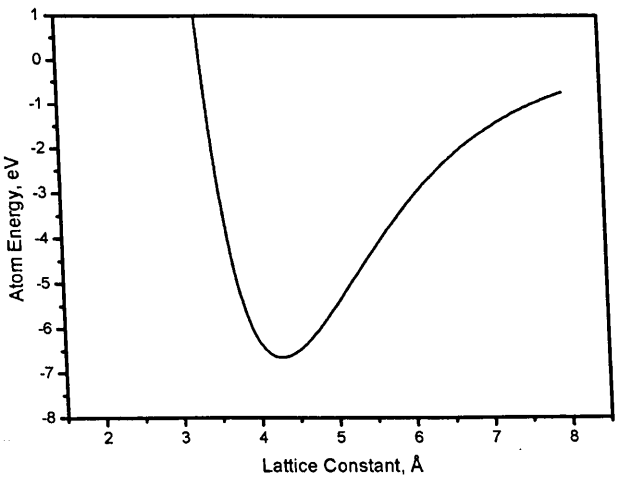

Figure 4.55: Cohesive energy of cubic aluminium nitride from Benkabou parameters

The Goumri-Said values cannot correctly reproduce the bulk modulus, the

[19]See [50]

shear modulus of the c_{44} elastic parameter, producing errors of 19%, 24% and 27% respectively and a ζ in error by 28%. The Powell parameters reproduce B and c_{44} to within 1% tolerance and shear modulus to 7% error. The value for Kleinmans internal displacement parameter is also predicted to be in error by 7% when using the Powell parameters.

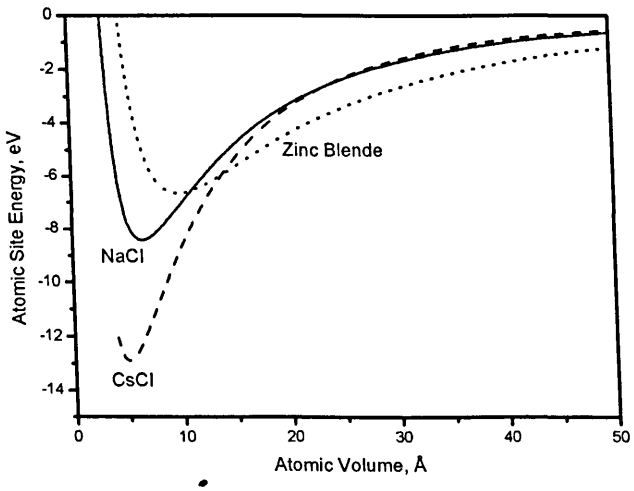

Figure 4.56: Energy vs. atomic volume for cubic aluminium nitride with Benkabou parameters

Figures 4.55, 4.57 and 4.59 show the energy vs. lattice parameter plots for the three AlN parameter sets. It is immediately obvious that the Benkabou set is massively in error. The Goumri-Said and Powell parameters produce very similar results demonstrating -5.75eV cohesive energy at 4.38Å which is correct to the experimental values.

The phase plots for the three parameterisations are shown in figures 4.56, 4.58 and 4.60 where it is again evident that the Benkabou parameters are completely wrong predicting CsCl as the lowest energy configuration. This is completely unsuitable for MD simulation. The Goumri-Said parameters produce a phase stability for zinc blende which demonstrates a 1eV gap until the CsCl and NaCl forms of the crystal. The Powell parameters provide zincblende as the lowest energy configuration and a phase change after 2eV to the NaCl crystal type.

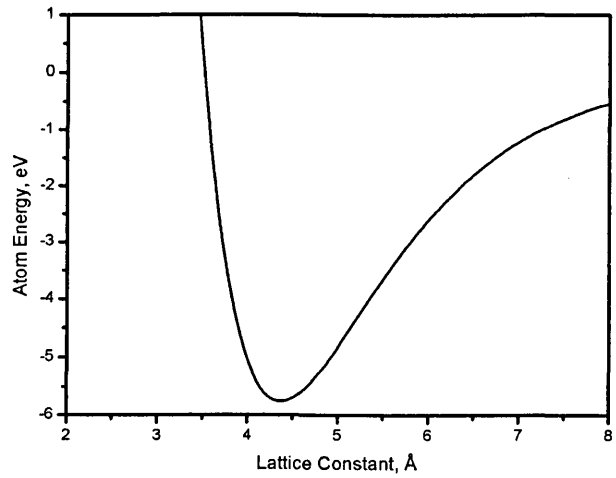

Figure 4.57: Cohesive energy of cubic aluminium nitride from Goumri-Said parameters

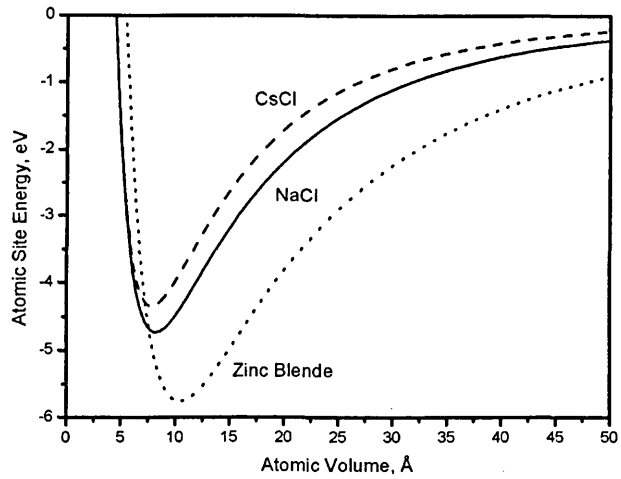

Figure 4.58: Energy vs. atomic volume for cubic aluminium nitride with Goumri-Said parameters

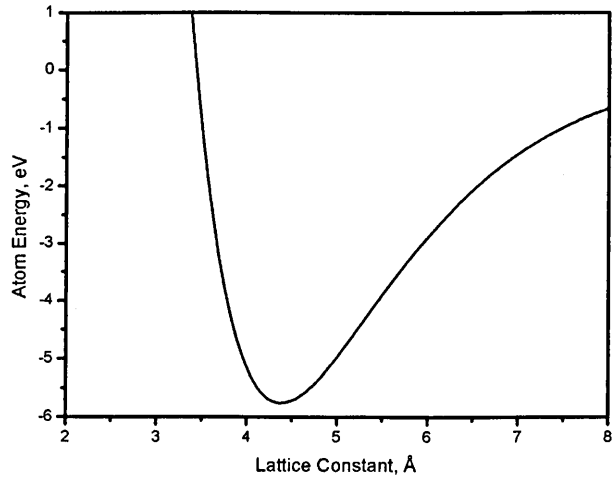

Figure 4.59: Cohesive energy of cubic aluminium nitride from Powell parameters

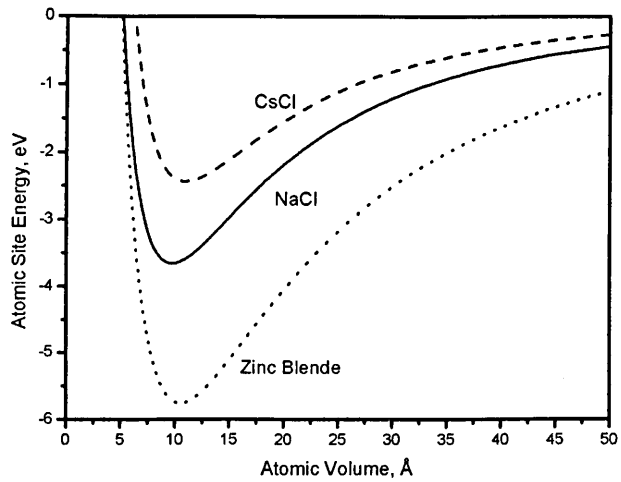

Figure 4.60: Energy vs. atomic volume for cubic aluminium nitride with Powell parameters

4.4 Elastic constants and Keyes' relation

Keyes[55] proposed a simple empirical relationship to link the elastic constant of the III-V materials to their lattice constant by studying the measured values available at the time. He reduced the elastic constants, through dimensional analysis, to dimensionless forms which are almost independent of the material. Keyes simply suggested that the elastic constants of the cubic crystals c_{11}, c_{12} and c_{44} could be reduced to c^*_{ij} by dividing by a normalising factor c_0 comprised of powers of the electronic charge e and the nearest neighbour bonding distance b

$$c^*_{ij} = c_{ij}/c_0 \tag{4.36}$$

$$c_0 = e^2/b^4 \tag{4.37}$$

$$e = 1.60217646 \times 10^{-19} \tag{4.38}$$

$$b = \left[3\left(\frac{a}{4}\right)^2\right]^{0.5} \tag{4.39}$$

This work was improved upon by Azuhata *et al*[56] who had access to a greater range of results and who proposed the following relations to predict the elastic properties of III-V zinc blende semiconductors

$$c^*_{11} = 1.333 + 2.998/a \tag{4.40}$$

$$c^*_{12} = 0.1521a \tag{4.41}$$

$$c^*_{44} = 0.01235a + 0.1609 + 3.777/a \tag{4.42}$$

Figure 4.61 shows the experimental data for the III-V compounds studied above and the trend lines suggested in equations 4.40. As can be clearly seen, the line suggested for the c^*_{12} data provided a reasonable fit, but the c^*_{11} line and the c_{12} line are high compared to the data points.

Motivated by a desire to predict the elastic properties of the popular cubic aluminium-V (AlAs, AlP, AlSb) materials it was decided to investigate this result further. The DFT results from above (mainly provided by Wang and Ye[18]) were also plotted against the equations that were proposed as a modification of Keyes' relation and a similar situation was found with the experimental data. This is shown in figure 4.62 and demonstrates a closer fit to the modified Keyes relation. Furthermore, the Tersoff fits from the Powell parameters for each of the semiconductors above was also plotted against the Azuhata relations. Although these Tersoff PEF results are mainly fitted to the DFT results they do vary in places and are included for completeness. As can be seen from figure 4.63 the results bear a

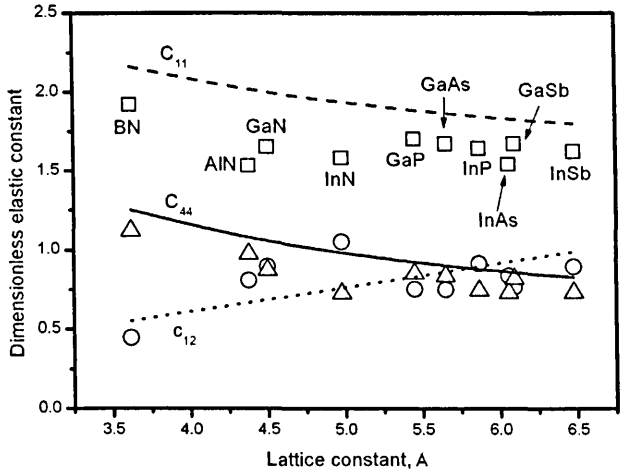

Figure 4.61: The experimental data from above and the trend provided by Azuhata. Symbol key: *open square* = c_{11} values, *open circle* = c_{12} values, *open triangle* = c_{44} values, *dashed line* = c_{11} relation, *dotted line* = c_{12} relation, *full line* = c_{44} relation.

similar failure.

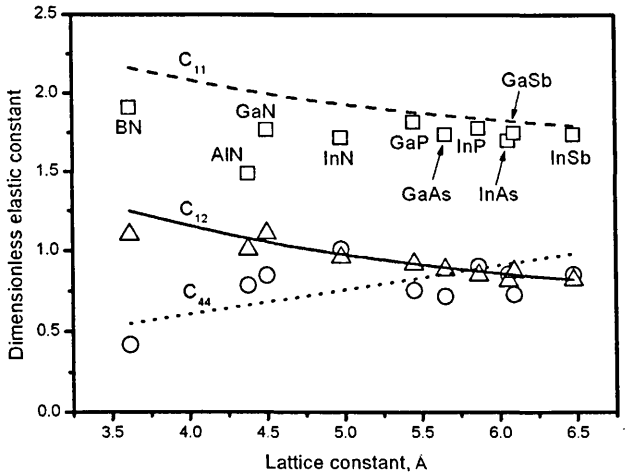

Figure 4.62: The DFT data from the previous subsections and the trend provided by Azuhata. Symbol key: *open square* = c_{11} values, *open circle* = c_{12} values, *open triangle* = c_{44} values, *dashed line* = c_{11} relation, *dotted line* = c_{12} relation, *full line* = c_{44} relation.

Using the information available for the DFT results and the experimental data for all of the III-V semiconductors listed above it was deemed interesting to see if the empirical relations suggested by Keyes could be improved upon and used to predict further elastic properties.

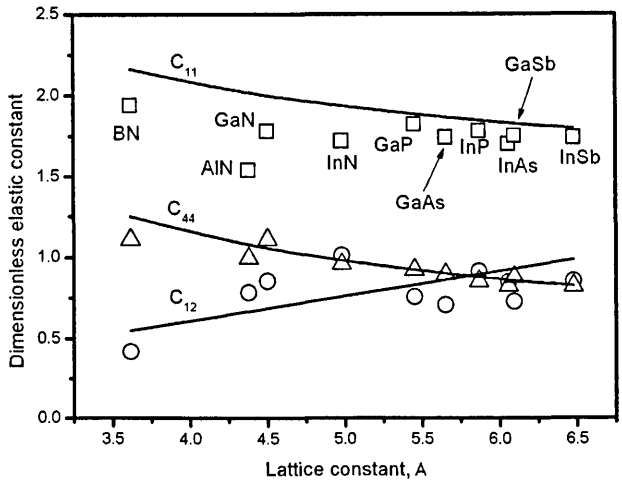

Figure 4.63: The Powell parameters Tersoff PEF data from above and the trend provided by Azuhata. Symbol key: *open square* = c_{11} values, *open circle* = c_{12} values, *open triangle* = c_{44} values, *dashed line* = c_{11} relation, *dotted line* = c_{12} relation, *full line* = c_{44} relation.

Using a 2^{nd} order polynomial fit to the lattice constant a, the following empirical relations have been developed as a fit to the experimental data

$$(Exp)c_{11}^{*} = 0.0764a^2 - 0.8313a + 3.8525 \tag{4.43}$$

$$(Exp)c_{12}^{*} = -0.1191a^2 + 1.2865a - 2.5738 \tag{4.44}$$

$$(Exp)c_{44}^{*} = 0.0564a^2 - 0.6893a + 2.8679 \tag{4.45}$$

Which has provided the trend lines shown in figure 4.64. Here it is clear to see that the data is a much better fit for all of the points available, even though the c_{12}^{*} data varies in quite an exaggerated fashion.

A further set of polynomial trend lines were acquired using a standard polynomial regression for the DFT data associated with each of the semiconductor compound above and are shown below

$$(DFT)c_{11}^{*} = 0.0504a^2 - 0.5211a + 3.0524 \tag{4.46}$$

$$(DFT)c_{12}^{*} = -0.1206a^2 + 1.3079a - 2.6653 \tag{4.47}$$

$$(DFT)c_{44}^{*} = -0.0054a^2 - 0.0562a + 1.3893 \tag{4.48}$$

These trend lines are plotted against the DFT data and shown in figure 4.65 and furthermore the Tersoff PEF results from the Powell parameterisations are shown in figure 4.66. here it can clearly be seen that the trend lines much more

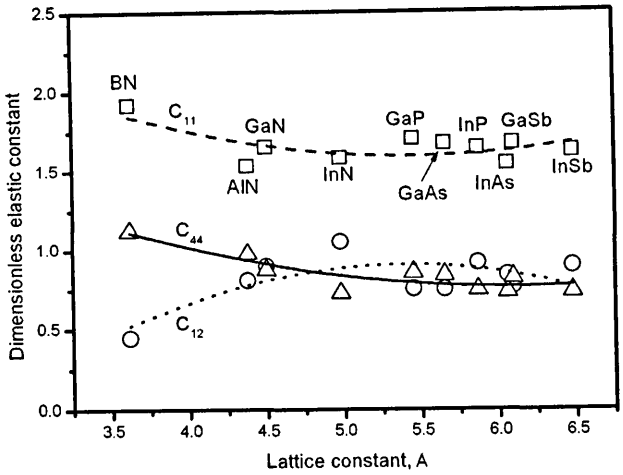

Figure 4.64: The experimental data from the previous subsections and the trend provided by Powell for the experimental data. Symbol key: *open square* = c_{11} values, *open circle* = c_{12} values, *open triangle* = c_{44} values, *dashed line* = c_{11} relation, *dotted line* = c_{12} relation, *full line* = c_{44} relation.

accurately represent the data available, although there is still the issue with the wide variance of the c_{12}^* parameter.

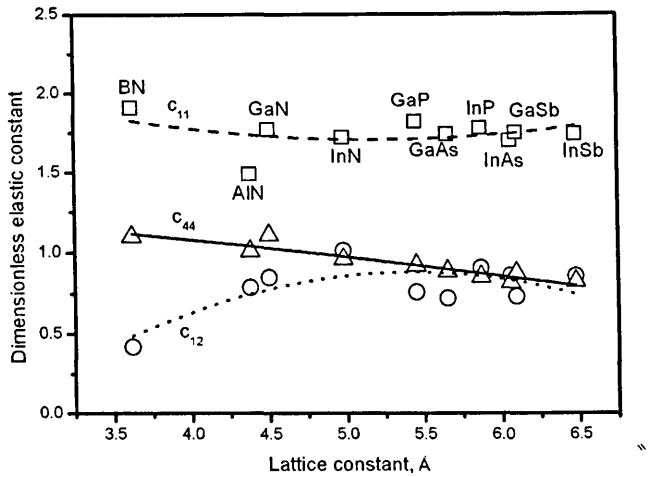

Figure 4.65: The DFT data from above and the trend provided by Powell for the DFT data. Symbol key: *open square* = c_{11} values, *open circle* = c_{12} values, *open triangle* = c_{44} values, *dashed line* = c_{11} relation, *dotted line* = c_{12} relation, *full line* = c_{44} relation.

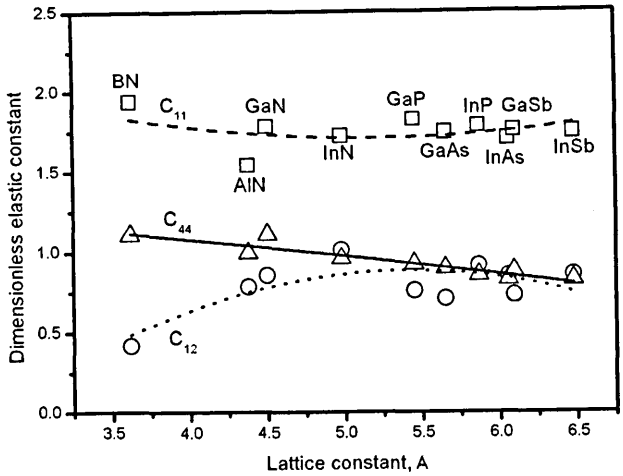

Figure 4.66: The Tersoff PEF data from above using the Powell parameterisations and the trend provided by Powell for the DFT results fit. Symbol key: *open square* = c_{11} values, *open circle* = c_{12} values, *open triangle* = c_{44} values, *dashed line* = c_{11} relation, *dotted line* = c_{12} relation, *full line* = c_{44} relation.

Predicting the aluminium-V elastic constants

By using the relations above (equation 4.43 for the experimental data and 4.46 for the DFT data) a fit for the AlAs, AlP and AlSb has been attempted. The results are shown in the tables below:

Aluminium Arsenide					
		a	c_{11}	c_{12}	c_{44}
	Exp.[20]	5.66172	1.199	0.575	0.566
Powell	Predict		1.1333	0.6340	0.594
	Error		11%	10%	3%
Azuhata	Predict		1.32	0.611	0.638
	Error		10%	6%	11%
	DFT[21]		1.131	0.555	0.574
Powell	Predict		1.2205	0.6209	0.6381
	Error		8%	11%	16%

Table 4.41: Predictions for the elastic constants of AlAs

Table 4.41 shows the predicted values for the AlAs and it is highlighted that the new relations for the experimental data fit perform only slightly better than the results given by the Azuhata relations. The results fitted to the DFT data perform slightly worse than expected but still, all results are in the range 3%-16% and can predict the elasic properties of the material with a general trend.

[20]See ref. [57]
[21]See Wang[18]
[22]See ref. [58]

Aluminium Phosphide					
		a	c_{11}	c_{12}	c_{44}
	Exp.[22]	5.463			
Azuhata	Predict		1.5426	0.6812	0.754
	Error		16%	2%	20%
	DFT[21]		1.325	0.667	0.627
Powell	Predict		1.401	0.721	0.7551
	Error		5%	8%	20%

Table 4.42: Predictions for the elastic constants of AlP

Table 4.42 shows the results for predictions of the AlP elastic properties. No experimental results could be found in the literature for measurements of AlP. This is probably because it is a highly reactive material and very difficult to work with. It has been simulated with DFT and the results are compared. Using the Powell DFT prediction trend the results for c_{11} and c_{12} are pleasing but both models can only predict the value of c_{44} to within 20%.

Aluminium Antimonide					
		a	c_{11}	c_{12}	c_{44}
	Exp.[23]	6.1355	0.8769	0.4341	0.4076
Powell	Predict		0.83887	0.4308	0.3925
	Error		4%	1%	3%
Azuhata	Predict		0.9386	0.4808	0.4391
	Error		7%	11%	8%
	DFT[21]		0.855	0.414	0.399
Powell	Predict		0.9029	0.4222	0.4334
	Error		5%	2%	8%

Table 4.43: Predictions for the elastic constants of AlSb

The predictions shown in table 4.43 for AlSb are good. The Powell model predicts the experimental results to within a good tolerance (less than 4%) and the Azuhata model shows results that are correct to within 11%. The Powell DFT model provides results that are within 8% of the predicted DFT values.

Finally, the original Keyes data points are shown in figure 4.67 plotted along with the trend lines provided by both Azuhata and Powell in equation 4.46 designated by (A) and (P) respectively. Both sets of lines appear to provide reasonable fits to the data provided by Keyes, hence not significantly altering his original result. But the added degrees of freedom provided by the equations provided here appear to have improved the quality of the data fit and the ability to predict the elastic constants for other materials.

[23]See [59]

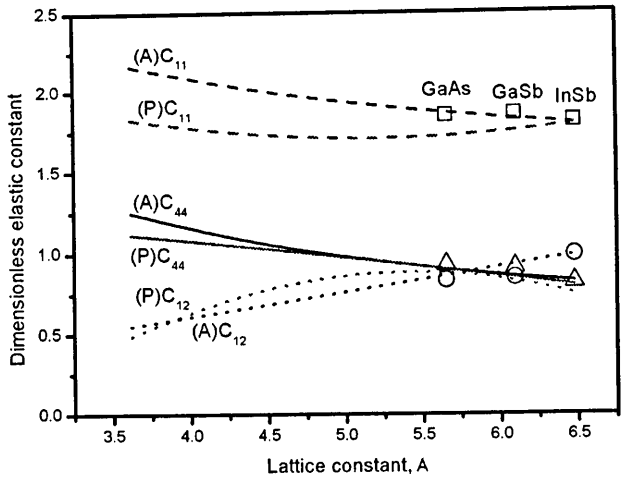

Figure 4.67: The original Keyes data points are plotted with the (P) Powell and (A) Azuhata data trend lines

4.5 Conclusions

The algorithm that provides the granular local search is a real *tour de force*. The original attempt to model the Tersoff parameters used a program that took 3 weeks to run and did not optimise the c_{44} or ζ material properties[26]. This timing has been brought down to 3 minutes per program run which allows the systems to be investigated very thoroughly, as is shown in the examination of the global search space with the global Tersoff parameters search routine. The high speed of execution of the computer program is based upon intelligent algorithm design coupled with high-speed scientific programming techniques including the use of binary arithmetic operators instead of decision-branch logic to avoid pipeline flushing and branch prediction faults and the use of a cache prefetching scheme to avoid costly page-faulting.

The global random search algorithm has provided a first look at the Tersoff ten-dimensional parameter landscape. It has been seen that for a given set of starting values, only a tenth of the randomly generated Tersoff parameter sets will evaluate and that only about 10% of these sets will provide a result that is noteworthy. This searching of the Tersoff parameter space is considered to be a topic for further investigation. An attempt to correlate the Tersoff parameter sets that evaluate with the material parameters would show interesting results and may produce methods that will guarantee success at a much higher rate.

The results that are provided by the local parameter search are all excellent. In all 13 cases the Tersoff parameters have been improved to under 1% tolerance

of the sought values of lattice parameter, cohesive energy and elastic constants. The inclusion of the Kleinman internal displacement parameter in the search metric has raised confidence that MD simulations of small scale strain relaxation in heterostructures and semiconductor systems can be successfully completed and will provide results on a large scale that tally with *ab initio* quantum mechanical methods.

The first results for the modelling of GaP, InP, GaSb and InSb have been successfully provided and the III-N materials have been re-parameterised to correct errors in the literature.

In terms of remodelling Keyes' relations and improving on the model proposed by Azuhata, the Powell relations appear to work at least as well as the Azuhata model and in the case of AlSb they work much better. The original Keyes data points have been maintained and hence the model has not significantly changed the results offered by Keyes, but the modelling of the smaller lattice constant materials appears to have been improved upon.

Bibliography

[1] H. S. John W. Harris, *Handbook of mathematics and computational science.* Springer-Verlag New York, Inc., 1998.

[2] K. A. Stroud, *Further engineering mathematics.*

[3] F. D. Murnaghan, "The compressibility of media under extreme pressures," *Proceedings of the National Academy of Sciences*, vol. 30, pp. 244–247, 1944.

[4] F. Birch, "Finite elastic strain of cubic crystals," *Phys. Rev.*, vol. 71, pp. 809–824, 1947.

[5] L. Kleinman, "Deformation potentials in silicon. I. uniaxial strain," *Phys. Rev.*, vol. 128, pp. 2614–2621, 1962.

[6] R. Wagner, "Mersenne twister random number generator." [Online]. Available: http://www-personal.engin.umich.edu/ wagnerr/MersenneTwister.html

[7] M. Grimsditch, *Handbook of Elastic Properties of Solids, Liquids, and Gases. Volume I: Dynamic Methods for Measuring the Elastic Properties of Solids.* Academic Press, New York, 2001.

[8] I. L. Fabelinskii, *Molecular Scattering of Light.* Plenum, New York, 1968.

[9] W. Hayes and R. Loudon, *Scattering of Light by Crystals.* Wiley, New York, 1978.

[10] W. A. Harrison, *Electronic structure and the properties of solids.* Dover Publications, Inc., 1980.

[11] S. P. Nikanorov, Y. A. Burenkov, and A. V. Stepanov, *Sov. Phys. Solid State*, vol. 13, no. 10, pp. 2516–2519, 1971. [Online]. Available: http://www.ioffe.rssi.ru/SVA/NSM/Semicond/Si

[12] J. Tersoff, "Modeling solid-state chemistry: Interatomic potentials for multicomponent systems," *Phys. Rev. B*, vol. 39, no. 8, pp. 5566–5568, 1989.

[13] M. T. Yin and M. L. Cohen, "Theory of static structural properties, crystal stability, and phase transformation: Applications to si and ge," *Phys. Rev. B*, vol. 26, p. 5668, 1982.

[14] H. J. McSkimin and P. Andreatch, "Elastic moduli of diamond as a function of pressure and temperature," *J. Appl. Phys.*, vol. 43, no. 7, pp. 2944–2948, 1972.

[15] S. Erkoc and S. Ozkaymak, "Energetics of carbon nanotubes," *Eur. Pys. J. D*, vol. 4, pp. 331–333, 1998.

[16] J. Tersoff, "Empirical interatomic potential for carbon with applications to amorphous carbon," *Phys. Rev. Lett.*, vol. 61, no. 25, pp. 2879–2882, 1988.

[17] H. J. McSkimin, "Measurement of elastic constants at low temperatures by means of ultrasonic waves data for silicon and germanium single crystals, and for fused silica," *J. Appl. Phys.*, vol. 24, no. 8, pp. 988–997, 1953.

[18] S. Q. Wang and H. Q. Ye, "First-principles study on elastic properties and phase stability of III-V compounds," *Phys. Stat. Sol. B*, vol. 240, no. 1, pp. 45–54, 2003.

[19] C. W. Garland and K. C. Park, "Low temperature elastic constants of gallium arsenide," *J. Appl. Phys.*, vol. 33, no. 2, pp. 759–760, 1962.

[20] Y. A. Burenkov, Y. M. Burdukov, S. Y. Davidov, and S. P. Nikanorov, *Sov. Phys. Solid State*, vol. 15, no. 6, pp. 1175–1177, 1973. [Online]. Available: http://www.ioffe.rssi.ru/SVA/NSM/Semicond/Ge

[21] R. Smith, "A semi-empirical many-body interatomic potential for modelling dynamical processes in gallium arsenide," *Nucl. Instr. Meth. Phys. Res. B*, vol. 67, pp. 335–339, 1992.

[22] M. Sayed, J. H. Jefferson, A. B. Walker, and A. G. Cullis, "Molecular dynamics simulations of implantation damage and recovery in semiconductors," *Nucl. Instr. Meth. Phys. Res. B*, vol. 102, pp. 218–222, 1995.

[23] S. Froyen and M. L. Cohen, "Structural properties of iii-v zinc-blende semiconductors under pressure," *Phys. Rev. B*, vol. 28, p. 3258, 1983.

[24] P. A. Ashu, J. H. Jefferson, A. G. Cullis, W. E. Hagston, and C. R. Whitehouse, "Molecular dynamics simulation of (100) InGaAs/GaAs strained layer relaxation processes," *J. Crys. Grow.*, vol. 150, pp. 176–179, 1995.

[25] K. Nordlund, J. Nord, J. Frantz, and J. Keinonen, "Strain-induced Kirkendall mixing at semiconductor interfaces," *Comp. Mater. Sci.*, vol. 18, no. 3, pp. 283–294, 2000.

[26] M. A. Migliorato, A. G. Cullis, M. Fearn, and J. H. Jefferson, "Atomistic simulation of strain relaxation in $In_xGa_{1-x}As/GaAs$ quantum dots with non uniform composition," *Phys. Rev. B*, vol. 65, p. 115316, 2002.

[27] Y. A. Burenkov, S. Y. Davydov, and S. P. Nikanorov, *Sov. Phys. Solid State*, vol. 17, no. 7, pp. 1446–1447, 1975. [Online]. Available: http://www.ioffe.rssi.ru/SVA/NSM/Semicond/InAs

[28] R. Weil and W. O. Groves, "The elastic constants of gallium phosphide," *J. Appl. Phys.*, vol. 39, no. 9, pp. 4049–4051, 1968.

[29] Y. K. Yogurtcu, A. J. Miller, and G. A. Saunders, "Pressure dependence of elastic behaviour and force constants of GaP," *J. Phys. Chem. Solids*, vol. 42, no. 1, pp. 49–56, 1981.

[30] D. N. Nichols, D. S. Rimai, and R. J. Sladek, "Elastic anharmonicity of InP: Its relationship to the high pressure transition," *Solid State Commun.*, vol. 36, no. 8, pp. 667–669, 1980.

[31] W. F. Boyle and R. J. Sladek, "Elastic constants and lattice anharmonicity of GaSb and GaP from ultrasonic-velocity measurements between 4.2 and 300 K," *Phys. Rev. B*, vol. 11, no. 8, pp. 2933–2940, 1975.

[32] L. J. Slutsky and C. W. Garland, "Elastic constants of indium antimonide from 4.2K to 300K," *Phys. Rev.*, vol. 113, no. 1, pp. 167–169, 1959.

[33] K. Albe and W. Moller, "Modelling of boron nitride: Aomic scale simulations on thin film growth," *Comp. Mat. Sci.*, vol. 10, pp. 111–115, 1998.

[34] W. Sekkal, A. Laref, H. Aourag, A. Zaoui, and M. Certier, "The miscibility of $Cu_XAg_{1-X}I$ using a Tersoff potential," *Superlatt. Microstruct.*, vol. 28, no. 1, pp. 55–66, 2000.

[35] ——, "The miscibility of copper halides using a three-body potential. Part II: $CuBr_XI_{1-X}$," *J. Mat. Sci.*, vol. 11, no. 1, pp. 123–129, 2000.

[36] M. Grimsditch, E. S. Zouboulis, and A. Polian, "Elastic constants of boron nitride," *J. Appl. Phys.*, vol. 76, no. 2, pp. 832–834, 1994.

[37] K. Shimada, T. Sota, and K. Suzuku, "First-principles study on electronic and elastic properties of BN, AlN, and GaN," *J. Appl. Phys.*, vol. 84, no. 9, pp. 4951–4958, 1998.

[38] S. Strite and H. Morkoc, "GaN, AlN and InN: A review," *J. Vac. Sci. Technol. B*, vol. 10, p. 1237, 1992.

[39] S. Nakamura, M. Senoh, and T. Mukai, "High power InGaN/GaN double heterostructure violet light emitting diodes," *Appl. Phys. Lett.*, vol. 62, p. 1237, 1993.

[40] H. Amono, T. Tanaka, Y. Kunii, K. Kato, S. T. Kim, and I. Akasaki, "Room temperature violet stimulated emission from optically pumped AlGaN/GaInN double heterostructure," *Appl. Phys. Lett.*, vol. 64, p. 1377, 1994.

[41] J. W. Orton and C. T. Foxton, "Group III nitride semiconductors for short wavelength light emitting diodes," *Rep. Prog. Phys.*, vol. 61, p. 1, 1998.

[42] F. Benkabou, H. Aourag, P. J. Becker, and M. Certier, "Molecular dynamics study of zinc blende GaN, AlN and InN," *Molecular Simulation*, vol. 23, pp. 327–341, 2000.

[43] W. H. Moon and H. J. Hwang, "Structural and thermodynamic properties of GaN: a molecular dynamics simulation," *Phys. Lett. A.*, vol. 315, pp. 319–324, 2003.

[44] T. Lei, T. D. Moustakas, R. J. Graham, Y. He, and S. J. Berkowitz, "Epitaxial growth and characterization of zinc-blende gallium nitride on (001) silicon," *J. Appl. Phys.*, vol. 71, no. 10, pp. 4933–4943, 1992.

[45] A. F. Wright, "Elastic properties of zinc blende and wurtzite AlN, GaN and InN," *J. Appl. Phys.*, vol. 82, no. 6, pp. 2833–2839, 1997.

[46] M. Nakamura, H. Fujioka, K. Ono, M. Takeuchi, T. Mitsui, and M. Oshima, "Molecular dynamics simulation of III-V compound semiconductor growth with MBE," *J. Crys. Grow.*, vol. 209, pp. 232–236, 2000.

[47] K. Kim, W. R. L. Lambrecht, and B. Segall, "Elastic constants and related properties of tetrahedrally bonded BN, AlN, GaN and InN," *Phys. Rev. B*, vol. 53, no. 24, pp. 16310–16326, 1996.

[48] F. Bechstedt, U. Grossner, and J. Furthmuller, "Dynamics and polarisation of group-III nitride lattices: A first principles study," *Phys. Rev. B*, vol. 62, no. 12, p. 8003, 2000.

[49] S. Q. Wang and H. Q. Ye, "Ab initio investigation of the pressure dependences of phonon and dielectric properties for III-V semiconductors," *J. Phys.: Condens. Matter*, vol. 17, pp. 4475–4488, 2005.

[50] M. E. Sherwin and T. J. Drummond, "Predicted elastic constants and critical layer thicknesses for cubic phase AlN, GaN and InN on β-SiC," *J. Appl. Phys.*, vol. 69, no. 12, pp. 8423–8425, 1991.

[51] J. A. Sanjurjo, E. Lopez-Cruz, P. Vogl, and M. Cardona, "Dependence on volume of the phonon frequencies and their effective charges of several III-V semiconductors," *Phys. Rev. B*, vol. 28, no. 8, pp. 4475–4488, 1983.

[52] A. R. Goni, H. Siegle, K. Syassen, C. Thomsen, and J. M. Wagner, "Effect of pressure on optical phonon modes and transverse effective charges in GaN and AlN," *Phys. Rev. B*, vol. 64, no. 3, p. 035205, 2001.

[53] S. Goumri-Said, M. B. Kanoun, A. E. Merad, G. Merad, and H. Aourag, "Prediction of structural and thermodynamic properties of zinc-blende AlN: molecular dynamics simulation," *Chem. Phys.*, vol. 302, pp. 135–141, 2004.

[54] J. M. Wagner and F. Bechstedt, "Pressure dependence of the dielectric and lattice-dynamical properties of GaN and AlN," *Phys. Rev. B*, vol. 62, no. 7, p. 4526, 2000.

[55] R. W. Keyes, "Elastic properties of the diamond-type semiconductors," *J. Appl. Phys.*, vol. 33, no. 11, pp. 3371–3372, 1962.

[56] T. Azuhata, T. Sota, and K. Suzuki, "Elastic constants of III-V compound semiconductors: modification of keyes' relation," *J. Phys.: Condens. Matter*, vol. 8, pp. 3111–3119, 1996.

[57] M. Kreiger, N. Herres, K. Bachem, and K. Kohler, "Elastic constants and Poisson ratio in the system AlAs-GaAs," *Appl. Phys. Lett.*, vol. 66, no. 6, pp. 682–684, 1995.

[58] G. J. Ackland, "High pressure phases of group IV and III-V semiconductors," *Rep. Prog. Phys.*, vol. 64, pp. 483–516, 2001.

[59] R. Weil, "Corrections to the elastic constants of GaSb," *J. Appl. Phys.*, vol. 43, no. 10, p. 4271, 1972.

Chapter 5

Vibrational Frequency Modelling

The usefulness of the Tersoff PEF for modelling the first-order elastic properties and small-scale strain effects accurately has been demonstrated in the previous chapter. By modelling the dynamical properties of the crystal lattices under investigation we can hopefully demonstrate the transferability of the Tersoff potential to higher-order crystal effects. We shall show here that the Tersoff PEF can be used to predict phonon energies and mode-Grüneisen parameters and hence is useful for modelling crystal dynamical properties.

5.1 Assembling the dynamical matrix

Section 2.3 contains the mathematical reasoning underpinning the modelling of the lattice phonon frequencies using the harmonic approximation. Practically, applying this to the lattice model and the Tersoff empirical potential energy model is quite an involved task and requires some explanation.

$$U_\alpha(\mathrm{lb}) = \frac{1}{\sqrt{m_b}} \sum_{\mathbf{q}} U_\alpha(\mathbf{q};\mathrm{b}) \exp\left[i(\mathbf{q}\cdot\mathbf{x}(\mathrm{l}) - \omega t)\right] \tag{5.1}$$

$$D_{\alpha\beta}(\mathrm{bb'}|\mathbf{q}) = \frac{1}{\sqrt{m_b m_{b'}}} \sum_{\mathrm{l'}} \Phi_{\alpha\beta}(\mathrm{0b};\mathrm{l'b'}) \exp\left[i\mathbf{q}\cdot\mathbf{x}(\mathrm{l'})\right] \tag{5.2}$$

Equation 5.2 for the Dynamical Matrix in three dimensional q space is known as the Fourier transformed 'D-type' matrix[1]. By choosing our equations of motion of the form shown in Equation 5.1 and by considering lattice periodicity we have reduced an infinite set of linear simultaneous equations to a set of $3d$ linear homogeneous equations in $3d$ unknowns: $U_\alpha(\mathbf{q};\mathrm{b})$ where d represents the number of atoms in the atomic basis set. For a type III-V zinc blende structure $d = 2$ and we have to solve a 6x6 Hamiltonian containing the summed contributions of

		x					y					z				
		i	j	k_1	k_2	k_3	i	j	k_1	k_2	k_3	i	j	k_1	k_2	k_3
x	i															
	j															
	k_1															
	k_2															
	k_3															
y	i															
	j															
	k_1															
	k_2															
	k_3															
z	i															
	j															
	k_1						X									
	k_2															
	k_3															

Table 5.1: The 15x15 matrix required for the partial second derivatives of the Tersoff potential

the force constant matrix based upon the second derivatives of the potential.

The second derivatives of the Tersoff potential are analytically derived and shown in Appendix A. The analytical partial second derivatives are split into individual components of the form

$$\frac{\partial^2 V_{ij}(x,y,z)}{\partial n_q \partial m_p}$$

where $m, n = [x, y, z]$ represents the direction of the component and the subscripts $p, q = [i, j, k_1, k_2, k_3]$ represent the atomic neighbours. For example if we wanted the second derivative of the energy of the y component of the i atom with respect to the z component of the k_1 atom we would take the partial derivative

$$\frac{\partial^2 V_{ij}(x,y,z)}{\partial z_{k_1} \partial y_i} \tag{5.3}$$

It can be seen that for any atom under consideration as an i atom there will be a matrix of 15x15 components required to describe all of the individual partial second derivative contributions that will appear as demonstrated in table 5.1. The position of the example component in Eq 5.3 is shown in the table with an X.

To approximate the lattice dynamics of a three dimensional diatomic system we must consider all possible interactions between the two atoms in the basis set and their neighbouring atoms. Figure 5.1 shows the two central atoms in the basis set of species b and b' which are labelled 1 and 2 respectively. These 2 atoms are in the central basis set cell called $l = 0$ in the D-matrix notation. All of the first nn of the central pair are shown in the diagram, $l \neq 0$. Using the Tersoff notation, if

	$atom_j$	$atom_j$	$atom_j$	$atom_j$
$atom_i = 1$	2	3	4	5
$atom_i = 2$	1	6	7	8
$atom_i = 3$	1	$3nn_1$	$3nn_2$	$3nn_3$
$atom_i = 4$	1	$4nn_1$	$4nn_2$	$4nn_3$
$atom_i = 5$	1	$5nn_1$	$5nn_2$	$5nn_3$
$atom_i = 6$	2	$6nn_1$	$6nn_2$	$6nn_3$
$atom_i = 7$	2	$7nn_1$	$7nn_2$	$7nn_3$
$atom_i = 8$	2	$8nn_1$	$8nn_2$	$8nn_3$

Table 5.2: The 4x8 interaction grid required to provide all possible atomic interactions for the central 2 atoms

we consider atom 1 to be the i atom then the following combinations are possible

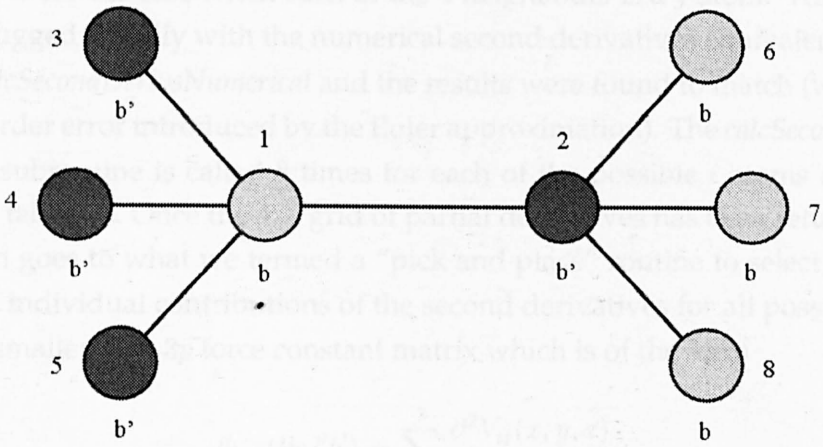

Figure 5.1: A diatomic chain and all correctly bonded first nearest neighbours

Atom $i = 1$: atoms $j = 2, k_1 = 3, k_2 = 4, k_3 = 5$
Atom $i = 1$: atoms $j = 3, k_1 = 2, k_2 = 4, k_3 = 5$
Atom $i = 1$: atoms $j = 4, k_1 = 2, k_2 = 3, k_3 = 5$
Atom $i = 1$: atoms $j = 5, k_1 = 2, k_2 = 3, k_3 = 4$

providing four possible combinations per choice of i atom. All 8 atoms in figure 5.1 are required to be considered as i atoms so that the $l = 0$ cell has all possible interactions with the neighbouring cells taken into account. To take all of these possible interactions into consideration requires us to produce a grid of data of size 4x8 that contains at each location the 15x15 second derivatives matrix. The interactions comprising this grid are shown in table 5.2 where the notation $3nn_1$ indicates that the j atom should be taken as the first neighbour of atom 3 and $4nn_2$ indicates that the j atoms should be the second neighbour of atom 4.

The subroutine called *calcSecondDerivsAnalytic* in the program is called with the lattice reference number of the i atom and performs an operation that returns with a 4x1 vector of 15x15 matrices containing the analytically calculated second

$1 = i$	$[1 = i; 1 - 2(p = i, q = i)$ $[1 = i; 1 - 4(p = i, q = i)$	$[1 = i; 1 - 3(p = i, q = i)$ $[1 = i; 1 - 5(p = i, q = i)$
$1 = j$	$[1 = j; 2 - 1(p = j, q = j)$ $[1 = j; 4 - 1(p = j, q = j)$ $[1 = j; 2 - 1(p = j, q = k_n)$ $[1 = j; 4 - 1(p = j, q = k_n)$	$[1 = j; 3 - 1(p = j, q = j)$ $[1 = j; 5 - 1(p = j, q = j)$ $[1 = j; 3 - 1(p = j, q = k_n)$ $[1 = j; 5 - 1(p = j, q = k_n)$
$1 = k_n$	$[1 = k_n; 2 - 6(p = k_n, q = j)$ $[1 = k_n; 2 - 8(p = k_n, q = j)$ $[1 = k_n; 2 - 7(p = k_n, q = k_n)$ $[1 = k_n; 3 - nn(p = k_n, q = j)$ $[1 = k_n; 5 - nn(p = k_n, q = j)$ $[1 = k_n; 4 - nn(p = k_n, q = k_n)$	$[1 = k_n; 2 - 7(p = k_n, q = j)$ $[1 = k_n; 2 - 6(p = k_n, q = k_n)$ $[1 = k_n; 2 - 8(p = k_n, q = k_n)$ $[1 = k_n; 4 - nn(p = k_n, q = j)$ $[1 = k_n; 3 - nn(p = k_n, q = k_n)$ $[1 = k_n; 5 - nn(p = k_n, q = k_n)$

Table 5.3: The interactions to be summed when considering the case $b - b$

derivatives for the case when each of the 4 neighbours is a j atom. This routine was debugged initially with the numerical second derivatives equivalent routine called *calcSecondDerivsNumerical* and the results were found to match (within the second order error introduced by the Euler approximation). The *calcSecondDerivs-Analytic* subroutine is called 8 times for each of the possible i atoms and the j atoms in table 5.2. Once the 4x8 grid of partial derivatives has been returned, the data then goes to what we termed a "pick and place" routine to select and sum all of the individual contributions of the second derivatives for all possible cases into the smaller $3p \times 3p$ force constant matrix which is of the form

$$\Phi_{\alpha\beta}(lb; l'b') = \sum_{l'=0}^{7} \frac{\partial^2 V_{ij}(x, y, z)}{\partial n_q m_p} \tag{5.4}$$

The pick and place routine selects all possible atomic combinations that have an effect on either of the central two atoms in the $l = 0$ cell and sums them into the force constants matrix. The interactions are described below for each of the 4 cases of the second derivatives that need considering: $b-b$, $b-b'$, $b'-b$ and $b'-b'$.

To consider a single case, the interaction between the $b - b$ atoms: When atom 1 is the i atom we have interaction contributions between atoms 1-2 so we choose this interaction grid and we need to select the case when $p = i$, $q = i$ and so we select these interactions from the second derivatives table. We will write this in shorthand as $[1 = i; 1 - 2(p = i, q = i)]$. Another interaction exists between atoms 1-3 when $p = i$, $q = i$ which we will write in shorthand as $[1 = i; 1-3(p = i, q = i)]$ and so on. All of the possible interactions, which must be summed for all $m, n = [x, y, z]$ cases, are tabulated in the shorthand in tables 5.3 - 5.6.

We are ultimately interested in constructing the D-matrix which is shown diagrammatically in figure 5.2. It can be seen from the diagram that the summed elements of the force constants matrix need to be multiplied by the complex expo-

$2 = i$	$[2 = i; 2 - 1(p = i, q = i)$ $[2 = i; 2 - 7(p = i, q = i)$	$[2 = i; 2 - 6(p = i, q = i)$ $[2 = i; 2 - 8(p = i, q = i)$
$2 = j$	$[2 = j; 1 - 2(p = j, q = j)$ $[2 = j; 7 - 2(p = j, q = j)$ $[2 = j; 1 - 2(p = j, q = k_n)$ $[2 = j; 7 - 2(p = j, q = k_n)$	$[2 = j; 6 - 2(p = j, q = j)$ $[2 = j; 8 - 2(p = j, q = j)$ $[2 = j; 6 - 2(p = j, q = k_n)$ $[2 = j; 8 - 2(p = j, q = k_n)$
$2 = k_n$	$[2 = k_n; 1 - 3(p = k_n, q = j)$ $[2 = k_n; 1 - 5(p = k_n, q = j)$ $[2 = k_n; 1 - 4(p = k_n, q = k_n)$ $[2 = k_n; 6 - nn(p = k_n, q = j)$ $[2 = k_n; 8 - nn(p = k_n, q = j)$ $[2 = k_n; 7 - nn(p = k_n, q = k_n)$	$[2 = k_n; 1 - 4(p = k_n, q = j)$ $[2 = k_n; 1 - 3(p = k_n, q = k_n)$ $[2 = k_n; 1 - 5(p = k_n, q = k_n)$ $[2 = k_n; 7 - nn(p = k_n, q = j)$ $[2 = k_n; 6 - nn(p = k_n, q = k_n)$ $[2 = k_n; 8 - nn(p = k_n, q = k_n)$

Table 5.4: The interactions to be summed when considering the case $b' - b'$

$1 = i$	$[1 = i; 1 - 2(p = i, q = j)$ $[1 = i; 1 - 4(p = i, q = j)$ $[1 = i; 1 - 2(p = i, q = k_n)$ $[1 = i; 1 - 4(p = i, q = k_n)$	$[1 = i; 1 - 3(p = i, q = j)$ $[1 = i; 1 - 5(p = i, q = j)$ $[1 = i; 1 - 3(p = i, q = k_n)$ $[1 = i; 1 - 5(p = i, q = k_n)$
$1 = j$	$[1 = j; 2 - 1(p = j, q = i)$ $[1 = j; 4 - 1(p = j, q = i)$	$[1 = j; 3 - 1(p = j, q = i)$ $[1 = j; 5 - 1(p = j, q = i)$
$1 = k_n$	$[1 = k_n; 2 - 6(p = k_n, q = i)$ $[1 = k_n; 2 - 8(p = k_n, q = i)$ $[1 = k_n; 4 - nn(p = k_n, q = i)$	$[1 = k_n; 2 - 7(p = k_n, q = i)$ $[1 = k_n; 3 - nn(p = k_n, q = i)$ $[1 = k_n; 5 - nn(p = k_n, q = i)$

Table 5.5: The interactions to be summed when considering the case $b - b'$

$2 = i$	$[2 = i; 2 - 1(p = i, q = j)$ $[2 = i; 2 - 7(p = i, q = j)$ $[2 = i; 2 - 1(p = i, q = k_n)$ $[2 = i; 2 - 7(p = i, q = k_n)$	$[2 = i; 2 - 6(p = i, q = j)$ $[2 = i; 2 - 8(p = i, q = j)$ $[2 = i; 2 - 6(p = i, q = k_n)$ $[2 = i; 2 - 8(p = i, q = k_n)$
$2 = j$	$[2 = j; 1 - 2(p = j, q = i)$ $[2 = j; 7 - 2(p = j, q = i)$	$[2 = j; 6 - 2(p = j, q = i)$ $[2 = j; 8 - 2(p = j, q = i)$
$2 = k_n$	$[2 = k_n; 1 - 3(p = k_n, q = i)$ $[2 = k_n; 1 - 5(p = k_n, q = i)$ $[2 = k_n; 7 - nn(p = k_n, q = i)$	$[2 = k_n; 1 - 4(p = k_n, q = i)$ $[2 = k_n; 6 - nn(p = k_n, q = i)$ $[2 = k_n; 8 - nn(p = k_n, q = i)$

Table 5.6: The interactions to be summed when considering the case $b' - b$

nent of the dot product of the Bravais vector between cells containing the two interacting atoms $\bar{\mathbf{x}}(l')$ and the wave vector associated with the location in k-space that we are attempting to characterise $\bar{\mathbf{q}}$ before they are added into the D-matrix representation. This value is a complex number and will produce a complex D-matrix. Furthermore, to assemble the final form of he D-matrix each of the values must be multiplied by the a factor of $(m_b \cdot m_{b'})^{-1/2}$ to account for the masses of the different atoms. The units of mass used in this calculation are taken in atomic mass units (AMU).

Once all of these operations have been performed and the D-matrix is assembled, the computer program then calls the LAPACK *zheev* diagonalisation routine with the 6x6 complex matrix which returns a 6x1 vector of eigenvalues. We can compute the system phonon values directly from these eigenvalues and it is simple to produce set of phonon dispersion curves from repeatedly performing

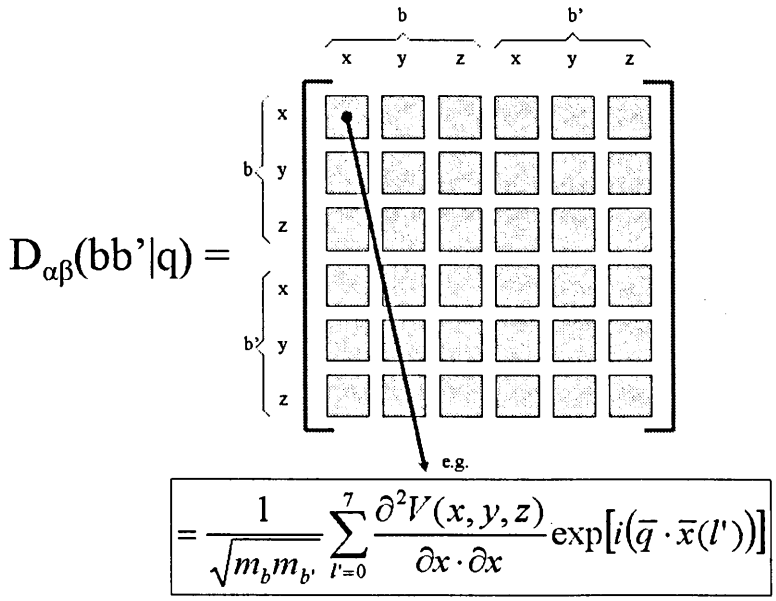

Figure 5.2: A visualisation to help understand the D-Matrix of a zinc blende crystal of a III-V material, e.g. $b = Ga$, $b' = As$

the above operations with iterative values of q-space vector between the two BZ symmetry points of interest (e.g. Γ and X).

The eigenvalues that are returned from the diagonalisation routine are in the form

$$\omega^2 = \frac{1}{m} \cdot \frac{\partial^2 E}{\partial x \partial x}$$

where ω is the angular frequency, E is the energy in eV, m is the mass in AMU and x is a length in Å. By dimensional analysis we can see that this equation is equivalent to the frequency squared

$$\begin{aligned} F &= m \cdot a \\ E &= F \cdot x = m \cdot a \cdot x = m \cdot \frac{x}{s^2} \cdot x = \frac{m \cdot x^2}{s^2} \\ f^2 &= \frac{1}{s^2} = \frac{E}{m \cdot x^2} \\ \omega^2 &= (2\pi)^2 f^2 \end{aligned}$$

Next we must convert the values from the dimensions $eV/(AMU \cdot \text{Å}^2)$ into MKS units. This is done with the following scaling factor

$$\times \frac{1.602 \times 10^{-19}}{1.660 \times 10^{-27} \cdot 1 \times 10^{-20}} = 9.647476 \times 10^{27}$$

where 1.602×10^{-19} converts Joules into eV, there are 1.660×10^{-27} kg in an AMU

and there are 1×10^{-10} m in an Angstrom, which is then further multiplied by 1×10^{-24} as it is common to quote phonon frequencies in values of THz. Overall the scaling factor may be written

$$\times 9.647476 \times 10^{27} \cdot 1 \times 10^{-24} = 9647.4756$$

Once this scaling has been applied to the 6 eigenvalues they are subject to a square root operation to obtain the individual angular frequencies ω and simply divided by a factor of 2π to produce the individual phonon values in THz.

Many authors provide phonon frequencies in THz (10^{12} Hz), however some prefer the units cm^{-1}. The conversion factor is shown below

$$1\text{eV} = 2.41796 \times 10^{14}\text{Hz} = 8.0655 \times 10^{3}\text{cm}^{-1}$$

$$\begin{aligned} 1 \times 10^{12}\text{Hz} &= \frac{8.0655 \times 10^{3}\text{cm}^{-1}}{241.796} \\ &= 33.3566\text{cm}^{-1} \end{aligned}$$

Plotting phonon dispersion curves

As was mentioned briefly above, the phonon dispersion curves are plotted by simply splitting the Brillouin zone region that we are interested in into a number of points and computing the phonon frequencies at these points. The BZ for a zinc blende (and diamond) structure can be considered as a regular octahedron that has been truncated. The Γ-point is in the BZ centre, which is the centre of the polyhedron, the X-point occurs at the centre of the square face provided by truncating the octahedron on its six polyhedron vertices. The L-point occurs at the centre of the hexagonal faces that are formed by the truncation of the octahedron. This truncated octahedron shape is shown diagrammatically in figure 5.3 along with a number of common BZ points of high symmetry. This diagram was taken from the experimental study of phonon dispersion in GaAs by Strauch and Dorner[2].

The phonon dispersion curves that are shown in the results section are split into three regions. Region 1 shows the phonon dispersion from the central BZ Γ-point at wave vector $\mathbf{q} = [0, 0, 0]$ to the BZ high symmetry X-point at wave vector $\mathbf{q} = [1, 0, 0]$. This region divided into 10 equal parts and so the eigenvalues were calculated 11 times at equal spacing. Region 2 shows the phonon dispersion from the a point with wave vector $\mathbf{q} = [0, 1, 1]$ which due to lattice symmetries in the zinc blende crystal has the same properties as the X-point. This dispersion

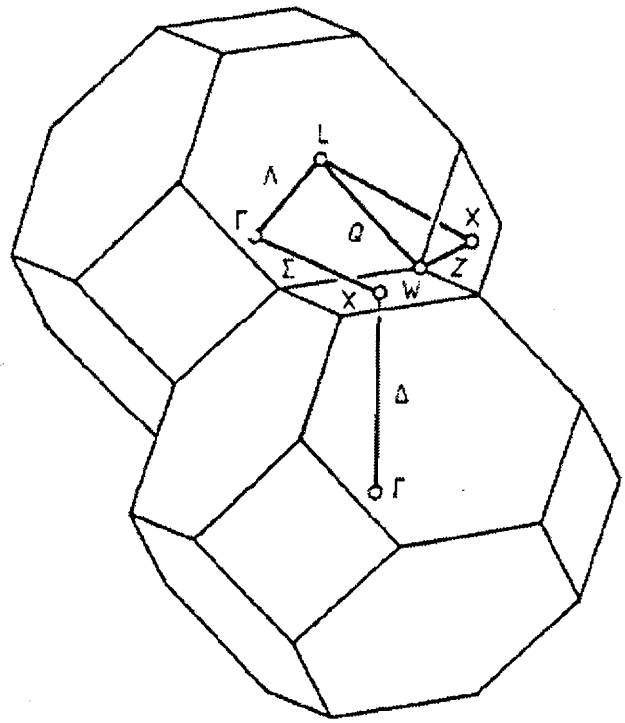

Figure 5.3: Two neighbouring Brillouin Zones for a zinc blende crystal and commonly considered points of high symmetry, copied from Strauch

is plotted back to the central Γ-point at wave vector $\mathbf{q} = [0, 0, 0]$ and is again graphed over 11 points to split the region into 10 equal spacings. Region 3 of the phonon dispersion curves shows the BZ Γ-point phonons plotted to another high symmetry BZ point at the wave vector $\mathbf{q} = [{}^1/_2, {}^1/_2, {}^1/_2]$ which is labelled the L-point. Again this phonon dispersion was graphed over 11 points, splitting the region into 10 parts.

The plots shown in the results section are produced by a piece of commercial software called *Origin* and the lines representing the phonon dispersions have been subject to an automated spline fitting routine.

The mode-Grüneisen parameters

Calculation of the mode-Grüneisen parameters depends directly upon the calculation of the phonon frequencies which is shown in Eq 2.15. There are 6 mode-Grüneisen parameters, corresponding to each of the phonon values, for each point in the phonon dispersion spectra we are interested in. As with the phonons we have chosen the BZ high-symmetry points Γ, X and L for the calculations. Practically the mode-Grüneisen parameters are calculated using a simple Euler

derivative approximation as follows:

The atomic lattice in memory is copied twice for each BZ point of interest and are labelled m_- and m_+. An amount of hydrostatic strain, h, is chosen and then m_- has the uniform Affine transform scaling vector $\hat{S} = [-h, -h, -h]$ applied to it and m_+ has the uniform Affine transform scaling vector $\hat{S} = [h, h, h]$ applied before the lattices are then sent to the *calcPhonons* routine with the appropriate wave vector which then performs the building and diagonalising of the D-matrix operations listed above. h is typically 1%. This produces a set of phonon frequencies for the hydrostatically transformed lattices ω_- and ω_+.

A common divisor d is calculated form the hydrostatic strain using the following operation

$$d = \log\left(\frac{[a(1+h)]^3}{[a(1-h)]^3}\right)$$

and the mode-Grüneisen parameters are found from the simple calculation

$$\gamma = \frac{-\log\left(\frac{\omega_+}{\omega_-}\right)}{d}$$

As can be clearly seen from the above equations the mode-Grüneisen parameters provide a measure of the anisotropy of the potential by predicting the dependence of the phonons on hydrostatic strain.

Computing the dynamical properties numerically

As mentioned earlier the analytic derivatives were checked against a simple second order Euler central differences approximation during the debugging process of the program. It is interesting to consider both the level of compound errors introduced into the final D-matrix and the timing involved in the computation of the second derivatives numerically.

The total process described above to calculate the phonon dispersion curves (a total of 33 phonon frequency calculations) and the mode-Grüneisen parameters at the three points of high symmetry (another 6 phonon frequency calculations) for the two atoms in the central Bravais lattice in the simulation takes 0.04 seconds on the laptop computing platform.

To perform the same number of operations by calculating the derivatives in three dimensions numerically using a standard second-order central differences routine takes 3.82 seconds. This demonstrates that it requires nearly 100 times more computational power to perform the simulation numerically.

Calculating the parameters numerically using 0.00001 Å for dx, dy and dz in

the central differences routine produced compound errors due to the summation of a great number of terms in the building of the force constants matrix. This is demonstrated with the Tersoff (T3) silicon parameters [3] below in table 5.7 which shows the experimentally measured values of the phonon frequencies against the analytic calculations and the numerical central differences calculations.

Phonon (THz)	Exp.	Tersoff Analytic	Tersoff Numerical
$\omega_{LTA}(\Gamma)$	0.0	0.0	1.10251
$\omega_{LTO}(\Gamma)$	15.5	16.0683	16.0002
$\omega_{TA}(X)$	4.5	6.89672	6.48499
$\omega_{LAO}(X)$	12.3	12.1921	11.7386
$\omega_{TO}(X)$	13.9	14.8908	14.8252
$\omega_{TA}(L)$	3.45	4.66893	4.72781
$\omega_{LA}(L)$	11.3	11.3122	10.2703
$\omega_{LO}(L)$	12.6	13.1545	12.7378
$\omega_{TO}(L)$	14.7	15.4265	15.2812

Table 5.7: The Tersoff phonon frequencies of silicon from analytic and numerical computation methods

Figures 5.4 and 5.5 show the phonon dispersion curves produced from the analytic and numerical methods respectively. The most obvious problem is that as the phonon frequencies go to zero at the Γ point, the numerical derivatives cannot predict a zero result as this would introduce divide-by-zero faults in the code and the machine tolerance would tend towards the hardware limit. Also there is an obvious splitting of the phonon branches in the wrong place due to compound errors being introduced and magnified by large scale summations. The experimental data are shown on the plots with open circle markers at the zone boundaries for comparison.

This data has demonstrated a clear need to calculate the second order partial derivatives analytically as provided in Appendix A.

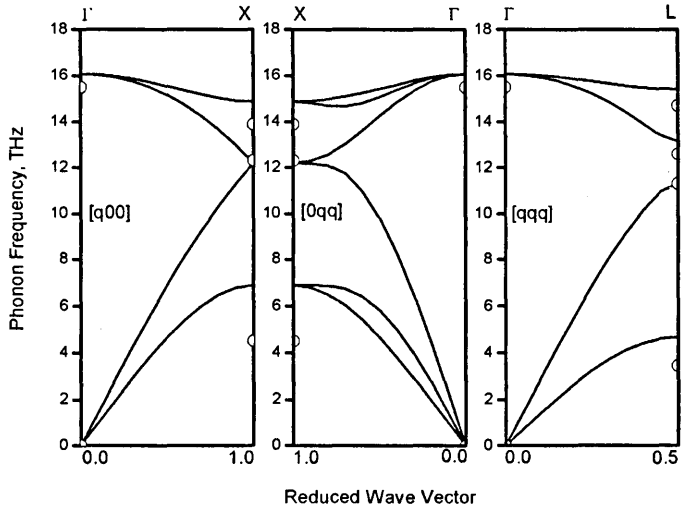

Figure 5.4: The silicon phonon dispersion predicted by the Tersoff (T3) parameters and the analytic derivatives code

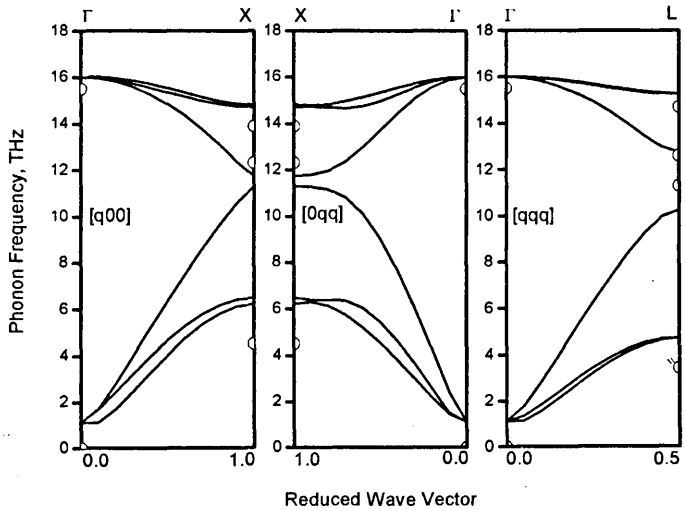

Figure 5.5: The silicon phonon dispersion curves characterised by the Tersoff (T3) parameters and the numerical derivatives code

5.2 Results

All of the results provided below (with the exception of the second set of silicon parameters) were calculated using the analytic derivatives code and the method presented above. All of the results are based upon the Tersoff potential parameters tabulated in the previous section on elastic property modelling. The average time required for the laptop computing platform to produce the numerical data for the phonon frequencies and mode-Grüneisen parameters and a phonon dispersion curve was 0.038 seconds.

The resultant data is compared, wherever possible, to experimentally measured results. The principle technique used in the cited papers for the measurement of phonon frequencies and the associated mode-Grüneisen parameters is Raman spectroscopy. Raman spectroscopy is a spectroscopic technique used in condensed matter physics and chemistry to study vibrational, rotational, and other low-frequency modes in a system. It relies on inelastic scattering, or Raman scattering of monochromatic light, usually from a laser in the visible, near infrared, or near ultraviolet range. Phonons or other excitations in the system are absorbed or emitted by the laser light, resulting in the energy of the laser photons being shifted up or down. The shift in energy gives information about the phonon modes in the system. Infrared spectroscopy yields similar, but complementary information. Typically, a sample is illuminated with a laser beam. Light from the illuminated spot is collected with a lens and sent through a monochromator. Wavelengths close to the laser line (due to elastic Rayleigh scattering) are filtered out and those in a certain spectral window away from the laser line are dispersed onto a detector. More information about Raman spectroscopy can be found in references [4, 5].

5.2.1 Silicon

Here we compare the phonon dispersion curves and mode-Grüneisen parameters from the literature with the values calculated for the Tersoff (T3) parameters and the improved Powell parameters provided in the elastic property modelling chapter. Table 5.8 shows the phonon frequencies and table 5.9 contains the mode-Grüneisen parameters for silicon.

With the exception of $\omega_{LO}(L)$ all of the Powell phonon frequencies are in greater error than the phonon frequencies predicted using the Tersoff parameters, which have an order of +5% error. It is not immediately obvious why this effect

[1] See [6, 7]

Phonon (THz)	Experiment[1]	Tersoff (T3)	Powell (P1)
$\omega_{LTO}(\Gamma)$	15.5	16.07	17.81
$\omega_{TA}(X)$	4.5	6.90	8.08
$\omega_{LAO}(X)$	12.3	12.19	13.31
$\omega_{TO}(X)$	13.9	14.89	15.18
$\omega_{TA}(L)$	3.45	4.67	5.60
$\omega_{LA}(L)$	11.3	11.31	12.90
$\omega_{LO}(L)$	12.6	13.15	13.14
$\omega_{TO}(L)$	14.7	15.43	16.51

Table 5.8: The phonon frequencies of Si

has occured. The $\omega_{LTO}(\Gamma)$ phonon energy is commonly used as a benchmark figure when describing the quality of phonon data and as can be clearly seen from the above table it is 15% too high. The reasons for this will be discussed fully in the results section of this chapter. The mode-Grüneisen parameters presented by the Tersoff parameterisation are further away from the measured values than the Powell parameters, except the Tersoff predictions for the γ_{TA} values at the X-point and L-point in the Brilluin Zone. Here the Tersoff (T3) silicon parameters manage to replicate the negative values correctly whereas the Powell parameters do not. As the mode-Grüneisen parameters are a measure of the change in phonon energies when the system is subject to a hydrostatic strain this is indicates that the current parameters cannot model the phonon dispersion correctly for strained semiconductor systems. This will be explored fully in the results section.

Grüneisen Param	Experiment	Tersoff (T3)	Powell (P1)
$\gamma_{LTO}(\Gamma)$	0.98[2]	1.32	1.25
$\gamma_{TA}(X)$	-1.4	-0.20	0.12
$\gamma_{LAO}(X)$	0.9	1.27	1.22
$\gamma_{TO}(X)$	1.5	1.60	1.58
$\gamma_{TA}(L)$	-1.3[4]	-0.31	0.08
$\gamma_{LA}(L)$		0.72	0.91
$\gamma_{LO}(L)$		1.65	1.52
$\gamma_{TO}(L)$	1.3	1.46	1.39

Table 5.9: The mode-Grüneisen parameters of Si

Figure 5.6 shows the phonon frequencies of silicon measured experimentally, copied from Dolling[6]. Figure 5.7 shows the phonon frequencies calculated analytically from the Tersoff (T3) parameters and figure 5.8 shows the new Powell (P1) parameterisation of silicon which was fit to the elastic properties from the previous section. Both of these graphs use open circle markers at the zone boundaries to represent the experimentally measured values from table 5.8.

The Tersoff (T3) phonon dispersion plot shows that although the reproduction of the shape of the phonon branches looks reasonably accurate there is a less

[2]from Porter *et al*[8]
[4]See [9]

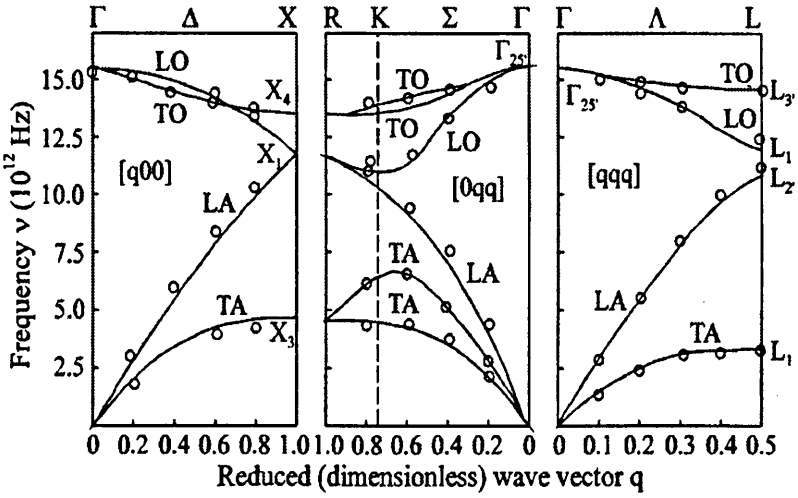

Figure 5.6: The experimentally measured phonon dispersion of silicon

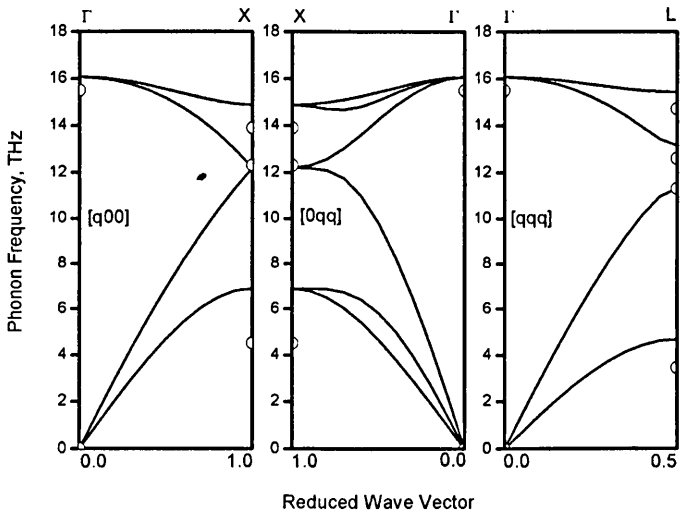

Figure 5.7: The silicon phonon dispersion predicted by the Tersoff (T3) parameters

defined effect in the TA branch splitting and the dip in the LO branch appears to have a smaller magnitude than was experimentally measured in the [0qq] region of the plot. The Tersoff parameters fail to reproduce the TA branch magnitude at the X and L-point boundaries.

The Powell parameter phonon dispersion for silicon appears similar to the Tersoff (T3) parameters phonon dispersion. There is a higher level of energy in the optical branch phonons as described in the table of results and the TA branch splitting is of a decreased magnitude as with the Tersoff results. The Powell parameterisation also fails to reproduce the magnitude of the TA branch phonons correctly.

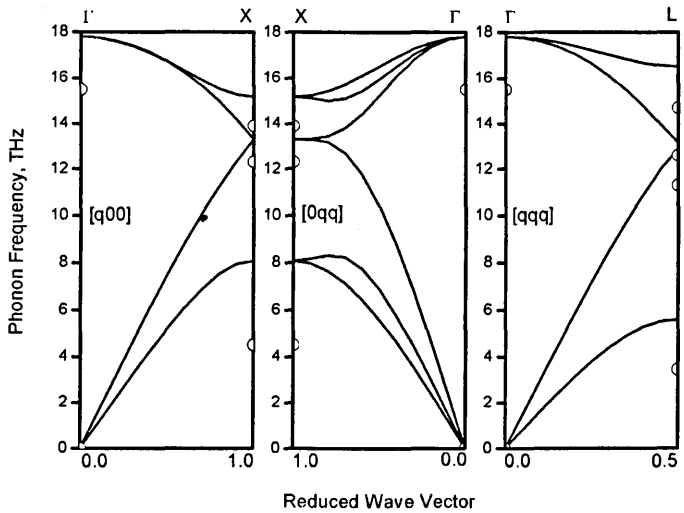

Figure 5.8: The silicon phonon dispersion curves predicted by the Powell (P1) parameters

5.2.2 Diamond Carbon

Here the phonon frequencies and the mode-Grüneisen parameters predicted by the Tersoff parameterisation of diamond carbon[3] are compared to the Powell parameters found in the previous chapter by fitting to the elastic properties. Table 5.10 contains the phonon frequencies and table 5.11 contains the mode-Grüneisen parameters.

Phonon (THz)	Experiment[3]	Tersoff (T3)	Powell
$\omega_{LTO}(\Gamma)$	39.9	47.11	47.75
$\omega_{TA}(X)$	24.2	30.17	28.17
$\omega_{LAO}(X)$	35.5	37.64	38.72
$\omega_{TO}(X)$	32.1	39.05	39.25
$\omega_{TA}(L)$	16.9	21.11	20.32
$\omega_{LA}(L)$	30.2	34.14	34.55
$\omega_{LO}(L)$	37.6	42.05	40.35
$\omega_{TO}(L)$	36.2	42.53	43.66

Table 5.10: The phonon frequencies of diamond carbon

It is clear from the table of phonon frequencies that the Tersoff parameters have up to a +18% error in the phonon frequencies in the case of the LTO phonon energy. The LTO phonon is so called as the LO and TO branches meet at the same frequency in the dispersion. The Powell parameters have not performed much better than the Tersoff parameters but there is a slight improvement in the accuracy of the prediction of the TA(X), TA(L)and LO(L) frequencies.

Grüneisen Param	Experiment[4]	Tersoff (T3)	Powell
$\gamma_{LTO}(\Gamma)$	0.98	1.13	1.16
$\gamma_{TA}(X)$	0.4	0.47	0.32
$\gamma_{LAO}(X)$		1.46	1.52
$\gamma_{TO}(X)$	2.0	1.04	1.06
$\gamma_{TA}(L)$		0.47	0.34
$\gamma_{LA}(L)$		1.47	1.56
$\gamma_{LO}(L)$		0.82	0.69
$\gamma_{TO}(L)$	1.4	1.19	1.30

Table 5.11: The mode-Grüneisen parameters of diamond carbon

The table of mode-Grüneisen parameters shows, for the few experimentally measured values, that both the Tersoff and Powell predictions for the Γ value have about a 16% error. The TO(X) mode-Grüneisen parameters are both about half of the value they should be but the Powell parameterisation has more success than the Tersoff parameters in predicting the TO(L) mode-Grüneisen parameter.

Figure 5.9 shows the experimental phonon values of diamond carbon, measured from the Oppenheimer diamond by Solin and Ramdas[10]. The central

[3]See [10]

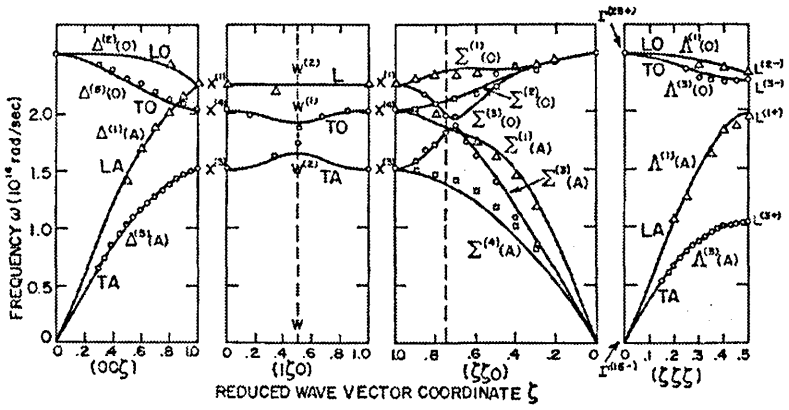

Figure 5.9: The phonon dispersion of diamond carbon measured experimentally, copied from Solin

[1ζ0] panel should be ignored as that part of the phonon dispersion is not related to this work. Figure 5.10 shows phonon energies plotted for the Tersoff (T3) diamond carbon parameters and figure 5.11 shows the phonon dispersion as predicted by the Powell parameters fitted to the elastic constants. As can be clearly seen both the Tersoff and Powell dispersions fail to replicate the high levels of phonon splitting away from the zone boundaries in the degenerate transverse branches. It is evident that both sets of parameters have overestimated the optical mode phonon frequencies and the LA branch phonon frequencies at the X points. The separation between the L point optical branches is correctly more pronounced in the Powell parameters than in the Tersoff parameters.

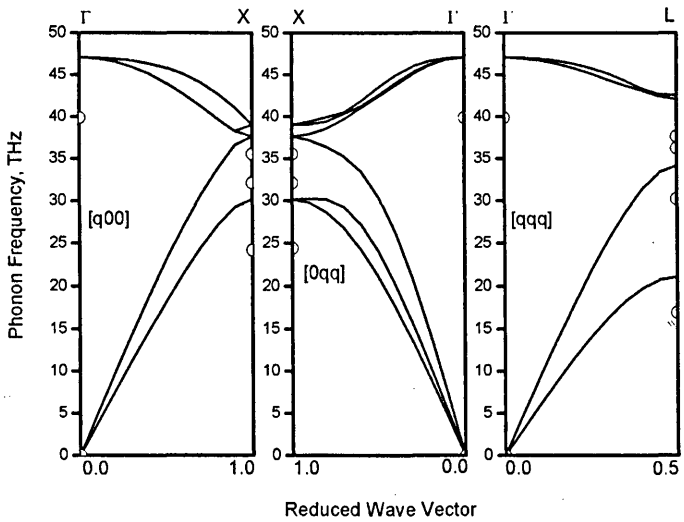

Figure 5.10: The phonon dispersion curves of diamond carbon characterised by the Tersoff (T3) parameters

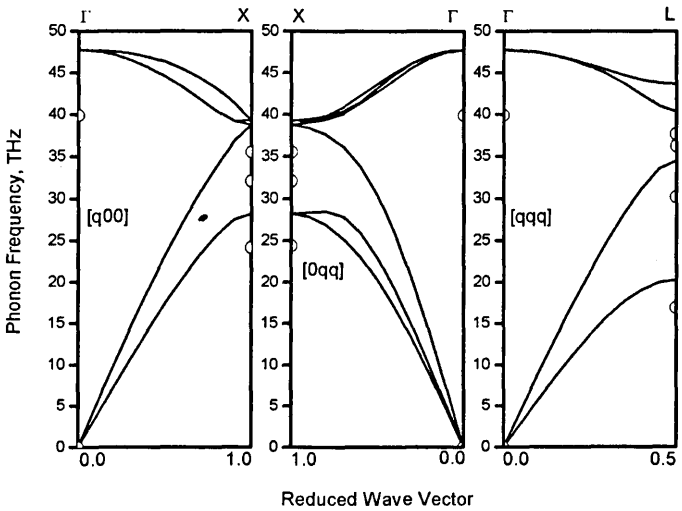

Figure 5.11: The diamond carbon phonon dispersion predicted by the Powell parameters

5.2.3 Germanium

Here the phonon frequencies and the mode-Grüneisen parameters predicted by the Tersoff[3] parameters for diamond lattice germanium are compared to the work in the previous chapter where a parameterisation was formed based upon fitting to the elastic properties of the material. Table 5.12 contains the experimental measurements compared to the two parameterisations and it is clear that in all cases the Powell parameters perform better then the Tersoff parameters. The largest error in the Powell parameters is 93% for the TA(X) phonon and the smallest error is less than 1% in the predicted LO(L) branch phonon. The closest Tersoff prediction is in the LO(L) branch phonon which is 1% in error.

Phonon (THz)	Experiment[5]	Tersoff (T3)	Powell
$\omega_{LTO}(\Gamma)$	9.02	9.89	9.59
$\omega_{TA}(X)$	2.385	4.68	4.61
$\omega_{LAO}(X)$	7.14	7.57	7.33
$\omega_{TO}(X)$	8.17	8.43	8.31
$\omega_{TA}(L)$	1.87	3.33	3.19
$\omega_{LA}(L)$	6.63	7.32	7.16
$\omega_{LO}(L)$	7.27	7.35	7.29
$\omega_{TO}(L)$	8.55	9.20	8.95

Table 5.12: The phonon frequencies of germanium

Table 5.13 shows the predicted mode-Grüneisen parameters against the experimental data. Only 2 points were available in the literature for germanium and both points were difficult to predict using the parameterisations available. The Tersoff parameters show a 15% and 59% error in the LTO(Γ) and TO(L) respectively while the errors predicted with the Powell parameters are 16% and 60% respectively.

Grüneisen Param	Experiment[4]	Tersoff (T3)	Powell
$\gamma_{LTO}(\Gamma)$	1.12	1.30	1.30
$\gamma_{TA}(X)$		0.21	0.21
$\gamma_{LAO}(X)$		1.25	1.25
$\gamma_{TO}(X)$		1.63	1.62
$\gamma_{TA}(L)$		0.22	0.17
$\gamma_{LA}(L)$		1.21	0.96
$\gamma_{LO}(L)$		1.30	1.53
$\gamma_{TO}(L)$	0.9	1.43	1.44

Table 5.13: The mode-Grüneisen parameters of germanium

Figure 5.12 shows the phonon dispersion plotted by Nilsson and Nelin[11]. Figure 5.13 shows the phonon dispersion predicted from the Tersoff (T3) parameters. It is clear that although the shape of the dispersion is roughly correct the Tersoff parameters cannot predict the optical branch phonon frequencies at the

[5] See [11]

X and L zone boundaries. Figure 5.14 shows the phonon dispersion as predicted by the Powell parameterisation. Here we can see that although the transverse acoustic branch phonons are too high, the rest of the dispersion appears to have the correct shape compared to the experimental data. Again, neither parameterisation could correctly reproduce the magnitude of the transverse branch splitting that is evident in the experimental data.

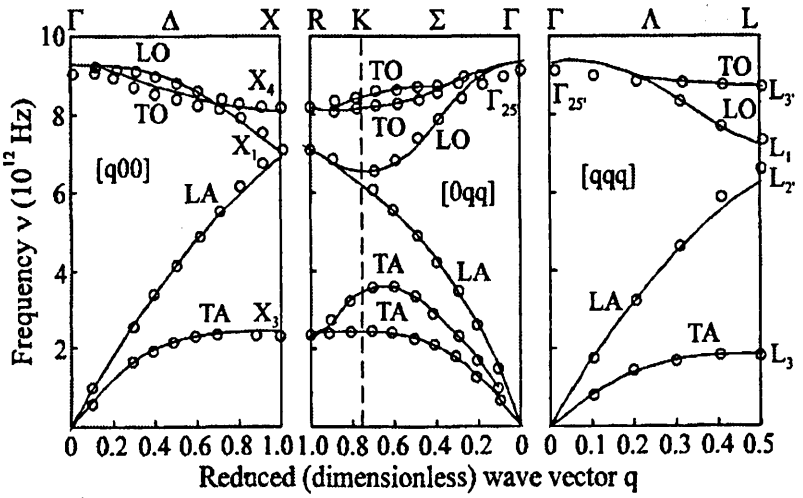

Figure 5.12: The phonon dispersion of germanium measured experimentally, copied from Nilsson and Nelin

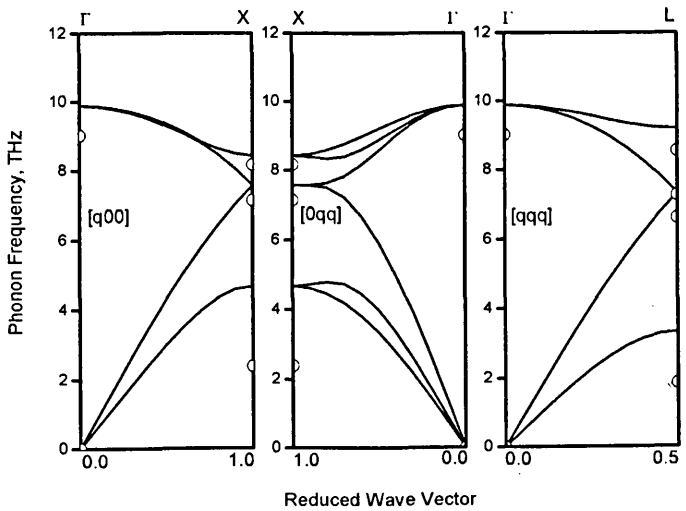

Figure 5.13: The phonon frequencies of germanium predicted by the Tersoff (T3) parameters

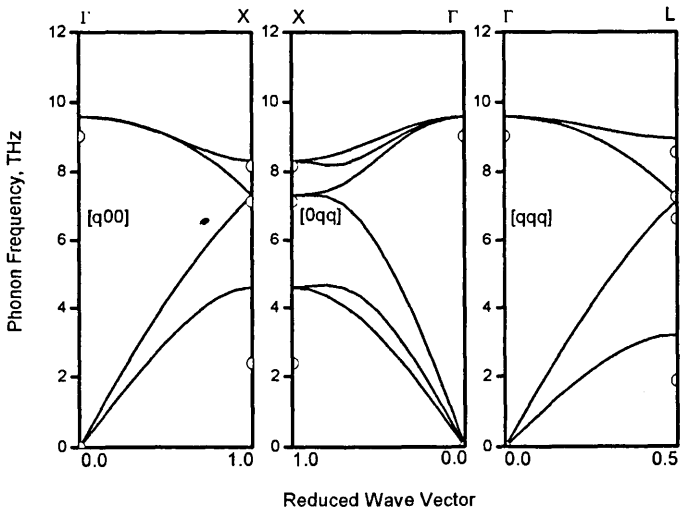

Figure 5.14: The germanium phonon dispersion characterised by the Powell parameters

5.2.4 Gallium Arsenide

Here we compare the phonon frequency predictions given by the Smith[12] and Sayed *et al*[13] parameters to the re-parameterisation of Gallium Arsenide found in the previous chapter fitted to the elastic properties. As can be seen in table 5.14, none of the parameterisations have managed to correctly predict the splitting of the optical branch phonons at the BZ centre. Although the phonon energies for Smith appear, on average, to be closer to the experimental values - the prediction shows that the transverse acoustic branch has zero frequency over the whole dispersion, which is incorrect. The Sayed and Powell parameters both predict TA branch phonons at the points of high symmetry to have twice as much energy as measured experimentally, but the Sayed parameters show reasonable agreement in the LO branch phonons at the X and L-points in the BZ. The lack of splitting between the Γ-point LO and TO branches is very obvious upon a first inspection of the data. This is clearly expected in an ionic zinc blende crystal and is not available using the current method of modelling due to the lack of consideration of the ionicity of the crystal. This will be explored further in the discussion section.

Phonon (THz)	Exp.[11]	DFT[7]	Smith	Sayed	Powell
$\omega_{LO}(\Gamma)$	8.55	8.68	8.74	9.41	9.85
$\omega_{TO}(\Gamma)$	8.02	8.11	8.74	9.41	9.85
$\omega_{TA}(X)$	2.36		0.03	4.60	4.57
$\omega_{LA}(X)$	6.80		6.07	6.97	7.21
$\omega_{LO}(X)$	7.22		6.29	7.23	7.47
$\omega_{TO}(X)$	7.56		8.74	8.29	8.43
$\omega_{TA}(L)$	1.86		0.02	3.03	3.10
$\omega_{LA}(L)$	6.26		4.37	7.04	7.13
$\omega_{LO}(L)$	7.15		7.57	7.38	7.42
$\omega_{TO}(L)$	7.84		8.74	8.79	9.12

Table 5.14: The phonon frequencies of gallium arsenide

A comparison with the few available mode-Grüneisen parameters are available in table 5.15 and it is evident that none of the parameterisations available can predict the negative value for the TA(X) mode-Grüneisen parameter. However, the TO(X) mode-Grüneisen parameter is predicted well by both the Smith and Sayed parameters and improved upon to a tolerance of 3% by the Powell parameters.

Figure 5.15 shows an experimentally measured GaAs phonon dispersion by Waugh and Dolling[14] which may be directly compared to the phonon dispersion plots given in figures 5.16, 5.17 and 5.18 which show the predicted dispersions by the parameters from Smith, Sayed and Powell respectively. The effect of

[11] See [14]
[7] In [15]
[12] See [16]

Grüneisen Param	Exp.[12]	DFT[7]	Smith	Sayed	Powell
$\gamma_{LO}(\Gamma)$	1.23	0.99	1.57	1.47	1.42
$\gamma_{TO}(\Gamma)$	0.9	1.09	1.57	1.47	1.42
$\gamma_{TA}(X)$	-1.62		1.13	0.19	0.19
$\gamma_{LA}(X)$			1.57	1.40	1.37
$\gamma_{LO}(X)$			1.57	1.40	1.37
$\gamma_{TO}(X)$	1.73		1.82	1.82	1.78
$\gamma_{TA}(L)$			1.13	0.06	0.11
$\gamma_{LA}(L)$			0.57	1.08	1.22
$\gamma_{LO}(L)$			1.91	1.65	1.51
$\gamma_{TO}(L)$			1.70	1.63	1.58

Table 5.15: The mode-Grüneisen parameters of GaAs

predicting the TA branch phonons as zero by Smith is immediately obvious as is the lack of curvature in the TO branch phonons. The elastic properties predicted by the Smith parameters have the same values for c_{11} and c_{12} which in turn lead to $B = c_{11}$ and $C' = c_{44} = 0$. Smith is the only author to have predicted zero for the shear elastic properties which is provided by a very small c/d ratio in his parameterisation, effectively removing the angular bonding term $g(\theta_{jik})$ from the Tersoff equations. The Sayed parameters predict the longitudinal branch phonons quite well but the TA and TO branch phonons all have values that are too high compared to the experimental data, which is shown at the zone boundaries by open circle markers. The optical branches of the Powell parameters have a greater error than the Sayed parameters and neither dispersion can correctly reproduce the transverse branch splitting observed in the experimental dispersion in the centre of the [0qq] plots. It should be noted that none of the parameterisations can reproduce the energy gap between the optical branch phonons at the BZ centre and the crossing of the optical branch frequencies observed in the experimental plot in the centre of the [q00] region.

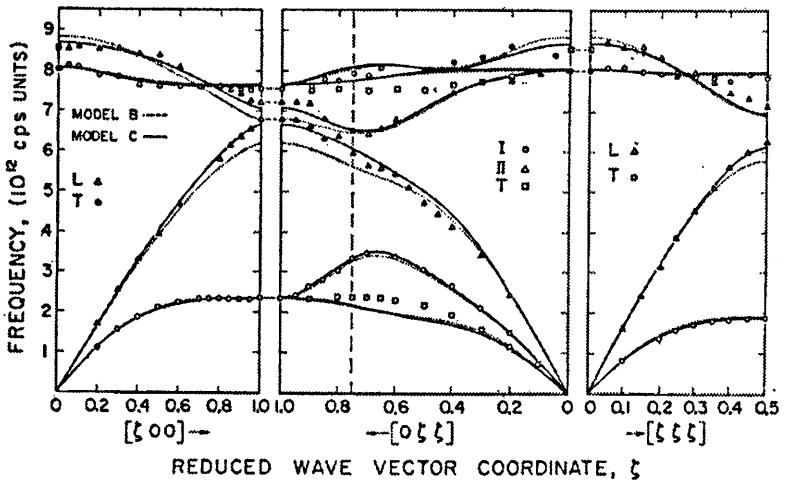

Figure 5.15: The phonon dispersion of gallium arsenide measured experimentally, copied from Waugh and Dolling

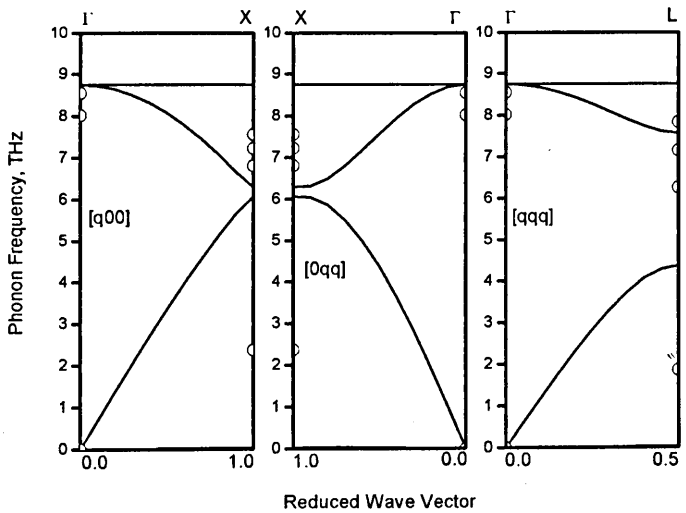

Figure 5.16: The GaAs phonon frequencies predicted by the Smith parameters

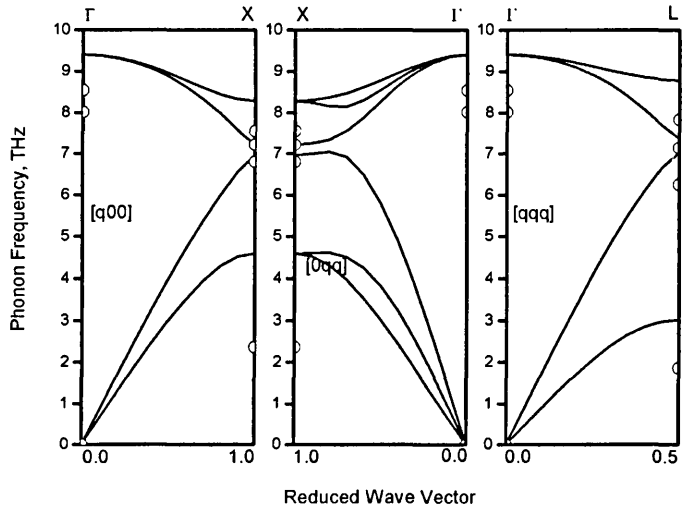

Figure 5.17: The phonon dispersion characterised by the Sayed parameters

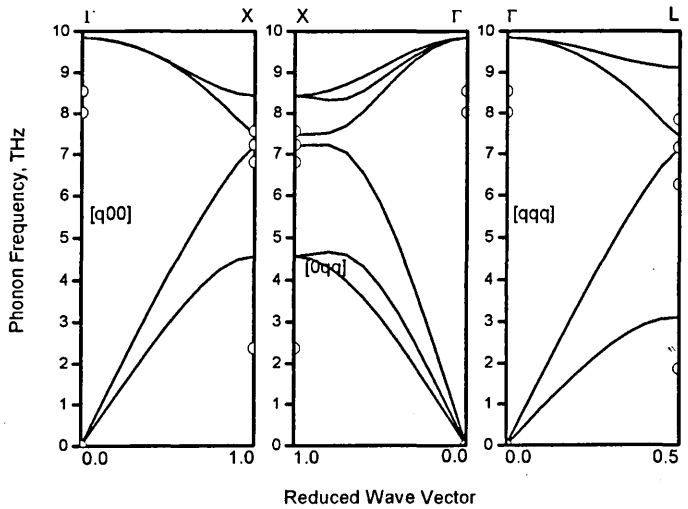

Figure 5.18: The phonon dispersion predicted by the Powell parameters

5.2.5 Indium Arsenide

The parameters presented by Ashu *et al*[17], Nordlund *et al*[18], Migliorato *et al*[19, 20] and the Powell (P1) parameters from the previous chapter are compared to experimental measurements for the phonon frequencies in table 5.16. Here we can see that there is no difference in the optical branch Γ-point phonon frequencies for any of the parameterisations and that all of the values are predicting phonon frequencies that are too high. Again, we can clearly note that all parameterisations are predicting transverse acoustic branch phonons that are too high at the X and L-points and that the Powell parameters produce values for the optical branch phonons that are too high when correctly fitted to the elastic properties.

Phonon (THz)	Exp.[8]	DFT[7]	Ashu	Nordlund	Migliorato	Powell
$\omega_{LO}(\Gamma)$	7.01	7.13	7.89	7.49	7.44	7.89
$\omega_{TO}(\Gamma)$	6.44	6.56	7.89	7.49	7.44	7.89
$\omega_{TA}(X)$	1.70		3.32	3.04	3.11	3.30
$\omega_{LA}(X)$	4.94		5.22	4.95	4.93	5.21
$\omega_{LO}(X)$	6.20		6.46	6.13	6.10	6.45
$\omega_{TO}(X)$	6.47		7.19	6.84	6.80	7.06
$\omega_{TA}(L)$	1.50		2.21	2.04	2.07	2.24
$\omega_{LA}(L)$	4.46		5.18	4.85	4.88	5.14
$\omega_{LO}(L)$	6.26		6.61	6.25	6.25	6.49
$\omega_{TO}(L)$	6.44		7.49	7.14	7.08	7.45

Table 5.16: The phonon frequencies of InAs

Table 5.17 shows the performance of the various parameterisations against the few measured and DFT predicted values of the mode-Grüneisen parameters. It can be seen that all of the parameterisations predict values for the Γ-point that are too high by about 50%. Furthermore, the other three parameterisations predict values for the TA(X) value that are negative and the Powell parameters are positive, but with no further information in the available literature it is difficult to say which value this should be.

Figure 5.19 shows a copy of the experimental phonon dispersion of InAs as measured by Carles *et al*[22]. Figures 5.20 and 5.21 show the Ashu and Nordlund phonon dispersion curves. Figures 5.22 and 5.23 show the Migliorato and Powell phonon dispersion graphics. It is obvious from all of these these graphs that none of the parameterisation can correctly reproduce the different phonon frequencies at the Γ point in the dispersion. Furthermore, there is no optical band crossing in evidence as there is in the [q00] portion of the experimental dispersion. All of the parameterisations fail to reproduce the magnitude of the transverse branch

[8] See [21, 9]
[7] In [15]

Grüneisen Param	Exp.[12]	DFT[7]	Smith	Sayed	Migliorato	Powell
$\gamma_{LO}(\Gamma)$		1.06	1.43	1.38	1.47	1.49
$\gamma_{TO}(\Gamma)$	0.85	1.16	1.43	1.38	1.47	1.49
$\gamma_{TA}(X)$			-0.04	-0.23	-0.05	0.04
$\gamma_{LA}(X)$			1.38	1.32	1.41	1.44
$\gamma_{LO}(X)$			1.38	1.32	1.41	1.44
$\gamma_{TO}(X)$			1.72	1.67	1.75	1.79
$\gamma_{TA}(L)$			-0.23	-0.39	-0.24	-0.09
$\gamma_{LA}(L)$			1.07	0.97	1.09	1.18
$\gamma_{LO}(L)$			1.55	1.52	1.59	1.59
$\gamma_{TO}(L)$			1.57	1.52	1.61	1.63

Table 5.17: The mode-Grüneisen parameters of indium arsenide

splitting in the [0qq] region of the graph and all of the dispersion show enlarged values of the TA branch phonons. The most accurate parameterisations are the Nordlund and Migliorato parameters which were fit to the experimental value of C'. The DFT prediction of C' and c_{44} was used for the parameterisation of the Powell parameters which predict higher optical phonon frequencies than the Migliorato and Nordlund parameters.

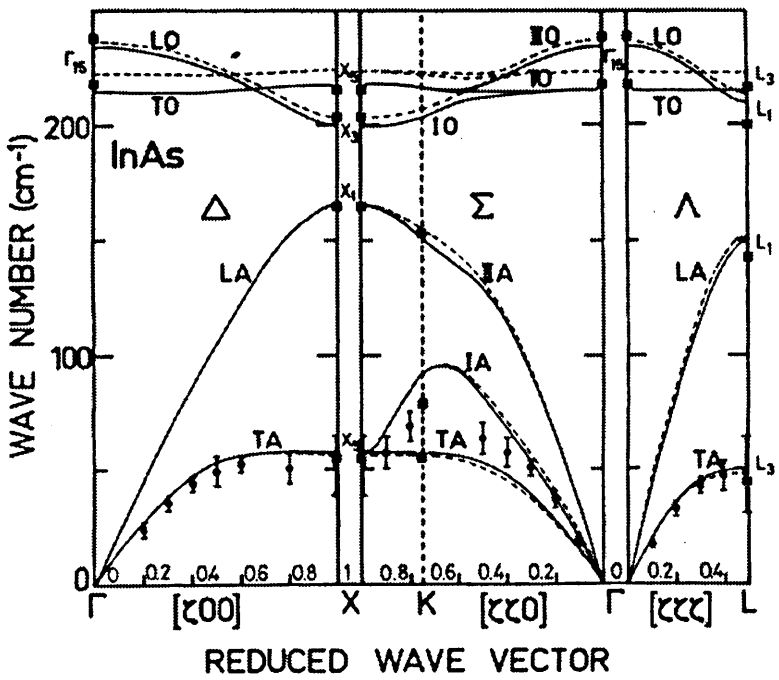

Figure 5.19: The phonon dispersion of indium arsenide measured experimentally, copied from Carles *et al*

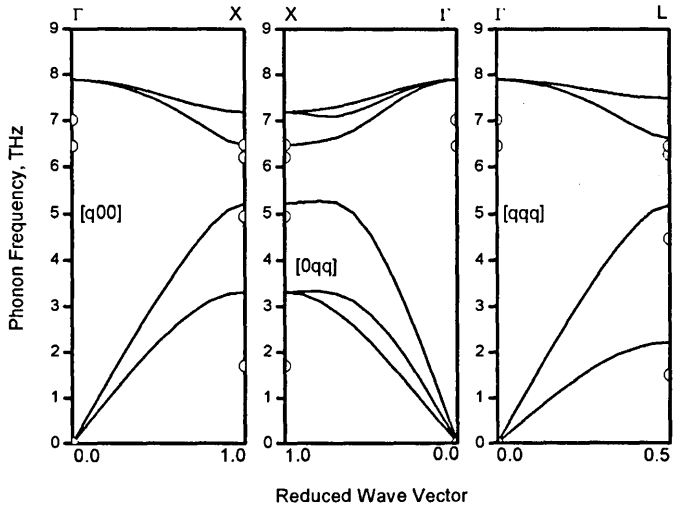

Figure 5.20: The phonon frequencies predicted by the Ashu parameters

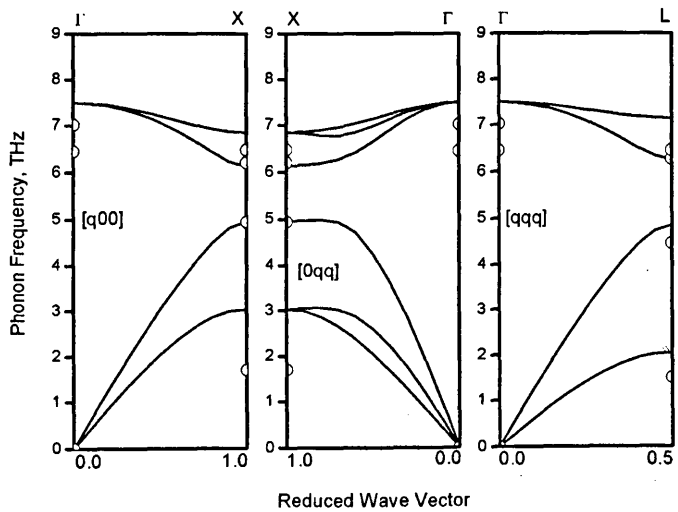

Figure 5.21: The phonon dispersion predicted by the Nordlund parameters

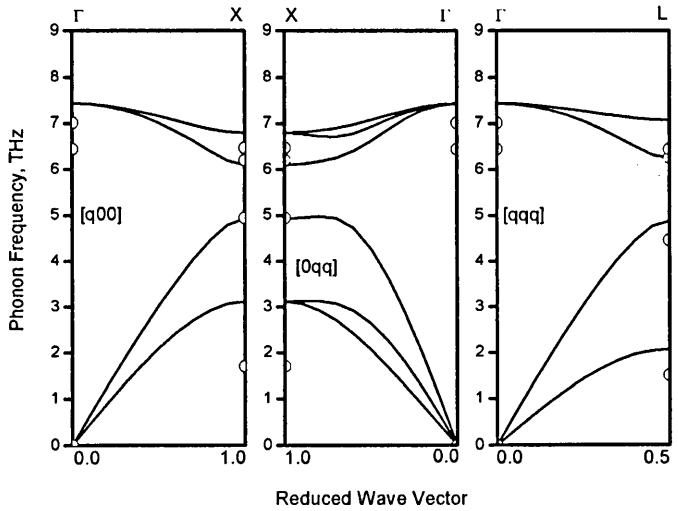

Figure 5.22: The phonon dispersion characterised by the Migliorato parameters

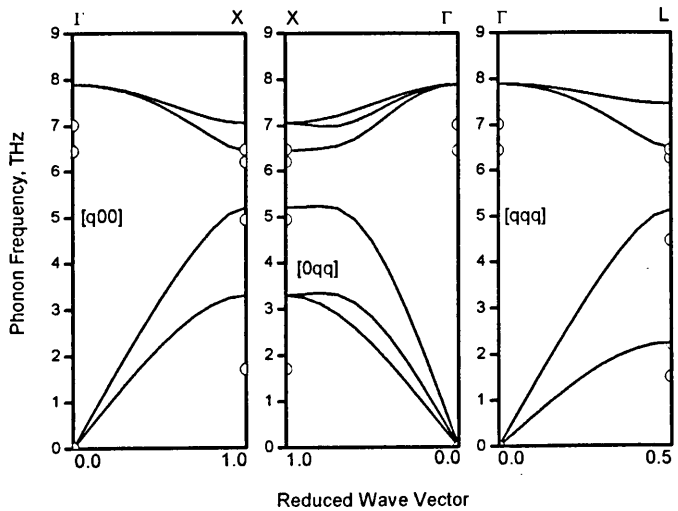

Figure 5.23: The phonon dispersion predicted by the Powell parameters

5.2.6 Gallium Phosphide

Table 5.18 compares the phonon frequencies taken from a number of experimental sources and the DFT predicted values to the parameterisation found in the previous chapter for zinc blende gallium phosphide. The prediction from the parameters shows reasonable agreement with the phonon energies but fails to reproduce either of the experimentally measured frequencies of the TA(X) phonon. The model based upon the Tersoff PEF used in this study again appears to have difficulty in predicting that the LO and TO Γ-point phonons which experimentally do not converge at the zone boundary. Table 5.19 shows the predicted mode-Grüneisen parameters against the experimental and DFT predicted values. Here we can see that negative transverse acoustic branch phonons are incorrectly predicted as positive values, but the TO parameters seem to be in reasonable agreement.

Phonon (THz)	Experiment[6]	DFT[7]	Powell
$\omega_{LO}(\Gamma)$	12.11	13.60	13.93
$\omega_{TO}(\Gamma)$	10.97	12.77	13.93
$\omega_{TA}(X)$	1.91, 3.16		5.73
$\omega_{LA}(X)$	6.35, 7.65		8.11
$\omega_{LO}(X)$	11.72, 11.30		12.17
$\omega_{TO}(X)$	11.03, 10.96		12.24
$\omega_{TA}(L)$	3.08		3.96
$\omega_{LA}(L)$	5.15		8.03
$\omega_{LO}(L)$	11.36		12.05
$\omega_{TO}(L)$	10.73		13.02

Table 5.18: The phonon frequencies of gallium phosphide

Grüneisen Param	Experiment[8]	DFT[6]	Powell
$\gamma_{LO}(\Gamma)$	0.95	0.95	1.41
$\gamma_{TO}(\Gamma)$	1.09	1.10	1.41
$\gamma_{TA}(X)$	-0.72		0.28
$\gamma_{LA}(X)$			1.37
$\gamma_{LO}(X)$			1.44
$\gamma_{TO}(X)$	1.31		1.60
$\gamma_{TA}(L)$	-0.81		0.13
$\gamma_{LA}(L)$			1.34
$\gamma_{LO}(L)$			1.39
$\gamma_{TO}(L)$	1.50		1.55

Table 5.19: The mode-Grüneisen parameters of GaP

Figure 5.24 shows the experimentally measure phonon dispersion for GaP by Borcherds *et al*[26]. The second panel should be ignored as that part of the phonon dispersion is not included in this study. Figure 5.25 shows the phonon dispersion predicted by the Powell parameters. Although the predicted phonon values at the

[6] See [23, 24, 25]
[7] In [15]

zone boundaries are too high, the general shape of the dispersion shows promise. The parameters have again failed to reproduce the magnitude of the transverse branch splitting away form the points of high symmetry in the Brillouin Zone.

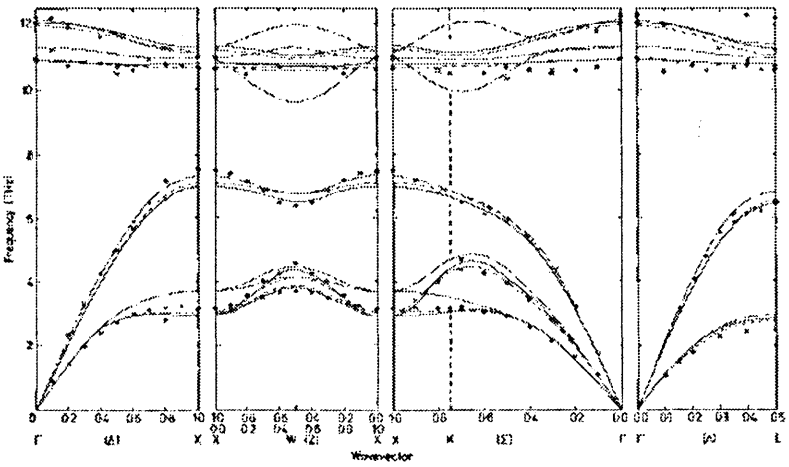

Figure 5.24: The phonon dispersion of gallium phosphide measured experimentally, copied from Borcherds *et al*

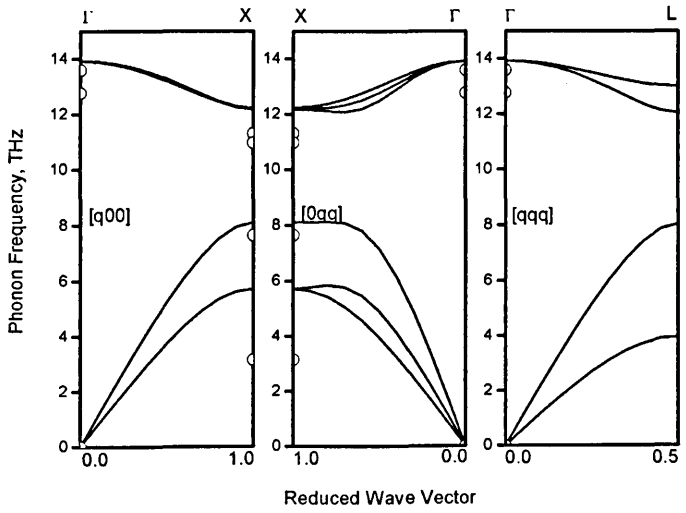

Figure 5.25: The phonon dispersion predicted by the Powell parameters

5.2.7 Indium Phosphide

Here we show the predicted values of the phonon frequencies and the mode-Grüneisen parameters for indium phosphide based upon the Powell parameters that were fit to the values of the elastic properties. Table 5.20 contains the experimental values of the phonons and a couple of DFT predictions for comparison. Once again there is no evidence of a split in the energy levels of the optical branch phonons at the Γ-point and the TA branch phonons are above the expected value in the X and L-points of the BZ. Although the magnitude of the optical branch phonons is above the experimental values, the LA branch phonons have a small error and are pleasing.

Phonon (THz)	Experiment[6]	DFT[7]	Powell
$\omega_{LO}(\Gamma)$	10.3	10.43	11.65
$\omega_{TO}(\Gamma)$	9.20	9.32	11.65
$\omega_{TA}(X)$	2.05		3.87
$\omega_{LA}(X)$	5.80		5.61
$\omega_{LO}(X)$	9.95		10.79
$\omega_{TO}(X)$	9.70		10.80
$\omega_{TA}(L)$	1.65		2.67
$\omega_{LA}(L)$	5.00		5.56
$\omega_{LO}(L)$	10.20		10.81
$\omega_{TO}(L)$	9.50		11.14

Table 5.20: The phonon frequencies of InP

The mode-Grüneisen parameters are shown in table 5.21 and are compared to experimentally measure values and the parameters predicted by first-principles methods. The TO(Γ) value is very close to the experimentally measured value and the TA(L) value correctly reproduces the sign of the negative experimental value, but the situation is not repeated for the TA(X) negative mode-Grüneisen parameter. The values for the transverse optical branch parameters are within a pleasing tolerance.

Grüneisen Param	Experiment[6]	DFT[7]	Powell
$\gamma_{LO}(\Gamma)$	1.24	1.02	1.47
$\gamma_{TO}(\Gamma)$	1.44	1.19	1.47
$\gamma_{TA}(X)$	-2.08		0.12
$\gamma_{LA}(X)$			1.42
$\gamma_{LO}(X)$			1.55
$\gamma_{TO}(X)$	1.42		1.64
$\gamma_{TA}(L)$	-2.00		-0.11
$\gamma_{LA}(L)$			1.28
$\gamma_{LO}(L)$			1.46
$\gamma_{TO}(L)$	1.42		1.57

Table 5.21: The mode-Grüneisen parameters of indium phosphide

Adachi[27] has measured the phonon dispersion of indium phosphide and this is copied and displayed in figure 5.26 for comparison. Figure 5.27 shows

the phonon dispersion predicted by the Powell parameters and as can be seen there is again no evidence of the energy splitting at the Γ-point optical phonon dispersion. Both optical branches are predicted to be too high compared to the experimental values. The magnitude of the transverse branch splitting is low compared to the experimental dispersion curves.

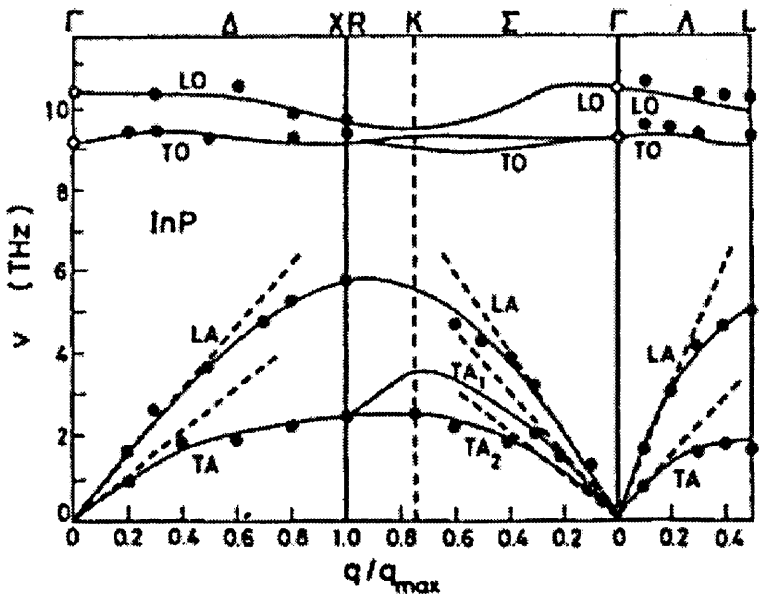

Figure 5.26: The phonon dispersion of indium phosphide measured experimentally, copied from Adachi

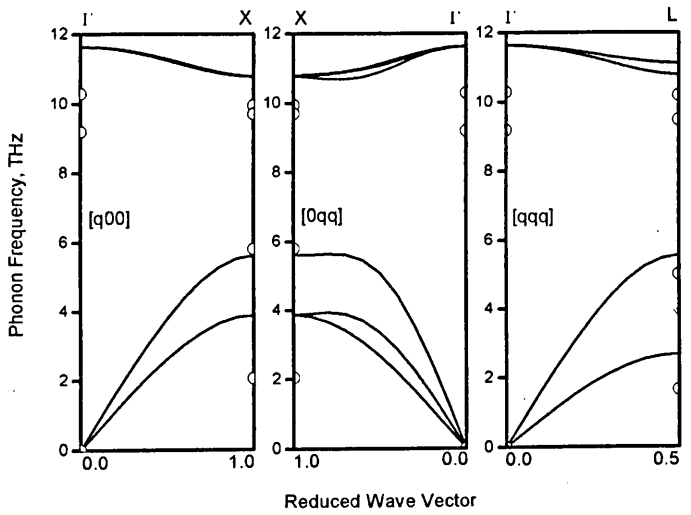

Figure 5.27: The phonon dispersion predicted by the Powell parameters

5.2.8 Gallium Antimonide

The parameterisation that was performed to fit to the elastic properties of the material are compared here in table 5.22 to the experimental values for gallium antimonide. The phonon frequencies predicted for the optical branches at the Γ points both have the same value and there is no split in the frequency values as is shown in the experimental data. The TA branch phonon values have the largest discrepancy with the experimental data with the X-point phonon begin 100% too high. The LO(L) branch phonon is closest to the experimental data being only 8% too high.

Phonon (THz)	Experiment[9]	Powell
$\omega_{LO}(\Gamma)$	6.97	7.98
$\omega_{TO}(\Gamma)$	6.70	7.98
$\omega_{TA}(X)$	1.70	3.45
$\omega_{LA}(X)$	4.99	5.08
$\omega_{LO}(X)$	6.35	6.71
$\omega_{TO}(X)$	6.36	6.96
$\omega_{TA}(L)$	1.37	2.38
$\omega_{LA}(L)$	4.60	5.01
$\omega_{LO}(L)$	6.15	6.63
$\omega_{TO}(L)$	6.48	7.45

Table 5.22: The phonon frequencies of gallium-antimonide

The mode-Grüneisen parameters are displayed in table 5.23 against the few experimentally measured points. The values predicted by the parameters are 17% high.

Grüneisen Param	Experiment[4]	Powell
$\gamma_{LO}(\Gamma)$	1.21	1.44
$\gamma_{TO}(\Gamma)$	1.23	1.44
$\gamma_{TA}(X)$		0.26
$\gamma_{LA}(X)$		1.40
$\gamma_{LO}(X)$		1.40
$\gamma_{TO}(X)$		1.74
$\gamma_{TA}(L)$		0.16
$\gamma_{LA}(L)$		1.34
$\gamma_{LO}(L)$		1.44
$\gamma_{TO}(L)$		1.58

Table 5.23: The mode-Grüneisen parameters of zinc blende GaSb

Figure 5.28 shows the experimental phonon dispersion curves of gallium antimonide, measured by Farr *et al*[30]. Figure 5.29 shows the predicted phonon dispersion by the Powell parameters for gallium antimonide and as can clearly be seen the splitting of the optical branch phonon energies at the Γ-point and the convergence at the X-point can not be correctly replicated. The crossing of the optical branches in the experimental [qqq] region is not predicted by the dispersion

[9] See [28, 29]

and the magnitude of the splitting of the transverse branches in the [0qq] region is not as large as it should be. However, the TA branch phonons show a good match with the experimental data.

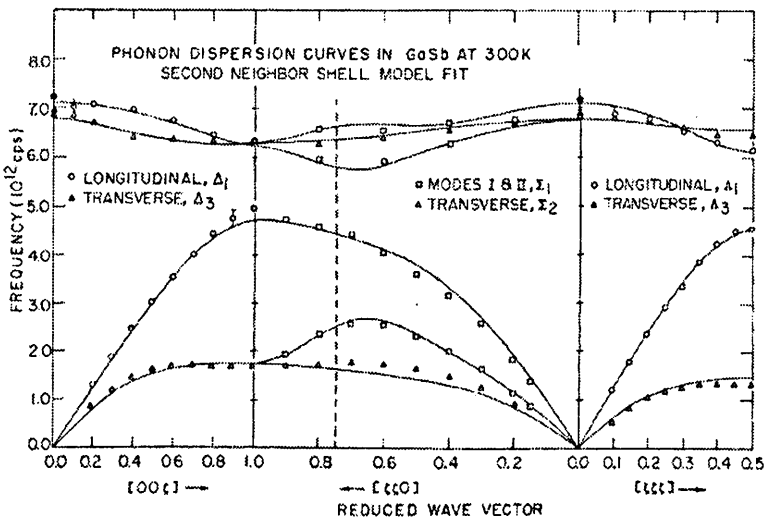

Figure 5.28: The phonon dispersion of gallium antimonide measured experimentally, copied from Farr *et al*

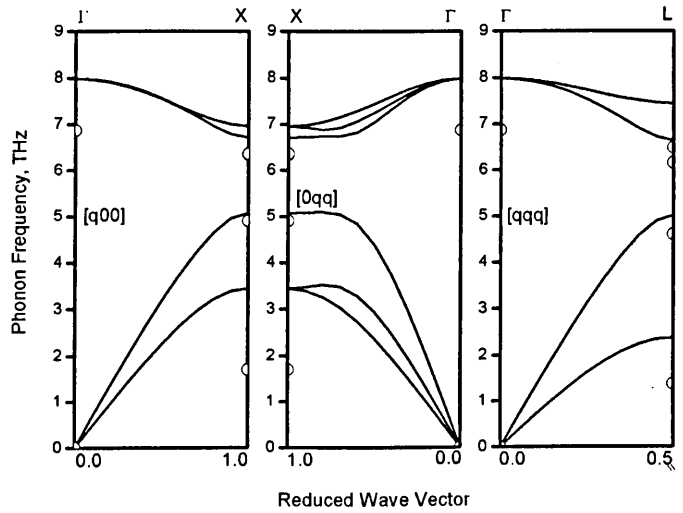

Figure 5.29: The phonon dispersion of gallium antimonide predicted by the Powell parameters

5.2.9 Indium Antimonide

Table 5.24 shows the results of the indium antimonide crystal dynamical calculations from the Powell parameters found in the previous chapter. The experimental phonons are compared to the frequencies found from the D-matrix algorithms described above and it can be seen that the predictions are all too high. The predicted values cannot replicate the energy level splitting observed in the Γ-point phonons and the TA branch phonon frequencies are twice as large as they should be. The LO branch phonons show good agreement with the experimental data.

Phonon (THz)	Experiment[10]	Powell
$\omega_{LO}(\Gamma)$	5.90	6.33
$\omega_{TO}(\Gamma)$	5.54	6.33
$\omega_{TA}(X)$	1.12	2.70
$\omega_{LA}(X)$	4.30	4.63
$\omega_{LO}(X)$	4.75	4.77
$\omega_{TO}(X)$	5.38	5.61
$\omega_{TA}(L)$	0.98	1.83
$\omega_{LA}(L)$	3.81	4.43
$\omega_{LO}(L)$	4.82	4.90
$\omega_{TO}(L)$	5.31	5.96

Table 5.24: The phonon frequencies of InSb

The mode-Grüneisen parameters predicted by the potential parameterisation are shown in the table 5.25. No experimental data or DFT predictions were available in the literature for this material. It has been common with other materials to expect experimental values of the mode-Grüneisen parameters to be negative for the TA branch. The TA(L) mode-Grüneisen parameter has a negative value but it is difficult to say if this trend is correct in the case of indium antimonide without any experimental data to compare to.

Grüneisen Param	Experiment	Powell
$\gamma_{LO}(\Gamma)$		1.52
$\gamma_{TO}(\Gamma)$		1.52
$\gamma_{TA}(X)$		0.04
$\gamma_{LA}(X)$		1.47
$\gamma_{LO}(X)$		1.47
$\gamma_{TO}(X)$		1.86
$\gamma_{TA}(L)$		-0.05
$\gamma_{LA}(L)$		0.95
$\gamma_{LO}(L)$		1.90
$\gamma_{TO}(L)$		1.67

Table 5.25: The mode-Grüneisen parameters of zinc blende indium antimonide

Figure 5.30 shows a copy of the measured indium antimonide phonon dispersion from Borcherds and Kunc[32] for comparison with the predicted values.

[10]See [31]

Also displayed below in figure 5.31 is the phonon dispersion predicted by the Powell parameters. The experimental data shows a large splitting in the transverse acoustic branch of the dispersion in the [0qq] region and a crossing of the optical branch phonons in the [qqq] region that are not well replicated. The values predicted for the LO branch phonons are in reasonable agreement with the experimental data but the TA branch phonon energies appear to be too high by a factor of 2.

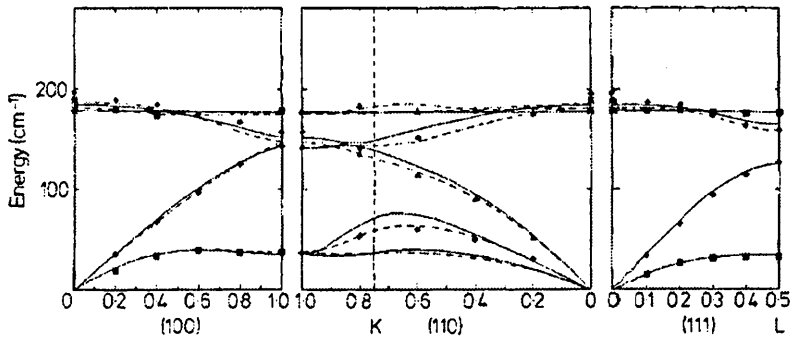

Figure 5.30: The phonon frequencies of indium antimonide measured experimentally, copied from Borcherds and Kunc. Note that for comparison purposes: 1 THz = 33.36 cm^{-1}, for example: 6 THz = 200 cm^{-1}.

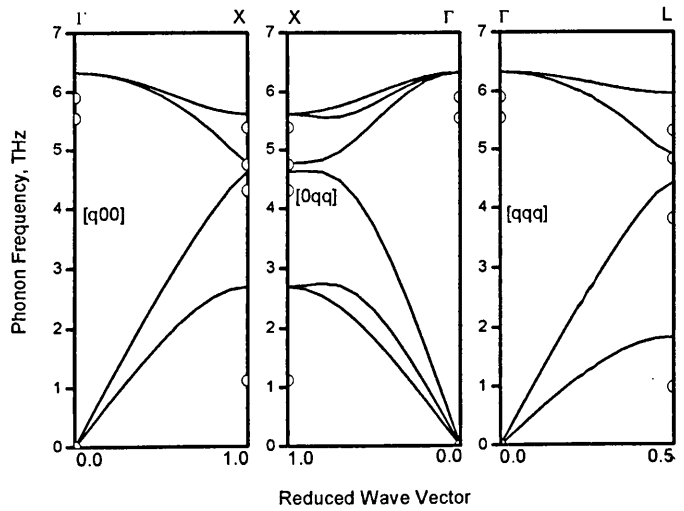

Figure 5.31: The phonon dispersion predicted by the Powell parameters

5.2.10 Boron Nitride

Albe and Moller[33] and Sekkal *et al*[34, 35] have presented a parameterisation for Boron Nitride which are compared in table 5.26 to the phonon values found from the Powell parameters, the experimental data and DFT predictions. It is immediately obvious that the Tersoff parameters from all authors predict phonons that are much higher than the experimental and DFT predictions. The Powell parameters have performed particularly poorly in the optical mode phonon frequencies and the closest value to the experimental data available from the Powell parameters is the TA(L) mode phonon which is 29% larger than the experimental value.

Phonon (THz)	Exp.[11]	DFT[12]	Albe	Sekkal	Powell
$\omega_{LO}(\Gamma)$	38.22	38.37	43.68	44.32	52.47
$\omega_{TO}(\Gamma)$	30.72	31.80	43.68	44.32	52.47
$\omega_{TA}(X)$	20.98	21.16	26.63	27.74	28.30
$\omega_{LA}(X)$	26.98	30.51	34.07	34.33	35.29
$\omega_{LO}(X)$	33.72	34.59	36.92	36.10	38.78
$\omega_{TO}(X)$	30.72	28.15	38.78	39.08	40.17
$\omega_{TA}(L)$	14.39	15.00	18.94	19.61	18.60
$\omega_{LA}(L)$	29.23	29.43	32.26	31.60	31.96
$\omega_{LO}(L)$	33.59	34.44	39.01	40.12	42.86
$\omega_{TO}(L)$	29.23	30.24	40.36	40.21	45.37

Table 5.26: The phonon frequencies of c-BN

Table 5.27 contains the mode-Grüneisen parameters predicted by the Tersoff parameters against a couple of experimental and DFT values. From the limited data available it appears that the Sekkal parameters performed well compared to the DFT predicted values of mode-Grüneisen parameter whilst the Albe parameters performed well compared to the experimental data. The prediction of the Powell parameters was too low in both cases.

Grüneisen Param	Exp.[13]	DFT[14]	Albe	Sekkal	Powell
$\gamma_{LO}(\Gamma)$	1.5	1.2	1.21	1.16	1.06
$\gamma_{TO}(\Gamma)$	1.5	1.2	1.21	1.16	1.06
$\gamma_{TA}(X)$			0.59	0.54	0.43
$\gamma_{LA}(X)$			1.14	1.06	1.05
$\gamma_{LO}(X)$			1.44	1.42	1.47
$\gamma_{TO}(X)$			1.14	1.42	1.05
$\gamma_{TA}(L)$			0.55	0.48	0.31
$\gamma_{LA}(L)$			1.41	1.43	1.58
$\gamma_{LO}(L)$			0.94	1.02	0.75
$\gamma_{TO}(L)$			1.31	1.28	1.23

Table 5.27: The mode-Grüneisen parameters of cubic boron nitride

[11]Read from graph in [36], compared to results from [21]
[12]See [37]

Displayed in figure 5.32 is a copy of the DFT predicted phonon dispersion by Bechstedt *et al*[37] of c-BN for comparison with figures 5.33, 5.34 and 5.35 which show the predicted phonon dispersions by the Albe, Sekkal and Powell parameters respectively. It should be noted here that the layout of the DFT graph in the Γ-X-Γ region is mirrored compared to the phonon dispersions provided by the method used here for the Tersoff potential dispersion. The experimental data points are shown on the predicted dispersions with open circle markers and it is clear that none of the calculated dispersions have the correct magnitude. The frequency splitting in the transverse acoustic branch that can be seen in the DFT graph is not well replicated by the Tersoff parameters of any author, but the magnitude of splitting is largest with the Powell parameters. Furthermore, the level of energy separation between the two optical mode phonon dispersions in the DFT graph is also incorrectly reproduced by the Tersoff parameterisations presented here.

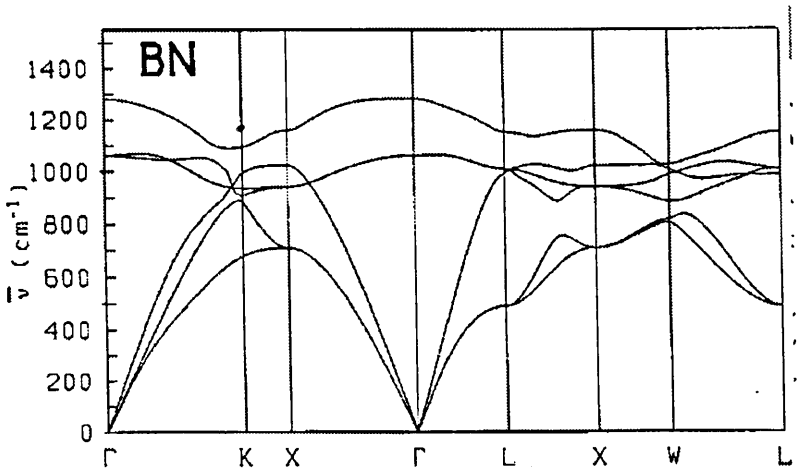

Figure 5.32: The phonon dispersion of cubic boron nitride calculated from first-principles, copied from Bechstedt *et al.* Note that for comparison purposes: 1 THz = 33.36 cm^{-1}, for example: 39 THz = 1300 cm^{-1}.

[13]See [21]
[14]See [38]

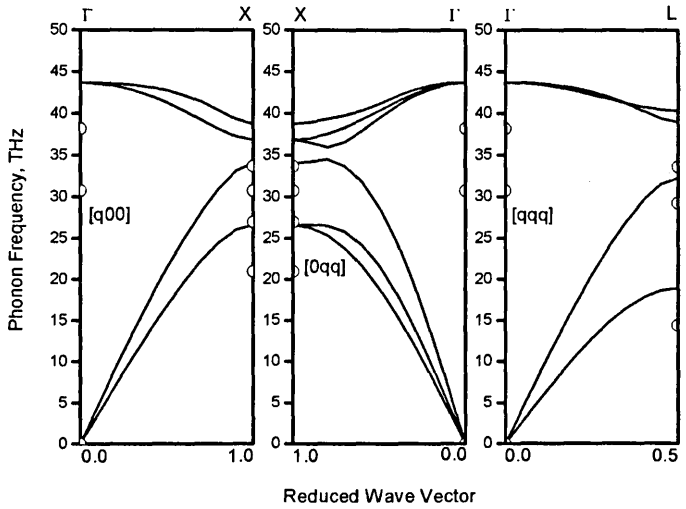

Figure 5.33: The phonon dispersion predicted by the Albe parameters

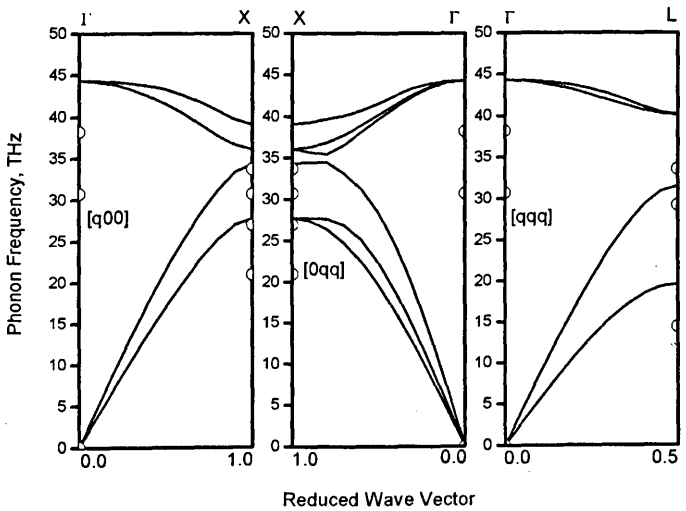

Figure 5.34: The phonon dispersion characterised by the Sekkal parameters

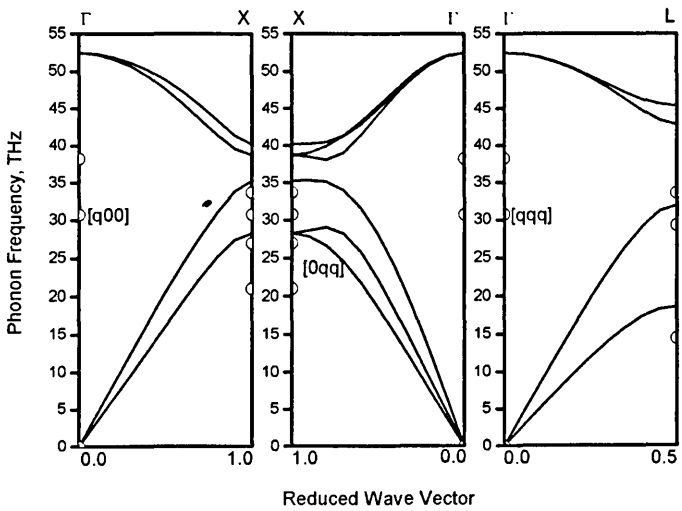

Figure 5.35: The phonon frequencies predicted by the Powell parameters

5.2.11 Gallium Nitride

Gallium nitride has been re-parameterised in the previous chapter and those parameters are used here along with the Benkabou *et al* parameters [39] to predict the values of the phonon frequencies (see table 5.28) and the mode-Grüneisen parameters (see table 5.29) of the material. The phonon frequencies are compared to experimental measurements and DFT predicted values and as can be seen; the error predicted by the Benkabou parameters is very large for all cases except the TA mode phonons. The Powell parameters produce respectable results for the LA mode phonons but overestimate the other phonon modes. The mode-Grüneisen parameters predicted by the Powell parameters overestimate the Γ-point mode-Grüneisen parameters but are generally within a better tolerance than the Benkabou parameters.

Phonon (THz)	Exp.[15]	DFT[16]	Benkabou	Powell
$\omega_{LO}(\Gamma)$	22.27	22.36, 21.93	10.88	26.03
$\omega_{TO}(\Gamma)$	16.57	16.99, 15.76	10.88	26.03
$\omega_{TA}(X)$		5.90	6.02	8.82
$\omega_{LA}(X)$		10.52	7.35	10.91
$\omega_{LO}(X)$		20.83	13.43	23.79
$\omega_{TO}(X)$		18.67	16.39	24.34
$\omega_{TA}(L)$		4.13	5.16	5.88
$\omega_{LA}(L)$		10.46	6.77	11.22
$\omega_{LO}(L)$		21.22	12.55	24.34
$\omega_{TO}(L)$		17.59	15.53	25.06

Table 5.28: The phonon frequencies of c-GaN

Grüneisen Param	Exp.[15]	DFT[18]	Benkabou	Powell
$\gamma_{LO}(\Gamma)$	1.2	1.8, 1.02	2.29	1.43
$\gamma_{TO}(\Gamma)$	1.4	1.8, 1.19	2.29	1.43
$\gamma_{TA}(X)$			1.61	0.55
$\gamma_{LA}(X)$			1.52	1.40
$\gamma_{LO}(X)$			1.66	1.56
$\gamma_{TO}(X)$			1.52	1.40
$\gamma_{TA}(L)$		-0.49	1.24	0.16
$\gamma_{LA}(L)$		0.92	1.76	1.42
$\gamma_{LO}(L)$		1.05	1.91	1.54
$\gamma_{TO}(L)$		1.23	1.49	1.37

Table 5.29: The mode-Grüneisen parameters of cubic gallium nitride

Figure 5.36 shows a predicted phonon dispersion of cubic gallium nitride from *ab initio* techniques by Bechstedt *et al*[37]. Figure 5.37 shows the phonon dispersion predicted by the Benkabou parameters and it can be seen that the TA mode phonons appear to have a reasonable fit to the DFT predicted values. However,

[15] See [40]
[16] See [37, 15]
[18] See [38, 41]

the general shape of the optical mode phonons appears to be reversed. The Powell phonon dispersion (see figure 5.38) shows a reasonable fit to the LA mode phonons but the other modes appear to have an overestimated magnitude. The splitting between the transverse mode phonons in the centre of the [0qq] region is too small and no separation of the Γ point branch energies is in evidence.

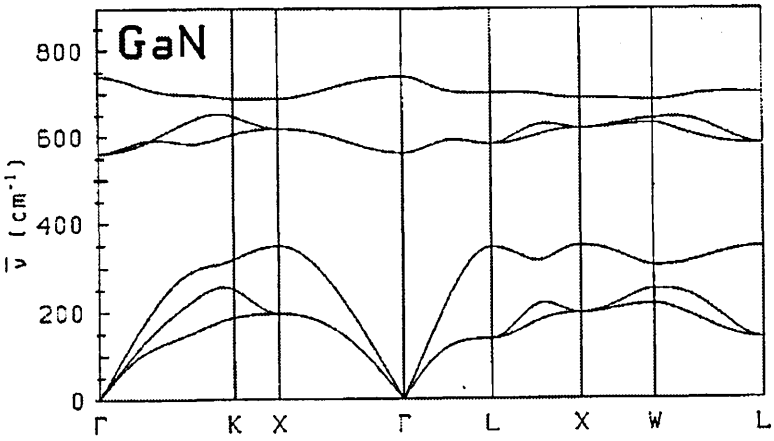

Figure 5.36: The phonon dispersion of cubic gallium nitride calculated from first-principles, copied from Bechstedt *et al.* Note that for comparison purposes: 1 THz = 33.36 cm^{-1}, for example: 22.5 THz = 750 cm^{-1}.

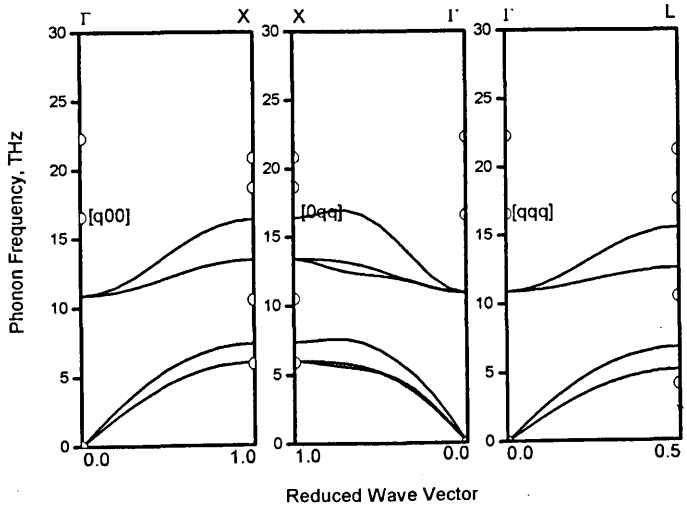

Figure 5.37: The phonon dispersion characterised by the Benkabou parameters

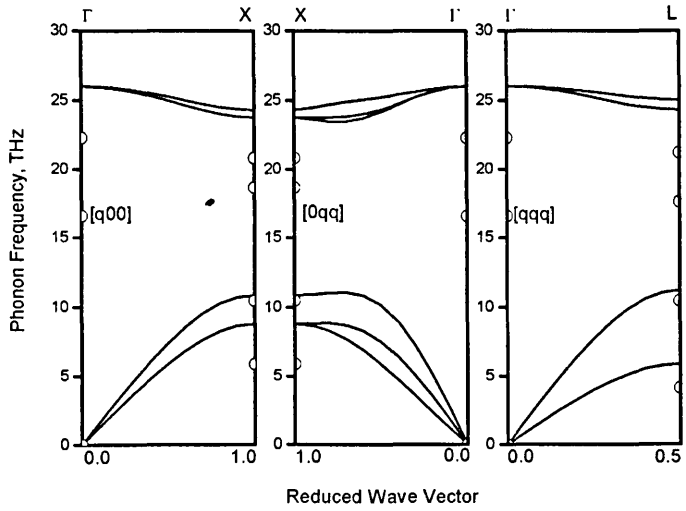

Figure 5.38: The phonon dispersion predicted by the Powell parameters

5.2.12 Indium Nitride

In this section the Benkabou *et al*[39] parameters are compared to the Powell fit to the elastic constants in the previous chapter. Table 5.30 shows the phonon frequency values predicted for InN by the parameterisations compared to DFT predictions. It is immediately obvious that the Benkabou parameterisation is completely wrong, being in error by over 2 orders of magnitude. The Powell parameters, again, show reasonable agreement in the LA branch phonons but fail to reproduce the Γ-point energy split that is evident in the DFT values. Furthermore, the optical branch phonons and the TA frequencies are overestimated.

Phonon (THz)	DFT[16]	Benkabou	Powell
$\omega_{LO}(\Gamma)$	17.86, 18.63	372.24	20.66
$\omega_{TO}(\Gamma)$	14.00, 14.41	372.24	20.66
$\omega_{TA}(X)$	3.47	80.53	5.31
$\omega_{LA}(X)$	6.93	125.35	7.09
$\omega_{LO}(X)$	17.00	350.33	20.13
$\omega_{TO}(X)$	15.53	358.90	20.29
$\omega_{TA}(L)$	2.33	56.12	3.53
$\omega_{LA}(L)$	6.80	122.23	7.25
$\omega_{LO}(L)$	17.18	355.86	20.02
$\omega_{TO}(L)$	14.63	359.35	20.91

Table 5.30: The phonon frequencies of cubic InN

Table 5.31 shows the mode-Grüneisen parameters predicted by the parameterisations against a couple of DFT predicted values. Here the Benkabou parameters are again in error by at least an order of magnitude whilst the Powell parameters make a reasonable prediction.

Grüneisen Param	DFT[14]	Benkabou	Powell
$\gamma_{LO}(\Gamma)$	1.5	0.108652	1.60046
$\gamma_{TO}(\Gamma)$	1.5	0.108652	1.60046
$\gamma_{TA}(X)$		-0.889342	0.295557
$\gamma_{LA}(X)$		0.120705	1.54504
$\gamma_{LO}(X)$		0.130628	1.65616
$\gamma_{TO}(X)$		0.120705	1.54504
$\gamma_{TA}(L)$		-1.10731	-0.147744
$\gamma_{LA}(L)$		0.0115528	1.38441
$\gamma_{LO}(L)$		0.124424	1.65904
$\gamma_{TO}(L)$		0.119328	1.5258

Table 5.31: The mode-Grüneisen parameters of cubic InN

Only a DFT prediction of the phonon dispersion of cubic indium nitride is available in the literature. This was done by Bechstedt *et al*[37] and is shown in figure 5.39. Figure 5.40 shows the Benkabou phonon dispersion and the DFT values are marked on the plot with open circle marks. There is obviously a massive over estimation of all phonon frequencies in this figure but the shape of the

acoustic branch phonons appears correctly. The dispersion predicted by the Powell parameters is shown in figure 5.41 and shows a reasonable accuracy for the LA branch phonon dispersion. There is no evidence of the energy level split at the Γ-point and the magnitude of the splitting of the TA branch phonons in the [0qq] region appears underestimated.

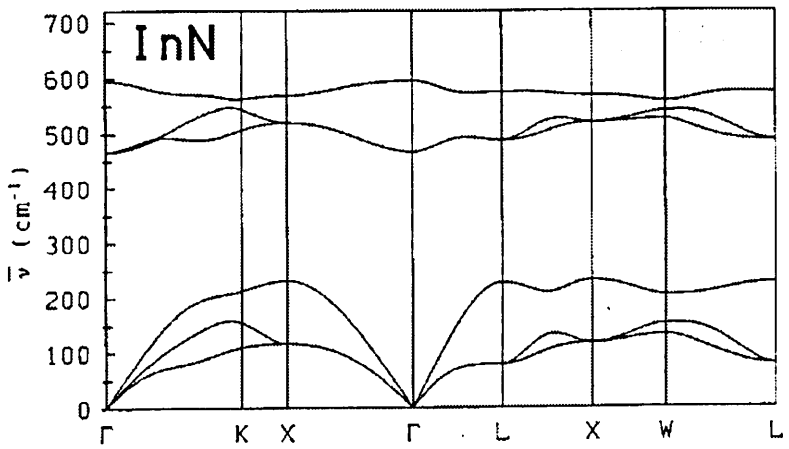

Figure 5.39: The phonon frequencies of cubic indium nitride calculated from first-principles, copied from Bechstedt *et al.* Note that for comparison purposes: 1 THz = 33.36 cm^{-1}, for example: 18 THz = 600 cm^{-1}.

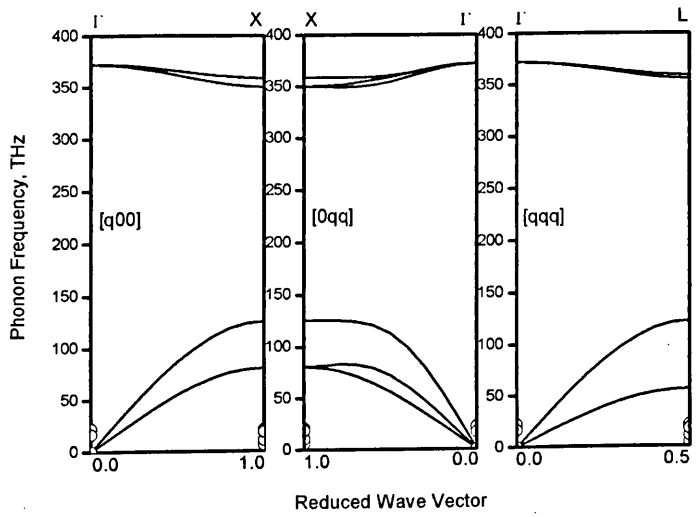

Figure 5.40: The phonon dispersion characterised by the Benkabou parameters

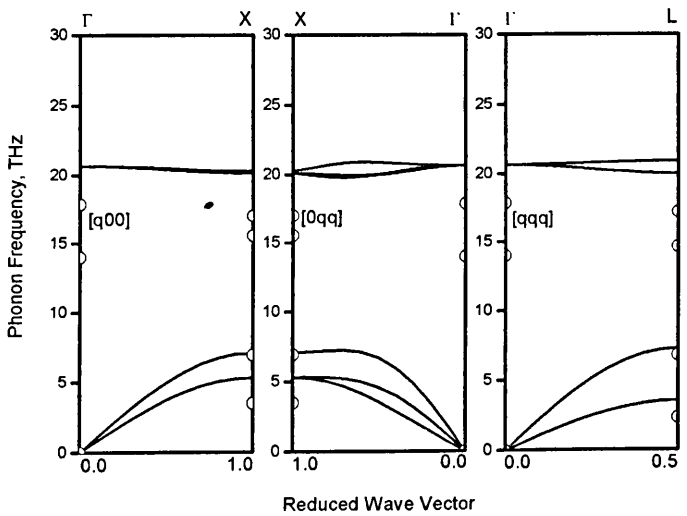

Figure 5.41: The phonon dispersion predicted by the Powell parameters

5.2.13 Aluminium Nitride

Table 5.32 shows the phonon frequencies predicted by the Goumri-Said *et al*[42], the Benkabou *et al*[39] and the Powell parameters from the previous chapter alongside the DFT predictions for the phonon values. As can be seen from the table, the Benkabou parameters for the LO mode phonons are nearly all correct. The Goumri-Said parameters predict the values of the acoustic branch phonons very well and the Powell parameters can reproduce the Γ-point LO phonon and the LA branch within reasonable accuracy.

Phonon (THz)	DFT[16]	Benkabou	Goumri-Said	Powell
$\omega_{LO}(\Gamma)$	26.68, 27.42	26.48	28.86	27.37
$\omega_{TO}(\Gamma)$	19.93, 20.12	26.48	28.86	27.37
$\omega_{TA}(X)$	10.22	2.30	10.29	12.69
$\omega_{LA}(X)$	17.63	15.52	17.34	16.71
$\omega_{LO}(X)$	21.46	21.55	24.07	23.19
$\omega_{TO}(X)$	20.02	26.39	26.85	24.43
$\omega_{TA}(L)$	6.77	1.55	6.66	8.11
$\omega_{LA}(L)$	17.53	12.53	16.99	17.37
$\omega_{LO}(L)$	22.03	23.42	24.86	24.11
$\omega_{TO}(L)$	19.63	26.43	27.65	25.47

Table 5.32: The phonon frequencies of cubic AlN

A comparison of the various predictions made for the mode-Grüneisen parameters against the experimental and DFT values has been made in table 5.33. Only 2 values for the experimental Γ-point mode-Grüneisen parameters are available in the literature and the Powell and Benkabou parameters both predict values that are 22% in error. The Goumri-Said parameters are 37% higher than the experimental values.

Grüneisen Param	Exp.[13]	DFT[19]	Benkabou	Goumri-Said	Powell
$\gamma_{LO}(\Gamma)$	1.00	0.89	1.23	1.37	1.21
$\gamma_{TO}(\Gamma)$	1.60	1.14	1.23	1.37	1.21
$\gamma_{TA}(X)$			-9.62	-0.49	0.25
$\gamma_{LA}(X)$			1.23	1.34	1.17
$\gamma_{LO}(X)$			1.23	1.34	1.17
$\gamma_{TO}(X)$			1.45	1.63	1.43
$\gamma_{TA}(L)$		-0.29	-8.49	-0.83	-0.02
$\gamma_{LA}(L)$		0.85	0.35	0.96	1.13
$\gamma_{LO}(L)$		1.31	1.47	1.49	1.16
$\gamma_{TO}(L)$		0.96	1.34	1.50	1.33

Table 5.33: The mode-Grüneisen parameters of cubic AlN

Aluminium nitride is notoriously difficult to manufacture in high quality samples and very difficult to work with due to its reactive nature. No experimental data is available for a phonon dispersion curve, but a DFT prediction is shown

[19]Ref. [41]

in figure 5.42 for comparison. This data was copied from Bechstedt *et al*[37]. The phonon dispersion shown in 5.43 is predicted by the Benkabou parameters and although the LO branch phonons appear correct there is a failure to predict the curvature of the TO mode phonons and the vales of the acoustic branches. The Goumri-Said phonon dispersion, which is shown in figure 5.44 makes a very accurate prediction of the acoustic branch phonons (apart form the level of splitting between the degenerate transverse phonons in the [0qq] region). The optical branch phonons are however overestimated. The Powell dispersion (figure 5.45) appears to show a good agreement with the general shape of the curves and the magnitude of the LO branch phonons, although the optical branch and TA branch phonons have the wrong scaling. All of the parameters fail to predict the splitting of the Γ point frequencies in the optical branches and none of the parameters can reproduce the level of splitting in the transverse mode frequencies in the [0qq] region.

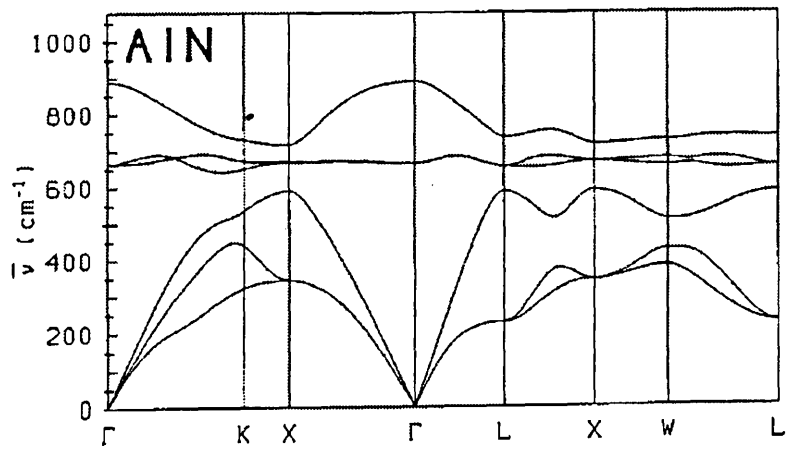

Figure 5.42: The phonon frequencies of cubic aluminium nitride calculated from first-principles, copied from Bechstedt *et al.* Note that for comparison purposes: 1 THz = 33.36 cm^{-1}, for example: 27 THz = 900 cm^{-1}.

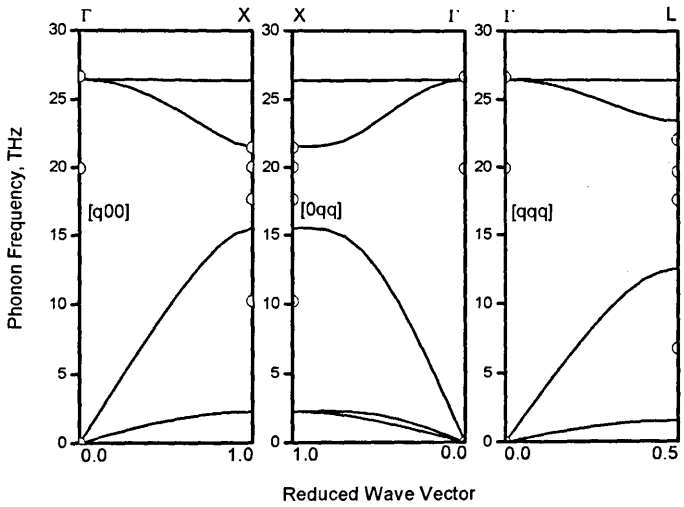

Figure 5.43: The phonon frequencies predicted by the Benkabou parameters

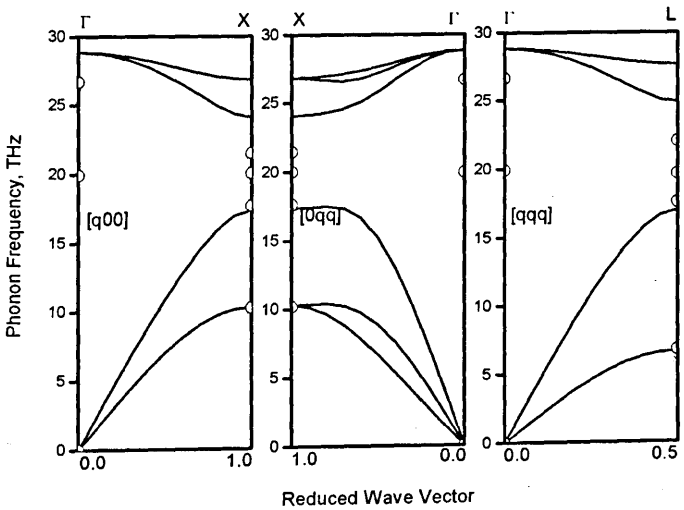

Figure 5.44: The phonon dispersion characterised by the Goumri-Said parameters

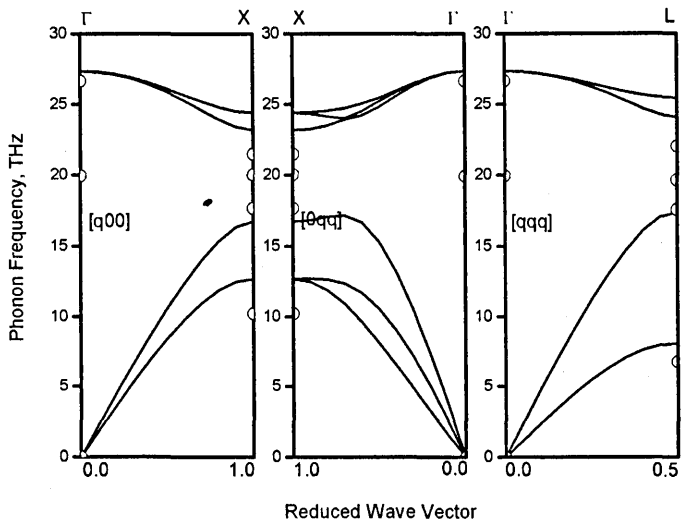

Figure 5.45: The phonon dispersion predicted by the Powell parameters

5.2.14 Re-parameterisation of silicon for a phonon frequency fit

The program code described in Chapter 4 for a global granular search against a calculated materials property metric was modified to fit the Tersoff potential to the phonon frequencies and to be less concerned with the elastic constants. The program code was run 20 times and the best set of results (named the Powell (P2) parameter set) are produced here for comparison against the Powell (P1) parameters, which were fit to just the elastic properties of the material. The results demonstrate that although the parameters can be designed to fit the phonon frequencies reasonably well, the elastic properties of the material suffer as a result of the fitting procedure.

Parameter	Tersoff (T3)	Powell (P1)	Powell (P2)
D_e	2.666029	2.36291	2.31633
S	1.431648	1.48565	2.39078
β	1.465552	1.46405	1.35209
r_e	2.295161	2.34358	2.32496
R	2.85	2.85	2.85
R_{cut}	0.15	0.15	0.15
c	100390	113031	83780.9
d	16.217	14.248	19.8881
h	-0.59825	-0.423876	-0.356865
n	0.78734	0.938777	0.736002
γ	1.1e-06	1.2467e-06	6.87108e-07
λ	1.5	1.4606	1.5004

Table 5.34: The modified Tersoff parameters for diamond silicon

Property (units)	Exp./Calc.	Tersoff (T3)	Powell (P1)	Powell (P2)
$E_{coh}(eV)$	-4.63[2]	-4.630	-4.630	-4.629
a (Å)	5.431[4]	5.432	5.431	5.370
B (MBar)	0.9783[3]	0.977	0.976	0.842
C' (MBar)	0.509[3]	0.336	0.511	0.242
C_{44} (MBar)	0.796[3]	0.690	0.797	0.347
ζ	0.524[2]	0.674	0.519	0.734

Table 5.35: The material properties of diamond silicon

Table 5.35 clearly shows that the Powell (P2) parameters for silicon which have been fitted to the phonon frequencies can not replicate the correct material properties. Although the cohesive energy of the material is in close agreement, the lattice parameter is 1% low, the bulk modulus and shear modulus are 14% and 52% low respectively and the c_{44} elastic property is in error by 56%.

Figure 5.46 shows the material phase plot for silicon using the Powell (P2) parameter set. As can be clearly seen the diamond phase is no longer the lowest energy configuration for silicon using these parameters: in fact it is the highest of the phases tested. The material would prefer the face centred cubic (fcc) lattice

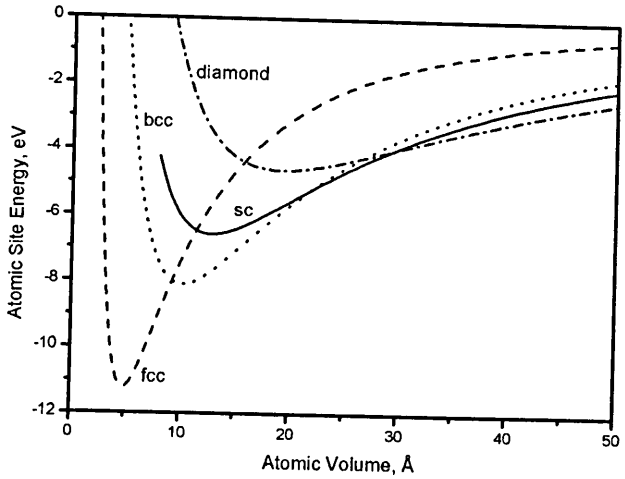

Figure 5.46: Energy vs. atomic volume for silicon with Powell (P2) parameters

configuration under the conditions of a high temperature MD simulation and would possibly phase transform providing incorrect results.

Phonon (THz)	Experiment[1]	Tersoff (T3)	Powell (P1)	Powell (P2)
$\omega_{LTO}(\Gamma)$	15.5	16.07	17.82	15.41
$\omega_{TA}(X)$	4.5	6.90	8.08	4.94
$\omega_{LAO}(X)$	12.3	12.19	13.31	11.28
$\omega_{TO}(X)$	13.9	14.89	15.18	14.09
$\omega_{TA}(L)$	3.45	4.67	5.60	3.63
$\omega_{LA}(L)$	11.3	11.31	12.90	9.59
$\omega_{LO}(L)$	12.6	13.15	13.14	12.14
$\omega_{TO}(L)$	14.7	15.43	16.51	14.79

Table 5.36: The phonon frequencies of Si including a phonon fit

The phonon frequencies calculated with the analytic derivatives method are shown in table 5.36. These are very pleasing with the largest error occurring at the L symmetry point in the BZ where the longitudinal acoustic branch phonon frequency is 15.2% low. The replication of the other phonons are quite accurate and the phonon plot is shown in figure 5.48 under the experimental curves plotted by Dolling[6] in figure 5.47. As can be seen from the graphs, although the mid-range transverse acoustic branch phonon splitting is too low in the $[0qq]$ plot, the rest of the reults are more accurate than the Tersoff and Powell (P1) parameter sets.

Table 5.37 shows the new Powell (P2) calculated mode-Grüneisen parameters against those calculated from the Tersoff (T3) and the Powell (P1) parameters. There are still some errors present in the data (compared to the experimental data) with the largest being the 18.5% error in the L point transverse acoustic branch but these are reduced when compared to the other parameter sets.

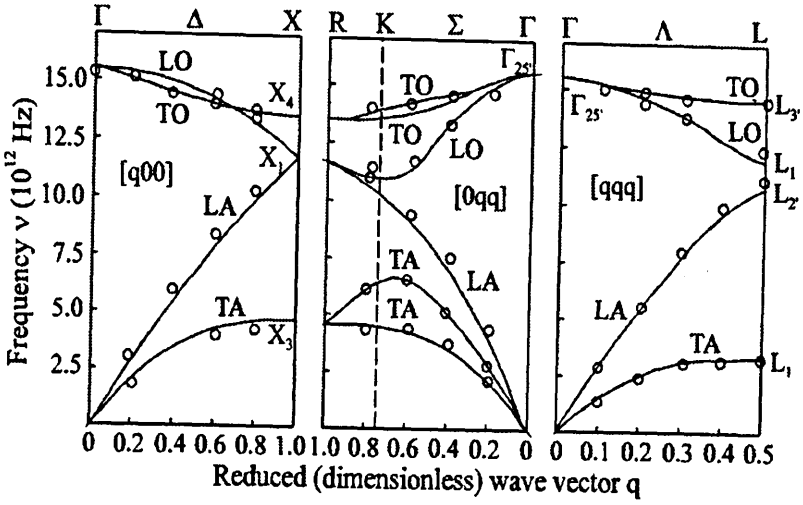

Figure 5.47: The experimentally measured phonon dispersion of silicon

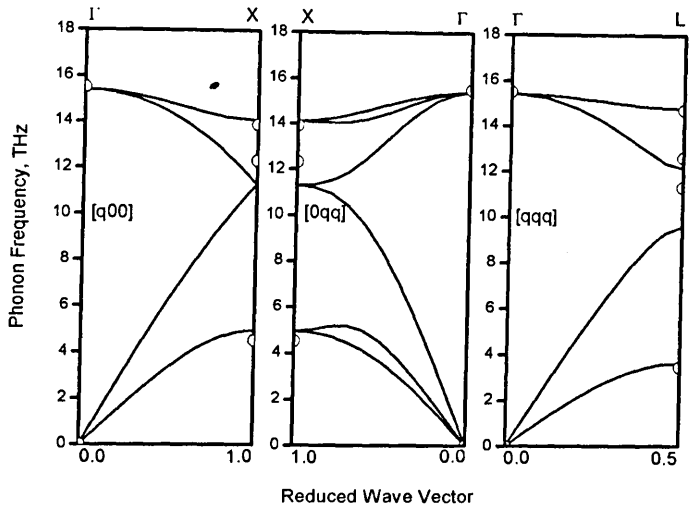

Figure 5.48: The silicon phonon frequencies dispersion by the Powell (P2) parameters

Grüneisen Param	Experiment	Tersoff (T3)	Powell (P1)	Powell (P2)
$\gamma_{LTO}(\Gamma)$	0.98[2]	1.32	1.25	1.21
$\gamma_{TA}(X)$	-1.4	-0.20	0.12	-1.21
$\gamma_{LAO}(X)$	0.9	1.26	1.22	1.18
$\gamma_{TO}(X)$	1.5	1.60	1.58	1.53
$\gamma_{TA}(L)$	-1.3[4]	-0.31	0.08	-1.06
$\gamma_{LA}(L)$		0.72	0.91	0.54
$\gamma_{LO}(L)$		1.65	1.52	1.63
$\gamma_{TO}(L)$	1.3	1.46	1.39	1.36

Table 5.37: The mode-Grüneisen parameters of silicon including a phonon fit

5.3 The effects of ionicity

The Tersoff bond-order PEF is a short-range potential function. It was designed for modelling the cohesive properties between semiconductor nearest neighbour atoms whilst preserving the open tetrahedral structure observed in type IV semiconductors. The long range effects of ionicity combined with the covalent bonding observed in the type III-V materials due to the two different atomic species in the basis set were never taken into account by Tersoff. The functional form of the Tersoff potential used in the above work is the one originally proposed by Tersoff to model the covalent bonding of type IV species.

Keyes[43] proposed that the difference in the masses of the two atomic species and the effects of ionicity in zinc blende semiconductors could account for the splitting between the optical and acoustic phonon branches and the crossing of the LO and TO branches in the region between the BZ points of high symmetry. This theory was based upon consideration of the equations of motion in the dynamical equations and the empirical observation of a small number of III-V systems. This theory was given further weight by Mitra[28] who considered the experimental measurements taken for a larger number of semiconductors and the effective ionic charges. Figure 5.49 summarises the main point of both authors work: the effective ionic charge q^* can be used to directly predict the level of splitting between the Γ-point optical phonon branches. As can be seen; when $q^* = 0$ as in the case of non-ionic type IV semiconductors we expect the optical phonon branches to coincide at the zone centre. As the effective ionic charge increases, so does the splitting in energy between the LO and TO branches of the Γ-point phonon frequencies. Keyes predicted that a value of $q^* = 0.7$ was an "intermediate" value where the LO and TO phonons would coincide at the BZ X-point boundary.

This effect can account for some of the errors involved in the above results for the predicted phonon frequencies of the different III-V crystal systems. None of the partly ionic systems described in the above results chapter predict a phonon energy split at the Γ point in the BZ, which is clearly evident in the experimental and DFT predictions.

The effective ionic charge of a material, called q^*, e^* or Z^* by a number of authors, is very complicated to calculate. A review by Catlow and Stoneham[44] highlighted some of the complex issues and common misunderstandings that are found when attempting to describe materials such as the polar semiconductors. The review paper suggests that many authors attempting to model the ionic charges of a polar crystal based upon the lattice dynamics of the material are over-

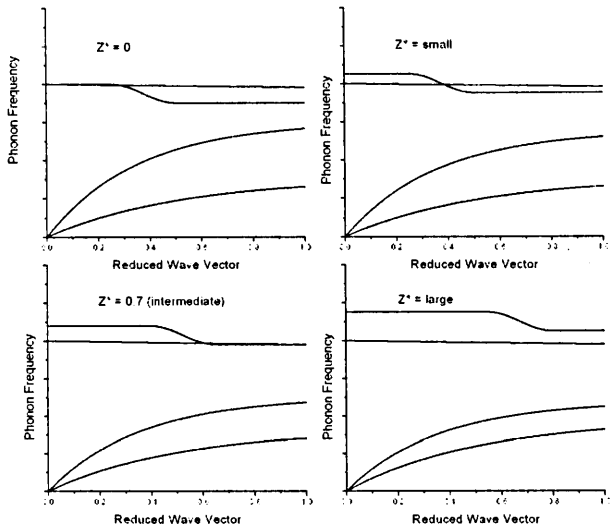

Figure 5.49: An illustration of the effect of ionicity on phonon frequencies

simplifying the problem. A number of different schemes that have been used to calculate the ionicity of a III-V crystal and the varied results is highlighted in table 5.38 which contains a number of values of effective ionic charge from various sources. As can be seen the predicted values from one method to the next vary greatly with little agreement on a value of preferred method.

Material	q^*
AlP	0.87[21]
AlAs	0.51[20], 0.74[21]
AlSb	0.31[20], 1.24[21]
GaP	0.43[20], 0.94[21]
GaAs	0.33[20], 0.87[21]
GaSb	0.14[20], 0.71[21]
InP	0.57[20], 1.21[21]
InAs	0.47[20], 1.03[21]
InSb	0.90[21]
BN	0.71[21], 2.0[22], 0.86[24], 0.91[25]
AlN	3.2[22], 1.16[24], 1.21[25]
GaN	2.5[22], 2.65[23], 1.11[24], 1.14[25]
InN	3.1[22], 1.03[24]

Table 5.38: The effective ionic charges of zinc blende lattices combined from various authors

The rigid ion model is the choice of Szigeti[47] who devised a scheme to link the polarisability α of a zinc blende structure with the normal vibrations of the

[20]Ref. [45]
[21]Ref. [46]
[22]Ref. [38]
[23]Ref. [40]
[24]Ref. [37]
[25]Ref. [36]

crystal - devised from the same lattice dynamical harmonic approxmation that is used here. The method has been used with success by many authors to predict material properties including, for example, Hambleton *et al*[48] who correctly predicted the high frequency (optical) dielectric constant of GaAs. The Szigeti model is based upon the phonon frequencies, the reduced mass and volume of the material and requires calculation of an effective transverse and longitudinal charge of the material, e_T^* and e_L^*

$$e_T^* = \left[(\omega_{LO}^2 - \omega_{TO}^2)\epsilon_\infty(M\Omega/4\pi\right]^{1/2} \tag{5.5}$$

$$e_L^* = \left[(\omega_{LO}^2 - \omega_{TO}^2)\epsilon_\infty^{-1}(M\Omega/4\pi\right]^{1/2} \tag{5.6}$$

where ω is the phonon frequency, ϵ_∞ is the high frequency (optical) dielectric constant of the material, M is the reduced mass and Ω is the cell volume. From the above two equations Szigeti formed a relation for the effective ionic charge e_S^* of the material

$$e_S^* = \frac{3}{\epsilon_\infty + 2}e_T^* = \frac{3\epsilon_\infty}{\epsilon_\infty + 2}e_L^* \tag{5.7}$$

The above procedure is reasonably complicated and requires values for the phonon frequencies and the high frequency dielectric constant of the material which are difficult to measure and prone to errors. Furthermore, due to the number of proposed models and techniques provided for the calculation of the effective ionic charge, it is difficult to find reliable data to compare predicted values to.

A "rule of thumb" is proposed here, based upon empirical observation of the experimental and DFT predictions from the previous section. By comparing the relations found by Keyes[43] which are summarised in figure 5.49 above and the experimental phonon dispersion, we can make an estimate of the value of the effective ionic charge of the material.

For example: looking at the experimental phonon dispersion of GaAs (figure 5.15) we can see that the energy gap between the Γ-point optical phonons and the X-point optical phonons appears roughly equal and we can estimate that $q^* = 0.35$. Upon inspection of the GaSb phonon dispersion (figure 5.28) the optical phonon frequency gap at the X-point is tending towards zero. Here we can make a guess that $q^* = 0.7$. And from inspection of the phonon dispersion in figure 5.30 for InSb we can see that the energy gap between the optical frequency phonons at the Γ-point is very small. So we could guess that $q^* = 0.1$ in this case.

A simple rule is proposed: for the calculation of the effective ionic charge of type III-V zinc blende semiconductors e_P^* we just add 0.7 to the value of the

separation of the X-point phonon frequencies (measured in THz).

$$e_P^* = 0.7 + [\omega_{LO}(X) - \omega TO(X)] \tag{5.8}$$

The estimates for the effective ionic charges and the values calculated based upon the above simple rule are shown in table 5.39. As can be seen, the "rule of thumb" makes an excellent estimate of the values of effective ionic charge compared to the estimates from the experimental and DFT graphs seen previously. This is an entirely empirical relationship based upon observations made from the experimental graphs and it is not based upon physical considerations. However, as can be seen - it works rather well for the zinc blende III-V lattice semiconductors. The cubic III-N semiconductors are predicted to have very high values for ionicity from this particular simple model, but it is not possible to tell from the relation suggested by Keyes what values of q^* to give them - the magnitude of the splitting of the X-point optical phonons is certainly much larger than the other semiconductors. The values provided from the mathematical models given by Harrison[46, 49] which are shown in table 5.38 for the cubic nitrides have values between 2.0 and 3.2 but a predicted value of 7.14 for Boron Nitride seems very high.

Material	Estimate	e_p^*
GaP	1	1.04
GaAs	0.35	0.36
GaSb	0.7	0.69
InP	1	0.95
InAs	0.4	0.43
InSb	0.1	0.07
BN	$\gg 1$	7.14
AlN	$\gg 1$	2.14
GaN	$\gg 1$	2.41
InN	$\gg 1$	2.17

Table 5.39: The estimated effective ionic charges of zinc blende crystals from by comparing the relation proposed in figure 5.49 and the experimental phonon dispersions for individual materials. Also shown is the value of e_p* calculated with eq. 5.8.

In the available literature only one other paper from Nakamura *et al*[50], has attempted to combine long range ionic effects with the Tersoff model to predict bonding behaviour at semiconductor surfaces during growth kinetics simulations. They modified the Tersoff potential to add a Coulombic term to account for the long-range ionic bonding effects in type III-V crystal lattices. This is shown below in equation 5.9 where Z is the atomic charge and e is the elementary electronic charge.

$$E = \sum_i \sum_{j \neq i} \left[\frac{Z_i Z_j e^2}{4\pi\epsilon_0 r_{ij}} + fc(f_{ij}) \left[V_R(r_{ij}) - b_{ij} V_A(r_{ij}) \right] \right] \tag{5.9}$$

It is suggested that if the Tersoff potential is to be able to model the correct energy splitting at the BZ boundaries and the crossing of the optical branches in the intrazone regions of the III-V materials, then the dynamical model used to calculate the phonon dispersions for the Tersoff PEF must take account of the ionicity of the material.

5.4 Modifications to the Tersoff potential

In the above work we have demonstrated a fast and accurate method of providing predictions of the dynamical properties of cubic crystal structures using the Tersoff potential. We have compared the analytic form of the second derivatives to standard numerical methods in terms of time and accuracy and proved that the analytic method is 100 times faster and can reproduce all of the dynamical information, whereas the numerical methods have problems at the zone centre due to divide-by-zero faults. The method presented above is for modelling a single atomic dimer pair held in an unstrained bulk matrix which may be simply extended to more complex models of strained solids or semiconductor interfaces by iterating the method across each of the bravis basis sets in a lattice descriptor or extending the size of the D-matrix.

The results for the phonon dispersion curves, mode-Grüneisen parameters and phonon energy values that were predicted by the Tersoff parameters in this section were unexpected. We have demonstrated a fast and accurate method of dynamical modelling of the Tersoff PEF, however, it is clearly unsuitable for predicting the phonon frequencies and the associated parameters in its current form. This leads to the questions: What are the limitations of the model? What can be done to improve the model?

If we return to the results that were predicted for the parameters that were fit to the elastic properties of the material there are trends that appear in the predicted results that can be used to identify the source of the problem:

1. The optical branch phonons are predicted to be too high at the zone centre and the zone boundaries for the IV and III-V materials.

2. The TA branch phonons are predicted to be too high at the zone boundaries for the IV and III-V materials.

3. The level of splitting between the degenerate TA branch phonons is too small for the IV and III-V materials.

4. The level of splitting between the degenerate TO branch phonons is too small for the IV and III-V materials.

5. The energy split between the optical branch phonons at the Γ-point cannot be predicted for the III-V materials.

6. The crossing of the optical branch phonons between the points of high symmetry and the BZ centre cannot be replicated for the III-V materials.

Of the above effects, numbers 5 and 6 appear to be due to the lack of long range ionicity modelling in the Tersoff potential and was therefore expected. However, although the effects of ionicity need to be taken into account for the III-V materials modelling, the other 4 trends also exist with the type IV diamond latices which have purely covalent bonding and no ionicity.

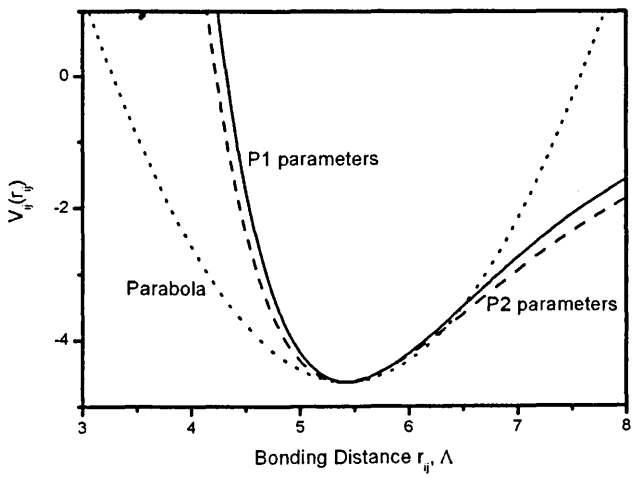

Figure 5.50: The energy functions of the Powell(P1) [solid line] and Powell(P2) [dashed line] parameters for silicon with a parabola for comparison

Initially we consider the harmonic approximation D-matrix for the lattice dynamics as a source of possible errors. Under the harmonic approximation we make the assumption that the cohesive energy curve can be approximated to a parabola. Figures 5.50 and 5.51 show the total site energy of the atoms in the lattice as a function of bond distance against a parabola for both the Powell (P1) elastic property fit and the Powell (P2) parameters for the phonon frequency fit.

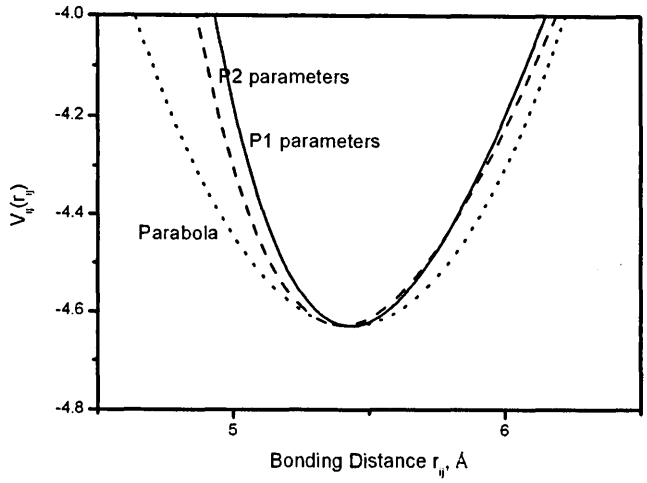

Figure 5.51: A close-up of the energy functions of the Powell(P1) [solid line] and Powell(P2) [dashed line] parameters for silicon

During the calculation of the D-matrix we take the analytic second derivatives of this form and assume that $\partial x \rightarrow 0$. As can be seen from the close-up of the cohesive energy curve both functional forms of the potential appear to approximate the parabola at the energy minima. Furthermore, although we understand the limitations of using a rigid-ion model, the DFT method uses a similar dynamical model and so we should be able to reproduce results of a similar quality to the ones shown for the III-N materials if the Tersoff potential is flexible enough to model the lattice dynamics and the elastic properties of the material.

The modelling of the diamond silicon properties demonstrated that, although the bulk modulus can be predicted, it is difficult to predict the elastic properties of the material that are related to shear strain operations when fitting the Tersoff parameters to the phonon frequencies. Figure 5.52 shows a plot of the shear factor ϵ against the lattice energy under a shear deformation for the two sets of Tersoff parameters for silicon: P1 for the elastic property fit and P2 for the phonon frequency fit. The shear modulus is calculated from the second derivative of this relation and it is immediately clear that the P1 parameters are flexible enough produce a much higher value of curvature for the energy than the P2 parameters.

By consideration of the functional form of the Tersoff potential we can identify which components of the Tersoff potential (equation 3.1) lack the flexibility required to model both the dynamic and the elastic properties of a material. The exponential Morse-like bonding terms are responsible for modelling the radial repulsive and attractive forces between atom i and neighbour atom j. These terms

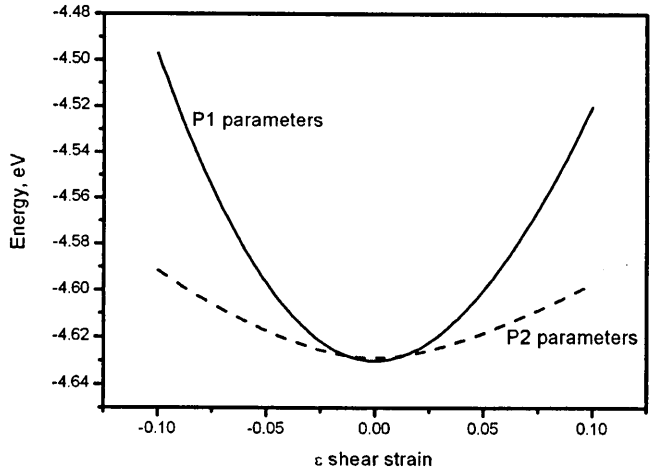

Figure 5.52: The energy of the Powell(P1) and Powell(P2) parameters for silicon plotted against the shear parameter ϵ

are only dependent upon the bonding distance r_{ij} and although they contribute to the hydrostatic strain energy and the cohesive energy, they have only a partial effect on the shear energy which is related to both the bond lengths and the angles subtended by the $i-j$ and the $i-k$ bonds.

Tersoff based the modelling of the bond-order term b_{ij} upon the empirically observed relation that $b_{ij} \propto z^{-1/2}$ and demonstrated that the term produced correct results for open lattice shapes. However, the value of the shear modulus is very strongly dependent on the angular bonding function $g(\theta_{jik})$ which models the bonding angles. Furthermore, the value of c_{44} is based upon the angular bonding function and the crystal anti-symmetry term ω_{ik} which models the lengths of the atomic bonds compared to the neighbouring bonds and these terms are both contained in the bond-order term b_{ij}.

Figure 5.53 highlights the massive difference between the the angular bonding term $g(\theta_{jik})$ for the two silicon parameterisations, where P1 is fit to the elastic properties and P2 is fit to the phonon frequencies. The nature of the parameterisation routine implies that although the Tersoff parameters that were fit to the phonon frequencies have a reduced angular bonding effect, the other parameters will be adjusted to compensate for this effect, producing a correct cohesive energy and lattice parameter.

This appears to be the source of the unexpected results. The balance between the radial and angular forces in the Tersoff model is very subtle and requires fine tuning by the parameterisation routine to predict the elastic properties of the material. Currently when the parameters are modified to fit to the dynamical

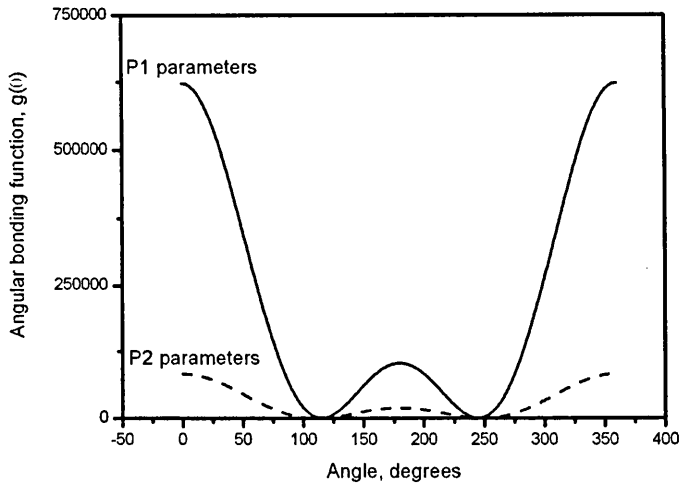

Figure 5.53: The angular functions of the Powell(P1) and Powell(P2) parameters for silicon

properties of the material, the lack of flexibility available to balance the two contributing factors, the radial and angular forces, is causing a trade-off in the ability to model both sets of material properties.

A change in the angular bonding term $g(\theta_{jik})$ is recommended to provide a more flexible form of the potential. The current form employs 3 parameters that are independent from the rest of the model c, d and h and takes the form:

$$g(\theta_{jik}) = 1 + \frac{c^2}{d^2} - \frac{c^2}{d^2 + (h - \cos(\theta_{jik}))^2} \tag{5.10}$$

Conrad and Scheerschmidt[51] provided a recommendation for a modification of the Tersoff angular bonding function $g_\sigma(\theta_{jik})$ that was numerically very similar to the Tersoff form which we extend here with another parameter and a further term to provide more flexibility in the Tersoff potential:

$$g^p(\theta_{jik}) = \psi_0 + \psi_1 \cos(\theta_{jik}) + \psi_2 \cos(2\theta_{jik}) + \psi_4 \cos(4\theta_{jik}) \tag{5.11}$$

Figure 5.54 shows the ω_{ik} term of the potential that is balancing the bonding energy of the k atoms with the angular bonding energy:

$$\omega_{ik} = \exp\left[\lambda^3 (r_{ij} - r_{ik})^3\right] \tag{5.12}$$

This is the only term in the potential that takes account of unbalanced bond

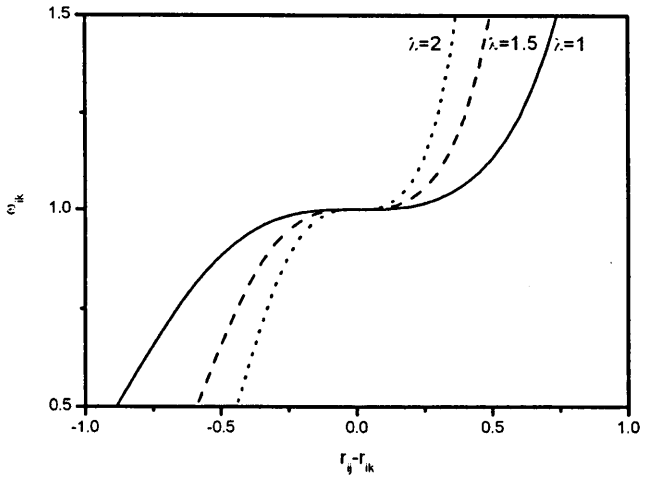

Figure 5.54: A graphic of the ω_{ik} function from eq. 5.12. The units of $r_{ij} - r_{ik}$ are Angstroms.

lengths in the tetrahedral bond. Although the form can be modified with the parameter λ the functional form has a symmetric region of the equation around zero - which is not physically correct. The change in energy when moving two atoms closer together is greater than when moving two atoms away from each other and this is not modelled by the current form of ω_{ik}. A change of the functional form of the Tersoff potential and the addition of a new parameter to the parameter space ρ is recommended based upon this reasoning. The new form of the anti-symmetric bonding term is labelled ω_{ik}^{p} and includes a simple linear term to add a slope to the current functional form to account for the different energies as the atom moves positively and negatively form the equilibrium location and is shown below:

$$\omega_{ik}^{p} = \exp\left[\lambda^3(r_{ij} - r_{ik})^3 + \rho(r_{ij} - r_{ik})\right] \tag{5.13}$$

The form of ω_{ik}^{p} is plotted in figure 5.55 and demonstrates the modification to the functional form to provide more flexibility and another parameter to improve the modelling of both the elastic and the dynamical properties of a material with a single set of Tersoff parameters[52].

5.5 Conclusions

In conclusion, the current form of the Tersoff PEF has been shown to be unsuitable to replicate both the elastic properties and the dynamical effects of diamond and

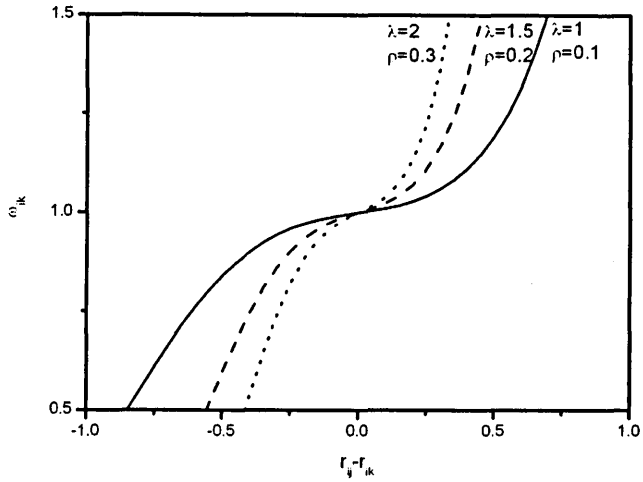

Figure 5.55: The modified ω_{ik}^{p} function

zinc blende solids. The source of this problem has been identified and a solution has been recommended based upon two simple modifications to the functional form of the Tersoff potential and the addition of 2 more Tersoff parameters bringing the total number of fitting parameters to 12.

Furthermore, a simple "rule of thumb" has been found to allow us to approximate the effective ionic charge of a lattice using only the optical X-point phonons. The rule appears to approximate the ionicity of polar semiconductors of type III-As, III-P and III-Sb with an amazing degree of accuracy compared to complicated models based upon physical reasoning.

A thorough investigation of the analytical form of the Tersoff potential has taken place and resulted in a modification to the functional form of the potential. A modified form of the Tersoff potential has been proposed that will address the issue of finding a single set of parameters to model both the elastic and dynamical properties whilst perserving the important bond-order properties.

There is plenty of scope for further work provided in the above investigation. The new form of the Tersoff potential needs to be thoroughly investigated and parameterised for the elastic and dynamical properties of the materials above. The limitations of the new form of the Tersoff potential need to be investigated and reported upon and finally the results from the investigation need to be published within the scientific community.

Bibliography

[1] A. A. Maradudin, E. W. Montroll, G. H. Weiss, and I. P. Ipatova, *Theory of lattice dynamics in the harmonic approximation.* Academic Press, New York & London, 1971.

[2] D. Strauch and B. Dorner, "Phonon dispersion in gaas," *J. Phys.: Condens. Matter*, vol. 2, no. 6, pp. 1457–1474, 1990.

[3] J. Tersoff, "Modeling solid-state chemistry: Interatomic potentials for multicomponent systems," *Phys. Rev. B*, vol. 39, no. 8, pp. 5566–5568, 1989.

[4] B. Schrader, *Infrared and Raman Spectroscopy.* VCH Publishers Inc., New York, 1995.

[5] M. D. Morris, *Applied Laser Spectroscopy.* VCH Publishers Inc., New York, 1992.

[6] G. Dolling, *Proc. Symp. Inelastic Scattering Neutrons in Solids and Liquids.* Chalk River, IAEA, Vienna, 1963, vol. 2.

[7] R. Tubino, L. Piseri, and G. Zerbi, "Lattice dynamics and spectroscopic properties by a valence force potential of diamondlike crystals: C, Si, Ge, and Sn," *J. Chem. Phys.*, vol. 56, no. 3, pp. 1022–1039, 1972.

[8] L. J. Porter, J. F. Justo, and S. Yip, "The importance of grüneisen parameters in developing interatomic potentials," *J. Appl. Phys.*, vol. 82, no. 11, pp. 5378–5381, 1997.

[9] R. Trommer, H. Muller, M. Cardona, and P. Vogl, "Dependence of the phonon spectrum of InP on hydrostatic pressure," *Phys. Rev. B*, vol. 21, no. 10, pp. 4869–4878, 1980.

[10] S. A. Solin and A. K. Ramdas, "Raman spectrum of diamond," *Phys. Rev. B*, vol. 1, no. 4, pp. 1687–1698, 1970.

[11] G. Nilsson and G. Nelin, "Study of the homology between silicon and germanium by thermal-neutron spectrometry," *Phys. Rev. B*, vol. 6, no. 10, pp. 3777–3786, 1972.

[12] R. Smith, "A semi-empirical many-body interatomic potential for modelling dynamical processes in gallium arsenide," *Nucl. Instr. Meth. Phys. Res. B*, vol. 67, pp. 335–339, 1992.

[13] M. Sayed, J. H. Jefferson, A. B. Walker, and A. G. Cullis, "Molecular dynamics simulations of implantation damage and recovery in semiconductors," *Nucl. Instr. Meth. Phys. Res. B*, vol. 102, pp. 218–222, 1995.

[14] J. L. T. Waugh and G. Dolling, "Crystal dynamics of gallium arsenide," *Phys. Rev.*, vol. 132, no. 6, pp. 2410–2412, 1963.

[15] S. Q. Wang and H. Q. Ye, "Ab initio investigation of the pressure dependences of phonon and dielectric properties for III-V semiconductors," *J. Phys.: Condens. Matter*, vol. 17, pp. 4475–4488, 2005.

[16] O. L. Lazarenkova, P. von Allmen, F. Oyafuso, S. Lee, and G. Klimeck, "Effect of anharmonicity of the strain energy on band offsets in semiconductor nanostructures," *Appl. Phys. Lett.*, vol. 85, no. 18, pp. 4193–4195, 2004.

[17] P. A. Ashu, J. H. Jefferson, A. G. Cullis, W. E. Hagston, and C. R. Whitehouse, "Molecular dynamics simulation of (100) InGaAs/GaAs strained layer relaxation processes," *J. Crys. Grow.*, vol. 150, pp. 176–179, 1995.

[18] K. Nordlund, J. Nord, J. Frantz, and J. Keinonen, "Strain-induced Kirkendall mixing at semiconductor interfaces," *Comp. Mater. Sci.*, vol. 18, no. 3, pp. 283–294, 2000.

[19] M. A. Migliorato, D. Powell, S. L. Liew, A. G. Cullis, M. Fearn, J. H. Jefferson, P. Navaretti, M. J. Steer, and M. Hopkinson, "Influence of composition on the piezoelectric fields and on the conduction band energy levels of $In_XGa_{1-X}As$/GaAs quantum dots," *J. Appl. Phys.*, vol. 96, p. 5169, 2004.

[20] M. A. Migliorato, D. Powell, E. A. Zibik, L. R. Wilson, M. Fearn, J. H. Jefferson, M. J. Steer, M. Hopkinson, and A. G. Cullis, "Anisotropy of the electron energy levels in $In_XGa_{1-X}As$/GaAs quantum dots with non-uniform composition," *Physica E*, vol. 26, p. 436, 2005.

[21] J. A. Sanjurjo, E. Lopez-Cruz, P. Vogl, and M. Cardona, "Dependence on volume of the phonon frequencies and their effective charges of several III-V semiconductors," *Phys. Rev. B*, vol. 28, no. 8, pp. 4475–4488, 1983.

[22] R. Carles, N. Saint-Cricq, J. B. Renucci, M. A. Renucci, , and A. Zwick, "Second-order raman scattering in InAs," *Phys. Rev. B*, vol. 22, pp. 4804–4815, 1980.

[23] A. S. Barker, "Dielectric dispersion and phonon line shape in GaP," *Phys. Rev.*, vol. 165, no. 3, pp. 917–922, 1968.

[24] M. V. Hobden and J. P. Russell, "The raman spectrum of gallium phosphide," *Phys. Lett.*, vol. 13, no. 1, pp. 39–41, 1964.

[25] K. Suto and J. Nishizawa, "Radiative recombination mechanisms in stoichiometry-controlled GaP crystals," *J. Appl. Phys.*, vol. 67, no. 1, p. 459, 1990.

[26] P. H. Borcherds, K. Kunc, G. F. Alfreys, and R. L. Hall, "The lattice dynamics of gallium phosphide," *J. Phys. C: Solid State Phys.*, vol. 12, pp. 4699–4706, 1979.

[27] S. Adachi, *Physical Properties of III-V Semiconductor Compounds : InP, InAs, GaAs, GaP, InGaAs, and InGaAsP.* Wiley & Sons, 1992.

[28] S. S. Mitra, "Phonon assignments in ZnSe and GaSb and some regularities in the phonon frequencies of zinc blende type semiconductors," *Phys. Rev.*, vol. 132, no. 3, pp. 986–991, 1963.

[29] P. S. Dutta, H. L. Bhat, and V. Kumar, "The physics and technology of gallium antimonide: An emerging optoelectronic material," *J. Appl. Phys.*, vol. 81, no. 9, pp. 5821–5870, 1997.

[30] M. K. Farr, J. G. Traylor, and S. K. Sinha, "Lattice dynamics of gasb," *Phys. Rev. B*, vol. 11, no. 4, pp. 1587–1594, 1974.

[31] D. L. Price, J. M. Rowe, and R. M. Nickov, "Lattice dynamics of grey tin and indium antimonide," *Phys. Rev. B*, vol. 3, no. 4, pp. 1268–1279, 1971.

[32] P. H. Borcherds and K. Kunc, "The lattice dynamics of indium pnictides," *J. Phys. C: Solid State Phys.*, vol. 11, pp. 4145–4155, 1978.

[33] K. Albe and W. Moller, "Modelling of boron nitride: Aomic scale simulations on thin film growth," *Comp. Mat. Sci.*, vol. 10, pp. 111–115, 1998.

[34] W. Sekkal, A. Laref, H. Aourag, A. Zaoui, and M. Certier, "The miscibility of $Cu_XAg_{1-X}I$ using a Tersoff potential," *Superlatt. Microstruct.*, vol. 28, no. 1, pp. 55–66, 2000.

[35] ——, "The miscibility of copper halides using a three-body potential. Part II: $CuBr_XI_{1-X}$," *J. Mat. Sci.*, vol. 11, no. 1, pp. 123–129, 2000.

[36] K. Karch and F. Bechstedt, "Ab initio lattice dynamics of BN and AlN: Covalent versus ionic forces," *Phys. Rev. B*, vol. 56, no. 12, pp. 7404–7415, 1997.

[37] F. Bechstedt, U. Grossner, and J. Furthmuller, "Dynamics and polarisation of group-III nitride lattices: A first principles study," *Phys. Rev. B*, vol. 62, no. 12, p. 8003, 2000.

[38] K. Kim, W. R. L. Lambrecht, and B. Segall, "Elastic constants and related properties of tetrahedrally bonded BN, AlN, GaN and InN," *Phys. Rev. B*, vol. 53, no. 24, pp. 16310–16326, 1996.

[39] F. Benkabou, H. Aourag, P. J. Becker, and M. Certier, "Molecular dynamics study of zinc blende GaN, AlN and InN," *Molecular Simulation*, vol. 23, pp. 327–341, 2000.

[40] A. R. Goni, H. Siegle, K. Syassen, C. Thomsen, and J. M. Wagner, "Effect of pressure on optical phonon modes and transverse effective charges in GaN and AlN," *Phys. Rev. B*, vol. 64, no. 3, p. 035205, 2001.

[41] J. M. Wagner and F. Bechstedt, "Pressure dependence of the dielectric and lattice-dynamical properties of GaN and AlN," *Phys. Rev. B*, vol. 62, no. 7, p. 4526, 2000.

[42] S. Goumri-Said, M. B. Kanoun, A. E. Merad, G. Merad, and H. Aourag, "Prediction of structural and thermodynamic properties of zinc-blende AlN: molecular dynamics simulation," *Chem. Phys.*, vol. 302, pp. 135–141, 2004.

[43] R. W. Keyes, "Trends in the lattice combination bands of zinc blende type semiconductors," *J. Chem. Phys.*, vol. 37, no. 1, pp. 72–73, 1962.

[44] C. R. A. Catlow and A. M. Stoneham, "Ionicity in solids," *J. Phys. C: Solid State Phys.*, vol. 16, pp. 4321–4338, 1983.

[45] W. R. Frensley and H. Kroemer, "Interstitial potential differences, electronegativity differences and effective ionic charges in zinc blende type semiconductors," *Appl. Phys. Lett.*, vol. 31, no. 1, pp. 48–49, 1977.

[46] W. A. Harrison, "Effective charges and piezoelectricity," *Phys. Rev. B*, vol. 10, no. 2, pp. 767–770, 1974.

[47] B. Szigeti, "Polarisability and dielectric constant of ionic crystals," *Trans. Faraday Soc.*, vol. 45, p. 155, 1949.

[48] K. G. Hambleton, C. Hilsum, and B. R. Holeman, "Determination of the effective ionic charge of gallium arsenide from direct measurements of the dielectric constant," *Proc. Phys. Soc.*, vol. 77, pp. 1147–1148, 1961.

[49] W. A. Harrison, *Electronic structure and the properties of solids.* Dover Publications, Inc., 1980.

[50] M. Nakamura, H. Fujioka, K. Ono, M. Takeuchi, T. Mitsui, and M. Oshima, "Molecular dynamics simulation of III-V compound semiconductor growth with MBE," *J. Crys. Grow.*, vol. 209, pp. 232–236, 2000.

[51] D. Conrad and K. Scheerschmidt, "Empirical bond-order potential for semiconductors," *Phys. Rev. B*, vol. 58, no. 8, pp. 4538–4542, 1998.

[52] D. Powell, M. A. Migliorato, and A. G. Cullis, "Modifications to the tersoff potential to improve the modelling of elasticity and dynamical properties," *To Be Submitted*, 2006.

Chapter 6

Conclusions & Further Work

6.1 Discussion & Conclusions

Modelling with the Tersoff empirical potential provides a fast and an accurate method of calculation of the interatomic forces in open cubic lattice structures. The literature review highlighted that, although the model is in use by many research groups around the world, many authors are relying upon the parameterisations of others which can be somewhat inaccurate. Many authors are still relying upon the original type IV elemental parameterisations by Tersoff in 1989 which have been demonstrated to provide reasonable results that are comparable to Keating's VFF method. However, the Tersoff potential provides a much larger parameter space and due to the bond-order nature of the functional form can approximate the second moment of electronic density - which is essential for modelling the higher order properties of semiconducting materials such as elasticity and lattice dynamics.

A local and a global parameterisation algorithm have been described and have been demonstrated to work extremely efficiently. However, the time required to search a 10 dimensional parameter space globally using stochastic methods (with 5000 starting points) was three orders of magnitude larger than the time required to search locally with a single known starting point provided by another author. The local search algorithm has been demonstrated as fast, efficient and accurate for minimising a multidimensional search space for a single objective function.

X-ray crystallography, inelastic neutron scattering and Raman spectroscopy data from the literature have been combined with the ab initio DFT predictions of elastic and small strain effects from various authors to produce a materials properties database for 13 different semiconductor systems. This materials properties database has been used to develop Tersoff parameterisations for each of the

different semiconductor systems and result in a library of Tersoff parameters of unparallelled accuracy. The work presented here improves upon the work of all previous authors in terms of the modelling of elastic properties of materials and predicting small strain effects (e.g. Kleinman's internal displacement parameter). The method of searching for parameters and testing them against the materials property databases has been refined both in terms of accuracy and speed and it is now possible to parameterise a new semiconductor system to match the elastic properties and small strain effects in under 5 minutes.

Inspection of the large database of materials properties showed trends in the experimental results and provided an excellent opportunity to examine Keyes' relations for a simple prediction of the elastic constants of III-V materials using only the lattice parameter. The work of another author was considered and improved upon and the elastic properties of the Aluminium-V materials were predicted with reasonable accuracy considering the complex relationships between the elastic properties of the materials and their constituent atomic components.

Second derivatives of the Tersoff potential have been calculated analytically and presented in Appendix A. The inclusion of these derivatives into a dynamical matrix computation has provided an opportunity to examine in detail the errors introduced into a computer program by the inclusion of numerical derivative methods. The form of the dynamical calculations, which includes a large number of summations, has demonstrated that the compound errors introduced by the use of numerical derivatives in D-matrix calculations is completely unacceptable. Furthermore, the numerical form of the second derivatives takes 2 orders of magnitude longer to compute than the analytical functional form. Although the numerical second derivatives routine has large errors at the zero energy points of the phonon dispersion, the errors in the higher frequency phonon values are smaller and provided a good method of debugging and testing the analytical routine.

A comparison of the numerical and analytical forms of the derivatives has allowed a computer program to be developed that will approximate the lattice dynamics of unstrained bulk semiconductor materials using a rigid-ion harmonic model. The program can predict the phonon dispersion curves between the BZ centre and 2 points of high symmetry including the associated mode-Grüneisen parameters for a single semiconductor system in 0.04 seconds on a laptop. This is quite a remarkable feat when compared to similar calculations using *ab initio* methods. This method is scaleable both in terms of the size of the model we can work with and the computing hardware it will run on. This provides an excellent opportunity to predict the phonon frequencies across a large-scale semiconductor

system (e.g. a 1,000,000 atom quantum dot model) in a reasonable amount of time.

Dynamical properties of 13 elemental type-IV diamond and III-V zinc blende compound semiconductor systems were calculated. Although the results were unexpected, a thorough investigation has taken place and the trends leading to the unpredicted results have been identified. A clear case has been made for the inclusion of an ionicity approximation which would improve the dynamical studies of III-V compound semiconductors to correctly model the optical phonon branch crossing and the energy splitting at the Brillouin Zone centre.

Included in the conclusions of the dynamical calculations are improvements to the functional form of the Tersoff potential to allow for flexibility when modelling both the elastic properties and the dynamical properties of semiconductor systems. The inclusion of two extra parameters and a slight modification to the functional form of the Tersoff potential will provide a model that can replicate the shear strain effects of the bulk lattice correctly and provide accurate predictions for the dynamical system properties using a rigid-ion calculation[1].

Combining the experimental and DFT predicted data for the phonon dispersion curved provided an opportunity to briefly examine the relationship between effective ionic charge and the X-point phonon frequencies. A very simple model has been suggested for the approximation of the effective ionic charge in a bulk unstrained solid that produced remarkable results. When compared to the vastly complicated calculations offered by a number of other authors, the simple calculation offers highly accurate predictions based upon a simple observation made by Keyes and clearly links together the phonon frequencies and the effective ionic charge of a III-V compound material.

Key to the usefulness of this thesis and future work has been the development of the library of Tersoff parameters for use in Molecular Dynamics code for the simulation of small-strain bulk semiconductors. The parameters for silicon, diamond carbon and germanium originally proposed by Tersoff have been vastly improved upon. The parameters for GaAs and InAs have been fit to DFT predictions and are more accurate than a number of other previous parameterisations. The first parameterisations of the materials GaP, InP, GaSb and InSb are now available and are can predict the elastic properties of the materials with an extremely low tolerance. A new set of parameters for each of the cubic III-N materials have been suggested here including Boron Nitride. These new parameters correct errors in previous work available in the literature and provide a more accurate method of calculation of the elastic properties of these important materials.

6.2 Recommendations for Future Work

Modifying the Tersoff Potential

A clear case has been made for the modification of the Tersoff potential to take account of the lack of flexibility when modelling both the elastic properties and the dynamical properties of the material. The proposed modifications are currently a theoretical prediction based upon observations of the functional behaviour of the potential and have not been included in the computer code. To include the proposed modifications in the computer code completely to test the quality of the modification and perform new parameterisations, a number of subroutines need to be modified and tested:

- Include the modification in the energy calculation routines.
- Calculate the analytical form of the second derivatives of the modifications.
- Include the modifications in the second derivative calculation routines.
- Increase the size of the parameter search space from 10 dimensions to 12 dimensions to account for the modified Tersoff potential.

Once the modifications to the Tersoff routine have been thoroughly tested to ensure error free operation of the computer code then the parameterisations can begin. The size of the search space has been increased by another 2 dimensions which is estimated to increase the time required to search the parameter space by global methods by another 2 orders of magnitude. It is recommended that the local search routine is used with the current parameters as starting points and that only type-IV cubic materials are parameterised to investigate the performance of the modified form of the Tersoff potential with respect to correcting the phonon dispersion trends seen in the previous chapter.

If the modifications to the Tersoff potential have the predicted effect and the materials can be parameterised correctly for both the elastic properties and the dynamical characteristics then it is recommended that a correction be made to the energy function to take account of the long range ionic bonding in the material. A simple Ewald summation of the form shown in equation 5.9 has been demonstrated by Nakamura[2] to work well for III-V growth simulations. A number of techniques exist but due to the long range nature of the forces to be considered, computational speed can be an issue with a simple long-range summation. A technique suggested by Greengard[3] called the Fast Multipole Method (FMM)

is popular as it is equivalent to the Ewald summation and has an O(N) performance. The FMM can be parallelised as demonstrated by Nakano[4] which allows for spatial decomposition across cell boundaries - which is essential for high speed parallel calculations. Another popular method in the literature is the Smooth Particle Mesh Ewald technique[5] which uses a combination of B-spline techniques and fast Fourier transformations to increase the calculation speed of the particle contributions to the ionic energy in k-space. Any further investigations into the dynamical properties of the III-V semiconductors must include an ionicity correction to allow for the prediction of the correct phonon behaviour.

Further Modifications to the Software

The software developed for this thesis does not include the hexagonal phases of the materials such as simple hexagonal (sh) and wurtzite. This is because it is not possible for the current or the modified Tersoff potential to take account of the spontaneous polarisation effects observed in the III-V wurtzite lattice structures. The spontaneous polarisation, which is an effect caused by a small movement of the cation sublattice compared to the anion sublattice in the relaxed hexagonal structure, is essential in atomistic scale modelling and is not a strain effect but rather a second order effect based upon the charge and location of the second nearest neighbours. Recent reports[6] have investigated use of the Berry-phase approach[7] to polarisation in solids for the DFT prediction of spontaneous polarisation in III-N wurtzite lattices. The Berry-phase is defined in crystalline solids by the reciprocal space bandstructure which requires a complex calculation of Born charge based upon the wavefunction values with respect to a phonon perturbation. This is clearly beyond the scope of this work and demands first principles computational methods, which are not in keeping with the essence of an empirical potential. However, work could be carried out to investigate increasing the bond-order term in the Tersoff potential to account for the second nearest neighbours in wurtzite geometry and provide a spontaneous unstrained lattice movement.

The global parameterisation routine included in this work is not very efficient and relies very heavily upon dumb stochastic search methods. The search technique could be vastly improved by the use of Evolutionary Algorithms such as Genetic Algorithm[8] or the more modern Particle Swarm Optimisation[9] technique which add an element of artificial intelligence to the search routines. There is a clear case for a thorough investigation into the searching of such a large and undefined parameter landscape provided by the Tersoff parameterisation. The

task could easily be decomposed into a Multiobjective Optimisation[10] given the nature of the 2 clear objective functions (minimise the error in both the elastic properties and the dynamical properties) and a search for the optimal Pareto Front[11] for a given Tersoff parameter set could be combined with an Evolutionary Algorithm. The information gleaned from this investigation could provide the ability to link together the materials properties and the Tersoff parameters in a way that could locate a Pareto optimal parameter set and circumvent the requirements to search the global parameter space when adding a new material to the parameter library. This is a very interesting problem and could make for an excellent body of work.

Due to time restrictions the software used in this work has only been subject to simple algorithmic and compiler-level optimisations. There is still much room for improvement in the speed of calculation of the Tersoff potential energy and the partial second derivatives analytically based upon techniques such as loop jamming, inline assembly coding maths functions such as the square root and power series evaluations and replacement of the trigonometric functions with look-up tables. A thorough investigation is recommended into the effects of these high-speed approximations upon the timing and accuracy of the final results compared to the methods based upon algorithmic optimisations. Due to the iterative nature of the calculations involved in MD software, every cycle that can be saved in an evaluation has a massive impact on the overall timing of the software.

The second derivatives of the Tersoff potential were added into the software after the elastic property calculations were written. The elastic property calculations are based upon numerical evaluation of the second derivatives of the Tersoff potential, which are now fully available in the code. By re-designing the code to take advantage of the analytic derivatives to evaluate the elastic properties we should be able to speed-up the code further and to remove any possible source of errors from the Euler approximations involved in the simple numerical derivatives. Although this is considered to have a minimal effect on the accuracy of the current parameters, it will add further impact to the accuracy of the technique as a large-scale competitor to first-principles DFT calculations.

Currently, the software written for this investigation is based upon high speed Tersoff parameterisation techniques and does not include any Molecular Dynamics or structural relaxation code. Modification of the Tersoff potential as described above will require Molecular Dynamics code that can take advantage of the the new functional form and the associated parameter library. The modification of existing open source Molecular Dynamics code is highly recommended as this will allow large-scale models to be constructed and studied under varying condi-

tions. This is essential to make a case for the modifications of the Tersoff potential and wide-spread adoption of the method as the definitive high-speed structural simulation technique for semiconductor modelling. The MD code should be fully portable, free of charge and easy to modify. The modified potential energy evaluation routines should be optimised for high speed operation and the MD code should be designed for parallel architecture use. All of this should be made available to as many people as possible to ensure the global recognition of the modified Tersoff potential.

In future there should be time to investigate novel methods of elastic property modelling such as the model proposed by Elder[12]) which describes the statics and dynamics of a conserved field. This is applied to the hexagonal ring structure demonstrated in lattice modelling and promises simulations that are many orders of magnitude faster then conventional relaxation.

The transferability of the Tersoff potential to modelling semiconductor surfaces and surface reconstructions has been briefly mentioned by a number of other authors in the literature. This has not been included in this work due to time and space restrictions, but a thorough investigation into the modelling of surface reconstructions using the Tersoff potential and the prediction of the relaxed energy states of the surface atoms compared to DFT modelling would make for an interesting piece of work. The modelling of the surface reconstructions could be also introduced into the objective functions for the locating the minima in the 12 dimensional parameter space offered by the modified Tersoff potential suggested here and this would lead to a three dimensional Pareto front. It is conjectured that the modified Tersoff potential will be able to better model the positions and energies of surface atoms due to the more flexible nature of the bonding angle terms and the modified bond anti-symmetry modelling.

Publication Strategy

The library of Tersoff parameters presented here include the type-IV elemental semiconductors and a large number of the cubic III-V systems. This library should be extended to include the Aluminium-V materials and the library should then be published with all of the associated results to demonstrate the usefulness of the parameters for MD relaxation and simulation of low-strain systems and to demonstrate that we have achieved the definitive library of Tersoff parameters for cubic III-V semiconductors. In addition, it would not require much work to extend the library to include the II-VI semiconductor systems such as ZnS and CdS and it is recommended that this follows the III-V library paper as soon as

possible.

Once the modified Tersoff potential has been proven to be able to accurately model the elasticity and the dynamical properties of the materials this should immediately be introduced to the scientific community. The impact of a publication that demonstrates the transferability of the Tersoff potential to dynamical modelling is anticipated to be large. Publications based upon the expansion of the dynamical modelling from a simple bulk dimer to large-scale models that predict the experimental phonon modes in strained semiconductor systems such as quantum dots would be well received and generate interest for the modified Tersoff potential. Obviously libraries of parameterisations for the modified Tersoff potential would be required for the type-IV elemental semiconductors, the III-V semiconductors and possibly II-VI componds.

A "how-to" style publication based upon the computational techniques involved in numerically computing the Tersoff potential and speeding up the Tersoff calculation routines and the second derivative calculations in a journal concerned with computational physics would draw more attention to the Tersoff potential and ensure that it is included in as many molecular dynamics codes as possible. This would have an obvious knock-on effect for the visibility of the Tersoff parameter libraries.

The development of code for an investigation into the Evolutionary Algorithms and the Pareto Front associated with the Tersoff potential would draw much interest in solving the potential as a test bench algorithm for the development of Genetic Algorithms and Particle Swarm Optimisation routines. When investigating the efficiency of an Evolutionary Algorithm it is common to test it against a number of as-yet unsolved problems in a multidimensional parameter space to measure the speed and efficiency of the solution convergence. The parameterisation of the Tersoff potential is ideal for this task and if the function could be demonstrated as a useful test bench for such purposes, this would further raise the visibility of the potential and the parameter library developed in this work.

An investigation into pseudomorphic growth strain and Kleinman's internal displacement parameter is proceeding based upon this work and the comparison of the Tersoff potential and DFT calculations for the prediction of the internal sublattice displacement in low-strain growth of InAs on GaAs. This was not included due to time and space restrictions, but it is anticipated that this will raise the profile and awareness of the Tersoff potential as an alternative to DFT simulation in situations that require large-scale simulations.

Finally, this entire work has been based upon parameterising the Tersoff po-

tential. There is a clear advantage available here as the library is fully available now and investigations into performing MD simulations in-house should begin at once. This will prove that the parameters offered here are more accurate for large-scale modelling such as quantum wells, wires and dots and for modelling nanotubes and carbon polytypes such as the C_{60} molecule. The publication of simulation papers using the Tersoff potential library will add weight to the importance of the parameters and demonstrate the usefulness of the parameters and the transferability of the potential to multiple large-scale models.

Bibliography

[1] D. Powell, M. A. Migliorato, and A. G. Cullis, "Modifications to the tersoff potential to improve the modelling of elasticity and dynamical properties," *To Be Submitted*, 2006.

[2] M. Nakamura, H. Fujioka, K. Ono, M. Takeuchi, T. Mitsui, and M. Oshima, "Molecular dynamics simulation of III-V compound semiconductor growth with MBE," *J. Crys. Grow.*, vol. 209, pp. 232–236, 2000.

[3] L. Greengard and V. Rokhlin, "A fast algorithm for particle simulations," *J. Computer. Phys.*, vol. 73, no. 2, pp. 325–348, 1987.

[4] A. Nakano, R. K. Kalia, and P. Vashishta, "Multiresolution molecular dynamics algorithm for realistic materials modeling on parallel computers," *Computer. Phys. Comm.*, vol. 83, no. 2, pp. 197–214, 1994.

[5] M. L. B. T. D. H. L. U. Essmann, L. Perera and L. G. Pedersen, "A smooth particle mesh ewald method," *J. Chem. Phys.*, vol. 103, p. 8577, 1995.

[6] F. Bernardini, V. Fiorentini, and D. Vanderbilt, "Spontaneous polarization and piezoelectric constants of iii-v nitrides," *Phys. Rev. B*, vol. 56, no. 16, p. R10024, 1997.

[7] M. V. Berry, "Quantal phase factors accompanying adiabatic changes," *Proc. R. Soc. London, Ser. A*, vol. 392, no. 1802, pp. 45–57, 1984.

[8] C. A. Coello, "An updated survey of GA-based multiobjective optimisation techniques," *ACM Computing Surveys*, vol. 32, no. 2, pp. 109–143, 2000.

[9] K. E. Parsopoulos and M. N. Vrahatis, "Particle swarm optimisation method in multiobjective problems," *Proceedings of the 2002 ACM symposium on applied computing*, pp. 603–607, 2002.

[10] C. M. Fonseca and P. J. Fleming, "An overview of evolutionary algorithms in multiobjective optimization. evolutionary computation," *Evolutionary Computation*, vol. 3, no. 1, pp. 1–16, 1995.

[11] D. A. Van Veldhuizen and G. B. Lamont, "Evolutionary computation and convergence to a pareto front," in *Late Breaking Papers at the Genetic Programming 1998 Conference*, J. R. Koza, Ed. University of Wisconsin, Madison, Wisconsin, USA: Stanford University Bookstore, 1998.

[12] K. R. Elder, M. Katakowski, M. Haataja, and M. Grant, "Modelling elasticity in crystal growth," *Phys. Rev. Lett.*, vol. 88, no. 24, p. 245701, 2002.

Appendix A

Derivatives of the Tersoff Empirical Potential

Here we manually calculate the first and second derivatives of the Tersoff potential with respect to the individual cartesian axes. This work is necessary to provide a computation for the atomic forces associated with the Tersoff potential (first derivatives) and the phonon frequencies (computed from the dynamical matrix of second deivatives).

Notation

Initially we shall define out loop iterators m, n, p and q to allow for simplified notation in this document. Here $m = n = [x, y, z]$ and $p = q = [i, j, k]$. Where x, y and z represent the standard Cartesian orthogonal axes and i, j and k represent the atoms under investigation.

Cartesian vector components: x_{ij}, y_{ij}, z_{ij}

$$
\begin{aligned}
m_{ij} &= m_j - m_i \\
\frac{\partial m_{ij}}{\partial m_k} &= 0 \\
\frac{\partial m_{ij}}{\partial m_j} &= 1 \\
\frac{\partial m_{ij}}{\partial m_i} &= -\frac{\partial m_{ij}}{\partial m_j} \\
\frac{\partial m_{ij}}{\partial n_q} &= 0 \quad [m \neq n] \\
\frac{\partial^2 m_{ij}}{\partial m_p \partial n_q} &= 0
\end{aligned}
$$

Cartesian vector components: x_{ik}, y_{ik}, z_{ik}

$$
\begin{aligned}
m_{ik} &= m_k - m_i \\
\frac{\partial m_{ik}}{\partial m_k} &= 1 \\
\frac{\partial m_{ik}}{\partial m_j} &= 0 \\
\frac{\partial m_{ik}}{\partial m_i} &= -\frac{\partial m_{ij}}{\partial m_k} \\
\frac{\partial m_{ik}}{\partial n_q} &= 0 \quad [n \neq n] \\
\frac{\partial^2 m_{ij}}{\partial m_p \partial n_q} &= 0
\end{aligned}
$$

Cartesian vector length: r_{ij}

$$r_{ij} = \left[x_{ij}^2 + y_{ij}^2 + z_{ij}^2\right]^{0.5}$$

$$
\begin{aligned}
\frac{\partial r_{ij}}{\partial m_p} &= 0.5 \left[x_{ij}^2 + y_{ij}^2 + z_{ij}^2\right]^{-0.5} 2 m_{ij} \frac{\partial m_{ij}}{\partial m_p} \\
\frac{\partial r_{ij}}{\partial m_p} &= \left[x_{ij}^2 + y_{ij}^2 + z_{ij}^2\right]^{-0.5} m_{ij} \frac{\partial m_{ij}}{\partial m_p} \\
\frac{\partial r_{ij}}{\partial m_p} &= \frac{m_{ij}}{r_{ij}} \frac{\partial m_{ij}}{\partial m_p}
\end{aligned}
$$

Hence:

$$\frac{\partial r_{ij}}{\partial m_k} = 0$$
$$\frac{\partial r_{ij}}{\partial m_j} = \frac{m_{ij}}{r_{ij}}$$
$$\frac{\partial r_{ij}}{\partial m_i} = -\frac{\partial r_{ij}}{\partial m_j}$$

$$\begin{aligned}\frac{\partial^2 r_{ij}}{\partial n_q \partial m_p} = & \frac{\partial \left[x_{ij}^2 + y_{ij}^2 + z_{ij}^2\right]^{-0.5}}{\partial n_q} m_{ij} \frac{\partial m_{ij}}{\partial m_p} \\ & + \left[x_{ij}^2 + y_{ij}^2 + z_{ij}^2\right]^{-0.5} \frac{\partial m_{ij}}{\partial n_q} \frac{\partial m_{ij}}{\partial m_p} \\ & + \left[x_{ij}^2 + y_{ij}^2 + z_{ij}^2\right]^{-0.5} m_{ij} \frac{\partial^2 m_{ij}}{\partial n_q \partial m_p}\end{aligned}$$

$$\frac{\partial^2 r_{ij}}{\partial n_q \partial m_p} = \frac{1}{r_{ij}} - \frac{m_{ij} n_{ij}}{r_{ij}^3} \qquad [m = n; p = q]$$
$$\frac{\partial^2 r_{ij}}{\partial n_q \partial m_p} = \frac{1}{r_{ij}} + \frac{m_{ij} n_{ij}}{r_{ij}^3} \qquad [m = n; p \neq q]$$
$$\frac{\partial^2 r_{ij}}{\partial n_q \partial m_p} = -\frac{m_{ij} n_{ij}}{r_{ij}^3} \qquad [m \neq n; p = q]$$
$$\frac{\partial^2 r_{ij}}{\partial n_q \partial m_p} = \frac{m_{ij} n_{ij}}{r_{ij}^3} \qquad [m \neq n; p \neq q]$$
$$\frac{\partial^2 r_{ij}}{\partial n_q \partial m_p} = 0 \qquad [p, q = k]$$

Cartesian vector length: r_{ik}

$$r_{ik} = \left[x_{ik}^2 + y_{ik}^2 + z_{ik}^2\right]^{0.5}$$

$$\frac{\partial r_{ik}}{\partial m_p} = 0.5 \left[x_{ik}^2 + y_{ik}^2 + z_{ik}^2\right]^{-0.5} 2 m_{ik} \frac{\partial m_{ik}}{\partial m_p}$$
$$\frac{\partial r_{ik}}{\partial m_p} = \left[x_{ik}^2 + y_{ik}^2 + z_{ik}^2\right]^{-0.5} m_{ik} \frac{\partial m_{ik}}{\partial m_p}$$
$$\frac{\partial r_{ik}}{\partial m_p} = \frac{m_{ik}}{r_{ik}} \frac{\partial m_{ik}}{\partial m_p}$$

Hence:

$$\frac{\partial r_{ik}}{\partial m_k} = \frac{m_{ik}}{r_{ik}}$$
$$\frac{\partial r_{ik}}{\partial m_j} = 0$$
$$\frac{\partial r_{ik}}{\partial m_i} = -\frac{\partial r_{ik}}{\partial m_k}$$

$$\begin{aligned}\frac{\partial^2 r_{ik}}{\partial n_q \partial m_p} &= \frac{\partial \left[x_{ik}^2 + y_{ik}^2 + z_{ik}^2\right]^{-0.5}}{\partial n_q} m_{ik} \frac{\partial m_{ik}}{\partial m_p} \\ &+ \left[x_{ik}^2 + y_{ik}^2 + z_{ik}^2\right]^{-0.5} \frac{\partial m_{ik}}{\partial n_q} \frac{\partial m_{ik}}{\partial m_p} \\ &+ \left[x_{ik}^2 + y_{ik}^2 + z_{ik}^2\right]^{-0.5} m_{ik} \frac{\partial^2 m_{ik}}{\partial n_q \partial m_p}\end{aligned}$$

$$\frac{\partial^2 r_{ik}}{\partial n_q \partial m_p} = \frac{1}{r_{ik}} - \frac{m_{ik} n_{ik}}{r_{ik}^3} \qquad [m = n; p = q]$$
$$\frac{\partial^2 r_{ik}}{\partial n_q \partial m_p} = \frac{1}{r_{ik}} + \frac{m_{ik} n_{ik}}{r_{ik}^3} \qquad [m = n; p \neq q]$$
$$\frac{\partial^2 r_{ik}}{\partial n_q \partial m_p} = -\frac{m_{ik} n_{ik}}{r_{ik}^3} \qquad [m \neq n; p = q]$$
$$\frac{\partial^2 r_{ik}}{\partial n_q \partial m_p} = \frac{m_{ik} n_{ik}}{r_{ik}^3} \qquad [m \neq n; p \neq q]$$
$$\frac{\partial^2 r_{ik}}{\partial n_q \partial m_p} = 0 \qquad [p, q = j]$$

Cut-off function: $fc\left(r_{ij}\right)$

$$f_c\left(r_{ij}\right) = \begin{cases} 0 & , r_{ij} > (R + D) \\ \frac{1}{2}\left[1 - \sin\left[\frac{\pi(r_{ij} - R)}{2D}\right]\right] & , |r_{ij} - R| \leq D \\ 1 & , r_{ij} < (R - D) \end{cases}$$

The only differentiable component is the part occuring in the region $(R - D) \leq r_{ij} \leq (R + D)$, hence:

$$\frac{\partial fc(r_{ij})}{\partial m_p} = -\frac{1}{2}\frac{\pi}{2D}cos\left[\frac{\pi(r_{ij}-R)}{2D}\right]\frac{\partial(r_{ij}-R)}{\partial m_p}$$
$$\frac{\partial fc(r_{ij})}{\partial m_p} = -\frac{\pi}{4D}cos\left[\frac{\pi(r_{ij}-R)}{2D}\right]\frac{\partial r_{ij}}{\partial m_p}$$
$$\frac{\partial fc(r_{ij})}{\partial m_p} = -\frac{\pi}{4D}cos\left[\frac{\pi(r_{ij}-R)}{2D}\right]\frac{m_{ij}}{r_{ij}}\frac{\partial m_{ij}}{\partial m_p}$$
$$\frac{\partial fc(r_{ij})}{\partial m_k} = 0$$

$$\frac{\partial^2 fc(r_{ij})}{\partial n_q \partial m_p} = -\frac{\pi}{4D}\left[\frac{\partial}{\partial n_q}cos\left[\frac{\pi(r_{ij}-R)}{2D}\right]\frac{\partial r_{ij}}{\partial m_p} + cos\left[\frac{\pi(r_{ij}-R)}{2D}\right]\frac{\partial^2 r_{ij}}{\partial n_q \partial m_p}\right]$$
$$\frac{\partial^2 fc(r_{ij})}{\partial n_q \partial m_p} = \frac{\pi}{4D}\frac{\pi}{2D}sin\left[\frac{\pi(r_{ij}-R)}{2D}\right]\frac{\partial r_{ij}}{\partial n_q}\frac{\partial r_{ij}}{\partial m_p}$$
$$-\frac{\pi}{4D}cos\left[\frac{\pi(r_{ij}-R)}{2D}\right]\frac{\partial^2 r_{ij}}{\partial n_q \partial m_p}$$
$$\frac{\partial^2 fc(r_{ij})}{\partial n_q \partial m_p} = \frac{\pi^2}{8D^2}sin\left[\frac{\pi(r_{ij}-R)}{2D}\right]\frac{m_{ij}n_{ij}}{r_{ij}^2}\frac{\partial n_{ij}}{\partial n_q}\frac{\partial m_{ij}}{\partial m_p}$$
$$-\frac{\pi}{4D}cos\left[\frac{\pi(r_{ij}-R)}{2D}\right]\frac{\partial^2 r_{ij}}{\partial n_q \partial m_p}$$
$$\frac{\partial^2 fc(r_{ij})}{\partial n_q \partial m_p} = 0 \qquad [p,q=k]$$

Cut-off function: $fc(r_{ik})$

$$f_c(r_{ik}) = \begin{cases} 0 & ,r_{ik} > (R+D) \\ \frac{1}{2}\left[1-\sin\left[\frac{\pi(r_{ik}-R)}{2D}\right]\right] & ,|r_{ik}-R| \le D \\ 1 & ,r_{ik} < (R-D) \end{cases}$$

The only differentiable component is the part occuring in the region $(R-D) \le r_{ik} \le (R+D)$, hence:

$$\frac{\partial fc(r_{ik})}{\partial m_p} = -\frac{1}{2}\frac{\pi}{2D}cos\left[\frac{\pi(r_{ik}-R)}{2D}\right]\frac{\partial(r_{ik}-R)}{\partial m_p}$$
$$\frac{\partial fc(r_{ik})}{\partial m_p} = -\frac{\pi}{4D}cos\left[\frac{\pi(r_{ik}-R)}{2D}\right]\frac{\partial r_{ik}}{\partial m_p}$$
$$\frac{\partial fc(r_{ik})}{\partial m_p} = -\frac{\pi}{4D}cos\left[\frac{\pi(r_{ik}-R)}{2D}\right]\frac{m_{ik}}{r_{ik}}\frac{\partial m_{ik}}{\partial m_p}$$
$$\frac{\partial fc(r_{ik})}{\partial m_j} = 0$$

$$\frac{\partial^2 fc(r_{ik})}{\partial n_q \partial m_p} = -\frac{\pi}{4D}\left[\frac{\partial}{\partial n_q}cos\left[\frac{\pi(r_{ik}-R)}{2D}\right]\frac{\partial r_{ik}}{\partial m_p} + cos\left[\frac{\pi(r_{ik}-R)}{2D}\right]\frac{\partial^2 r_{ik}}{\partial n_q \partial m_p}\right]$$
$$\frac{\partial^2 fc(r_{ik})}{\partial n_q \partial m_p} = \frac{\pi}{4D}\frac{\pi}{2D}sin\left[\frac{\pi(r_{ik}-R)}{2D}\right]\frac{\partial r_{ik}}{\partial n_q}\frac{\partial r_{ik}}{\partial m_p}$$
$$-\frac{\pi}{4D}cos\left[\frac{\pi(r_{ik}-R)}{2D}\right]\frac{\partial^2 r_{ik}}{\partial n_q \partial m_p}$$
$$\frac{\partial^2 fc(r_{ik})}{\partial n_q \partial m_p} = \frac{\pi^2}{8D^2}sin\left[\frac{\pi(r_{ik}-R)}{2D}\right]\frac{m_{ik}n_{ik}}{r_{ik}^2}\frac{\partial n_{ik}}{\partial n_q}\frac{\partial m_{ik}}{\partial m_p}$$
$$-\frac{\pi}{4D}cos\left[\frac{\pi(r_{ik}-R)}{2D}\right]\frac{\partial^2 r_{ik}}{\partial n_q \partial m_p}$$
$$\frac{\partial^2 fc(r_{ik})}{\partial n_q \partial m_p} = 0 \qquad [p,q=j]$$

Bonding angle: $cos(\theta_{ijk})$

$$cos(\theta_{ijk}) = \frac{\vec{X}_j \cdot \vec{X}_k}{r_{ij}r_{ik}} = \frac{(x_{ij}x_{ik})+(y_{ij}y_{ik})+(z_{ij}z_{ik})}{r_{ij}r_{ik}}$$

This function contains components in i, j and k so must be explicitly written:

$$\frac{\partial cos(\theta_{ijk})}{\partial x_j} = \frac{\partial(x_{ij}x_{ik})+(y_{ij}y_{ik})+(z_{ij}z_{ik})}{\partial x_j}\frac{1}{r_{ij}r_{ik}}$$
$$+\frac{(x_{ij}x_{ik})+(y_{ij}y_{ik})+(z_{ij}z_{ik})}{r_{ik}}\frac{\partial r_{ij}^{-1}}{\partial x_j}$$
$$\frac{\partial cos(\theta_{ijk})}{\partial x_j} = \frac{x_{ik}}{r_{ij}r_{ik}} + \frac{(x_{ij}x_{ik})+(y_{ij}y_{ik})+(z_{ij}z_{ik})}{r_{ik}}\frac{-\frac{1}{2}2x_{ij}}{r_{ij}^3}$$

Therefore, we may write:

$$\frac{\partial cos\left(\theta_{ijk}\right)}{\partial m_k} = \frac{m_{ij}}{r_{ij}r_{ik}} - \frac{m_{ik}}{r_{ik}^2} cos\left(\theta_{ijk}\right)$$
$$\frac{\partial cos\left(\theta_{ijk}\right)}{\partial m_j} = \frac{m_{ik}}{r_{ij}r_{ik}} - \frac{m_{ij}}{r_{ij}^2} cos\left(\theta_{ijk}\right)$$
$$\frac{\partial cos\left(\theta_{ijk}\right)}{\partial m_i} = -\left[\frac{\partial cos\left(\theta_{ijk}\right)}{\partial m_j} + \frac{\partial cos\left(\theta_{ijk}\right)}{\partial m_k}\right]$$

The second derivatives are obtained:

$$\begin{aligned}\frac{\partial^2 cos\left(\theta ijk\right)}{\partial n_q \partial m_j} &= \frac{\partial m_{ik}}{\partial n_q}\frac{1}{r_{ij}r_{ik}} + \frac{m_{ik}}{r_{ik}}\frac{\partial \left[r_{ij}\right]^{-1}}{\partial n_q} + \frac{m_{ik}}{r_{ij}}\frac{\partial \left[r_{ik}\right]^{-1}}{\partial n_q} \\ &- \frac{\partial m_{ij}}{\partial n_q}\frac{1}{r_{ij}^2} cos\left(\theta_{ijk}\right) - m_{ij}\frac{\partial \left[r_{ij}\right]^{-2}}{\partial n_q} cos\left(\theta_{ijk}\right) - \frac{m_{ij}}{r_{ij}^2}\frac{\partial cos\left(\theta_{ijk}\right)}{\partial n_q} \\ \frac{\partial^2 cos\left(\theta ijk\right)}{\partial n_q \partial m_j} &= \frac{\partial m_{ik}}{\partial n_q}\frac{1}{r_{ij}r_{ik}} + \frac{m_{ik}}{r_{ik}}\frac{-n_{ij}}{r_{ij}^3}\frac{\partial n_{ij}}{\partial n_q} + \frac{m_{ik}}{r_{ij}}\frac{-n_{ik}}{r_{ik}^3}\frac{\partial n_{ik}}{\partial n_q} \\ &- \left[\frac{\partial m_{ij}}{\partial n_q}\frac{1}{r_{ij}^2} + m_{ij}\frac{-2n_{ij}}{r_{ij}^4}\frac{\partial n_{ij}}{\partial n_q}\right] cos\left(\theta_{ijk}\right) - \frac{m_{ij}}{r_{ij}^2}\frac{\partial cos\left(\theta_{ijk}\right)}{\partial n_q}\end{aligned}$$

Hence, we may write:

$$\begin{aligned}\frac{\partial^2 cos\left(\theta ijk\right)}{\partial n_q \partial m_k} &= \frac{\partial m_{ij}}{\partial n_q}\frac{1}{r_{ij}r_{ik}} - \frac{m_{ij}n_{ik}}{r_{ik}^3 r_{ij}}\frac{\partial n_{ik}}{\partial n_q} - \frac{m_{ij}n_{ij}}{r_{ik}r_{ij}^3}\frac{\partial n_{ij}}{\partial n_q} \\ &- \left[\frac{\partial m_{ik}}{\partial n_q}\frac{1}{r_{ik}^2} + m_{ik}\frac{-2n_{ik}}{r_{ik}^4}\frac{\partial n_{ik}}{\partial n_q}\right] cos\left(\theta_{ijk}\right) - \frac{m_{ik}}{r_{ik}^2}\frac{\partial cos\left(\theta_{ijk}\right)}{\partial n_q} \\ \frac{\partial^2 cos\left(\theta ijk\right)}{\partial n_q \partial m_j} &= \frac{\partial m_{ik}}{\partial n_q}\frac{1}{r_{ij}r_{ik}} - \frac{m_{ik}n_{ij}}{r_{ij}^3 r_{ik}}\frac{\partial n_{ij}}{\partial n_q} - \frac{m_{ik}n_{ik}}{r_{ij}r_{ik}^3}\frac{\partial n_{ik}}{\partial n_q} \\ &- \left[\frac{\partial m_{ij}}{\partial n_q}\frac{1}{r_{ij}^2} + m_{ij}\frac{-2n_{ij}}{r_{ij}^4}\frac{\partial n_{ij}}{\partial n_q}\right] cos\left(\theta_{ijk}\right) - \frac{m_{ij}}{r_{ij}^2}\frac{\partial cos\left(\theta_{ijk}\right)}{\partial n_q} \\ \frac{\partial^2 cos\left(\theta_{ijk}\right)}{\partial n_q \partial m_i} &= -\left[\frac{\partial^2 cos\left(\theta_{ijk}\right)}{\partial n_q \partial m_j} + \frac{\partial^2 cos\left(\theta_{ijk}\right)}{\partial n_q \partial m_k}\right]\end{aligned}$$

Angular dependence function: $g\left(\theta_{ijk}\right)$

$$g\left(\theta_{ijk}\right) = 1 + \frac{c^2}{d^2} - \frac{c^2}{d^2 + \left(h - cos\left(\theta_{ijk}\right)\right)^2}$$

The first derivatives are obtained:

$$\frac{\partial g(\theta_{ijk})}{\partial x_j} = c^2 \frac{1}{\left(d^2 + (h - cos(\theta_{ijk}))^2\right)^2} \frac{\partial (h - cos(\theta_{ijk}))^2}{\partial x_j}$$
$$\frac{\partial g(\theta_{ijk})}{\partial x_j} = c^2 \frac{1}{\left(d^2 + (h - cos(\theta_{ijk}))^2\right)^2} 2(h - cos(\theta_{ijk})) \frac{\partial - cos(\theta_{ijk})}{\partial x_j}$$
$$\frac{\partial g(\theta_{ijk})}{\partial x_j} = -\frac{2c^2 (h - cos(\theta_{ijk}))}{\left(d^2 + (h - cos(\theta_{ijk}))^2\right)^2} \frac{\partial cos(\theta_{ijk})}{\partial x_j}$$

Note that:

$$\frac{\partial g(\theta_{ijk})}{\partial m_p} = -\frac{2c^2 (h - cos(\theta_{ijk}))}{\left(d^2 + (h - cos(\theta_{ijk}))^2\right)^2} \frac{\partial cos(\theta_{ijk})}{\partial m_p}$$

And the second derivative can be written:

$$\frac{\partial^2 g(\theta_{ijk})}{\partial n_q \partial m_p} = \frac{\partial}{\partial n_q} \left[\frac{2c^2 (h - cos(\theta_{ijk}))}{\left[d^2 + (h - cos(\theta_{ijk}))^2\right]^2} \frac{\partial cos(\theta_{ijk})}{\partial m_p} \right]$$
$$\frac{\partial^2 g(\theta_{ijk})}{\partial n_q \partial m_p} = \frac{\partial 2c^2 (h - cos(\theta_{ijk}))}{\partial n_q} \frac{1}{\left[d^2 + (h - cos(\theta_{ijk}))^2\right]^2} \frac{\partial cos(\theta_{ijk})}{\partial m_p}$$
$$+ 2c^2 (h - cos(\theta_{ijk})) \frac{\partial \left[d^2 + (h - cos(\theta_{ijk}))^2\right]^{-2}}{\partial n_q} \frac{\partial cos(\theta_{ijk})}{\partial m_p}$$
$$+ \frac{2c^2 (h - cos(\theta_{ijk}))}{\left[d^2 + (h - cos(\theta_{ijk}))^2\right]^2} \frac{\partial^2 cos(\theta_{ijk})}{\partial n_q \partial m_p}$$

To make our lives easier:

$$\alpha = (h - cos(\theta_{ijk}))$$
$$\beta = \left[d^2 + (h - cos(\theta_{ijk}))^2\right]$$

$$\begin{aligned}\frac{\partial^2 g(\theta_{ijk})}{\partial n_q \partial m_p} &= -2c^2 \frac{\partial cos(\theta_{ijk})}{\partial n_q} \frac{1}{\beta^2} \frac{\partial cos(\theta_{ijk})}{\partial m_p} \\ &+ 2c^2\alpha \frac{4\alpha}{\beta^3} \frac{\partial cos(\theta_{ijk})}{\partial n_q} \frac{\partial cos(\theta_{ijk})}{\partial m_p} \\ &+ \frac{2c^2\alpha}{\beta^2} \frac{\partial^2 cos(\theta_{ijk})}{\partial n_q \partial m_p}\end{aligned}$$

And extracting common terms:

$$\begin{aligned}\frac{\partial^2 g(\theta_{ijk})}{\partial n_q \partial m_p} = \frac{-2c^2\alpha}{\beta^2} \Bigg[&\frac{1}{\alpha} \frac{\partial cos(\theta_{ijk})}{\partial n_q} \frac{\partial cos(\theta_{ijk})}{\partial m_p} \\ &- \frac{4\alpha}{\beta} \frac{\partial cos(\theta_{ijk})}{\partial n_q} \frac{\partial cos(\theta_{ijk})}{\partial m_p} - \frac{\partial^2 cos(\theta_{ijk})}{\partial n_q \partial m_p} \Bigg]\end{aligned}$$

Crystal anti-symmetry scaling: ω_{ij}

$$\omega_{ij} = exp\left[\lambda^3 (r_{ij} - r_{ik})^3\right]$$

The first derivatives are simply obtained:

$$\begin{aligned}\frac{\partial \omega_{ij}}{\partial m_k} &= \frac{\partial \left[\lambda^3 (r_{ij} - r_{ik})^3\right]}{\partial m_k} exp\left[\lambda^3 (r_{ij} - r_{ik})^3\right] \\ \frac{\partial \omega_{ij}}{\partial m_k} &= 3\left[\lambda (r_{ij} - r_{ik})\right]^2 \frac{\partial \left[\lambda (r_{ij} - r_{ik})\right]}{\partial m_k} exp\left[\lambda^3 (r_{ij} - r_{ik})^3\right] \\ \frac{\partial \omega_{ij}}{\partial m_k} &= 3\left[\lambda (r_{ij} - r_{ik})\right]^2 \lambda \frac{\partial - r_{ik}}{\partial m_k} exp\left[\lambda^3 (r_{ij} - r_{ik})^3\right]\end{aligned}$$

We may simplify the above with previous results and write:

$$\frac{\partial \omega_{ij}}{\partial m_k} = -3\lambda^3 (r_{ij} - r_{ik})^2 exp\left[\lambda^3 (r_{ij} - r_{ik})^3\right] \frac{m_{ik}}{r_{ik}}$$
$$\frac{\partial \omega_{ij}}{\partial m_k} = -3\lambda^3 (r_{ij} - r_{ik})^2 \omega_{ij} \frac{m_{ik}}{r_{ik}}$$
$$\frac{\partial \omega_{ij}}{\partial m_j} = 3\lambda^3 (r_{ij} - r_{ik})^2 exp\left[\lambda^3 (r_{ij} - r_{ik})^3\right] \frac{m_{ij}}{r_{ij}}$$
$$\frac{\partial \omega_{ij}}{\partial m_j} = 3\lambda^3 (r_{ij} - r_{ik})^2 \omega_{ij} \frac{m_{ij}}{r_{ij}}$$
$$\frac{\partial \omega_{ij}}{\partial m_i} = -3\lambda^3 (r_{ij} - r_{ik})^2 exp\left[\lambda^3 (r_{ij} - r_{ik})^3\right] \left[\frac{m_{ij}}{r_{ij}} - \frac{m_{ik}}{r_{ik}}\right]$$
$$\frac{\partial \omega_{ij}}{\partial m_i} = -\left[\frac{\partial \omega_{ij}}{\partial m_j} + \frac{\partial \omega_{ij}}{\partial m_k}\right]$$

The second derivatives may now be obtained, simplified with the use of previous results and grouped:

$$\begin{aligned}
\frac{\partial^2 \omega_{ij}}{\partial n_k \partial m_k} &= -3\lambda^3 2 (r_{ij} - r_{ik}) \frac{\partial r_{ik}}{\partial n_k} \omega_{ij} \frac{\partial r_{ik}}{\partial m_k} \\
&\quad - 3\lambda^3 (r_{ij} - r_{ik})^2 \frac{\partial \omega_{ij}}{\partial n_k} \frac{\partial r_{ik}}{\partial m_k} \\
&\quad - 3\lambda^3 (r_{ij} - r_{ik})^2 \omega_{ij} \frac{\partial^2 r_{ik}}{\partial n_k \partial m_k} \\
\frac{\partial^2 \omega_{ij}}{\partial n_j \partial m_k} &= -3\lambda^3 2 (r_{ij} - r_{ik}) \frac{\partial r_{ij}}{\partial n_j} \omega_{ij} \frac{\partial r_{ik}}{\partial m_k} \\
&\quad - 3\lambda^3 (r_{ij} - r_{ik})^2 \frac{\partial \omega_{ij}}{\partial n_j} \frac{\partial r_{ik}}{\partial m_k} \\
&\quad - 3\lambda^3 (r_{ij} - r_{ik})^2 \omega_{ij} \frac{\partial^2 r_{ik}}{\partial n_j \partial m_k} \\
\frac{\partial^2 \omega_{ij}}{\partial n_i \partial m_k} &= -3\lambda^3 2 (r_{ij} - r_{ik}) \left(\frac{\partial r_{ij}}{\partial n_i} - \frac{\partial r_{ik}}{\partial n_i}\right) \omega_{ij} \frac{\partial r_{ik}}{\partial m_k} \\
&\quad - 3\lambda^3 (r_{ij} - r_{ik})^2 \frac{\partial \omega_{ij}}{\partial n_i} \frac{\partial r_{ik}}{\partial m_k} \\
&\quad - 3\lambda^3 (r_{ij} - r_{ik})^2 \omega_{ij} \frac{\partial^2 r_{ik}}{\partial n_i \partial m_k}
\end{aligned}$$

$$\frac{\partial^2\omega_{ij}}{\partial n_k \partial m_j} = 3\lambda^3 2\left(r_{ij}-r_{ik}\right)\frac{\partial r_{ik}}{\partial n_k}\frac{\partial r_{ij}}{\partial m_j} + 3\lambda^3\left(r_{ij}-r_{ik}\right)^2\frac{\partial \omega_{ij}}{\partial n_k}\frac{\partial r_{ij}}{\partial m_j} + 3\lambda^3\left(r_{ij}-r_{ik}\right)^2\omega_{ij}\frac{\partial^2 r_{ij}}{\partial n_k \partial m_j}$$

$$\frac{\partial^2\omega_{ij}}{\partial n_j \partial m_j} = 3\lambda^3 2\left(r_{ij}-r_{ik}\right)\frac{\partial r_{ij}}{\partial n_j}\omega_{ij}\frac{\partial r_{ij}}{\partial m_j} + 3\lambda^3\left(r_{ij}-r_{ik}\right)^2\frac{\partial \omega_{ij}}{\partial n_j}\frac{\partial r_{ij}}{\partial m_j} + 3\lambda^3\left(r_{ij}-r_{ik}\right)^2\omega_{ij}\frac{\partial^2 r_{ij}}{\partial n_j \partial m_j}$$

$$\frac{\partial^2\omega_{ij}}{\partial n_i \partial m_j} = 3\lambda^3\left(r_{ij}-r_{ik}\right)\left(\frac{\partial r_{ij}}{\partial n_i}-\frac{\partial r_{ik}}{\partial n_i}\right)\omega_{ij}\frac{\partial r_{ij}}{\partial m_j} + 3\lambda^3\left(r_{ij}-r_{ik}\right)^2\frac{\partial \omega_{ij}}{\partial n_i}\frac{\partial r_{ij}}{\partial m_j} + 3\lambda^3\left(r_{ij}-r_{ik}\right)^2\omega_{ij}\frac{\partial^2 r_{ij}}{\partial n_i \partial m_j}$$

$$\frac{\partial^2\omega_{ij}}{\partial n_q \partial m_i} = -\left[\frac{\partial^2\omega_{ij}}{\partial n_q \partial m_j} + \frac{\partial^2\omega_{ij}}{\partial n_q \partial m_k}\right]$$

Components of the many-body term: ζ_{ij}

$$\zeta_{ij} = \sum_{k\neq i,j} fc\left(r_{ik}\right) g\left(\theta_{ijk}\right)\omega_{ij}$$

The first derivatives are simply available:

$$\frac{\partial\zeta_{ij}}{\partial m_k} = \left[\frac{\partial fc\left(r_{ik}\right)}{\partial m_k} g\left(\theta_{ijk}\right)\omega_{ij} + fc\left(r_{ik}\right)\frac{\partial g\left(\theta_{ijk}\right)}{\partial m_k}\omega_{ij} + fc\left(r_{ik}\right) g\left(\theta_{ijk}\right)\frac{\partial\omega_{ij}}{\partial m_k}\right]$$

$$\frac{\partial\zeta_{ij}}{\partial m_j} = \sum_{k\neq i,j}\left[fc\left(r_{ik}\right)\frac{\partial g\left(\theta_{ijk}\right)}{\partial m_j}\omega_{ij} + fc\left(r_{ik}\right) g\left(\theta_{ijk}\right)\frac{\partial\omega_{ij}}{\partial m_j}\right]$$

$$\frac{\partial\zeta_{ij}}{\partial m_i} = \sum_{k\neq i,j}\left[\frac{\partial fc\left(r_{ik}\right)}{\partial m_i} g\left(\theta_{ijk}\right)\omega_{ij} + fc\left(r_{ik}\right)\frac{\partial g\left(\theta_{ijk}\right)}{\partial m_i}\omega_{ij} + fc\left(r_{ik}\right) g\left(\theta_{ijk}\right)\frac{\partial\omega_{ij}}{\partial m_i}\right]$$

And the second derivatives can be obtained with similar simplicity:

$$\begin{aligned}
\frac{\partial^2 \zeta_{ij}}{\partial n_k \partial m_k} &= \left[\frac{\partial^2 fc(r_{ik})}{\partial n_k \partial m_k} g(\theta_{ijk}) \omega_{ij} + \frac{\partial fc(r_{ik})}{\partial m_k} \frac{\partial g(\theta_{ijk})}{\partial n_k} \omega_{ij} \right. \\
&+ \frac{\partial fc(r_{ik})}{\partial m_k} g(\theta_{ijk}) \frac{\partial \omega_{ij}}{\partial n_k} + \frac{\partial fc(r_{ik})}{\partial n_k} \frac{\partial g(\theta_{ijk})}{\partial m_k} \omega_{ij} \\
&+ fc(r_{ik}) \frac{\partial^2 g(\theta_{ijk})}{\partial n_k \partial m_k} \omega_{ij} + fc(r_{ik}) \frac{\partial g(\theta_{ijk})}{\partial m_k} \frac{\partial \omega_{ij}}{\partial n_k} \\
&+ \frac{\partial fc(r_{ik})}{\partial n_k} g(\theta_{ijk}) \frac{\partial \omega_{ij}}{\partial m_k} + fc(r_{ik}) \frac{\partial g(\theta_{ijk})}{\partial n_k} \frac{\partial \omega_{ij}}{\partial m_k} \\
&\left. + fc(r_{ik}) g(\theta_{ijk}) \frac{\partial^2 \omega_{ij}}{\partial n_k \partial m_k} \right] \\
\frac{\partial^2 \zeta_{ij}}{\partial n_j \partial m_k} &= \left[\frac{\partial^2 fc(r_{ik})}{\partial n_j \partial m_k} g(\theta_{ijk}) \omega_{ij} + \frac{\partial fc(r_{ik})}{\partial m_k} \frac{\partial g(\theta_{ijk})}{\partial n_j} \omega_{ij} \right. \\
&+ \frac{\partial fc(r_{ik})}{\partial m_k} g(\theta_{ijk}) \frac{\partial \omega_{ij}}{\partial n_j} + \frac{\partial fc(r_{ik})}{\partial n_j} \frac{\partial g(\theta_{ijk})}{\partial m_k} \omega_{ij} \\
&+ fc(r_{ik}) \frac{\partial^2 g(\theta_{ijk})}{\partial n_j \partial m_k} \omega_{ij} + fc(r_{ik}) \frac{\partial g(\theta_{ijk})}{\partial m_k} \frac{\partial \omega_{ij}}{\partial n_j} \\
&+ \frac{\partial fc(r_{ik})}{\partial n_j} g(\theta_{ijk}) \frac{\partial \omega_{ij}}{\partial m_k} + fc(r_{ik}) \frac{\partial g(\theta_{ijk})}{\partial n_j} \frac{\partial \omega_{ij}}{\partial m_k} \\
&\left. + fc(r_{ik}) g(\theta_{ijk}) \frac{\partial^2 \omega_{ij}}{\partial n_j \partial m_k} \right] \\
\frac{\partial^2 \zeta_{ij}}{\partial n_i \partial m_k} &= \left[\frac{\partial^2 fc(r_{ik})}{\partial n_i \partial m_k} g(\theta_{ijk}) \omega_{ij} + \frac{\partial fc(r_{ik})}{\partial m_k} \frac{\partial g(\theta_{ijk})}{\partial n_i} \omega_{ij} \right. \\
&+ \frac{\partial fc(r_{ik})}{\partial m_k} g(\theta_{ijk}) \frac{\partial \omega_{ij}}{\partial n_i} + \frac{\partial fc(r_{ik})}{\partial n_i} \frac{\partial g(\theta_{ijk})}{\partial m_k} \omega_{ij} \\
&+ fc(r_{ik}) \frac{\partial^2 g(\theta_{ijk})}{\partial n_i \partial m_k} \omega_{ij} + fc(r_{ik}) \frac{\partial g(\theta_{ijk})}{\partial m_k} \frac{\partial \omega_{ij}}{\partial n_i} \\
&+ \frac{\partial fc(r_{ik})}{\partial n_i} g(\theta_{ijk}) \frac{\partial \omega_{ij}}{\partial m_k} + fc(r_{ik}) \frac{\partial g(\theta_{ijk})}{\partial n_i} \frac{\partial \omega_{ij}}{\partial m_k} \\
&\left. + fc(r_{ik}) g(\theta_{ijk}) \frac{\partial^2 \omega_{ij}}{\partial n_i \partial m_k} \right]
\end{aligned}$$

$$\frac{\partial^2 \zeta_{ij}}{\partial n_k \partial m_j} = \sum_{k \neq i,j} \left[\frac{\partial fc(r_{ik})}{\partial n_k} \frac{\partial g(\theta_{ijk})}{\partial m_j} \omega_{ij} + fc(r_{ik}) \frac{\partial^2 g(\theta_{ijk})}{\partial n_k \partial m_j} \omega_{ij} \right.$$
$$+ fc(r_{ik}) \frac{\partial g(\theta_{ijk})}{\partial m_j} \frac{\partial \omega_{ij}}{\partial n_k} + \frac{\partial fc(r_{ik})}{\partial n_k} g(\theta_{ijk}) \frac{\partial \omega_{ij}}{\partial m_j}$$
$$\left. + fc(r_{ik}) \frac{\partial g(\theta_{ijk})}{\partial n_k} \frac{\partial \omega_{ij}}{\partial m_j} + fc(r_{ik}) g(\theta_{ijk}) \frac{\partial^2 \omega_{ij}}{\partial n_k \partial m_j} \right]$$

$$\frac{\partial^2 \zeta_{ij}}{\partial n_j \partial m_j} = \sum_{k \neq i,j} \left[\frac{\partial fc(r_{ik})}{\partial n_j} \frac{\partial g(\theta_{ijk})}{\partial m_j} \omega_{ij} + fc(r_{ik}) \frac{\partial^2 g(\theta_{ijk})}{\partial n_j \partial m_j} \omega_{ij} \right.$$
$$+ fc(r_{ik}) \frac{\partial g(\theta_{ijk})}{\partial m_j} \frac{\partial \omega_{ij}}{\partial n_j} + \frac{\partial fc(r_{ik})}{\partial n_j} g(\theta_{ijk}) \frac{\partial \omega_{ij}}{\partial m_j}$$
$$\left. + fc(r_{ik}) \frac{\partial g(\theta_{ijk})}{\partial n_j} \frac{\partial \omega_{ij}}{\partial m_j} + fc(r_{ik}) g(\theta_{ijk}) \frac{\partial^2 \omega_{ij}}{\partial n_j \partial m_j} \right]$$

$$\frac{\partial^2 \zeta_{ij}}{\partial n_i \partial m_j} = \sum_{k \neq i,j} \left[\frac{\partial fc(r_{ik})}{\partial n_i} \frac{\partial g(\theta_{ijk})}{\partial m_j} \omega_{ij} + fc(r_{ik}) \frac{\partial^2 g(\theta_{ijk})}{\partial n_i \partial m_j} \omega_{ij} \right.$$
$$+ fc(r_{ik}) \frac{\partial g(\theta_{ijk})}{\partial m_j} \frac{\partial \omega_{ij}}{\partial n_i} + \frac{\partial fc(r_{ik})}{\partial n_i} g(\theta_{ijk}) \frac{\partial \omega_{ij}}{\partial m_j}$$
$$\left. + fc(r_{ik}) \frac{\partial g(\theta_{ijk})}{\partial n_i} \frac{\partial \omega_{ij}}{\partial m_j} + fc(r_{ik}) g(\theta_{ijk}) \frac{\partial^2 \omega_{ij}}{\partial n_i \partial m_j} \right]$$

$$\frac{\partial^2\zeta_{ij}}{\partial n_k \partial m_i} = \sum_{k\neq i,j}\left[\frac{\partial^2 fc(r_{ik})}{\partial n_k \partial m_i} g(\theta_{ijk})\,\omega_{ij} + \frac{\partial fc(r_{ik})}{\partial m_i}\frac{\partial g(\theta_{ijk})}{\partial n_k}\omega_{ij} + \frac{\partial fc(r_{ik})}{\partial m_i} g(\theta_{ijk})\frac{\partial \omega_{ij}}{\partial n_k} + \frac{\partial fc(r_{ik})}{\partial n_k}\frac{\partial g(\theta_{ijk})}{\partial m_i}\omega_{ij} + fc(r_{ik})\frac{\partial^2 g(\theta_{ijk})}{\partial n_k \partial m_i}\omega_{ij} + fc(r_{ik})\frac{\partial g(\theta_{ijk})}{\partial m_i}\frac{\partial \omega_{ij}}{\partial n_k} + \frac{\partial fc(r_{ik})}{\partial n_k} g(\theta_{ijk})\frac{\partial \omega_{ij}}{\partial m_i} + fc(r_{ik})\frac{\partial g(\theta_{ijk})}{\partial n_k}\frac{\partial \omega_{ij}}{\partial m_i} + fc(r_{ik})\, g(\theta_{ijk})\frac{\partial^2 \omega_{ij}}{\partial n_k \partial m_i}\right]$$

$$\frac{\partial^2\zeta_{ij}}{\partial n_j \partial m_i} = \sum_{k\neq i,j}\left[\frac{\partial^2 fc(r_{ik})}{\partial n_j \partial m_i} g(\theta_{ijk})\,\omega_{ij} + \frac{\partial fc(r_{ik})}{\partial m_i}\frac{\partial g(\theta_{ijk})}{\partial n_j}\omega_{ij} + \frac{\partial fc(r_{ik})}{\partial m_i} g(\theta_{ijk})\frac{\partial \omega_{ij}}{\partial n_j} + \frac{\partial fc(r_{ik})}{\partial n_j}\frac{\partial g(\theta_{ijk})}{\partial m_i}\omega_{ij} + fc(r_{ik})\frac{\partial^2 g(\theta_{ijk})}{\partial n_j \partial m_i}\omega_{ij} + fc(r_{ik})\frac{\partial g(\theta_{ijk})}{\partial m_i}\frac{\partial \omega_{ij}}{\partial n_j} + \frac{\partial fc(r_{ik})}{\partial n_j} g(\theta_{ijk})\frac{\partial \omega_{ij}}{\partial m_i} + fc(r_{ik})\frac{\partial g(\theta_{ijk})}{\partial n_j}\frac{\partial \omega_{ij}}{\partial m_i} + fc(r_{ik})\, g(\theta_{ijk})\frac{\partial^2 \omega_{ij}}{\partial n_j \partial m_i}\right]$$

$$\frac{\partial^2\zeta_{ij}}{\partial n_i \partial m_i} = \sum_{k\neq i,j}\left[\frac{\partial^2 fc(r_{ik})}{\partial n_i \partial m_i} g(\theta_{ijk})\,\omega_{ij} + \frac{\partial fc(r_{ik})}{\partial m_i}\frac{\partial g(\theta_{ijk})}{\partial n_i}\omega_{ij} + \frac{\partial fc(r_{ik})}{\partial m_i} g(\theta_{ijk})\frac{\partial \omega_{ij}}{\partial n_i} + \frac{\partial fc(r_{ik})}{\partial n_i}\frac{\partial g(\theta_{ijk})}{\partial m_i}\omega_{ij} + fc(r_{ik})\frac{\partial^2 g(\theta_{ijk})}{\partial n_i \partial m_i}\omega_{ij} + fc(r_{ik})\frac{\partial g(\theta_{ijk})}{\partial m_i}\frac{\partial \omega_{ij}}{\partial n_i} + \frac{\partial fc(r_{ik})}{\partial n_i} g(\theta_{ijk})\frac{\partial \omega_{ij}}{\partial m_i} + fc(r_{ik})\frac{\partial g(\theta_{ijk})}{\partial n_i}\frac{\partial \omega_{ij}}{\partial m_i} + fc(r_{ik})\, g(\theta_{ijk})\frac{\partial^2 \omega_{ij}}{\partial n_i \partial m_i}\right]$$

Many body term: b_{ij}

$$b_{ij} = \left[1 + (\beta\zeta_{ij})^n\right]^{-\frac{1}{2n}}$$

First derivatives:

$$\frac{\partial b_{ij}}{\partial m_p} = -\frac{1}{2n}\left[1+(\beta\zeta_{ij})^n\right]^{-\frac{1}{2n}-1}\frac{\partial}{\partial m_p}\left[1+(\beta\zeta_{ij})^n\right]$$
$$\frac{\partial b_{ij}}{\partial m_p} = -\frac{1}{2}\frac{b_{ij}}{n}\left[1+(\beta\zeta_{ij})^n\right]^{-1} n\left(\beta\zeta_{ij}\right)^{n-1}\beta\frac{\partial\zeta_{ij}}{\partial m_p}$$
$$\frac{\partial b_{ij}}{\partial m_p} = -\frac{1}{2}\frac{b_{ij}\beta^n\zeta_{ij}^{n-1}}{\left[1+(\beta\zeta_{ij})^n\right]}\frac{\partial\zeta_{ij}}{\partial m_p}$$

Before we calculate the second derivatives, we may make a substitution to make our lives easier:

$$\text{Let:}\quad -\frac{1}{2}\frac{\beta^n\zeta_{ij}^{n-1}}{\left[1+(\beta\zeta_{ij})^n\right]} = -\frac{\beta^n}{2\left(\zeta_{ij}^{1-n}+\beta^n\zeta_{ij}\right)}$$

$$\frac{\partial^2 b_{ij}}{\partial n_q\partial m_p} = \frac{\partial}{\partial n_q}\left[-\frac{\beta^n}{2\left(\zeta_{ij}^{1-n}+\beta^n\zeta_{ij}\right)}b_{ij}\frac{\partial\zeta_{ij}}{\partial m_p}\right]$$
$$\frac{\partial^2 b_{ij}}{\partial n_q\partial m_p} = \frac{\beta^n}{2\left(\zeta_{ij}^{1-n}+\beta^n\zeta_{ij}\right)^2}\frac{\partial}{\partial n_q}\left[\zeta_{ij}^{1-n}+\beta^n\zeta_{ij}\right]b_{ij}\frac{\partial\zeta_{ij}}{\partial m_p}$$
$$-\frac{\beta^n}{2\left(\zeta_{ij}^{1-n}+\beta^n\zeta_{ij}\right)}\left[\frac{\partial b_{ij}}{\partial n_q}\frac{\partial\zeta_{ij}}{\partial m_p}+b_{ij}\frac{\partial^2\zeta_{ij}}{\partial n_q\partial m_p}\right]$$
$$\frac{\partial^2 b_{ij}}{\partial n_q\partial m_p} = \frac{\beta^n}{2\left(\zeta_{ij}^{1-n}+\beta^n\zeta_{ij}\right)^2}\left[(1-n)\,\zeta_{ij}^{-n}+\beta^n\right]b_{ij}\frac{\partial\zeta_{ij}}{\partial n_q}\frac{\partial\zeta_{ij}}{\partial m_p}$$
$$-\frac{\beta^n}{2\left(\zeta_{ij}^{1-n}+\beta^n\zeta_{ij}\right)}\left[\frac{\partial b_{ij}}{\partial n_q}\frac{\partial\zeta_{ij}}{\partial m_p}+b_{ij}\frac{\partial^2\zeta_{ij}}{\partial n_q\partial m_p}\right]$$

Repulsive exponential: V_R

$$V_R = \left(\frac{De}{S-1}\right)exp\left[-\beta\sqrt{2S}\left(r_{ij}-r_e\right)\right]$$

First derivatives:

$$\frac{\partial V_R}{\partial m_p} = \left(\frac{-De\beta\sqrt{2S}}{S-1}\right)exp\left[-\beta\sqrt{2S}\left(r_{ij}-r_e\right)\right]\frac{\partial r_{ij}}{\partial m_p}$$

Let:

$$A = -\beta\sqrt{2S}$$

$$\frac{\partial V_R}{\partial m_p} = V_R A\frac{\partial r_{ij}}{\partial m_p}$$

Second derivatives:

$$\frac{\partial^2 V_R}{\partial n_q m_p} = A\left(\frac{\partial V_R}{n_q}\frac{\partial r_{ij}}{\partial m_p} + V_R\frac{\partial^2 r_{ij}}{\partial n_q m_p}\right)$$
$$= AV_R\left(A\frac{\partial r_{ij}}{\partial n_q}\frac{\partial r_{ij}}{\partial m_p} + \frac{\partial^2 r_{ij}}{\partial n_q \partial m_p}\right)$$

Attractive exponential: V_A

$$V_A = \left(\frac{SDe}{S-1}\right) exp\left[-\beta\sqrt{\frac{2}{S}}\left(r_{ij} - r_e\right)\right]$$

First derivatives:

$$\frac{\partial V_A}{\partial m_p} = \left(\frac{-SDe\beta\sqrt{\frac{2}{S}}}{S-1}\right) exp\left[-\beta\sqrt{\frac{2}{S}}\left(r_{ij} - r_e\right)\right]\frac{\partial r_{ij}}{\partial m_p}$$

Let:

$$B = -\beta\sqrt{\frac{2}{S}}$$

$$\frac{\partial V_A}{\partial m_p} = V_A B\frac{\partial r_{ij}}{\partial m_p}$$

Second derivatives:

$$\frac{\partial^2 V_A}{\partial n_q m_p} = B\left(\frac{\partial V_A}{n_q}\frac{\partial r_{ij}}{\partial m_p} + V_A\frac{\partial^2 r_{ij}}{\partial n_q m_p}\right)$$
$$= BV_A\left(B\frac{\partial r_{ij}}{\partial n_q}\frac{\partial r_{ij}}{\partial m_p} + \frac{\partial^2 r_{ij}}{\partial n_q \partial m_p}\right)$$

The energy function: V_{ij}

$$V_{ij} = fc\left(r_{ij}\right)\left[V_R - b_{ij}V_A\right]$$

First derivatives:

$$\frac{\partial V_{ij}}{\partial m_p} = \frac{\partial fc(r_{ij})}{\partial m_p}\left[V_R - b_{ij}V_A\right] + fc(r_{ij})\frac{\partial\left[V_R - b_{ij}V_A\right]}{\partial m_p}$$
$$\frac{\partial V_{ij}}{\partial m_p} = \frac{\partial fc(r_{ij})}{\partial m_p}\left[V_R - b_{ij}V_A\right] + fc(r_{ij})\left[\frac{\partial V_R}{\partial m_p} - \left[\frac{\partial b_{ij}}{\partial m_p}V_A + b_{ij}\frac{\partial V_A}{\partial m_p}\right]\right]$$

Second derivatives:

$$\begin{aligned}\frac{\partial^2 V_{ij}}{\partial n_q \partial m_p} &= \frac{\partial^2 fc(r_{ij})}{\partial n_q \partial m_p}\left[V_R - b_{ij}V_A\right] \\ &+ \frac{\partial fc(r_{ij})}{\partial m_p}\left[\frac{\partial V_R}{\partial n_q} - \left[\frac{\partial b_{ij}}{\partial n_q}V_A + b_{ij}\frac{\partial V_A}{\partial n_q}\right]\right] \\ &+ \frac{\partial fc(r_{ij})}{\partial n_q}\left[\frac{\partial V_R}{\partial m_p} - \left[\frac{\partial b_{ij}}{\partial m_p}V_A + b_{ij}\frac{\partial V_A}{\partial m_p}\right]\right] \\ &+ fc(r_{ij})\frac{\partial^2 V_R}{\partial n_q \partial m_p} \\ &- \left[fc(r_{ij})\frac{\partial^2 b_{ij}}{\partial n_q \partial m_p}V_A + fc(r_{ij})\frac{\partial b_{ij}}{\partial m_p}\frac{\partial V_A}{\partial n_q}\right] \\ &- \left[fc(r_{ij})\frac{\partial b_{ij}}{\partial n_q}\frac{\partial V_A}{\partial m_p} + fc(r_{ij})\,b_{ij}\frac{\partial^2 V_A}{\partial n_q \partial m_p}\right]\end{aligned} \tag{A.1}$$

Appendix B

Schrödinger Wavefunction Solver

Presented here is a brief description of the design and coding of the Schrödinger wavefunction solver used in the singleband $\mathbf{k} \cdot \mathbf{p}$ code. The modelling chain of section 1 describes a specific set of operations used to characterise an $In_XGa_{1-X}As$ quantum dot grown on a GaAs sample which were published by Migliorato *et al*[1, 2].

Initially a computer model of the quantum dot (including wetting layer and capping material) was constructed and comprised some 800,000 atoms to provide a simulation of a realistically scaled atomic system. The quantum dot model was then subject to a structural relaxation using the Tersoff potential and the potential energy at each location in a regularly spaced grid was obtained. The level of strain at each atomic location was calculated and from this information the piezoelectric potential was calculated. For a full treatment of the strain calculations, the calculation of the piezoelectric potential, the gridding of the potential energy and the construction of the large scale quantum dot model the reader is referred to the thesis of Dr. Migliorato[3]. The potential energy and the piezoelectric potential calculated from the quantum dot model were used as input data for the Schrödinger solver code which is outlined below.

Solving Schrödingers Equation

To calculate the wavefunctions in the system we need to solve Schrödingers equation in three dimensions which is given by the eigenvalue problem

$$H\psi^i = E_i\psi^i \tag{B.1}$$

where ψ represents the wavefunctions, E is the system energy, i is the energy level index and H is the Hamiltonian which can be considered to be the sum of

the kinetic and potential energies is described by

$$H = -\frac{\hbar^2}{2m_0}\nabla \cdot \left(\frac{1}{m_{eff}} \cdot \nabla\right) + V(\mathbf{r}) \tag{B.2}$$

where m_0 represents the mass of the atom, m_{eff} is the effective mass tensor and V is the confining potential.

A planewave expansion of the wavefunction is required with a basis that satisfies the condition of having a zero value at the boundaries of the system. A normalised sinusoidal wavefunction is a natural choice for this basis and for a three dimensional system and a box of size $L_x \times L_y \times L_z$ we choose

$$\Phi_{k_x,k_y,k_z} = 2\frac{\sqrt{2}}{\sqrt{L_x L_y L_z}} \sin(k_x x)\sin(k_y y)\sin(k_z z) \tag{B.3}$$

Wavefunctions that satisfy the eigenvalue problem in eq. B.1 can now be written as

$$\psi^i(\mathbf{r}) = \sum_{k_x,k_y,k_z}^{n_x,n_y,n_z} a^i_{k_x,k_y,k_z}\phi_{k_x,k_y,k_z}(\mathbf{r}) \tag{B.4}$$

where a^i are the coefficients to be found as the solutions of the eigenvalue problem, n indicates the number of plane waves used in the expansion and the k values are provided by $k_i = (\pi/L_i)m_i$ where m is a non-zero integer that ensures correct boundary conditions.

The solution of the eigenvalue problem can now be found by diagonalising the matrix whose elements are given

$$H(k_x,k_y,k_z,k'_x,k'_y,k'_z) = \iiint dxdydz \cdot \Phi_{k'_x,k'_y,k'_z}(x,y,z)H(x,y,z)\Phi_{k_x,k_y,k_z}(x,y,z) \tag{B.5}$$

The value of n chosen equates to the number of plane waves selected to solve the problem. It is not possible to know in advance which value of n to select for a particular problem but by iterating the solution of the Hamiltonian with increasing values of n_x, n_y, n_z and comparing the values of the previous and current solutions - the eigenvalue error can be brought to within a user defined tolerance.

Equation B.4 can be seen as a three dimensional Fourier transform of the function in real-space with the a values as the Fourier coefficients and the Hamiltonian matrix elements given above in eq. B.5 is the equivalent of calculating the Hamiltonian in k-space. To ensure the fast and accurate computation of the wavefunctions we have dismissed methods involving numerical computation of the 3D integrals in eq. B.5 and a more sophisticated Fourier transform approach has

been used to allow the analytic integrals to be inserted into the code. This requires the Fourier transform of the spatially gridded potential to be obtained so we may reduce our operations to a set of integrals on k-space values. We use the notation k^3 to indicate the k-space values of the confining potential and distinguish from the k' and k values of the wavefunctions in eq. B.4.

Initially we split the Hamiltonian in 2 separate parts to represent the kinetic and the potential energy contributions to the Hamiltonian

$$H = H_{kin} + H_{pot} \tag{B.6}$$

and consider the discrete Fourier transform[4] denoted $\mathbb{F}$ and the inverse discrete Fourier transform denoted $\mathbb{F}^{-1}$ which are given by the following relations

$$\mathbb{F} = \frac{1}{N} \sum_{x=-(1/2)N}^{(1/2)N-1} f(x) \cdot \exp^{-i2\pi(k/N)x} \tag{B.7}$$

$$\mathbb{F}^{-1} = \sum_{k=-(1/2)N}^{(1/2)N-1} f(k) \cdot \exp^{i2\pi(k/N)x} \tag{B.8}$$

where $f(x)$ is the spatial function and $f(k)$ is the function of k-space. Using the knowledge that $\exp^{-i\theta} = \cos\theta + i\sin\theta$, we can then break the Hamiltonian into 2 components and operate on them individually.

Potential energy contribution

First the potential energy contribution to the Hamiltonian is considered

$$\begin{aligned}
&H_{pot}(k_x, k_y, k_z, k'_x, k'_y, k'_z) \\
&\quad = \iiint dxdydz \cdot \Phi_{k'_x,k'_y,k'_z}(x,y,z) \cdot V(x,y,z) \cdot \Phi_{k_x,k_y,k_z}(x,y,z) \\
&\quad = \iiint dx_1 dx_2 dx_3 \cdot \Phi_{k'_x,k'_y,k'_z}(x_1,x_2,x_3) \\
&\qquad \cdot \left[\frac{1}{N_x N_y N_z} \sum_{j_1}^{N_x} \sum_{j_2}^{N_y} \sum_{j_3}^{N_z} a_{j_1,j_2,j_3} \cos\left(2\pi \sum_{i=1,2,3} \frac{j_i}{N_i} x_i \right) \right. \\
&\qquad \left. + \frac{1}{N_x N_y N_z} \sum_{j_1}^{N_x} \sum_{j_2}^{N_y} \sum_{j_3}^{N_z} b_{j_1,j_2,j_3} \sin\left(2\pi \sum_{i=1,2,3} \frac{j_i}{N_i} x_i \right) \right] \\
&\qquad \cdot \Phi_{k_x,k_y,k_z}(x_1,x_2,x_3)
\end{aligned} \tag{B.9}$$

where $x_i(i = 1,2,3)$ has been substituted for x, y, z to compact the expressions and N is the number of sampling points. We will make the assumption that it is understood that the b coefficient terms of the sinusoidal components of the previous equation and the equations that follow are multiplied by the complex variable $i = sqrt(-1)$. This is done for convenience as we are grouping the real and imaginary components separately. We can further work this equation to bring the summations outside of the integrals as follows

$$
\begin{aligned}
&H_{pot}(k_x, k_y, k_z, k'_x, k'_y, k'_z) \\
&\quad = \frac{1}{N_x N_y N_z} \sum_{j_1}^{N_x} \sum_{j_2}^{N_y} \sum_{j_3}^{N_z} \iiint dx_1 dx_2 dx_3 \\
&\quad \left[a_{j_1,j_2,j_3} \cdot \Phi_{k'_x,k'_y,k'_z}(x_1, x_2, x_3) \cdot \cos\left(2\pi \sum_{i=1,2,3} \frac{j_i}{N_i} x_i \right) \cdot \Phi_{k_x,k_y,k_z}(x_1, x_2, x_3) \right. \\
&\quad \left. + b_{j_1,j_2,j_3} \cdot \Phi_{k'_x,k'_y,k'_z}(x_1, x_2, x_3) \cdot \sin\left(2\pi \sum_{i=1,2,3} \frac{j_i}{N_i} x_i \right) \cdot \Phi_{k_x,k_y,k_z}(x_1, x_2, x_3) \right]
\end{aligned}
\tag{B.10}
$$

We can now use the following important trigonometric relations to separate the variables of the potential energy contribution into manageable parts. We now replace $x_i(i = 1,2,3)$ with x, y, z and obtain for the cosine contribution

$$
\begin{aligned}
&\iiint dx_1 dx_2 dx_3 \cdot \Phi_{k'_x,k'_y,k'_z}(x_1, x_2, x_3) \cdot \cos\left(2\pi \sum_{i=1,2,3} \frac{j_i}{N_i} x_i \right) \cdot \Phi_{k_x,k_y,k_z}(x_1, x_2, x_3) \\
&= \frac{8}{L_x L_y L_z} \cdot \iiint dx dy dz \\
&\cdot \left[\sin(k'_x x) \sin(k_x x) \cos(k^3_x x) \cdot \sin(k'_y y) \sin(k_y y) \cos(k^3_y y) \cdot \sin(k'_z z) \sin(k_z z) \cos(k^3_z z) \right. \\
&- \sin(k'_x x) \sin(k_x x) \cos(k^3_x x) \cdot \sin(k'_y y) \sin(k_y y) \sin(k^3_y y) \cdot \sin(k'_z z) \sin(k_z z) \sin(k^3_z z) \\
&- \sin(k'_x x) \sin(k_x x) \sin(k^3_x x) \cdot \sin(k'_y y) \sin(k_y y) \cos(k^3_y y) \cdot \sin(k'_z z) \sin(k_z z) \sin(k^3_z z) \\
&\left. - \sin(k'_x x) \sin(k_x x) \cos(k^3_x x) \cdot \sin(k'_y y) \sin(k_y y) \sin(k^3_y y) \cdot \sin(k'_z z) \sin(k_z z) \cos(k^3_z z) \right]
\end{aligned}
\tag{B.11}
$$

and for the sine component contribution

$$\iiint dx_1dx_2dx_3 \cdot \Phi_{k'_x,k'_y,k'_z}(x_1,x_2,x_3) \cdot \sin\left(2\pi \sum_{i=1,2,3} \frac{j_i}{N_i} x_i\right) \cdot \Phi_{k_x,k_y,k_z}(x_1,x_2,x_3)$$
$$= \frac{8}{L_xL_yL_z} \cdot \iiint dxdydz$$
$$\cdot \left[\sin(k'_x x)\sin(k_x x)\sin(k_x^3 x) \cdot \sin(k'_y y)\sin(k_y y)\cos(k_y^3 y) \cdot \sin(k'_z z)\sin(k_z z)\cos(k_z^3 z)\right.$$
$$+ \sin(k'_x x)\sin(k_x x)\cos(k_x^3 x) \cdot \sin(k'_y y)\sin(k_y y)\sin(k_y^3 y) \cdot \sin(k'_z z)\sin(k_z z)\cos(k_z^3 z)$$
$$+ \sin(k'_x x)\sin(k_x x)\cos(k_x^3 x) \cdot \sin(k'_y y)\sin(k_y y)\cos(k_y^3 y) \cdot \sin(k'_z z)\sin(k_z z)\sin(k_z^3 z)$$
$$\left. - \sin(k'_x x)\sin(k_x x)\sin(k_x^3 x) \cdot \sin(k'_y y)\sin(k_y y)\sin(k_y^3 y) \cdot \sin(k'_z z)\sin(k_z z)\sin(k_z^3 z)\right] \tag{B.12}$$

Kinetic energy contribution

The kinetic energy contribution to the Hamiltonian from the strained quantum dot model has a varying effective mass associated with the different locations on the three dimensional energy grid and so the kinetic part of the Hamiltonian ceases to be diagonal. The kinetic part needs to be split into two parts

$$H = -\frac{\hbar^2}{2m_0}\nabla \cdot \left(\frac{1}{m_{eff}} \cdot \nabla\right) \tag{B.13}$$
$$= -\frac{\hbar^2}{2m_0 m_{eff}}\nabla^2 - \frac{\hbar^2}{2m_0}\left(\nabla \cdot \frac{1}{m_{eff}}\right) \cdot \nabla \tag{B.14}$$

The first component of eq. B.13 which we will label H_{kin_1} can be decomposed using the Fourier transform technique from before to

$$H_{kin_1}(k_x,k_y,k_z,k'_x,k'_y,k'_z)$$
$$= \frac{\hbar^2}{2m_0} \iiint dx_1dx_2dx_3 \Phi_{k'_x,k'_y,k'_z}$$
$$\cdot \left[k_x \cdot \mathbb{F}\left(\frac{1}{m_{eff}^{xx}}\right) + k_y \cdot \mathbb{F}\left(\frac{1}{m_{eff}^{yy}}\right) + k_z \cdot \mathbb{F}\left(\frac{1}{m_{eff}^{zz}}\right)\right] \tag{B.15}$$
$$\cdot \Phi_{k_x,k_y,k_z}$$

where $\mathbb{F}$ indicates the Fourier transform to obtain

$$\begin{aligned}
&H_{kin_1}(k_x, k_y, k_z, k'_x, k'_y, k'_z) \\
&\quad = \frac{1}{N_1 N_2 N_3} \sum_{j_1}^{N_1} \sum_{j_2}^{N_2} \sum_{j_3}^{N_3} \frac{\hbar^2}{2m_0} \iiint dx_1 dx_2 dx_3 \\
&\quad \cdot \Bigg[\left(k_x^3 \cdot a^{xx}_{j_1,j_2,j_3} + k_y^3 \cdot a^{yy}_{j_1,j_2,j_3} + k_z^3 \cdot a^{zz}_{j_1,j_2,j_3} \right) \\
&\quad \cdot \Phi_{k'_x,k'_y,k'_z} \cdot \cos\left(2\pi \sum_{i=1,2,3} \frac{j_i}{N_i} x_i \right) \cdot \Phi_{k_x,k_y,k_z} \\
&\quad + \left(k_x^3 \cdot b^{xx}_{j_1,j_2,j_3} + k_y^3 \cdot b^{yy}_{j_1,j_2,j_3} + k_z^3 \cdot b^{zz}_{j_1,j_2,j_3} \right) \\
&\quad \cdot \Phi_{k'_x,k'_y,k'_z} \cdot \sin\left(2\pi \sum_{i=1,2,3} \frac{j_i}{N_i} x_i \right) \cdot \Phi_{k_x,k_y,k_z} \Bigg]
\end{aligned} \tag{B.16}$$

As a check on the above derivation, we make the effective masses constant and equal to 1 and reduce the expression in B.16 to

$$\begin{aligned}
&H_{kin_1}(k_x, k_y, k_z, k'_x, k'_y, k'_z) \\
&\quad = \frac{\hbar^2}{2m_0} \iiint dx_1 dx_2 dx_3 \Phi_{k'_x,k'_y,k'_z} \cdot (k_x + k_y + k_z) \cdot \Phi_{k_x,k_y,k_z} \\
&\quad = \frac{\hbar^2}{2m_0} (k_x + k_y + k_z) \cdot \delta_{k'_x,k_x} \cdot \delta_{k'_y,k_y} \cdot \delta_{k'_z,k_z}
\end{aligned} \tag{B.17}$$

and obtain the usual diagonal form of the kinetic energy for a three dimensional system[5].

The second component of eq. B.13 is labelled H_{kin_2} and is the product of two summations. The first one $H_{kin_{2a}}$ is the gradient of the mass tensor and the second $H_{kin_{2b}}$ is the gradient of the wavefunction:

$$\begin{aligned}
H_{kin_{2a}} &= \left(\nabla \cdot \frac{1}{m_{eff}} \right) \\
&= \begin{pmatrix} \sum_{i=1}^{3} - \left(\frac{2\pi}{L_x} j_x \right) \left[a^{xx}_{j_i} \cdot \cos\left(2\pi \sum_{i=1}^{3} \frac{j_i}{N_i} x_i \right) - b^{xx}_{j_i} \cdot \sin\left(2\pi \sum_{i=1}^{3} \frac{j_i}{N_i} x_i \right) \right] \\ \sum_{i=1}^{3} - \left(\frac{2\pi}{L_y} j_y \right) \left[a^{yy}_{j_i} \cdot \cos\left(2\pi \sum_{i=1}^{3} \frac{j_i}{N_i} x_i \right) - b^{yy}_{j_i} \cdot \sin\left(2\pi \sum_{i=1}^{3} \frac{j_i}{N_i} x_i \right) \right] \\ \sum_{i=1}^{3} - \left(\frac{2\pi}{L_z} j_z \right) \left[a^{zz}_{j_i} \cdot \cos\left(2\pi \sum_{i=1}^{3} \frac{j_i}{N_i} x_i \right) - b^{zz}_{j_i} \cdot \sin\left(2\pi \sum_{i=1}^{3} \frac{j_i}{N_i} x_i \right) \right] \end{pmatrix}
\end{aligned} \tag{B.18}$$

$$
\begin{aligned}
H_{kin_{2b}} &= \nabla\Phi_{k_x,k_y,k_z} \\
&= \frac{2\sqrt{2}}{\sqrt{L_xL_yL_z}} \cdot \begin{pmatrix} \cos(k_xx)\cdot\sin(k_yy)\cdot\sin(k_zz) \\ \sin(k_xx)\cdot\cos(k_yy)\cdot\sin(k_zz) \\ \sin(k_xx)\cdot\sin(k_yy)\cdot\cos(k_zz) \end{pmatrix}
\end{aligned} \tag{B.19}
$$

Finally, by combining eq. B.18 and eq. B.18 we can find the kinetic contribution to the Hamiltonian from the effective masses to be

$$
\begin{aligned}
&H_{m_{eff}}(k_x,k_y,k_z,k'_x,k'_y,k'_z) \\
&= \frac{\hbar^2}{2m_0}\cdot\frac{2\sqrt{2}}{\sqrt{L_xL_yL_z}}\cdot\iiint dx_1dx_2dx_3 \\
&\cdot\left\{\sum_{i=1}^{3} -\left(\frac{2\pi}{L_x}j_x\right)\cdot\cos(k_xx)\cdot\sin(k_yy)\cdot\sin(k_zz)\right. \\
&\cdot\left[a_{j_i}^{xx}\cdot\cos\left(2\pi\sum_{i=1}^{3}\frac{j_i}{N_i}x_i\right) - b_{j_i}^{xx}\cdot\sin\left(2\pi\sum_{i=1}^{3}\frac{j_i}{N_i}x_i\right)\right] \\
&+\sum_{i=1}^{3} -\left(\frac{2\pi}{L_y}j_y\right)\cdot\sin(k_xx)\cdot\cos(k_yy)\cdot\sin(k_zz) \\
&\cdot\left[a_{j_i}^{yy}\cdot\cos\left(2\pi\sum_{i=1}^{3}\frac{j_i}{N_i}x_i\right) - b_{j_i}^{yy}\cdot\sin\left(2\pi\sum_{i=1}^{3}\frac{j_i}{N_i}x_i\right)\right] \\
&+\sum_{i=1}^{3} -\left(\frac{2\pi}{L_z}j_z\right)\cdot\sin(k_xx)\cdot\sin(k_yy)\cdot\cos(k_zz) \\
&\cdot\left.\left[a_{j_i}^{zz}\cdot\cos\left(2\pi\sum_{i=1}^{3}\frac{j_i}{N_i}x_i\right) - b_{j_i}^{zz}\cdot\sin\left(2\pi\sum_{i=1}^{3}\frac{j_i}{N_i}x_i\right)\right]\right\}
\end{aligned} \tag{B.20}
$$

As with the case of potential energy contribution to the Hamiltonian in eq. B.10 the kinetic energy contribution in eq. B.20 has now become a series of analytic integrals which may be solved with the aid of eq. B.11 and B.12. The C/C++ code used to calculate the analytic integrals of the triple sin/cos functions are shown at the end of this section.

Practical evaluation of the Schrödinger wavefunctions

The Schrödinger wavefunction solver code can be considered to be a "black box" system where the inputs are the confining potential calculated for the three dimensional computer model on an evenly spaced grid and the piezoelectric potential in the system due to the local strain effects observed in the compound semiconductor quantum dot model.

Initially the files containing the potential energy grid resulting from the Ter-

soff calculations and the piezoelectric potential grid from the strain calculations are read into the computer program. The first step of the algorithm is to calculate the kinetic energy contribution to the Hamiltonian and the effective masses as described above using the analytic integral code. The potential part of the Hamiltonian is then calculated from the confining potential data and the analytic integral code and the 2 Hamiltonian contributions are combined. The code then diagonalises the Hamiltonian to obtain the eigenvalues of the secular equation using the LAPACK numerical library. This process is repeated for increasing values of n (eq. B.4) until the energy difference between the previous and current values of the ground s and double degenerate p state wavefunctions has been reduced to within a reasonable tolerance (e.g. 0.5meV). This iterative solution is generally found within 6 steps.

A typical run of the Schrödinger solver software for an 800,000 atom model of a strained quantum dot model takes 40 hours on a single processor 1GHz desktop Pentium III processor with 1.5Gb of 200MHz RAM. The code uses the Fastest Fourier Transform in the West (FFTW) library code and the BLAS and LAPACK libraries for the diagonalisation of complex matrices.

Analytic triple integrals

The analytic triple integrals of the sine and cosine components described above can be found in standard integral tables and have been included in the computer code. The computer code has been designed with the if...else statements stacked to "fall through" in order of likelihood of execution. This makes for a moderate time saving compared to writing the execution in an arbitrary order. They are simplified by taking into account the various cases of when $k' = k$, $k^3 = 0$, etc.

Four computer sub routines were devised and named *integrateSinSinCos*, *integrateSinCosSin*, *integrateSinCosCos* and *integrateSinSinSin* which are called with the values k', k, k^3, L and r. The value r represents the resolution and the evaluations performed by the subroutines are described in the included computer code below.

Conclusions

The above derivations and the code listings below have been used to successfully study the effect of the atomic composition and the piezoelectric field observed locally for an $In_XGa_{1-X}As/GaAs$ quantum dot[1]. The predictions from

the quantum dot model identified a splitting of the doubly degenerate p-state wavefunctions by upto 7meV and a spatial anisotropy of the wavefunctions confined within the quantum dot. These predictions mirrored experimental findings from photoluminescence and intersubband absorbtion experiments which have identified a 7.9meV splitting between the excited states[2]. The analytic nature of the calculations and the secure and timely execution of the code due to good algorithm design and memory management techniques has allowed for the theoretical prediction of experimental observations. These results have provided an excellent level of confidence in both the experimental findings and the modelling techniques used here.

Code

The first section of code shown below is the C/C++ code for the calculation of the analytical integral of the term $\sin(k')\sin(k)\cos(k^3)$:

```
// ********************************************************
// Analytic Integration of Sin(k_prime) * Sin(k) * Cos(k3)
double
IntegrateSinSinCos (double k_prime, double k, double k3,
        double L, int res)
{
  double sum = 0.0;
  res--; // To correct for the Fourier transform limits

 if (k3 == 0.0) {
   if (k_prime == k)
     return ((double) L / (double) 2);
   else
     return 0.0;
 }
 else {
   if (k_prime == k) {
     if ((2 * k_prime) == k3) {
               sum -= sin (k3 * (res)) / (double) (2 * k3);
               sum *= (L / (res));
               sum += 0.25 * L;
               return ((double) sum);
     }
     else {
               sum += sin (k3 * (res)) / (double) (2 * k3);
               sum -= 0.25 * sin (((2 * k_prime) + k3) * (res))
                 / (double) ((2 * k_prime) + k3);
               sum -= 0.25 * sin (((2 * k_prime) - k3) * (res))
                 / (double) ((2 * k_prime) - k3);
              return ((double) L * sum) / (res);
   }
 }
 else {
   if ((k_prime - k3) == k) {
             sum += 0.25 * sin ((k_prime - k + k3) * (res))
               / (double) (k_prime - k + k3);
```

```
                sum -= 0.25 * sin ((k_prime + k + k3) * (res))
                  / (double) (k_prime + k + k3);
                sum *= (L / (res));
                sum += 0.25 * L;
                return ((double) sum);
        }
        else if ((k_prime - k3) == -k) {
                sum += 0.25 * sin ((k_prime - k + k3) * (res))
                  / (double) (k_prime - k + k3);
                sum -= 0.25 * sin ((k_prime + k + k3) * (res))
                  / (double) (k_prime + k + k3);
                sum *= (L / (res));
                sum += 0.25 * L;
                return ((double) sum);
        }
        else if ((k_prime + k3) == k) {
                sum += 0.25 * sin ((k_prime - k - k3) * (res))
                  / (double) (k_prime - k - k3);
                sum -= 0.25 * sin ((k_prime + k - k3) * (res))
                  / (double) (k_prime + k - k3);
                sum *= (L / (res));
                sum += 0.25 * L;
                return ((double) sum);
        }
        else if ((k_prime + k3) == -k) {
                sum += 0.25 * sin ((k_prime - k - k3) * (res))
                  / (double) (k_prime - k - k3);
                sum -= 0.25 * sin ((k_prime + k - k3) * (res))
                  / (double) (k_prime + k - k3);
                sum *= (L / (res));
                sum -= 0.25 * L;
                return ((double) sum);
        }
        else {
                sum += 0.25 * sin ((k_prime - k + k3) * (res))
                  / (double) (k_prime - k + k3);
                sum += 0.25 * sin ((k_prime - k - k3) * (res))
                  / (double) (k_prime - k - k3);
                sum -= 0.25 * sin ((k_prime + k + k3) * (res))
                  / (double) (k_prime + k + k3);
                sum -= 0.25 * sin ((k_prime + k - k3) * (res))
                  / (double) (k_prime + k - k3);
                return ((double) L * sum) / (res);
        }
      }
    }
    return 0.0;
}
```

The next section of code shown is for the analytical integration of the term $\sin(k')\cos(k)\cos(k^3)$:

```
// ******************************************************
// Analytic Integration of Sin(k_prime) * Cos(k) * Cos(k3)
double
IntegrateSinCosCos (double k_prime, double k, double k3,
        double L, int res)
{
```

```
double sum = 0.0;
res--; // To correct for the Fourier transform limits

if (k3 == 0.0) {
  if (k_prime == k)
    return 0.0;
  else {
    sum -= 0.5 * (cos ((k_prime + k) * (res)) - 1)
              / (double) (k_prime + k);
    sum += 0.5 * (cos ((k - k_prime) * (res)) - 1)
              / (double) (k - k_prime);
    return ((double) L * sum) / (res);
  }
}
else {
  if (k_prime == k) {
    if ((2 * k_prime) == k3)
              return 0.0;
    else {
              sum -= 0.25 * (cos (((2 * k_prime) + k3) * (res)) - 1)
                / (double) ((2 * k_prime) + k3);
              sum -= 0.25 * (cos (((2 * k_prime) - k3) * (res)) - 1)
                / (double) ((2 * k_prime) - k3);
              return ((double) L * sum) / (res);
    }
  }
  else {
    if ((k_prime - k) == k3) {
              sum -= 0.25 * (cos ((k_prime + k + k3) * (res)) - 1)
                / (double) (k_prime + k + k3);
              sum += 0.25 * (cos ((k_prime - k + k3) * (res)) - 1)
                / (double) (k_prime - k + k3);
              sum += 0.25;
              return ((double) L * sum) / (res);
    }
    else if ((k_prime - k) == -k3) {
              sum -= 0.25 * (cos ((k_prime + k + k3) * (res)) - 1)
                / (double) (k_prime + k + k3);
              sum += 0.25 * (cos ((k_prime - k + k3) * (res)) - 1)
                / (double) (k_prime - k + k3);
              sum -= 0.25;
              return ((double) L * sum) / (res);
    }
    else if ((k_prime + k) == k3) {
              sum -= 0.25 * (cos ((k_prime + k - k3) * (res)) - 1)
                / (double) (k_prime + k - k3);
              sum += 0.25 * (cos ((k_prime - k - k3) * (res)) - 1)
                / (double) (k_prime - k - k3);
              sum += 0.25;
              return ((double) L * sum) / (res);
    }
    else if ((k_prime + k) == -k3) {
              sum -= 0.25 * (cos ((k_prime + k - k3) * (res)) - 1)
                / (double) (k_prime + k - k3);
              sum += 0.25 * (cos ((k_prime - k - k3) * (res)) - 1)
                / (double) (k_prime - k - k3);
              sum -= 0.25;
              return ((double) L * sum) / (res);
    }
    else {
              sum -= 0.25 * (cos ((k_prime - k + k3) * (res)) - 1)
                / (double) (k_prime - k + k3);
              sum -= 0.25 * (cos ((k_prime - k - k3) * (res)) - 1)
```

```
                / (double) (k_prime - k - k3);
              sum -= 0.25 * (cos ((k_prime + k + k3) * (res)) - 1)
                / (double) (k_prime + k + k3);
              sum -= 0.25 * (cos ((k_prime + k - k3) * (res)) - 1)
                / (double) (k_prime + k - k3);
              return ((double) L * sum) / (res);
        }
      }
    }
    return 0.0;
}
```

The third code section shown below performs the analytical integration of the term $\sin(k')\cos(k)\sin(k^3)$:

```
// ********************************************************
// Analytic Integration of Sin(k_prime) * Cos(k) * Sin(k3)
double
IntegrateSinCosSin (double k_prime, double k, double k3,
        double L, int res)
{
  double sum;
  res--; // To correct for the Fourier transform limits

  if (k3 == 0.0) {
    return 0.0;
  }
  else {
    if (k_prime == k) {
      if ((2 * k_prime) == k3) {
              sum += 0.25;
              return ((double) L * sum) / (res);
      }
      else {
              sum = 0.0;
              sum -= 0.25 * (sin (((2 * k_prime) + k3) * (res)))
                / (double) ((2 * k_prime) + k3);
              sum += 0.25 * (sin (((2 * k_prime) - k3) * (res)))
                / (double) ((2 * k_prime) - k3);
              return ((double) L * sum) / (res);
      }
    }
    else {
      if ((k_prime - k3) == k) {
              sum += 0.25 * (sin ((k_prime - k + k3) * (res)))
                / (double) (k_prime - k + k3);
              sum -= 0.25 * (sin ((k_prime + k + k3) * (res)))
                / (double) (k_prime + k + k3);
              sum -= 0.25;
              return ((double) L * sum) / (res);
      }
      else if ((k_prime - k3) == -k) {
              sum += 0.25 * (sin ((k_prime - k + k3) * (res)))
                / (double) (k_prime - k + k3);
              sum -= 0.25 * (sin ((k_prime + k + k3) * (res)))
                / (double) (k_prime + k + k3);
              sum += 0.25;
              return ((double) L * sum) / (res);
      }
      else if ((k_prime + k3) == k) {
```

```
                sum -= 0.25 * (sin ((k_prime - k - k3) * (res)))
                  / (double) (k_prime - k - k3);
                sum += 0.25 * (sin ((k_prime + k - k3) * (res)))
                  / (double) (k_prime + k - k3);
                sum += 0.25;
                return ((double) L * sum) / (res);
        }
        else if ((k_prime + k3) == -k) {
                sum -= 0.25 * (sin ((k_prime - k - k3) * (res)))
                  / (double) (k_prime - k - k3);
                sum += 0.25 * (sin ((k_prime + k - k3) * (res)))
                  / (double) (k_prime + k - k3);
                sum -= 0.25;
                return ((double) L * sum) / (res);
        }
        else {
                sum -= 0.25 * (sin ((k_prime - k + k3) * (res)))
                  / (double) (k_prime - k + k3);
                sum += 0.25 * (sin ((k_prime - k - k3) * (res)))
                  / (double) (k_prime - k - k3);
                sum -= 0.25 * (sin ((k_prime + k + k3) * (res)))
                  / (double) (k_prime + k + k3);
                sum += 0.25 * (sin ((k_prime + k - k3) * (res)))
                  / (double) (k_prime + k - k3);
                return ((double) L * sum) / (res);
        }
      }
    }
    return 0.0;
}
```

The final section of code shown below is for the analytical integral of the term $\sin(k')\sin(k)\sin(k^3)$:

```
// ********************************************************
// Analytic Integration of Sin(k_prime) * Sin(k) * Sin(k3)
double
IntegrateSinSinSin (double k_prime, double k, double k3,
        double L, int res)
{
  double sum;
  res--; // To correct for the Fourier transform limits

  if (k3 == 0.0) {
    return 0.0;
  }
  else {
    if (k_prime == k) {
      if ((2 * k_prime) == k3) {
                sum -= (cos (k3 * (res)) - 1) / (double) (2 * k3);
                sum *= (L / (res));
                sum -= 0.25 * L;
                return ((double) sum);
      }
      else {
                sum -= (cos (k3 * (res)) - 1) / (double) (2 * k3);
                sum += 0.25 * (cos (((2 * k_prime) + k3) * (res)) - 1)
                  / (double) ((2 * k_prime) + k3);
                sum -= 0.25 * (cos (((2 * k_prime) - k3) * (res)) - 1)
                  / (double) ((2 * k_prime) - k3);
```

```
                return ((double) L * sum) / (res);
        }
      }
      else {
        if ((k_prime - k3) == k) {
                sum -= 0.25 * (cos ((k_prime - k + k3) * (res)) - 1)
                  / (double) (k_prime - k + k3);
                sum += 0.25 * (cos ((k_prime + k + k3) * (res)) - 1)
                  / (double) (k_prime + k + k3);
                sum *= (L / (res));
                sum -= 0.25 * L;
                return ((double) sum);
        }
        else if ((k_prime - k3) == -k) {
                sum -= 0.25 * (cos ((k_prime - k + k3) * (res)) - 1)
                  / (double) (k_prime - k + k3);
                sum += 0.25 * (cos ((k_prime + k + k3) * (res)) - 1)
                  / (double) (k_prime + k + k3);
                sum *= (L / (res));
                sum += 0.25 * L;
                return ((double) sum);
        }
        else if ((k_prime + k3) == k) {
                sum -= 0.25 * (cos ((k_prime - k - k3) * (res)) - 1)
                  / (double) (k_prime - k - k3);
                sum += 0.25 * (cos ((k_prime + k - k3) * (res)) - 1)
                  / (double) (k_prime + k - k3);
                sum *= (L / (res));
                sum -= 0.25 * L;
                return ((double) sum);
        }
        else if ((k_prime + k3) == -k) {
                sum -= 0.25 * (cos ((k_prime - k - k3) * (res)) - 1)
                  / (double) (k_prime - k - k3);
                sum += 0.25 * (cos ((k_prime + k - k3) * (res)) - 1)
                  / (double) (k_prime + k - k3);
                sum *= (L / (res));
                sum += 0.25 * L;
                return ((double) sum);
        }
        else {
                sum -= 0.25 * (cos ((k_prime - k + k3) * (res)) - 1)
                  / (double) (k_prime - k + k3);
                sum += 0.25 * (cos ((k_prime - k - k3) * (res)) - 1)
                  / (double) (k_prime - k - k3);
                sum += 0.25 * (cos ((k_prime + k + k3) * (res)) - 1)
                  / (double) (k_prime + k + k3);
                sum -= 0.25 * (cos ((k_prime + k - k3) * (res)) - 1)
                  / (double) (k_prime + k - k3);
                return ((double) L * sum) / (res);
        }
      }
    }
    return 0.0;
}
```

Bibliography

[1] M. A. Migliorato, D. Powell, S. L. Liew, A. G. Cullis, M. Fearn, J. H. Jefferson, P. Navaretti, M. J. Steer, and M. Hopkinson, "Influence of composition on the piezoelectric fields and on the

conduction band energy levels of $In_XGa_{1-X}As/GaAs$ quantum dots," *J. Appl. Phys.*, vol. 96, p. 5169, 2004.

[2] M. A. Migliorato, D. Powell, E. A. Zibik, L. R. Wilson, M. Fearn, J. H. Jefferson, M. J. Steer, M. Hopkinson, and A. G. Cullis, "Anisotropy of the electron energy levels in $In_XGa_{1-X}As/GaAs$ quantum dots with non-uniform composition," *Physica E*, vol. 26, p. 436, 2005.

[3] M. A. Migliorato, "Atomistic modelling of InGaAs quantum dots with non-uniform composition," Ph.D. thesis, University of Sheffield, Department of Electronic and Electrical Engineering, Sheffield, UK. S1 3JD., 2003, see Appendix E.

[4] R. N. Bracewell, *The Fourier transform and its applications*. McGraw-Hill International Editions, 1986.

[5] J. Singh, *The physics of semiconductors and their heterostructures*. McGraw-Hill Inc., 1993.